TRANSIENT ANALYSIS AND VIBRATION SUPPRESSION OF A CRACKED ROTATING SHAFT WITH IDEAL AND NONIDEAL MOTOR PASSING THROUGH A CRITICAL SPEED

by

Surjani Suherman

Dissertation submitted to the Faculty of the

Virginia Polytechnic Institute and State University

in partial fulfillment of the requirements for the degree of

DOCTOR OF PHILOSOPHY

in

Civil Engineering

APPROVED

Raymond H. Plaut, Chairman

R. Gordon Kirk

Alfred L. Wicks

Siegfried M. Holzer

Scott L. Hendricks

April, 1996

Blacksburg, Virginia

Key words: critical speeds, rotating shaft, transient analysis, vibration control, ideal motor, nonideal motor

TRANSIENT ANALYSIS AND VIBRATION SUPPRESSION OF A CRACKED ROTATING SHAFT WITH IDEAL AND NONIDEAL MOTOR PASSING THROUGH A CRITICAL SPEED

by

Surjani Suherman

Raymond H. Plaut, Chairman

Civil Engineering

(ABSTRACT)

In the first part of this study, the dynamic behavior of a cracked rotating shaft with a rigid disk is analyzed, with an ideal and a nonideal motor, passing through its critical speed. The shaft contains a single transverse crack that is assumed to be either completely open or completely closed at any given time, depending on the curvature of the shaft at the cross section containing the crack. Flexible, damped supports and overhangs with a mass at one end are included. The supports are modeled with elastic springs and dashpots. The influence of gyroscopic moments of the disk (with an ideal motor) is investigated. For a nonideal motor, there is an interaction between the shaft and the motor.

Eccentricity of the disk, gravitational forces, and internal and external damping are included. The equations of motion and boundary conditions are derived by

Hamilton's Principle. To eliminate the spatial dependence, the Extended Galerkin Method is applied. Longitudinal vibration, shear deformation and torsional vibration are neglected.

In the second part of this study, the vibration suppression of a cracked, simply supported, rotating shaft with a rigid disk is discussed, with an ideal and a nonideal motor, passing through the critical speed. The use of a flexible internal constraint is introduced to suppress the vibration. By activating this additional internal support, the shaft is prevented from passing its critical speed. Transient motions occur at the time of activation or deactivation of the constraint. The maximum displacement of the shaft during acceleration (run-up) or deceleration (coast-down) can be reduced significantly by appropriate application of this flexible internal support.

ACKNOWLEDGMENTS

I would like to express my sincere gratitude to my advisor, Dr. Raymond H. Plaut, for his guidance, patience, understanding, and support throughout my work on this research. His advice and expertise with respect to this dissertation were essential and highly appreciated.

I would also like to express my appreciation to the members of my committee, Dr. R. Gordon Kirk, Dr. Alfred L. Wicks, Dr. Scott L. Hendricks, and Dr. Siegfried M. Holzer, for their support and suggestions. Dr. Hendricks helped with the derivation of the equations of motion, and Dr. Kirk with his expertise in rotordynamics gave useful opinions on the research. Also, I would like to thank Dr. J. Wauer from the University of Karlsruhe, Germany, for his advice and guidance on nonideal motors during his visit at Virginia Tech.

I gratefully acknowledge the National Science Foundation for supporting this research under Grant No. MSS-9114529.

I would like to thank my husband for his love and support throughout the years of this study. Finally, I would like to dedicate this work to my parents.

TABLE OF CONTENTS

CHAPTER 4. VIBRATION SUPPRESSION WITH THE USE OF AN INTERNAL FLEXIBLE CONSTRAINT

LIST OF FIGURES

LIST OF TABLES

NOMENCLATURE

a: crack height

b, $\tilde{b}$: dimensional and nondimensional crack location (p. 35)

c, $\tilde{c}$: dimensional and nondimensional disk location (p. 35)

c_{44}, c_{55}, $\tilde{c}_{44}$, $\tilde{c}_{55}$: dimensional and nondimensional reciprocals of stiffness coefficients k_{44}, k_{55} (p. 36)

d_e, $\tilde{d}_e$: dimensional and nondimensional external damping coefficient (p. 36)

d_i, $\tilde{d}_i$: dimensional and nondimensional internal damping coefficient (p. 36)

d_s: diameter of shaft

e_d, $\tilde{e}_d$: dimensional and nondimensional disk eccentricity (p. 35)

E: Young's modulus

g: gravitational constant

G: shear modulus of shaft

I: cross -sectional moment of inertia of shaft

I_d: diametral mass moment of inertia of disk

I_p: polar mass moment of inertia of disk

I_{dc}: diametral mass moment of inertia of overhung disk

I_{pc}: polar mass moment of inertia of overhung disk

L: length of shaft

l_1, $\tilde{l}_1$: dimensional and nondimensional length of left overhang (p. 35)

l_2, $\tilde{l}_2$: dimensional and nondimensional length of right overhang (p. 35)

m, $\tilde{m}$: dimensional and nondimensional disk mass (p. 35)

m_b, $\tilde{m}_b$: dimensional and nondimensional non-rotating mass at supports (p. 36)

m_c, $\tilde{m}_c$: dimensional and nondimensional mass of disk on right overhang (p. 36)

p, $\tilde{p}$: dimensional and nondimensional support damping coefficient (p. 36)

R: nondimensional radius of displacement

r_s, $\tilde{r}_s$: dimensional and nondimensional radius of shaft (p. 35)

r_d, $\tilde{r}_d$: dimensional and nondimensional radius of disk (p. 35)

s, $\tilde{s}$: dimensional and nondimensional support stiffness coefficient (p. 36)

s_i, $\tilde{s}_i$: dimensional and nondimensional internal support stiffness (p. 131)

t: time

v, $\tilde{v}$: dimensional and nondimensional transverse displacement in η-direction (p. 35)

w, $\tilde{w}$: dimensional and nondimensional transverse displacement in ζ-direction (p. 35)

x, $\tilde{x}$: dimensional and nondimensional location of measurement (p. 35)

x_i, $\tilde{x}_i$: dimensional and nondimensional internal support location (p. 131)

x, y, z: fixed coordinates

z: nondimensional transverse displacement in vertical direction (p. 36)

z_{max} : nondimensional maximum z-displacement

α : restoring torque factor

β : range factor

δ_d : disk eccentricity angle

ε: crack width parameter

κ : motor torque

κ_b : restoring torque

λ: nondimensional angular acceleration/deceleration rate for ideal motor (p. 36)

Λ: crack condition parameter; Λ=1 for open crack, Λ=0 for closed crack

μ, $\tilde{\mu}$: dimensional and nondimensional shaft mass per unit length (p. 36)

θ : rotational angle (in radians)

$\dot{\theta}$: nondimensional angular velocity

$\ddot{\theta}$: nondimensional angular acceleration

ν : Poisson's ratio

ρ : density of shaft

τ : nondimensional time (p. 36)

τ_{cr} : nondimensional time when the angular velocity passes the critical speed

τ_{max} : nondimensional time corresponding to z_{max}

ξ, η, ζ : shaft coordinates

$\bar{\upsilon}_0$, υ_0 : dimensional and nondimensional initial motor torque (p. 101)

$\bar{\upsilon}_1$, υ_1 : dimensional and nondimensional gradient of motor torque (p. 101)

Ω : nondimensional angular velocity (p. 36)

Ω_{cr} : first critical speed

Note: in the figures, all parameters are nondimensional (tilde is left off).

CHAPTER 1

INTRODUCTION

1.1. Scope

There are two major parts of this study, (i) the analysis of the dynamic behavior and (ii) the vibration suppression of a cracked rotating shaft with a rigid disk, driven by an ideal or a nonideal motor, passing through the first critical speed. In the system with a nonideal motor, there is an interaction between the shaft and the motor. The shaft has a single transverse crack that is assumed to be either completely open or completely closed at any given time, depending on the curvature of the shaft at the cracked cross section.

Eccentricity of the disk, gravitational forces, and internal and external damping are included. The equations of motion and boundary conditions are derived by Hamilton's Principle. The Extended Galerkin Method is utilized to eliminate the spatial dependence of the solution, and the resulting equations are integrated numerically by an Adams-Moulton method. Longitudinal vibration, shear deformation, and torsional vibration are neglected.

The transient motion of a cracked rotating shaft passing through the first critical speed is analyzed in Chapters 2 and 3 for ideal and nonideal motors, respectively. The

shaft is supported by flexible supports, modeled by elastic springs and dashpots. The influence of the support stiffness and damping, the disk eccentricity angle, and the external and internal damping are examined. Also, the effect of overhangs with a mass at one end is discussed. The effect of the gyroscopic moments of the disk is studied for the case with an ideal motor. The shaft with an ideal motor is accelerated or decelerated, passing through the critical speed. The detection of a crack is possible by monitoring the dynamic behavior of the rotating shaft.

The interaction between the motor and the rotating shaft is included in the equations of motion for the system with a nonideal motor, whose angular velocity is not specified. The dynamic behavior of the cracked rotating shaft with a nonideal motor is investigated during run-up and coast-down, passing through the critical speed. Different motor characteristics during run-up are studied. During coast-down, the motor torque is assumed to be zero, and the shaft rotates until it stops.

As is widely known, large displacements may occur when the shaft passes a critical speed. The use of an additional flexible constraint is introduced in chapter 4 to suppress this vibration for cases with and without an ideal motor. By activating the additional internal support, the shaft speed is prevented from coinciding with the critical speed. Transient motion occurs due to the switching. The influence of the switching type, the motor characteristic, the external damping, and the internal support stiffness and location are studied.

The results are illustrated in graphs and tables. Based on those results, the conclusions are drawn in chapter 5. Finally, suggestions for future research are presented.

1.2. Literature Review

Extensive analytical and experimental studies of rotating shafts with cracks have been carried out in recent years. A literature review on the dynamics of cracked rotors was written by Wauer (1990b), including crack modeling and crack detection procedures. Dimarogonas (1995) also reviewed vibration monitoring of cracked rotating shafts.

In Gasch's paper (1976) that studied the dynamic behavior of a cracked rotor with a disk, the crack was replaced by a simple mechanism to describe the breathing action. Schmied and Krämer (1984) presented the calculation of vibrational behavior of a rotor with a cross-sectional crack, where the opening and closing of the crack was described by a certain function. Using a finite element model, Nelson and Nataraj (1986) described analytically the dynamics of a rotor with a transverse crack. Baschmid et al. (1984) also used a finite element model to investigate the unbalance effects on a cracked rotor. The unbalance could reduce the vibration levels of a cracked rotor passing through a critical speed.

Ying (1987) studied the transient whirling of a rotor shaft with an unbalanced disk. He showed that for rotating shafts with low acceleration and low damping, the

maximum response decreases as the acceleration increases. Wang et al. (1987) discussed the response of a simple rotor with a transverse surface crack. They also showed the transitional response of the rotor passing through a subcritical speed. Wauer and Wei (1991) investigated the flexural vibrations of a horizontal, rotating, curved shaft. The shaft was simply supported, axially restrained, and rotated at a constant speed. Gao and Zhu (1992) analyzed the vibrational behavior of a vertical rotor containing a transverse crack with unbalanced excitation. It was suggested that the phenomenon of parametric resonance can be used to diagnose a crack.

Ishida and Yamamoto (1993) analyzed vibrations of a rotating shaft with a transverse crack at a secondary critical speed. They found that resonance occurred when the gravity and an unbalance force worked simultaneously. The oscillation was stable at this secondary critical speed. Ishida et al. (1994) continued to study the vibrations of a horizontal rotating shaft with a transverse crack at the major critical speed. They found that the angular position of the unbalance relative to the crack face influenced the shape of the resonance curve and the stability of the shaft. In another paper, Ishida et al. (1995) observed the vibration characteristics of the 3/2-order super-subharmonic and 1/2-order subharmonic resonances of a cracked rotor. They showed that these two kinds of resonances have similar characteristics.

Dimarogonas (1993) considered a bilinear analysis for closing cracks in a rotating shaft. He suggested that a closing crack can be detected by using the spectrum response for a given forcing function. Horrigan et al. (1993) used finite element analysis to study

modal aspects of cracks in rotors. Coupled torsional and bending vibrations of a rotor with an open crack were examined by Ostachowicz and Krawczuk (1992). The stiffness matrix was developed by using finite element and fracture mechanics techniques. Plaut and Wauer (1995) considered coupled flexural and torsional oscillations of an unbalanced rotating shaft and analyzed its stability.

Papadopoulos and Dimarogonas (1987a, b, 1988a, b, 1992) published a series of papers on rotating and non-rotating shafts with an open crack. They derived a local flexibility matrix that depends on the crack depth. The nondiagonal terms of this matrix cause coupling between the longitudinal, torsional, and bending vibrations. The stiffness of the system depends on the crack depth and the slenderness ratio of the shaft. Wauer (1986) studied secondary effects in transient vibrations of rotating shafts during passage through a critical speed. He considered non-symmetry and the torsional stiffness of the shaft. In another paper, Wauer (1990a) derived the equations of motion for a cracked, rotating, Timoshenko shaft including extension and torsion. He formulated the open-close conditions and replaced the crack with a force discontinuity at the crack location. Based on Wauer's derivation, Andruet (1991) and Plaut et al. (1994) analyzed the behavior of a rotating Euler-Bernoulli shaft with a breathing crack under acceleration and deceleration through a critical speed. They neglected torsional and longitudinal vibrations.

Kato et al. (1992) derived equations of motion for a shaft-rotor system with variable rotating speed. They examined the difference between Lagrange's and Euler's

equations of motion and indicated that both lead to an equivalent result. Jun et al. (1992a, b, 1993) and Lee et al. (1992a, b) derived the equations of motion for a simple rotor with a breathing crack, based on fracture mechanics. They used the switching crack model having two different stiffnesses to model the breathing condition.

When the rotor reaches the critical speed, the amplitudes may become large. This is an important condition for the design of high-speed rotors and has been studied extensively. Researchers have investigated the behavior of the rotor during acceleration and deceleration through a critical speed, and have evaluated the maximum amplitude of the shaft. Among them, Lewis (1932) derived an exact solution for a single-degree-of-freedom system with linear damping during acceleration through a critical speed. Under different rates of constant angular acceleration and deceleration, Baker (1939) investigated the vibration of an unbalanced rotor. He also discussed the effect of the spring constant, damping, and mass. Capello (1967) also studied the transient motion of a rotor during acceleration through a critical speed. A closed-form solution obtained by an energy approach was used by Bodger (1967) to solve the problem of a single-degree-of-freedom rotor decelerating slowly through a critical speed. Aiba (1976) considered the vibration of a rotating shaft passing through a critical speed under a constant or a variable angular acceleration, and the gyroscopic effect of the rotor. He solved the equations of motion using Runge-Kutta-Gill's numerical method.

Naveh and Brach (1977) analyzed the response of an eccentric rotating shaft and disk with an exponential transition of the angular velocity through a critical speed. The

response had larger amplitudes compared to the response under a linear transition of angular velocity. Gasch et al. (1979) considered the bending vibrational behavior of a flexible rotor passing a critical speed under a driving torque. They showed that the effect of the torsional flexibility of the shaft on the bending response was negligible. The vibration of a rotating shaft passing through two critical speeds successively under uniform acceleration was analyzed by Yanabe and Tamura (1980). They neglected the mass of the shaft and the effects of gyroscopic moments and gravity forces. Tsuchiya (1982) also worked on the nonstationary oscillations of a rotor passing through a critical speed. His analysis was based on the method of multiple scales and the method of matched asymptotic expansions.

Ishida et al. (1989) dealt with the vibration of a flexible rotating shaft with nonlinear spring characteristics during constant acceleration and deceleration through a critical speed. They examined the influence of the angular acceleration and angular position of the unbalance at the start of the acceleration. They ascertained the validity of theoretical results by experiments. Lee et al. (1992a) examined the transient vibration of asymmetric rotor systems during acceleration passing through critical speeds. They solved the dynamic equations of a rotor system by a finite element model. Genta and Delprete (1995) analyzed the dynamic behavior of rotors under unbalance effects and imposed angular acceleration. They included the nonlinear behavior of the rotor and its geometrical or inertial anisotropy. The rotor was considered as being torsionally stiff.

The transient analysis of a vertical cracked rotor passing through a critical speed was studied by Jiang et al. (1990, 1992). They used perturbation solutions and Runge-Kutta-Fehlberg numerical integration. Suherman (1992) and Suherman and Plaut (1993) investigated the nonstationary behavior of a cracked rotating shaft with a disk. They examined flexural and torsional vibration of the shaft as it was accelerated or decelerated through a critical speed. Galerkin's method was applied and the equations of motion were solved numerically. Sekhar and Prabhu (1994b) also discussed the transient vibration of a cracked rotor passing through its critical speed, using the finite element method. From their investigation, a crack caused fast oscillations near the critical speed. In another paper, Sekhar and Prabhu (1994a) presented the vibration and stress fluctuations in cracked shafts. A finite element analysis was used for free and forced vibrations.

Many investigations have been carried out to detect shaft cracks as early as possible. Muszynska (1982) suggested the on-line monitoring of synchronous 1x and nonsynchronous 2x rotor vibrations as a method to detect a shaft crack. She presented analytical and experimental results for nonsymmetrical rotating shafts with gaping or breathing cracks and constant angular velocity. It was shown that increased nonsymmetry of the cracked shaft decreased the damping level. The crack was modeled by local changes in stiffness. Bently and Muszynska (1986) discussed the method of detection of rotor cracks by vibration monitoring. They also described the factors causing a crack on a shaft. Jialiu and Nanqei (1986) proposed a method to monitor the initiation

and development of a crack of a cantilevered rotor. They suggested that the third-order harmonic component of the unbalance response was the most effective monitoring quantity.

Detection of cracks in rotating Timoshenko shafts by using axial impulses at a constant angular speed was analyzed by Collins et al. (1991). The breathing conditions during motion were represented by generalized forces and moments. Free and forced longitudinal vibrations of a cantilevered bar with a transverse crack were also investigated by Collins et al. (1992). Liao and Gasch (1992) presented a new technique for detecting cracks in rotating shafts. They formed the difference between the actual state of the rotor and the reference state in the time domain before applying the Fast Fourier Transform.

In another study, Muszynska et al. (1992) identified torsional vibrations, monitored along with lateral vibrations, that could be useful in early detection of a cracking shaft. Iwatsubo et al. (1992) detected a transverse crack in a rotor shaft by adding an external force, e.g., a periodic or impact force. In addition to the experimental analysis, they also investigated the response numerically by using the finite element method. Söffker et al. (1993) developed another method to detect shaft cracks in rotors. They applied the theory of Lyapunov exponents for nonsmooth dynamical systems and found chaotic motions and strange attractors in the case of a cracked rotor.

Kemke et al. (1994) did theoretical and experimental studies to utilize the dynamic behavior of cracked rotating shafts for detecting cracks based on signal analysis.

On the other hand, Müller et al. (1994) used state observers and Kavarana and Kirk (1995) used the unbalance excitation technique to detect rotor cracks. Seibold et al. (1995) also dealt with the identification of cracks in rotors. Their procedure was based on the Extended Kalman Filter and the Instrumental Variables. Ratan et al. (1993, 1996) obtained the Fourier Transform of the cracked shaft response to be used in a residue vector to identify and locate the crack. Other studies on detection of rotor cracks were performed by Bently (1993), Dirr et al. (1994), and Meng and Hahn (1993).

Meng and Gasch (1992) discussed the nonlinear influence of the whirl speed on the stability and dynamic response of a cracked rotor. They considered the effects of speed ratio, stiffness change ratio, crack angle, and unbalance ratio. In Meng and Gasch (1993), they investigated the stability of a cracked flexible rotor supported on various journal bearings. They found that the unstable zones always lie within certain speed ratios, not dependent on the kind of bearings, but dependent on the speed ratio, stiffness change ratio, and mass ratio. Huang et al. (1993) evaluated the dynamic response and stability of a rotating shaft containing a breathing crack. They employed the energy approach to derive the equations of motion and showed that instability occurred depending on the crack depth and rotational speed. Shneerson (1993) also discussed the dynamic stability of a horizontal rotor with a crack.

The effect of support flexibility and damping on the synchronous response of a single-mass flexible rotor was analyzed by Kirk and Gunter (1972). In that study, they neglected the mass of the shaft, rotor acceleration, and disk gyroscopic moments. An

experimental study on the vibration of a rotor with a flexible damped support and a disk at the center was performed by Li-Tang and Qi-Han (1981). They analyzed the rotor during passage through the first and second critical speeds. On the other hand, Rajalingham et al. (1992) investigated the stability of rotors with flexible and damped supports. The effect of distributed bearing stiffness on the shaft critical speeds was studied by Craggs (1993). He used a finite element model and considered hydrodynamic bearings. A recent paper by Suherman and Plaut (1995) analyzed the effects of flexible supports and gyroscopic moments on a cracked shaft passing through a critical speed. The equations of motion and boundary conditions were derived with the use of Hamilton's Principle.

The nonstationary vibration of a rotor with gyroscopic effects passing through a critical speed was studied by Nonami and Miyashita (1978) analytically and experimentally. Their analysis used an asymptotic method. In another paper (1980), they continued the study with a rotating shaft on flexible supports. Nonami (1983a, b) used the finite element method to analyze the response of a distributed flexible rotor system passing through a critical speed with and without gyroscopic effects. Yanabe (1980) reported the effects of gyroscopic moments on the nonstationary vibration of a shaft passing through its critical speed at a uniform acceleration rate. He found that the maximum amplitude of the nonstationary vibration of the gyroscopic system becomes small.

The influence of gyroscopic effects on resonance avoidance during acceleration of unbalanced flexible rotors was examined by Zobnin et al. (1987). Chen and Ku (1992) showed that gyroscopic moments could enlarge the regions of dynamic instability and make the system unstable. Chang and Cheng (1993) included the gyroscopic effects in the analysis of the nonlinear dynamic behavior of a rotating shaft-disk system through its critical speeds. They assumed that torsional motion, longitudinal inertia, shear deformation of the shaft, and gravity were negligible, and the shaft was simply supported at both ends and rotated at a constant speed.

Khader (1995) evaluated the effects of the gyroscopic moments of a rotating cantilevered shaft with a rigid disk at its free end. The shaft was loaded by a follower axial load and a torque. El-Dannanh and Farghaly (1994) discussed the natural vibration of an open cracked shaft carrying elastically mounted end masses with flexible supports.

Young and Liou (1993) investigated the dynamic response of rotor-bearing systems with time-dependent spin rates. They used the Extended Galerkin's Method to eliminate the dependence on the spatial coordinates. This method was also used by Abdel-Mooty and Roorda (1991) and Yun and Lee (1993).

In recent years, there has been a tendency to analyze the nonstationary behavior of a rotating shaft more realistically with a rotor driven by a limited power supply (nonideal power supply). Therefore, the interaction between the energy source and the rotating shaft is included in the equations of motion. Macchia (1963) considered an unbalanced rotor driven by a nonideal motor passing through its critical speed. He neglected the

gyroscopic effects, and the influence of shaft mass and damping. He assumed that the driving torque was constant. A damped Laval rotor with a nonideal motor was studied by Christ (1969). He showed how the Sommerfeld effect depended on the interaction of the system and the motor.

Iwatsubo et al. (1972) investigated the nonstationary behavior of an asymmetric rotor with a limited power supply. They used an asymptotic method developed by Kononenko. Kotera (1974) and Iwatsubo (1976) studied the vibration of a rotor driven by a limited power supply passing through its critical speed. A rotor having uncoupled oscillations with two degrees of freedom under a driving torque was studied by Matsuura (1977). De Choudhury (1986) presented a method to analyze the torsional response relative to synchronous motor start-up with a variable-frequency power supply system. He analyzed the effects due to different average motor torques, pulsating torques containing different power-supply harmonics, and known compressor load torque.

Prabhu et al. (1987) analyzed the coast-down phenomenon in rotors by using an energy approach and a quasi-steady-state assumption to solve the nonlinear equations of motion. They showed the relationship between dynamic unbalance, damping, and deceleration during coast-down. In Fang and Luo (1989), the nonlinear and nonstationary characteristics of transient response of an asymmetric rotor system passing through critical speed were investigated under limited power supply. They considered the gyroscopic effect of the disk, the asymmetry of the rotor, and the initial phase angle of the static unbalance. Yamakawa (1988) and Yamakawa and Murakami (1989) discussed the

optimum design of an operating curve for a rotating shaft system with a limited power supply. They showed a case of a system which did not operate beyond the critical speed due to a shortage of power. Qiu (1992) derived the differential equations for coupling of the transient process for an electrical machine and transverse and torsional vibrations of the rotor. Dimentberg et al. (1994) also included a nonideal energy source for a simple one-degree-of-freedom system.

As is widely known, vibrations may become large when the system passes a critical speed. Some investigations to reduce this vibration have been reported in recent years. Iwata and Nonami (1984) investigated a vertical shaft with a central rotor and a flexible support at the base. At certain angular velocity, the support stiffness increased monotonically. By this method, the displacement near the second critical speed was reduced. Nagaya et al. (1987) described a method of active vibration control for passing through a critical speed of a rotating shaft by changing the stiffness of the supports with the use of memory metals. By heating and cooling the support springs, the variation of the supports was accomplished. Viderman and Porat (1987) studied an optimal control method for a flexible rotor during passage through resonance. They determined the necessary number of dampers and their optimal location. In another way, Turkstra and Semercigil (1993b) eliminated the resonance of a beam with the use of a switching tensile support. In another paper (1993a), they discussed the bending vibrations of a beam carrying an unbalanced rotor. They reduced the transient vibrations by an add-on switching support to change the bending rigidity of the system. Segalman et al. (1993)

changed the stiffness of a rotational spring to suppress resonance vibrations of a rigid disk pinned to a rotating rigid shaft. Dimentberg et al. (1994) discussed a method for reducing the displacement of a nonideal system by switching the system stiffness. A recent paper by Wauer and Suherman (1996) suggested a method to suppress the vibrations of a rotating shaft passing through the critical speed by switching the shaft stiffness. They assumed that the rotor was driven by a limited power supply and the shaft had unequal bending stiffnesses.

CHAPTER 2

GENERAL FORMULATION FOR IDEAL MOTOR

2.1. Physical Model

The geometry of the cracked rotating shaft with disk and overhang is shown in Fig. 2.1 horizontally. The idealized model consists of a uniform circular shaft of length L*, with radius r_s, diameter d_s, mass per unit length μ, Young's modulus E, shear modulus G, Poisson's ratio ν, and cross-sectional moment of inertia $I = 0.25\,\pi\,r_s^4$. A single disk, located at $x = c$, has mass m, radius r_d, mass polar moment of inertia $I_p = 0.5\,m\,r_d^2$, and diametral mass moment of inertia $I_d = 0.5\,I_p$. There is a transverse crack at $x = b$. At both supports ($x = 0$ and $x = L$), there are non-rotating masses m_b, springs with stiffness coefficients s, and dashpots with damping coefficients p. The resistance is assumed to be the same in all transverse directions at the supports. The lengths of the left overhang and the right overhang are denoted l_1 and l_2, respectively. At the end of the right overhang, there is a disk with mass m_c, radius r_c, mass polar moment of inertia $I_{pc} = 0.5\,m_c\,r_c^2$, and diametral mass moment of inertia $I_{dc} = 0.5\,I_{pc}$.

Two coordinate systems are used to define the model (Fig. 2.2), i.e., fixed

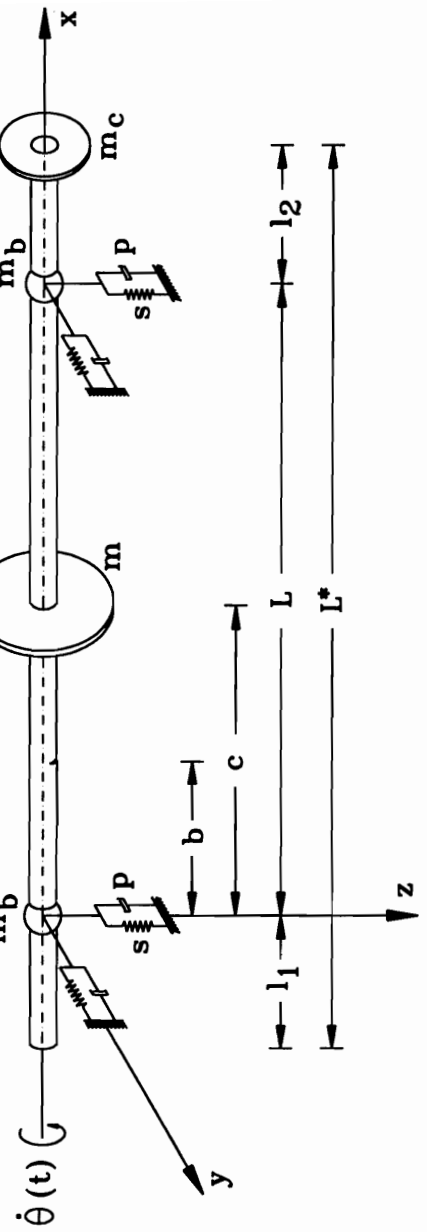

Fig. 2.1 Geometry of Cracked Shaft with Disk and Overhangs

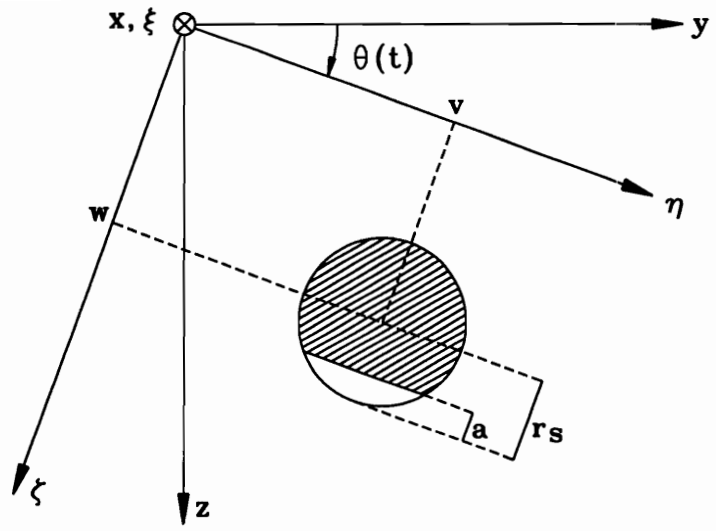

Fig. 2.2 Geometry of Cross Section with Crack

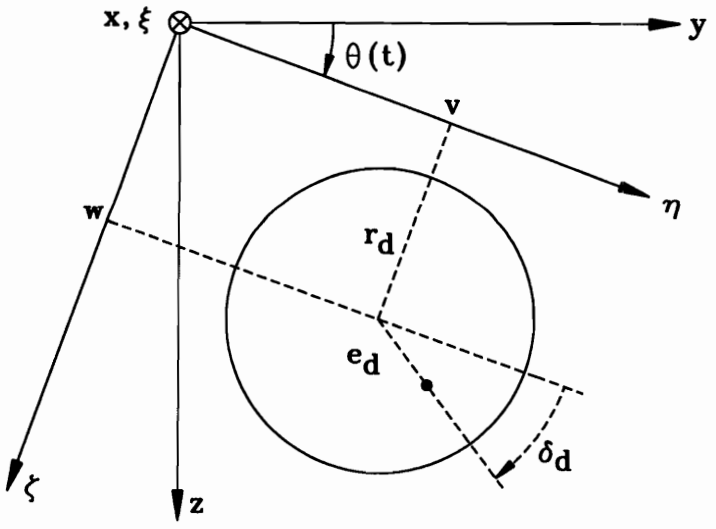

Fig. 2.3 Geometry of Disk

coordinates (x,y,z) that are stationary in space, and shaft coordinates (ξ, η, ζ) that rotate with the same angular velocity as the shaft. The x-axis coincides with the axial direction of the shaft $(\xi - \text{axis})$ horizontally, passing through the centroids of the cross sections. The z-axis is in the gravitational direction, positive downward. The angle of rotation $\theta(t)$ is measured from the y-axis, and the angular velocity and acceleration are $\dot{\theta}(t)$ and $\ddot{\theta}(t)$, respectively, where the overdot denotes differentiation.

The transverse displacements v(x,t) and w(x,t) are measured in the shaft coordinate system in relation to the transverse direction $(\eta-, \zeta - \text{axes, respectively})$. In this study, longitudinal displacements and shear deformation are neglected. However, gyroscopic moments are included.

The geometry of the shaft cross section with the crack is also shown in Fig. 2.2. The shaft has no eccentricity. The crack depth is 'a', and the crack face is parallel to the $\eta - \text{axis}$. Figure 2.3 shows the geometry of the circular disk, with eccentricity e_d and eccentricity angle δ_d. The ratio of e_d to r_d is assumed to be small; therefore, the mass polar moment of inertia of the disk can be calculated about its geometric center.

2.2. Analysis

The open crack causes a discontinuity in stiffness. To avoid the complexity of this discontinuity, the open crack is replaced by self-equilibrating moments

M_η, M_ζ, m_η, and m_ζ at the crack location, i.e., at $x = b_-$ and $x = b_+$, where $b_- = b - \varepsilon/2$, $b_+ = b + \varepsilon/2$, and ε is a small crack width parameter.

Based on statics, the deformation at the crack location can be described by (Wauer, 1990b)

$$\Delta \underline{u}(b) = \varepsilon S \underline{F} \tag{2.1}$$

and its time derivatives

$$\Delta \underline{u}_t(b) = \varepsilon \frac{S}{d_i} \underline{f} \tag{2.2}$$

where

$$\underline{u} = \left[v_x, w_x\right]^T, \quad \underline{F} = \left[M_\zeta, M_\eta\right]^T, \quad \underline{f} = \left[m_\zeta, m_\eta\right]^T, \quad \varepsilon = b_+ - b_-$$

$$S = \begin{bmatrix} \frac{1}{EI} & 0 \\ 0 & -\frac{1}{EI} \end{bmatrix} \tag{2.3}$$

Subscripts x and t denote partial derivatives. Combining the equations (2.1) and (2.2) gives

$$\Delta \underline{u}(b) + d_i \Delta \underline{u}_t(b) = \varepsilon S(\underline{F} + \underline{f}) \tag{2.4}$$

In other words, one can write

$$v_x(b_+, t) - v_x(b_-, t) = \varepsilon \frac{M_\zeta}{EI} \tag{2.5.a}$$

$$w_x(b_+, t) - w_x(b_-, t) = -\varepsilon \frac{M_\eta}{EI} \tag{2.5.b}$$

and

$$v_{tx}(b_+,t) - v_{tx}(b_-,t) = \varepsilon \frac{m_\zeta}{d_i\, EI} \tag{2.6.a}$$

$$w_{tx}(b_+,t) - w_{tx}(b_-,t) = -\varepsilon \frac{m_\eta}{d_i\, EI} \tag{2.6.b}$$

The transition conditions at the crack location for an open crack at time t are

$$\underline{P}(b_-,t) = \underline{P}(b_+,t) \tag{2.7}$$

$$\underline{P}(b_+,t) = K\left[\Delta \underline{u}(b,t) + d_i\, \Delta \underline{u}_t(b,t)\right] \tag{2.8}$$

where

$$\underline{P} = \begin{bmatrix} EI(v_{xx} + d_i\, v_{txx}) \\ EI(w_{xx} + d_i\, w_{txx}) \end{bmatrix} \text{ and } K = \begin{bmatrix} k_{44} & 0 \\ 0 & k_{55} \end{bmatrix} \tag{2.9}$$

The relation of the deformation and the transition condition is as follows:

$$\varepsilon S(\underline{F} + \underline{f}) = K^{-1}\, \underline{P}(b_+,t) \tag{2.10}$$

$$M_\zeta + m_\zeta = c_{44} \frac{(EI)^2}{\varepsilon}(v_{xx} + d_i\, v_{txx})\Big|_{x=b} \tag{2.11.a}$$

$$M_\eta + m_\eta = -c_{55} \frac{(EI)^2}{\varepsilon}(w_{xx} + d_i\, w_{txx})\Big|_{x=b} \tag{2.11.b}$$

The compliances c_{44} and c_{55} are the reciprocals of the stiffness coefficients k_{44} and k_{55}, respectively. They are obtained from Papadopoulos and Dimarogonas (1987) and are functions of the relative crack depth, i.e., the ratio of the crack depth and the shaft diameter.

The crack is assumed to be completely open or completely closed at any given time t, and is called a breathing crack. This condition depends on the curvature of the shaft at the crack location, and is defined as follows:

$$w_{xx}(b,t) \le 0 \quad \text{for an open crack} \tag{2.12.a}$$

$$w_{xx}(b,t) > 0 \quad \text{for a closed crack} \tag{2.12.b}$$

To indicate the state of the crack, the parameter Λ is used, where $\Lambda = 1$ if the crack is open and $\Lambda = 0$ if the crack is closed.

Two types of damping are considered, i.e., external damping with coefficient d_e and internal damping with coefficient d_i, in addition to the support damping. Shear and longitudinal deformations of the shaft are neglected. Euler-Bernoulli theory is applied. The gyroscopic effects of the disk are included, which influence the bending moment equations across the disk, stiffen the shaft, and raise the critical speeds (Rao, 1991). This is especially important when the disk location is not at the middle of a symmetrical shaft or when the disk is located on an overhang.

The equations of motion and boundary conditions for the cracked rotating shaft are derived by Hamilton's Principle (see derivation in Appendix A), which is given by

$$\delta \int_{t0}^{tl} (T - V)\,dt + \int_{t0}^{tl} \delta W\,dt = 0 \tag{2.13}$$

where T is the kinetic energy due to translation and rotation of the shaft and disk,

V is the potential energy due to gravity and the springs at the supports,

δW is the virtual work due to external damping, internal damping, support

damping, and the moments at the crack, and

t0, t1 are initial and final times, respectively.

In this study, the kinetic energy of the shaft due to rotation is neglected, because it is small. The equations of motion can be written as $GE_v = 0$ and $GE_w = 0$, where "v-equation":

$$GE_v \equiv EI\, v_{xxxx} + d_e\,\mu\left(v_t - \dot{\theta} w\right) + d_i\, EI\, v_{txxxx}$$

$$+\left[\mu + m\delta(x-c)\right]\left(v_{tt} - 2\dot{\theta} w_t - \dot{\theta}^2 v - \ddot{\theta} w\right)$$

$$+\Lambda\left[\delta'\left(x-b_+\right) - \delta'\left(x-b_-\right)\right]\left(c_{44}/\varepsilon\right)(EI)^2\left[v_{xx} + d_i v_{txx}\right]_{x=b}$$

$$-I_d\,\delta(x-c)\left(v_{ttxx} - 2\dot{\theta} w_{txx} - \dot{\theta}^2 v_{xx} - \ddot{\theta} w_{xx}\right)$$

$$-I_d\,\delta'(x-c)\left(v_{ttx} - 2\dot{\theta} w_{tx} - \dot{\theta}^2 v_x - \ddot{\theta} w_x\right)$$

$$-I_p\,\delta(x-c)\left(\dot{\theta}^2 v_{xx} + \dot{\theta} w_{txx} + \ddot{\theta} w_{xx}\right)$$

$$-I_p\,\delta'(x-c)\left(\dot{\theta}^2 v_x + \dot{\theta} w_{tx} + \ddot{\theta} w_x\right)$$

$$-\left[\mu + m\delta(x-c)\right] g \sin\theta - m e_d\,\delta(x-c)\left(\ddot{\theta}\sin\delta_d + \dot{\theta}^2\cos\delta_d\right) = 0 \qquad (2.14.a)$$

"w-equation":

$$GE_w \equiv EI\, w_{xxxx} + d_e\,\mu\left(w_t + \dot{\theta} v\right) + d_i\, EI\, w_{txxxx}$$

$$+\left[\mu + m\delta(x-c)\right]\left(w_{tt} + 2\dot{\theta} v_t - \dot{\theta}^2 w + \ddot{\theta} v\right)$$

$$+\Lambda\left[\delta'(x-b_+)-\delta'(x-b_-)\right](c_{55}/\varepsilon)(EI)^2\left[w_{xx}+d_i w_{txx}\right]_{x=b}$$

$$-I_d\,\delta(x-c)\left(w_{ttxx}+2\dot\theta\,v_{txx}-\dot\theta^2 w_{xx}+\ddot\theta\,v_{xx}\right)$$

$$-I_d\,\delta'(x-c)\left(w_{ttx}+2\dot\theta\,v_{tx}-\dot\theta^2 w_x+\ddot\theta\,v_x\right)$$

$$-I_p\,\delta(x-c)\left(\dot\theta^2 w_{xx}-\dot\theta\,v_{txx}\right)-I_p\,\delta'(x-c)\left(\dot\theta^2 w_x-\dot\theta\,v_{tx}\right)$$

$$-\left[\mu+m\delta(x-c)\right]g\cos\theta-me_d\,\delta(x-c)\left(-\ddot\theta\cos\delta_d+\dot\theta^2\sin\delta_d\right)=0 \qquad (2.14.b)$$

Here δ is the Dirac delta function and δ' is its derivative. Gyroscopic effects are associated with the terms involving I_p and I_d. The boundary conditions are as follows:

At $x=0$:

$$BC_1 \equiv EI\left(v_{xx}+d_i\,v_{txx}\right)\Big|_{x=0^+}-EI\left(v_{xx}+d_i\,v_{txx}\right)\Big|_{x=0^-}=0 \qquad (2.15.a)$$

$$BC_2 \equiv EI\left(w_{xx}+d_i\,w_{txx}\right)\Big|_{x=0^+}-EI\left(w_{xx}+d_i\,w_{txx}\right)\Big|_{x=0^-}=0 \qquad (2.15.b)$$

$$BC_3 \equiv EI\left(v_{xxx}+d_i\,v_{txxx}\right)\Big|_{x=0^+}-EI\left(v_{xxx}+d_i\,v_{txxx}\right)\Big|_{x=0^-}+p(v_t-\dot\theta\,w)$$
$$+m_b\left(v_{tt}-2\dot\theta\,w_t-\dot\theta^2 v-\ddot\theta\,w\right)+m_b\,g\,\sin\theta+sv=0 \qquad (2.15.c)$$

$$BC_4 \equiv EI\left(w_{xxx}+d_i\,w_{txxx}\right)\Big|_{x=0^+}-EI\left(w_{xxx}+d_i\,w_{txxx}\right)\Big|_{x=0^-}+p(w_t+\dot\theta\,v)$$
$$+m_b\left(w_{tt}+2\dot\theta\,v_t-\dot\theta^2 w+\ddot\theta\,v\right)+m_b\,g\,\cos\theta+sw=0 \qquad (2.15.d)$$

$$BC_5 \equiv v\big|_{x=0^+}-v\big|_{x=0^-}=0 \qquad (2.15.e)$$

$$BC_6 \equiv w|_{x=0^+} - w|_{x=0^-} = 0 \tag{2.15.f}$$

$$BC_7 \equiv v_x|_{x=0^+} - v_x|_{x=0^-} = 0 \tag{2.15.g}$$

$$BC_8 \equiv w_x|_{x=0^+} - w_x|_{x=0^-} = 0 \tag{2.15.h}$$

At $x = L$:

$$BC_9 \equiv EI\left(v_{xx} + d_i\, v_{txx}\right)\Big|_{x=L^+} - EI\left(v_{xx} + d_i\, v_{txx}\right)\Big|_{x=L^-} = 0 \tag{2.15.i}$$

$$BC_{10} \equiv EI\left(w_{xx} + d_i\, w_{txx}\right)\Big|_{x=L^+} - EI\left(w_{xx} + d_i\, w_{txx}\right)\Big|_{x=L^-} = 0 \tag{2.15.j}$$

$$BC_{11} \equiv EI\left(v_{xxx} + d_i\, v_{txxx}\right)\Big|_{x=L^+} - EI\left(v_{xxx} + d_i\, v_{txxx}\right)\Big|_{x=L^-} + p\,(v_t - \dot{\theta}\, w)$$
$$+ m_b\left(v_{tt} - 2\dot{\theta}\, w_t - \dot{\theta}^2 v - \ddot{\theta}\, w\right) + m_b\, g\, \sin\theta + s v = 0 \tag{2.15.k}$$

$$BC_{12} \equiv EI\left(w_{xxx} + d_i\, w_{txxx}\right)\Big|_{x=L^+} - EI\left(w_{xxx} + d_i\, w_{txxx}\right)\Big|_{x=L^-} + p(w_t + \dot{\theta}\, v)$$
$$+ m_b\left(w_{tt} + 2\dot{\theta}\, v_t - \dot{\theta}^2 w + \ddot{\theta}\, v\right) + m_b\, g\, \cos\theta + s v = 0 \tag{2.15.l}$$

$$BC_{13} \equiv v|_{x=L^+} - v|_{x=L^-} = 0 \tag{2.15.m}$$

$$BC_{14} \equiv w|_{x=L^+} - w|_{x=L^-} = 0 \tag{2.15.n}$$

$$BC_{15} \equiv v_x|_{x=L^+} - v_x|_{x=L^-} = 0 \tag{2.15.o}$$

$$BC_{16} \equiv w_x|_{x=L^+} - w_x|_{x=L^-} = 0 \tag{2.15.p}$$

At $x = -l_1$:

$$BC_{17} \equiv EI\left(v_{xx} + d_i\, v_{txx}\right) = 0 \tag{2.15.q}$$

$$BC_{18} \equiv EI\left(w_{xx} + d_i\, w_{txx}\right) = 0 \tag{2.15.r}$$

$$BC_{19} \equiv EI\left(v_{xxx} + d_i\, v_{txxx}\right) = 0 \tag{2.15.s}$$

$$BC_{20} \equiv EI\left(w_{xxx} + d_i\, w_{txxx}\right) = 0 \tag{2.15.t}$$

At $x = L + l_2$:

$$BC_{21} \equiv EI\left(v_{xx} + d_i\, v_{txx}\right) + I_{dc}\left(\ddot{v}_x - 2\dot{\theta}\dot{w}_x - \dot{\theta}^2 v_x - \ddot{\theta} w_x\right)$$

$$+ I_{pc}\left(\dot{\theta}^2 v_x + \dot{\theta}\dot{w}_x + \ddot{\theta} w_x\right) = 0 \tag{2.15.u}$$

$$BC_{22} \equiv EI\left(w_{xx} + d_i\, w_{txx}\right) + I_{dc}\left(\ddot{w}_x + 2\dot{\theta}\dot{v}_x - \dot{\theta}^2 w_x + \ddot{\theta} v_x\right)$$

$$+ I_{pc}\left(\dot{\theta}^2 w_x - \dot{\theta}\dot{v}_x\right) = 0 \tag{2.15.v}$$

$$BC_{23} \equiv EI\left(v_{xxx} + d_i\, v_{txxx}\right) - m_c\left(v_{tt} - 2\dot{\theta} w_t - \dot{\theta}^2 v - \ddot{\theta} w\right)$$

$$- m_c\, g \sin\theta = 0 \tag{2.15.w}$$

$$BC_{24} \equiv EI\left(w_{xxx} + d_i\, w_{txxx}\right) - m_c\left(w_{tt} + 2\dot{\theta} v_t - \dot{\theta}^2 w + \ddot{\theta} v\right)$$

$$- m_c\, g \cos\theta = 0 \tag{2.15.x}$$

Galerkin's method is used to eliminate the spatial variable in the equations of motion. The approximate displacement functions are chosen as

$$v(x,t) = \sum_{k=1}^{N} v_k(t) \sin\frac{k\pi x}{L} + a_1(t)\, x + a_2(t) \tag{2.16.a}$$

$$w(x,t) = \sum_{k=1}^{N} w_k(t) \sin\frac{k\pi x}{L} + a_3(t)\, x + a_4(t) \tag{2.16.b}$$

Some of the boundary conditions are not satisfied by these functions. Therefore, the Extended Galerkin Method (Leipholz (1987), Abdel-Moody and Roorda (1991), Young and Liou (1993), Yun and Lee (1993)) is used, as follows:

$$\int_{-l_1}^{L+l_2} (GE)\,\phi\, dx + \left[(BM)\,\phi' - (BF)\,\phi\right]_{-l_1}^{L+l_2} = 0 \tag{2.17}$$

where:

GE is the residue, i.e., the difference between the exact solution and the approximate solution in the governing equation

BM is the residue due to the boundary moments

BF is the residue due to the shear forces

ϕ is one of the approximate displacement functions

ϕ' is the derivative of ϕ with respect to x

This leads to the following equations:

$$\int_{-l_1}^{L+l_2} GE_v\,\phi_j\, dx + \left[BC_1\,\phi_j' - BC_3\,\phi_j\right]_{x=0} + \left[BC_9\,\phi_j' - BC_{11}\,\phi_j\right]_{x=L}$$

$$+\left[BC_{17}\,\phi_j' - BC_{19}\,\phi_j\right]_{x=-l_1} + \left[BC_{21}\,\phi_j' - BC_{23}\,\phi_j\right]_{x=L+l_2} = 0 \quad (2.18.a)$$

$$\int_{-l_1}^{L+l_2} GE_w\,\phi_j\,dx + \left[BC_2\,\phi_j' - BC_4\,\phi_j\right]_{x=0} + \left[BC_{10}\,\phi_j' - BC_{12}\,\phi_j\right]_{x=L}$$

$$+\left[BC_{18}\,\phi_j' - BC_{20}\,\phi_j\right]_{x=-l_1} + \left[BC_{22}\,\phi_j' - BC_{24}\,\phi_j\right]_{x=L+l_2} = 0 \quad (2.18.b)$$

where GE_v, GE_w, BC_k $(k = 1, \ldots, 24)$ are defined in equations (2.14) - (2.15), and j=1,2,3. The approximation functions ϕ_j are as follows (n=1,2,...,N):

$$\phi_1 = \sin\frac{n\pi x}{L} \qquad \phi_1' = \frac{n\pi}{L}\cos\frac{n\pi x}{L} \quad (2.19.a)$$

$$\phi_2 = x \qquad \phi_2' = 1 \quad (2.19.b)$$

$$\phi_3 = 1 \qquad \phi_3' = 0 \quad (2.19.c)$$

Based on the integration formulas in Appendix B, and using $I_p = 2\,I_d$ and equations (2.19.a-c), equations (2.18.a) become

$$\mu\left[\ddot{v}_n\frac{L}{2} - \ddot{a}_1\frac{L^2}{n\pi}\cos n\pi + \ddot{a}_2\frac{L}{n\pi}\left(1-(-1)^n\right)\right]$$

$$+ m\left[\sum_{k=1}^{N}\ddot{v}_k\sin\frac{k\pi c}{L}\sin\frac{n\pi c}{L} + c\,\ddot{a}_1\sin\frac{n\pi c}{L} + \ddot{a}_2\sin\frac{n\pi c}{L}\right]$$

$$-2\mu\dot{\theta}\left[\dot{w}_n\frac{L}{2}-\dot{a}_3\frac{L^2}{n\pi}\cos n\pi+\dot{a}_4\frac{L}{n\pi}\left(1-(-1)^n\right)\right]$$

$$-2m\dot{\theta}\sin\frac{n\pi c}{L}\left[\sum_{k=1}^{N}\dot{w}_k\sin\frac{k\pi c}{L}+\dot{a}_3 c+\dot{a}_4\right]$$

$$-\mu\dot{\theta}^2\left[v_n\frac{L}{2}-a_1\frac{L^2}{n\pi}\cos n\pi+a_2\frac{L}{n\pi}\left(1-(-1)^n\right)\right]$$

$$-m\dot{\theta}^2\sin\frac{n\pi c}{L}\left[\sum_{k=1}^{N}v_k\sin\frac{k\pi c}{L}+a_1 c+a_2\right]$$

$$-\mu\ddot{\theta}\left[w_n\frac{L}{2}-a_3\frac{L^2}{n\pi}\cos n\pi+a_4\frac{L}{n\pi}\left(1-(-1)^n\right)\right]$$

$$-m\ddot{\theta}\sin\frac{n\pi c}{L}\left[\sum_{k=1}^{N}w_k\sin\frac{k\pi c}{L}+a_3 c+a_4\right]$$

$$+d_e\mu\left[\dot{v}_n\frac{L}{2}-\dot{a}_1\frac{L^2}{n\pi}\cos n\pi+\dot{a}_2\frac{L}{n\pi}\left(1-(-1)^n\right)\right]$$

$$-d_e\mu\dot{\theta}\left[w_n\frac{L}{2}-a_3\frac{L^2}{n\pi}\cos n\pi+a_4\frac{L}{n\pi}\left(1-(-1)^n\right)\right]$$

$$-me_d\sin\frac{n\pi c}{L}\left[\dot{\theta}^2\cos\delta_d+\ddot{\theta}\sin\delta_d\right]+EI\frac{L}{2}\left(\frac{n\pi}{L}\right)^4\left(v_n+d_i\dot{v}_n\right)$$

$$-\mu g\sin\theta\frac{L}{n\pi}\left[1-(-1)^n\right]-mg\sin\theta\sin\frac{n\pi c}{L}$$

$$+I_d\cos\frac{n\pi c}{L}\left[\sum_{k=1}^{N}\left(\ddot{v}_k+\ddot{\theta}w_k+\dot{\theta}^2v_k\right)\left(\frac{kn\pi^2}{L^2}\cos\frac{k\pi c}{L}\right)+\left(\ddot{a}_1+\ddot{\theta}a_3+\dot{\theta}^2a_1\right)\frac{n\pi}{L}\right]$$

$$+\Lambda\, c_{44}(EI)^2\left(\frac{n\pi}{L}\right)^2 \sin\frac{n\pi b}{L}\sum_{k=1}^{N}\left(v_k + d_i\,\dot{v}_k\right)\left(\frac{k\pi}{L}\right)^2 \sin\frac{k\pi b}{L}$$

$$+\left\{\frac{L^2}{(n\pi)^2}\left[\sin\frac{n\pi l_1}{L}+\sin\frac{n\pi(L+l_2)}{L}\right]-\frac{L}{n\pi}\left[l_1\cos\frac{n\pi l_1}{L}+(L+l_2)\cos\frac{n\pi(L+l_2)}{L}\right]\right.$$

$$\left.+\frac{L^2}{n\pi}\cos n\pi\right\}\left[\mu\left(\ddot{a}_1-2\dot{\theta}\dot{a}_3-\ddot{\theta}a_3-\dot{\theta}^2 a_1\right)+d_e\,\mu\left(\dot{a}_1-\dot{\theta}a_3\right)\right]$$

$$+\sum_{k=1}^{N}\left\{\begin{array}{ll} k=n & \left[-\frac{L}{4k\pi}\sin\frac{2k\pi l_1}{L}-\frac{L}{4k\pi}\sin\frac{2k\pi(L+l_2)}{L}+\frac{(l_1+l_2)}{2}\right] \\ k\neq n & \left[-\frac{1}{2}\frac{L}{(k+n)\pi}\left\langle\sin\frac{(k+n)\pi l_1}{L}+\sin\frac{(k+n)\pi(L+l_2)}{L}\right\rangle\right. \\ & \left.+\frac{1}{2}\frac{L}{(k-n)\pi}\left\langle\sin\frac{(k-n)\pi l_1}{L}+\sin\frac{(k-n)\pi(L+l_2)}{L}\right\rangle\right] \end{array}\right.$$

$$\left[EI\left(\frac{k\pi}{L}\right)^4\left(v_k+d_i\dot{v}_k\right)+\mu\left(\ddot{v}_k-2\dot{\theta}\dot{w}_k-\ddot{\theta}w_k-\dot{\theta}^2 v_k\right)+d_e\mu\left(\dot{v}_k-\dot{\theta}w_k\right)\right]$$

$$-\frac{L}{n\pi}\left[1-\cos\frac{n\pi l_1}{L}+\cos\frac{n\pi(L+l_2)}{L}-(-1)^n\right]$$

$$\left[\mu\left(\ddot{a}_2-2\dot{\theta}\dot{a}_4-\ddot{\theta}a_4-\dot{\theta}^2 a_2\right)+d_e\,\mu\left(\dot{a}_2-\dot{\theta}a_4\right)-\mu g\sin\theta\right]$$

$$-EI\frac{n\pi}{L}\cos\frac{n\pi l_1}{L}\sum_{k=1}^{N}\left(\frac{k\pi}{L}\right)^2\sin\frac{k\pi l_1}{L}\left(v_k+d_i\,\dot{v}_k\right)$$

$$-EI\frac{n\pi}{L}\cos\frac{n\pi(L+l_2)}{L}\sum_{k=1}^{N}\left(\frac{k\pi}{L}\right)^2\sin\frac{k\pi(L+l_2)}{L}\left(v_k+d_i\,\dot{v}_k\right)$$

$$+EI\sin\frac{n\pi l_1}{L}\sum_{k=1}^{N}\left(\frac{k\pi}{L}\right)^3\cos\frac{k\pi l_1}{L}\left(v_k+d_i\dot{v}_k\right)$$

$$+EI\sin\frac{n\pi(L+l_2)}{L}\sum_{k=1}^{N}\left(\frac{k\pi}{L}\right)^3\cos\frac{k\pi(L+l_2)}{L}\left(v_k+d_i\dot{v}_k\right)$$

$$+I_{dc}\frac{n\pi}{L}\cos\frac{n\pi(L+l_2)}{L}$$

$$\left[\sum_{k=1}^{N}\frac{k\pi}{L}\cos\frac{k\pi(L+l_2)}{L}\left(\ddot{v}_k+\ddot{\theta}w_k+\dot{\theta}^2v_k\right)+\ddot{a}_1+\ddot{\theta}a_3+\dot{\theta}^2a_1\right]$$

$$+m_c\sin\frac{n\pi(L+l_2)}{L}\sum_{k=1}^{N}\sin\frac{k\pi(L+l_2)}{L}\left(\ddot{v}_k-2\dot{\theta}\dot{w}_k-\ddot{\theta}w_k-\dot{\theta}^2v_k\right)$$

$$+m_c\sin\frac{n\pi(L+l_2)}{L}\left[(L+l_2)\left(\ddot{a}_1-2\dot{\theta}\dot{a}_3-\ddot{\theta}a_3-\dot{\theta}^2a_1\right)\right.$$

$$\left.+\ddot{a}_2-2\dot{\theta}\dot{a}_4-\ddot{\theta}a_4-\dot{\theta}^2a_2+g\sin\theta\right]=0 \qquad (2.20.a)$$

(n=1,2,...,N)

$$\mu\left[-\frac{L^2}{k\pi}\sum_{k=1}^{N}\ddot{v}_k\cos k\pi+\frac{1}{3}\ddot{a}_1L^3+\frac{1}{2}\ddot{a}_2L^2\right]+mc\left[\sum_{k=1}^{N}\ddot{v}_k\sin\frac{k\pi c}{L}+\ddot{a}_1c+\ddot{a}_2\right]$$

$$-2\mu\dot{\theta}\left[-\frac{L^2}{k\pi}\sum_{k=1}^{N}\dot{w}_k\cos k\pi+\frac{1}{3}\dot{a}_3L^3+\frac{1}{2}\dot{a}_4L^2\right]$$

$$-\mu\dot{\theta}^2\left[-\frac{L^2}{k\pi}\sum_{k=1}^{N}v_k\cos k\pi+\frac{1}{3}a_1L^3+\frac{1}{2}a_2L^2\right]$$

$$-\mu\ddot{\theta}\left[-\frac{L^2}{k\pi}\sum_{k=1}^{N} w_k \cos k\pi + \frac{1}{3}a_3 L^3 + \frac{1}{2}a_4 L^2\right]$$

$$-2mc\dot{\theta}\left[\sum_{k=1}^{N} \dot{w}_k \sin\frac{k\pi c}{L} + \dot{a}_3 c + \dot{a}_4\right] - mc\dot{\theta}^2\left[\sum_{k=1}^{N} v_k \sin\frac{k\pi c}{L} + a_1 c + a_2\right]$$

$$-mc\ddot{\theta}\left[\sum_{k=1}^{N} w_k \sin\frac{k\pi c}{L} + a_3 c + a_4\right]$$

$$+d_e\mu\left[-\frac{L^2}{k\pi}\sum_{k=1}^{N} \dot{v}_k \cos k\pi + \frac{1}{3}\dot{a}_1 L^3 + \frac{1}{2}\dot{a}_2 L^2\right]$$

$$-d_e\mu\dot{\theta}\left[-\frac{L^2}{k\pi}\sum_{k=1}^{N} w_k \cos k\pi + \frac{1}{3}a_3 L^3 + \frac{1}{2}a_4 L^2\right]$$

$$-EI\left[\sum_{k=1}^{N}\left(v_k + d_i \dot{v}_k\right)\frac{L^2}{k\pi}\left(\frac{k\pi}{L}\right)^4 \cos k\pi\right]$$

$$-\frac{1}{2}\mu g L^2 \sin\theta - mgc\sin\theta - me_d c\left[\dot{\theta}^2 \cos\delta_d + \ddot{\theta}\sin\delta_d\right]$$

$$+I_d\left[\sum_{k=1}^{N}\left(\ddot{v}_k + \ddot{\theta} w_k + \dot{\theta}^2 v_k\right)\frac{k\pi}{L}\cos\frac{k\pi c}{L} + \ddot{a}_1 + \ddot{\theta} a_3 + \dot{\theta}^2 a_1\right]$$

$$+\sum_{k=1}^{N}\left\{\frac{L^2}{(k\pi)^2}\left[\sin\frac{k\pi l_1}{L} + \sin\frac{k\pi(L+l_2)}{L}\right] - \frac{L}{k\pi}\left[l_1\cos\frac{k\pi l_1}{L} + (L+l_2)\right.\right.$$

$$\left.\left.\cos\frac{k\pi(L+l_2)}{L}\right] + \frac{L^2}{k\pi}\cos k\pi\right\}\left[EI\left(\frac{k\pi}{L}\right)^4\left(v_k + d_i \dot{v}_k\right)\right.$$

$$\left.+\mu\left(\ddot{v}_k - 2\dot{\theta}\dot{w}_k - \ddot{\theta} w_k - \dot{\theta}^2 v_k\right) + d_e\mu\left(\dot{v}_k - \dot{\theta} w_k\right)\right]$$

$$+\frac{1}{3}\left[l_1{}^3+(L+l_2)^3-L^3\right]\left[\mu\left(\ddot{a}_1-2\dot{\theta}\dot{a}_3-\ddot{\theta}a_3-\dot{\theta}^2a_1\right)+d_e\mu\left(\dot{a}_1-\dot{\theta}a_3\right)\right]$$

$$-\frac{1}{2}\left[l_1{}^2-(L+l_2)^2+L^2\right]\left[\mu\left(\ddot{a}_2-2\dot{\theta}\dot{a}_4-\ddot{\theta}a_4-\dot{\theta}^2a_2\right)+d_e\mu\left(\dot{a}_2-\dot{\theta}a_4\right)-\mu g\sin\theta\right]$$

$$+m_b L\left[L\left(\ddot{a}_1-2\dot{\theta}\dot{a}_3-\ddot{\theta}a_3-\dot{\theta}^2a_1\right)+\ddot{a}_2-2\dot{\theta}\dot{a}_4-\ddot{\theta}a_4-\dot{\theta}^2a_2\right]$$

$$+m_b gL\sin\theta+sL(a_1L+a_2)+pL\left[\dot{a}_1L+\dot{a}_2-\dot{\theta}(a_3L+a_4)\right]$$

$$-EI\sum_{k=1}^{N}\left(\frac{k\pi}{L}\right)^2(v_k+d_i\dot{v}_k)\left[\sin\frac{k\pi l_1}{L}+\sin\frac{k\pi(L+l_2)}{L}\right]$$

$$+EI\sum_{k=1}^{N}\left(\frac{k\pi}{L}\right)^3(v_k+d_i\dot{v}_k)\left[l_1\cos\frac{k\pi l_1}{L}+(L+l_2)\cos\frac{k\pi(L+l_2)}{L}\right]$$

$$+I_{dc}\left[\sum_{k=1}^{N}\left(\ddot{v}_k+\ddot{\theta}w_k+\dot{\theta}^2v_k\right)\frac{k\pi}{L}\cos\frac{k\pi(L+l_2)}{L}+\ddot{a}_1+\ddot{\theta}a_3+\dot{\theta}^2a_1\right]$$

$$+m_c(L+l_2)\sum_{k=1}^{N}\sin\frac{k\pi(L+l_2)}{L}\left(\ddot{v}_k-2\dot{\theta}\dot{w}_k-\ddot{\theta}w_k-\dot{\theta}^2v_k\right)$$

$$+m_c(L+l_2)\left[(L+l_2)\left(\ddot{a}_1-2\dot{\theta}\dot{a}_3-\ddot{\theta}a_3-\dot{\theta}^2a_1\right)\right.$$

$$\left.+\ddot{a}_2-2\dot{\theta}\dot{a}_4-\ddot{\theta}a_4-\dot{\theta}^2a_2+g\sin\theta\right]=0 \qquad (2.20.b)$$

$$\mu\left[\sum_{k=1}^{N}\ddot{v}_k\frac{L}{k\pi}(1-\cos k\pi)+\frac{1}{2}\ddot{a}_1L^2+\ddot{a}_2L\right]$$

$$+ m\left[\sum_{k=1}^{N} \ddot{v}_k \sin\frac{k\pi c}{L} + \ddot{a}_1 c + \ddot{a}_2\right]$$

$$-2\mu\dot{\theta}\left[\sum_{k=1}^{N} \dot{w}_k \frac{L}{k\pi}(1-\cos k\pi) + \frac{1}{2}\dot{a}_3 L^2 + \dot{a}_4 L\right]$$

$$-\mu\dot{\theta}^2\left[\sum_{k=1}^{N} v_k \frac{L}{k\pi}(1-\cos k\pi) + \frac{1}{2}a_1 L^2 + a_2 L\right]$$

$$-\mu\ddot{\theta}\left[\sum_{k=1}^{N} w_k \frac{L}{k\pi}(1-\cos k\pi) + \frac{1}{2}a_3 L^2 + a_4 L\right]$$

$$-2m\dot{\theta}\left[\sum_{k=1}^{N} \dot{w}_k \sin\frac{k\pi c}{L} + \dot{a}_3 c + \dot{a}_4\right] - m\dot{\theta}^2\left[\sum_{k=1}^{N} v_k \sin\frac{k\pi c}{L} + a_1 c + a_2\right]$$

$$- m\ddot{\theta}\left[\sum_{k=1}^{N} w_k \sin\frac{k\pi c}{L} + a_3 c + a_4\right]$$

$$+ d_e \mu\left[\sum_{k=1}^{N} \dot{v}_k \frac{L}{k\pi}(1-\cos k\pi) + \frac{1}{2}\dot{a}_1 L^2 + \dot{a}_2 L\right]$$

$$- d_e \mu\dot{\theta}\left[\sum_{k=1}^{N} w_k \frac{L}{k\pi}(1-\cos k\pi) + \frac{1}{2}a_3 L^2 + a_4 L\right]$$

$$-\mu g L\sin\theta - mg\sin\theta - me_d\left[\dot{\theta}^2\cos\delta_d + \ddot{\theta}\sin\delta_d\right]$$

$$-\sum_{k=1}^{N} \frac{L}{k\pi}\left[1-\cos\frac{k\pi l_1}{L}+\cos\frac{k\pi(L+l_2)}{L}-\cos k\pi\right]\left[EI\left(\frac{k\pi}{L}\right)^4(v_k + d_i\dot{v}_k)\right.$$

$$\left.+\mu\left(\ddot{v}_k - 2\dot{\theta}\dot{w}_k - \ddot{\theta}w_k - \dot{\theta}^2 v_k\right) + d_e\mu\left(\dot{v}_k - \dot{\theta}w_k\right)\right]$$

$$-\frac{1}{2}\left[l_1{}^2+(L+l_2)^2-L^2\right]\left[\mu\left(\ddot{a}_1-2\dot{\theta}\dot{a}_3-\ddot{\theta}a_3-\dot{\theta}^2a_1\right)+d_e\mu\left(\dot{a}_1-\dot{\theta}a_3\right)\right]$$

$$+(l_1+l_2)\left[\mu\left(\ddot{a}_2-2\dot{\theta}\dot{a}_4-\ddot{\theta}a_4-\dot{\theta}^2a_2\right)+d_e\mu\left(\dot{a}_2-\dot{\theta}a_4\right)-\mu g\sin\theta\right]$$

$$+m_b\left[\ddot{a}_1L+2\ddot{a}_2-2\dot{\theta}(\dot{a}_3L+2\dot{a}_4)-\dot{\theta}^2(a_1L+2a_2)-\ddot{\theta}(a_3L+2a_4)+2g\sin\theta\right]$$

$$+s(a_1L+2a_2)+p\left[(\dot{a}_1L+2\dot{a}_2)-\dot{\theta}(a_3L+2a_4)\right]$$

$$-EI\sum_{k=1}^{N}\left(\frac{k\pi}{L}\right)^3(v_k+d_i\dot{v}_k)\cos\frac{k\pi l_1}{L}$$

$$+EI\sum_{k=1}^{N}\left(\frac{k\pi}{L}\right)^3(v_k+d_i\dot{v}_k)\cos\frac{k\pi(L+l_2)}{L}$$

$$+m_c\sum_{k=1}^{N}\sin\frac{k\pi(L+l_2)}{L}\left(\ddot{v}_k-2\dot{\theta}\dot{w}_k-\ddot{\theta}w_k-\dot{\theta}^2v_k\right)$$

$$+m_c\left[(L+l_2)\left(\ddot{a}_1-2\dot{\theta}\dot{a}_3-\ddot{\theta}a_3-\dot{\theta}^2a_1\right)\right.$$

$$\left.+\ddot{a}_2-2\dot{\theta}\dot{a}_4-\ddot{\theta}a_4-\dot{\theta}^2a_2+g\sin\theta\right]=0 \qquad (2.20.c)$$

There are N+2 similar equations based on equations (2.18.b).

Calculations are carried out in nondimensionalized form. The nondimensional quantities are defined as follows:

$$\tilde{v}_n=\frac{v_n}{L},\quad \tilde{w}_n=\frac{w_n}{L},\quad \tilde{b}=\frac{b}{L},\quad \tilde{c}=\frac{c}{L},\quad \tilde{x}=\frac{x}{L},\quad \tilde{l}_1=\frac{l_1}{L},\quad \tilde{l}_2=\frac{l_2}{L},$$

$$\tilde{l}_{12}=1+\tilde{l}_2,\quad \tilde{r}_s=\frac{r_s}{L},\quad \tilde{r}_d=\frac{r_d}{L},\quad \tilde{r}_c=\frac{r_c}{L},\quad \tilde{e}_d=\frac{e_d}{L},\quad \tilde{m}=\frac{2m}{\mu L},$$

$$\tilde{\mu} = \frac{2L^3 \mu g}{\pi^5 EI}, \quad \tilde{m}_b = \frac{2m_b}{\mu L}, \quad \tilde{m}_c = \frac{2m_c}{\mu L}, \quad \tilde{d}_i = \frac{\pi^2}{L^2}\sqrt{\frac{EI}{\mu}}\, d_i,$$

$$\tilde{d}_e = \frac{L^2}{\pi^2}\sqrt{\frac{\mu}{EI}}\, d_e, \quad \tau = \frac{\pi^2}{L^2}\sqrt{\frac{EI}{\mu}}\, t, \quad \Omega = \frac{d\theta}{d\tau}, \quad \lambda = \frac{d\Omega}{d\tau} = \frac{d^2\theta}{d\tau^2},$$

$$\tilde{c}_{44} = \frac{EI}{L} c_{44}, \quad \tilde{c}_{55} = \frac{EI}{L} c_{55}, \quad \tilde{a}_1 = a_1, \quad \tilde{a}_2 = \frac{a_2}{L}, \quad \tilde{a}_3 = a_3, \quad \tilde{a}_4 = \frac{a_4}{L},$$

$$\tilde{p} = \frac{pL}{\pi}\sqrt{\frac{1}{\mu EI}}, \quad \tilde{s} = \frac{sL^3}{\pi^3 EI} \tag{2.21}$$

Additionally, the nondimensional vertical, horizontal, and radial motions in fixed coordinates are, respectively,

$$z(\tilde{x},\tau) = \tilde{v}(\tilde{x},\tau)\sin\theta(\tau) + \tilde{w}(\tilde{x},\tau)\cos\theta(\tau)$$

$$y(\tilde{x},\tau) = \tilde{v}(\tilde{x},\tau)\cos\theta(\tau) - \tilde{w}(\tilde{x},\tau)\sin\theta(\tau)$$

$$R(\tilde{x},\tau) = \sqrt{z^2 + y^2} \tag{2.22}$$

Then the governing equations become

$$\ddot{\tilde{v}}_n - \ddot{\tilde{a}}_1 \frac{2}{n\pi}(-1)^n + \ddot{\tilde{a}}_2 \frac{2}{n\pi}\left(1-(-1)^n\right)$$

$$+ \tilde{m}\sin n\pi\tilde{c}\left[\sum_{k=1}^{N} \ddot{\tilde{v}}_k \sin k\pi\tilde{c} + \tilde{c}\ \ddot{\tilde{a}}_1 + \ddot{\tilde{a}}_2\right]$$

$$+ \frac{1}{4}\tilde{m}\,\tilde{r}_d{}^2\, n\pi\cos n\pi\tilde{c}\left[\sum_{k=1}^{N} \ddot{\tilde{v}}_k\, k\pi\cos k\pi\tilde{c} + \ddot{\tilde{a}}_1\right]$$

$$+\sum_{k=1}^{N}\begin{cases} k=n & \left[-\frac{1}{2k\pi}\sin 2k\pi\,\tilde{l}_1-\frac{1}{2k\pi}\sin 2k\pi\,\tilde{l}_{12}+\tilde{l}_1+\tilde{l}_2\right]\ddot{\tilde{v}}_k \\ k\neq n & \left[-\frac{1}{(k+n)\pi}\left\langle\sin(k+n)\pi\,\tilde{l}_1+\sin(k+n)\pi\,\tilde{l}_{12}\right\rangle\right. \\ & \left.+\frac{1}{(k-n)\pi}\left\langle\sin(k-n)\pi\,\tilde{l}_1+\sin(k-n)\pi\,\tilde{l}_{12}\right\rangle\right]\ddot{\tilde{v}}_k \end{cases}$$

$$+\frac{2}{n\pi}\,\ddot{\tilde{a}}_1\left[\frac{1}{n\pi}\left(\sin n\pi\,\tilde{l}_1+\sin n\pi\,\tilde{l}_{12}\right)-\tilde{l}_1\cos n\pi\,\tilde{l}_1+\tilde{l}_{12}\cos n\pi\,\tilde{l}_{12}+(-1)^n\right]$$

$$-\frac{2}{n\pi}\,\ddot{\tilde{a}}_2\left[1-\cos n\pi\,\tilde{l}_1+\cos n\pi\,\tilde{l}_{12}-(-1)^n\right]$$

$$+\frac{n\pi}{4}\,\tilde{m}_c\,\tilde{r}_c{}^2\cos n\pi\,\tilde{l}_{12}\left(\sum_{k=1}^{N}k\pi\,\ddot{\tilde{v}}_k\cos k\pi\,\tilde{l}_{12}+\ddot{\tilde{a}}_1\right)$$

$$+\tilde{m}_c\sin n\pi\,\tilde{l}_{12}\left(\sum_{k=1}^{N}\ddot{\tilde{v}}_k\sin k\pi\,\tilde{l}_{12}+\tilde{l}_{12}\,\ddot{\tilde{a}}_1+\ddot{\tilde{a}}_2\right)$$

$$=\frac{1}{n}\,\tilde{\mu}\sin\theta\left[1-(-1)^n\right]+\frac{\pi}{2}\,\tilde{m}\tilde{\mu}\sin\theta\sin n\pi\tilde{c}$$

$$+\tilde{m}\,\tilde{e}_d\sin n\pi\tilde{c}\left[\Omega^2\cos\delta_d+\lambda\sin\delta_d\right]-n^4\left(\tilde{v}_n+\tilde{d}_i\,\dot{\tilde{v}}_n\right)$$

$$+2\Omega\left\{\dot{\tilde{w}}_n-\dot{\tilde{a}}_3\frac{2}{n\pi}(-1)^n+\dot{\tilde{a}}_4\frac{2}{n\pi}\left[1-(-1)^n\right]\right\}$$

$$+2\tilde{m}\Omega\sin n\pi\tilde{c}\left[\sum_{k=1}^{N}\dot{\tilde{w}}_k\sin k\pi\tilde{c}+\dot{\tilde{a}}_3\,c+\dot{\tilde{a}}_4\right]$$

$$+\Omega^2\left\{\tilde{v}_n-\tilde{a}_1\frac{2}{n\pi}(-1)^n+\tilde{a}_2\frac{2}{n\pi}\left[1-(-1)^n\right]\right\}$$

$$+\tilde{m}\Omega^2 \sin n\pi\tilde{c}\left[\sum_{k=1}^{N}\tilde{v}_k \sin k\pi\tilde{c} + \tilde{a}_1\tilde{c} + \tilde{a}_2\right]$$

$$+\lambda\left\{\tilde{w}_n - \tilde{a}_3\frac{2}{n\pi}(-1)^n + \tilde{a}_4\frac{2}{n\pi}\left[1-(-1)^n\right]\right\}$$

$$+\tilde{m}\lambda \sin n\pi\tilde{c}\left[\sum_{k=1}^{N}\tilde{w}_k \sin k\pi\tilde{c} + \tilde{a}_3\tilde{c} + \tilde{a}_4\right]$$

$$-\tilde{d}_e\left\{\dot{\tilde{v}}_n - \dot{\tilde{a}}_1\frac{2}{n\pi}(-1)^n + \dot{\tilde{a}}_2\frac{2}{n\pi}\left[1-(-1)^n\right]\right\}$$

$$+\tilde{d}_e\,\Omega\left\{\tilde{w}_n - \tilde{a}_3\frac{2}{n\pi}(-1)^n + \tilde{a}_4\frac{2}{n\pi}\left[1-(-1)^n\right]\right\}$$

$$-\frac{1}{4}\tilde{m}\,\tilde{r}_d{}^2\, n\pi \cos n\pi\tilde{c}\left[\sum_{k=1}^{N}\left(\lambda\tilde{w}_k + \Omega^2\tilde{v}_k\right)k\pi\cos k\pi\tilde{c} + \lambda\tilde{a}_3 + \Omega^2\tilde{a}_1\right]$$

$$+2\,\Lambda\,\tilde{c}_{44}\,n^2 \sin n\pi\tilde{b}\sum_{k=1}^{N}\left(\tilde{v}_k + \tilde{d}_i\,\dot{\tilde{v}}_k\right)k^2 \sin k\pi\tilde{b}$$

$$+\sum_{k=1}^{N}\left\{\begin{array}{ll} k=n & \left[-\frac{1}{2k\pi}\sin 2k\pi\,\tilde{l}_1 - \frac{1}{2k\pi}\sin 2k\pi\,\tilde{l}_{12} + \tilde{l}_1 + \tilde{l}_2\right] \\ k\neq n & \left[-\frac{1}{(k+n)\pi}\left\langle\sin(k+n)\pi\,\tilde{l}_1 + \sin(k+n)\pi\,\tilde{l}_{12}\right\rangle\right. \\ & \left.+\frac{1}{(k-n)\pi}\left\langle\sin(k-n)\pi\,\tilde{l}_1 + \sin(k-n)\pi\,\tilde{l}_{12}\right\rangle\right] \end{array}\right.$$

$$*\left[-k^4\left(\tilde{v}_k + d_i\,\dot{\tilde{v}}_k\right) + 2\Omega\,\dot{\tilde{w}}_k + \lambda\,\tilde{w}_k + \Omega^2\,\tilde{v}_k - \tilde{d}_e\left(\dot{\tilde{v}}_k - \Omega\tilde{w}_k\right)\right]$$

$$+\frac{2}{n\pi}\left[\frac{1}{n\pi}\left(\sin n\pi\,\tilde{l}_1 + \sin n\pi\,\tilde{l}_{12}\right) - \tilde{l}_1\cos n\pi\,\tilde{l}_1 + \tilde{l}_{12}\cos n\pi\,\tilde{l}_{12} + (-1)^n\right]$$

$$\left[-2\Omega\dot{\tilde{a}}_3+\lambda\tilde{a}_3+\Omega^2\tilde{a}_1-\tilde{d}_e\left(\dot{\tilde{a}}_1-\Omega\tilde{a}_3\right)\right]$$

$$-\frac{2}{n\pi}\left[1-\cos n\pi\tilde{l}_1+\cos n\pi\tilde{l}_{12}-(-1)^n\right]$$

$$*\left[2\Omega\dot{\tilde{a}}_4+\lambda\tilde{a}_4+\Omega^2\tilde{a}_2-\tilde{d}_e\left(\dot{\tilde{a}}_2-\Omega\tilde{a}_4\right)+\frac{1}{2}\tilde{\mu}\pi\sin\theta\right]$$

$$+2\sum_{k=1}^{N}\frac{k^2n}{\pi}\left(\tilde{v}_k+\tilde{d}_i\dot{\tilde{v}}_k\right)\left(\sin k\pi\tilde{l}_1\cos n\pi\tilde{l}_1+\sin k\pi\tilde{l}_{12}\cos n\pi\tilde{l}_{12}\right)$$

$$-2\sum_{k=1}^{N}\frac{k^3}{\pi}\left(\tilde{v}_k+\tilde{d}_i\dot{\tilde{v}}_k\right)\left(\cos k\pi\tilde{l}_1\sin n\pi\tilde{l}_1+\cos k\pi\tilde{l}_{12}\sin n\pi\tilde{l}_{12}\right)$$

$$-\frac{n\pi}{4}\tilde{m}_c\tilde{r}_c{}^2\cos n\pi\tilde{l}_{12}\left[\sum_{k=1}^{N}k\pi\cos k\pi\tilde{l}_{12}\left(\lambda\tilde{w}_k+\Omega^2\tilde{v}_k\right)+\lambda\tilde{a}_3+\Omega^2\tilde{a}_1\right]$$

$$+\tilde{m}_c\sin n\pi\tilde{l}_{12}\left[\tilde{l}_{12}\left(2\Omega\dot{\tilde{a}}_3+\lambda\tilde{a}_3+\Omega^2\tilde{a}_1\right)+2\Omega\dot{\tilde{a}}_4+\lambda\tilde{a}_4+\Omega^2\tilde{a}_2-\frac{\pi}{2}\tilde{\mu}\sin\theta\right]$$

$$+\tilde{m}_c\sin n\pi\tilde{l}_{12}\sum_{k=1}^{N}\sin k\pi\tilde{l}_{12}\left(2\Omega\dot{\tilde{w}}_k+\lambda\tilde{w}_k+\Omega^2\tilde{v}_k\right) \qquad (2.23.a)$$

(n=1,2,...,N)

$$\sum_{k=1}^{N}\ddot{\tilde{v}}_k\left(-\frac{2}{k\pi}\right)(-1)^k+\frac{2}{3}\ddot{\tilde{a}}_1+\ddot{\tilde{a}}_2+\tilde{m}\tilde{c}\left[\sum_{k=1}^{N}\ddot{\tilde{v}}_k\sin k\pi\tilde{c}+\ddot{\tilde{a}}_1\tilde{c}+\ddot{\tilde{a}}_2\right]$$

$$+\frac{1}{4}\tilde{m}\tilde{r}_d{}^2\left[\sum_{k=1}^{N}\ddot{\tilde{v}}_k k\pi\cos k\pi\tilde{c}+\ddot{\tilde{a}}_1\right]+\tilde{m}_b\left(\ddot{\tilde{a}}_1+\ddot{\tilde{a}}_2\right)$$

$$+\sum_{k=1}^{N}\frac{2}{k\pi}\,\ddot{\tilde{v}}_k\left[\frac{1}{k\pi}\left(\sin k\pi\,\tilde{l}_1+\sin k\pi\,\tilde{l}_{12}\right)-\tilde{l}_1\cos k\pi\,\tilde{l}_1-\tilde{l}_{12}\cos k\pi\,\tilde{l}_{12}+(-1)^k\right]$$

$$+\frac{2}{3}\,\ddot{\tilde{a}}_1\left(\tilde{l}_1{}^3+\tilde{l}_{12}{}^3-1\right)-\ddot{\tilde{a}}_2\left(\tilde{l}_1{}^2-\tilde{l}_{12}{}^2+1\right)$$

$$+\frac{1}{4}\tilde{m}_c\,\tilde{r}_c{}^2\left(\sum_{k=1}^{N}k\pi\,\ddot{\tilde{v}}_k\cos k\pi\,\tilde{l}_{12}+\ddot{\tilde{a}}_1\right)+\tilde{m}_c\,\tilde{l}_{12}\left(\sum_{k=1}^{N}\ddot{\tilde{v}}_k\sin k\pi\,\tilde{l}_{12}+\ddot{\tilde{a}}_1\tilde{l}_{12}+\ddot{\tilde{a}}_2\right)$$

$$=2\Omega\left[-\sum_{k=1}^{N}\dot{\tilde{w}}_k\,\frac{2}{k\pi}\,(-1)^k+\frac{2}{3}\dot{\tilde{a}}_3+\dot{\tilde{a}}_4\right]+\Omega^2\left[-\sum_{k=1}^{N}\tilde{v}_k\,\frac{2}{k\pi}(-1)^k+\frac{2}{3}\tilde{a}_1+\tilde{a}_2\right]$$

$$-\lambda\left[\sum_{k=1}^{N}\tilde{w}_k\,\frac{2}{k\pi}(-1)^k-\frac{2}{3}\tilde{a}_3-\tilde{a}_4\right]+\tilde{m}\tilde{c}\lambda\left[\sum_{k=1}^{N}\tilde{w}_k\sin k\pi\tilde{c}+\tilde{a}_3\,c+\tilde{a}_4\right]$$

$$+2\,\tilde{m}\tilde{c}\Omega\left[\sum_{k=1}^{N}\dot{\tilde{w}}_k\sin k\pi\tilde{c}+\dot{\tilde{a}}_3\,\tilde{c}+\dot{\tilde{a}}_4\right]+\tilde{m}\tilde{c}\Omega^2\left[\sum_{k=1}^{N}\tilde{v}_k\sin k\pi\tilde{c}+\tilde{a}_1\,\tilde{c}+\tilde{a}_2\right]$$

$$+\tilde{d}_e\left[\sum_{k=1}^{N}\dot{\tilde{v}}_k\,\frac{2}{k\pi}(-1)^k-\frac{2}{3}\dot{\tilde{a}}_1-\dot{\tilde{a}}_2\right]-\tilde{d}_e\,\Omega\left[\sum_{k=1}^{N}\tilde{w}_k\,\frac{2}{k\pi}(-1)^k-\frac{2}{3}\tilde{a}_3-\tilde{a}_4\right]$$

$$+\frac{1}{2}\tilde{\mu}\,\pi\sin\theta+\frac{\pi}{2}\tilde{m}\,\tilde{\mu}\,\tilde{c}\sin\theta+\tilde{m}\,\tilde{e}_d\;\tilde{c}\left[\Omega^2\cos\delta_d+\lambda\,\sin\delta_d\right]$$

$$-\frac{1}{4}\tilde{m}\tilde{r}_d{}^2\left[\sum_{k=1}^{N}\left(\Omega^2\,\tilde{v}_k+\lambda\,\tilde{w}_k\right)k\pi\cos k\pi\tilde{c}+\lambda\,\tilde{a}_3+\Omega^2\,\tilde{a}_1\right]$$

$$+\sum_{k=1}^{N}\frac{2k^3}{\pi}(-1)^k\left(\tilde{v}_k+\tilde{d}_i\,\dot{\tilde{v}}_k\right)$$

$$+\sum_{k=1}^{N}\frac{2}{k\pi}\left[\frac{1}{k\pi}\left(\sin k\pi\,\tilde{l}_1+\sin k\pi\,\tilde{l}_{12}\right)-\tilde{l}_1\cos k\pi\,\tilde{l}_1-\tilde{l}_{12}\cos k\pi\,\tilde{l}_{12}+(-1)^k\right]$$

$$*\left[-\tilde{v}_k - \tilde{d}_i\dot{\tilde{v}}_k + 2\Omega\dot{\tilde{w}}_k + \lambda\tilde{w}_k + \Omega^2\tilde{v}_k - \tilde{d}_e\left(\dot{\tilde{v}}_k - \Omega\tilde{w}_k\right)\right]$$

$$+\frac{2}{3}\left(\tilde{l}_1{}^3 + \tilde{l}_{12}{}^3 - 1\right)\left[2\Omega\dot{\tilde{a}}_3 + \lambda\tilde{a}_3 + \Omega^2\tilde{a}_1 - \tilde{d}_e\left(\dot{\tilde{a}}_1 - \Omega\tilde{a}_3\right)\right]$$

$$-\left(\tilde{l}_1{}^2 - \tilde{l}_{12}{}^2 + 1\right)\left[2\Omega\dot{\tilde{a}}_4 + \lambda\tilde{a}_4 + \Omega^2\tilde{a}_2 - \tilde{d}_e\left(\dot{\tilde{a}}_2 - \Omega\tilde{a}_4\right) + \frac{1}{2}\mu\pi\sin\theta\right]$$

$$+\tilde{m}_b\left[2\Omega\left(\dot{\tilde{a}}_3 + \dot{\tilde{a}}_4\right) + \Omega^2\left(\tilde{a}_1 + \tilde{a}_2\right) + \lambda\left(\tilde{a}_3 + \tilde{a}_4\right) - \frac{\pi}{2}\tilde{\mu}\sin\theta\right]$$

$$-\frac{2}{\pi}\tilde{s}\left(\tilde{a}_1 + \tilde{a}_2\right) - \frac{2}{\pi}\tilde{p}\left[\dot{\tilde{a}}_1 + \dot{\tilde{a}}_2 - \Omega\left(\tilde{a}_3 + \tilde{a}_4\right)\right]$$

$$+2\sum_{k=1}^{N}\frac{k^2}{\pi^2}\left(\tilde{v}_k + \tilde{d}_i\dot{\tilde{v}}_k\right)\left(\sin k\pi\tilde{l}_1 + \sin k\pi\tilde{l}_{12}\right)$$

$$-2\sum_{k=1}^{N}\frac{k3}{\pi^2}\left(\tilde{v}_k + \tilde{d}_i\dot{\tilde{v}}_k\right)\left(\tilde{l}_1\cos k\pi\tilde{l}_1 + \tilde{l}_{12}\cos k\pi\tilde{l}_{12}\right)$$

$$-\frac{1}{4}\tilde{m}_c\tilde{r}_c{}^2\left[\sum_{k=1}^{N}k\pi\cos k\pi\tilde{l}_{12}\left(\Omega^2\tilde{v}_k + \lambda\tilde{w}_k\right) + \Omega^2\tilde{a}_1 + \lambda\tilde{a}_3\right]$$

$$+\tilde{m}_c\tilde{l}_{12}\left[\tilde{l}_{12}\left(2\Omega\dot{\tilde{a}}_3 + \lambda\tilde{a}_3 + \Omega^2\tilde{a}_1\right) + 2\Omega\dot{\tilde{a}}_4 + \lambda\tilde{a}_4 + \Omega^2\tilde{a}_2 - \frac{\pi}{2}\tilde{\mu}\sin\theta\right]$$

$$+\tilde{m}_c\tilde{l}_{12}\sum_{k=1}^{N}\sin k\pi\tilde{l}_{12}\left(2\Omega\dot{\tilde{w}}_k + \lambda\tilde{w}_k + \Omega^2\tilde{v}_k\right) \qquad (2.23.b)$$

$$\sum_{k=1}^{N}\ddot{\tilde{v}}_k\frac{2}{k\pi}\left[1-(-1)^k\right] + \ddot{\tilde{a}}_1 + 2\ddot{\tilde{a}}_2$$

$$+\tilde{m}\left[\sum_{k=1}^{N}\ddot{\tilde{v}}_k \sin k\pi\tilde{c}+\ddot{\tilde{a}}_1\,\tilde{c}+\ddot{\tilde{a}}_2\right]+\tilde{m}_b\left(\ddot{\tilde{a}}_1+2\,\ddot{\tilde{a}}_2\right)$$

$$-\sum_{k=1}^{N}\frac{2}{k\pi}\,\ddot{\tilde{v}}_k\left[1-\cos k\pi\,\tilde{l}_1+\cos k\pi\,\tilde{l}_{12}-(-1)^k\right]$$

$$-\left(\tilde{l}_1{}^2-\tilde{l}_{12}{}^2+1\right)\ddot{\tilde{a}}_1+2\left(\tilde{l}_1+\tilde{l}_2\right)\ddot{\tilde{a}}_2+\tilde{m}_c\left(\sum_{k=1}^{N}\ddot{\tilde{v}}_k \sin k\pi\tilde{l}_{12}+\ddot{\tilde{a}}_1\tilde{l}_{12}+\ddot{\tilde{a}}_2\right)$$

$$=2\Omega\left\{\sum_{k=1}^{N}\dot{\tilde{w}}_k\frac{2}{k\pi}\left[1-(-1)^k\right]+\dot{\tilde{a}}_3+2\,\dot{\tilde{a}}_4\right\}$$

$$+\Omega^2\left\{\sum_{k=1}^{N}\tilde{v}_k\frac{2}{k\pi}\left[1-(-1)^k\right]+\tilde{a}_1+2\,\tilde{a}_2\right\}$$

$$+\lambda\left\{\sum_{k=1}^{N}\tilde{w}_k\frac{2}{k\pi}\left[1-(-1)^k\right]+\tilde{a}_3+2\,\tilde{a}_4\right\}$$

$$+\tilde{m}\lambda\left[\sum_{k=1}^{N}\tilde{w}_k \sin k\pi\tilde{c}+\tilde{a}_3\,\tilde{c}+\tilde{a}_4\right]+2\,\tilde{m}\Omega\left[\sum_{k=1}^{N}\dot{\tilde{w}}_k \sin k\pi\tilde{c}+\dot{\tilde{a}}_3\,\tilde{c}+\dot{\tilde{a}}_4\right]$$

$$+\tilde{m}\Omega^2\left[\sum_{k=1}^{N}\tilde{v}_k \sin k\pi\tilde{c}+\tilde{a}_1\,\tilde{c}+\tilde{a}_2\right]-\sum_{k=1}^{N}\frac{2k^3}{\pi}\left[1-(-1)^k\right]\left(\tilde{v}_k+\tilde{d}_i\dot{\tilde{v}}_k\right)$$

$$-\tilde{d}_e\left\{\sum_{k=1}^{N}\dot{\tilde{v}}_k\frac{2}{k\pi}\left[1-(-1)^k\right]+\dot{\tilde{a}}_1+2\,\dot{\tilde{a}}_2\right\}$$

$$+\tilde{d}_e\,\Omega\left\{\sum_{k=1}^{N}\tilde{w}_k\frac{2}{k\pi}\left[1-(-1)^k\right]+\tilde{a}_3+2\,\tilde{a}_4\right\}$$

$$+\pi\tilde{\mu}\sin\theta+\frac{\pi}{2}\tilde{m}\tilde{\mu}\,\sin\theta+\tilde{m}\,\tilde{e}_d\left[\Omega^2\cos\delta_d+\lambda\,\sin\delta_d\right]$$

$$-\sum_{k=1}^{N}\frac{2}{k\pi}\ddot{\tilde{v}}_k\left[1-\cos k\pi\,\tilde{l}_1+\cos k\pi\,\tilde{l}_{12}-(-1)^k\right]\left[-k^4\left(\tilde{v}_k+\tilde{d}_i\,\dot{\tilde{v}}_k\right)\right.$$

$$\left.+2\Omega\dot{\tilde{w}}_k+\lambda\,\tilde{w}_k+\Omega^2\,\tilde{v}_k-\tilde{d}_e\left(\dot{\tilde{v}}_k-\Omega\,\tilde{w}_k\right)\right]$$

$$-\left(\tilde{l}_1-\tilde{l}_{12}+1\right)\left[2\Omega\dot{\tilde{a}}_3+\lambda\,\tilde{a}_3+\Omega^2\,\tilde{a}_1-\tilde{d}_e\left(\dot{\tilde{a}}_1-\Omega\,\tilde{a}_3\right)\right]$$

$$+2\left(\tilde{l}_1+\tilde{l}_2\right)\left[2\Omega\dot{\tilde{a}}_4+\lambda\,\tilde{a}_4+\Omega^2\,\tilde{a}_2-\tilde{d}_e\left(\dot{\tilde{a}}_2-\Omega\,\tilde{a}_4\right)+\frac{\pi}{2}\tilde{\mu}\sin\theta\right]$$

$$+\tilde{m}_b\left[2\Omega\left(\dot{\tilde{a}}_3+2\dot{\tilde{a}}_4\right)+\Omega^2\left(\tilde{a}_1+2\,\tilde{a}_2\right)+\lambda\left(\tilde{a}_3+2\,\tilde{a}_4\right)-\pi\tilde{\mu}\sin\theta\right]$$

$$-\frac{2}{\pi}\tilde{s}\left(\tilde{a}_1+2\,\tilde{a}_2\right)-\frac{2}{\pi}\tilde{p}\left[\dot{\tilde{a}}_1+2\,\dot{\tilde{a}}_2-\Omega\left(\tilde{a}_3+2\,\tilde{a}_4\right)\right]$$

$$-2\sum_{k=1}^{N}\frac{k^3}{\pi}\left(\tilde{v}_k+\tilde{d}_i\,\dot{\tilde{v}}_k\right)\left[-\cos k\pi\,\tilde{l}_1+\cos k\pi\,\tilde{l}_{12}\right]$$

$$+\tilde{m}_c\left[\tilde{l}_{12}\left(2\Omega\dot{\tilde{a}}_3+\lambda\tilde{a}_3+\Omega^2\tilde{a}_1\right)+2\Omega\,\dot{\tilde{a}}_4+\lambda\,\tilde{a}_4+\Omega^2\,\tilde{a}_2+\frac{\pi}{4}\tilde{\mu}\sin\theta\right]$$

$$+\tilde{m}_c\sum_{k=1}^{N}\sin k\pi\,\tilde{l}_{12}\left(2\Omega\dot{\tilde{w}}_k+\lambda\,\tilde{w}_k+\Omega^2\,\tilde{v}_k\right) \qquad (2.23.c)$$

$$\ddot{\tilde{w}}_n-\ddot{\tilde{a}}_3\frac{2}{n\pi}(-1)^n+\ddot{\tilde{a}}_4\frac{2}{n\pi}\left[1-(-1)^n\right]$$

$$+\tilde{m}\sin n\pi\tilde{c}\left[\sum_{k=1}^{N}\ddot{\tilde{w}}_k\sin k\pi\tilde{c}+\tilde{c}\;\ddot{\tilde{a}}_3+\ddot{\tilde{a}}_4\right]$$

$$+\frac{1}{4}\tilde{m}\,\tilde{r}_d{}^2\;n\pi\cos n\pi\tilde{c}\left[\sum_{k=1}^{N}\ddot{\tilde{w}}_k\,k\pi\cos k\pi\tilde{c}+\;\ddot{\tilde{a}}_3\right]$$

$$+\sum_{k=1}^{N}\begin{cases} k=n & \left[-\frac{1}{2k\pi}\sin 2k\pi\,\tilde{l}_1-\frac{1}{2k\pi}\sin 2k\pi\,\tilde{l}_{12}+\tilde{l}_1+\tilde{l}_2\right]\ddot{\tilde{w}}_k \\ k\neq n & \left[-\frac{1}{(k+n)\pi}\left\langle\sin(k+n)\pi\,\tilde{l}_1+\sin(k+n)\pi\,\tilde{l}_{12}\right\rangle\right. \\ & \left.+\frac{1}{(k-n)\pi}\left\langle\sin(k-n)\pi\,\tilde{l}_1+\sin(k-n)\pi\,\tilde{l}_{12}\right\rangle\right]\ddot{\tilde{w}}_k \end{cases}$$

$$+\frac{2}{n\pi}\;\ddot{\tilde{a}}_3\left[\frac{1}{n\pi}\left(\sin n\pi\,\tilde{l}_1+\sin n\pi\,\tilde{l}_{12}\right)-\tilde{l}_1\cos n\pi\,\tilde{l}_1+\tilde{l}_{12}\cos n\pi\,\tilde{l}_{12}+(-1)^n\right]$$

$$-\frac{2}{n\pi}\;\ddot{\tilde{a}}_4\left[1-\cos n\pi\,\tilde{l}_1+\cos n\pi\,\tilde{l}_{12}-(-1)^n\right]$$

$$+\frac{n\pi}{4}\tilde{m}_c\,\tilde{r}_c{}^2\cos n\pi\tilde{l}_{12}\left(\sum_{k=1}^{N}k\pi\,\ddot{\tilde{w}}_k\cos k\pi\,\tilde{l}_{12}+\ddot{\tilde{a}}_3\right)$$

$$+\tilde{m}_c\sin n\pi\tilde{l}_{12}\left(\sum_{k=1}^{N}\ddot{\tilde{w}}_k\sin k\pi\tilde{l}_{12}+\tilde{l}_{12}\,\ddot{\tilde{a}}_3+\ddot{\tilde{a}}_4\right)$$

$$=\frac{1}{n}\,\tilde{\mu}\cos\theta\left[1-(-1)^n\right]+\frac{\pi}{2}\,\tilde{m}\tilde{\mu}\cos\theta\sin n\pi\tilde{c}$$

$$+\tilde{m}\,\tilde{e}_d\sin n\pi\tilde{c}\left[\Omega^2\sin\delta_d-\lambda\cos\delta_d\right]-n^4\left(\tilde{w}_n+\tilde{d}_i\,\dot{\tilde{w}}_n\right)$$

$$-2\Omega\left\{\dot{\tilde{v}}_n-\dot{\tilde{a}}_1\frac{2}{n\pi}(-1)^n+\dot{\tilde{a}}_2\frac{2}{n\pi}\left[1-(-1)^n\right]\right\}$$

$$+2\,\tilde{m}\Omega\sin n\pi\tilde{c}\left[\sum_{k=1}^{N}\dot{\tilde{v}}_k\,\sin k\pi\tilde{c}+\;\dot{\tilde{a}}_1 c\;+\;\dot{\tilde{a}}_2\right]$$

$$+\Omega^2\left\{\tilde{w}_n - \tilde{a}_3\frac{2}{n\pi}(-1)^n + \tilde{a}_4\frac{2}{n\pi}\left[1-(-1)^n\right]\right\}$$

$$+\tilde{m}\Omega^2\sin n\pi\tilde{c}\left[\sum_{k=1}^{N}\tilde{w}_k\sin k\pi\tilde{c} + \tilde{a}_3\tilde{c} + \tilde{a}_4\right]$$

$$-\lambda\left\{\tilde{v}_n - \tilde{a}_1\frac{2}{n\pi}(-1)^n + \tilde{a}_2\frac{2}{n\pi}\left[1-(-1)^n\right]\right\}$$

$$-\tilde{m}\lambda\sin n\pi\tilde{c}\left[\sum_{k=1}^{N}\tilde{v}_k\sin k\pi\tilde{c} + \tilde{a}_1\tilde{c} + \tilde{a}_2\right]$$

$$-\tilde{d}_e\left\{\dot{\tilde{w}}_n - \dot{\tilde{a}}_3\frac{2}{n\pi}(-1)^n + \dot{\tilde{a}}_4\frac{2}{n\pi}\left[1-(-1)^n\right]\right\}$$

$$-\tilde{d}_e\Omega\left\{\tilde{v}_n - \tilde{a}_1\frac{2}{n\pi}(-1)^n + \tilde{a}_2\frac{2}{n\pi}\left[1-(-1)^n\right]\right\}$$

$$-\frac{1}{4}\tilde{m}\tilde{r}_d{}^2\, n\pi\cos n\pi\tilde{c}\left[\sum_{k=1}^{N}\left(\lambda\tilde{v}_k+\Omega^2\tilde{w}_k\right)k\pi\cos k\pi\tilde{c}+\lambda\tilde{a}_1+\Omega^2\tilde{a}_3\right]$$

$$+2\,\Lambda\,\tilde{c}_{55}\,n^2\sin n\pi\tilde{b}\sum_{k=1}^{N}\left(\tilde{w}_k+\tilde{d}_i\,\dot{\tilde{w}}_k\right)k^2\sin k\pi\tilde{b}$$

$$+\sum_{k=1}^{N}\begin{cases} k=n & \left[-\dfrac{1}{2k\pi}\sin 2k\pi\,\tilde{I}_1-\dfrac{1}{2k\pi}\sin 2k\pi\,\tilde{I}_{12}+\tilde{I}_1+\tilde{I}_2\right] \\ k\neq n & \left[-\dfrac{1}{(k+n)\pi}\left\langle\sin(k+n)\pi\,\tilde{I}_1+\sin(k+n)\pi\,\tilde{I}_{12}\right\rangle\right. \\ & \left.+\dfrac{1}{(k-n)\pi}\left\langle\sin(k-n)\pi\,\tilde{I}_1+\sin(k-n)\pi\,\tilde{I}_{12}\right\rangle\right] \end{cases}$$

$$*\left[-k^4\left(\tilde{w}_k+d_i\,\dot{\tilde{w}}_k\right)-2\Omega\,\dot{\tilde{v}}_k-\lambda\,\tilde{v}_k+\Omega^2\,\tilde{w}_k-\tilde{d}_e\left(\dot{\tilde{w}}_k+\Omega\tilde{v}_k\right)\right]$$

$$+\frac{2}{n\pi}\left[\frac{1}{n\pi}\left(\sin n\pi\,\tilde{l}_1+\sin n\pi\,\tilde{l}_{12}\right)-\tilde{l}_1\cos n\pi\,\tilde{l}_1+\tilde{l}_{12}\cos n\pi\,\tilde{l}_{12}+(-1)^n\right]$$

$$\left[-2\Omega\dot{\tilde{a}}_1-\lambda\,\tilde{a}_1+\Omega^2\,\tilde{a}_3-\tilde{d}_e\left(\dot{\tilde{a}}_3+\Omega\,\tilde{a}_1\right)\right]$$

$$-\frac{2}{n\pi}\left[1-\cos n\pi\,\tilde{l}_1+\cos n\pi\,\tilde{l}_{12}-(-1)^n\right]$$

$$*\left[-2\Omega\dot{\tilde{a}}_2-\lambda\,\tilde{a}_2+\Omega^2\,\tilde{a}_4-\tilde{d}_e\left(\dot{\tilde{a}}_4+\Omega\,\tilde{a}_2\right)+\frac{1}{2}\tilde{\mu}\pi\cos\theta\right]$$

$$+2\sum_{k=1}^{N}\frac{k^2 n}{\pi}\left(\tilde{w}_k+\tilde{d}_i\,\dot{\tilde{w}}_k\right)\left(\sin k\pi\,\tilde{l}_1\cos n\pi\,\tilde{l}_1+\sin k\pi\,\tilde{l}_{12}\cos n\pi\,\tilde{l}_{12}\right)$$

$$-2\sum_{k=1}^{N}\frac{k^3}{\pi}\left(\tilde{w}_k+\tilde{d}_i\,\dot{\tilde{w}}_k\right)\left(\cos k\pi\,\tilde{l}_1\sin n\pi\,\tilde{l}_1+\cos k\pi\,\tilde{l}_{12}\sin n\pi\,\tilde{l}_{12}\right)$$

$$-\frac{n\pi}{4}\,\tilde{m}_c\,\tilde{r}_c{}^2\cos n\pi\,\tilde{l}_{12}\left[\sum_{k=1}^{N}k\pi\cos k\pi\,\tilde{l}_{12}\left(\lambda\,\tilde{v}_k+\Omega^2\,\tilde{w}_k\right)+\lambda\,\tilde{a}_1+\Omega^2\,\tilde{a}_3\right]$$

$$+\tilde{m}_c\sin n\pi\,\tilde{l}_{12}\left[\tilde{l}_{12}\left(-2\Omega\dot{\tilde{a}}_1-\lambda\tilde{a}_1+\Omega^2\tilde{a}_3\right)-2\Omega\dot{\tilde{a}}_2-\lambda\,\tilde{a}_2+\Omega^2\,\tilde{a}_4-\frac{\pi}{2}\tilde{\mu}\cos\theta\right]$$

$$+\tilde{m}_c\sin n\pi\,\tilde{l}_{12}\sum_{k=1}^{N}\sin k\pi\,\tilde{l}_{12}\left(-2\Omega\dot{\tilde{v}}_k-\lambda\,\tilde{v}_k+\Omega^2\,\tilde{w}_k\right)\qquad(2.24.a)$$

(n=1,2,...,N)

$$\sum_{k=1}^{N}\ddot{\tilde{w}}_k\left(-\frac{2}{k\pi}\right)(-1)^k+\frac{2}{3}\,\ddot{\tilde{a}}_3+\ddot{\tilde{a}}_4+\tilde{m}\,\tilde{c}\left[\sum_{k=1}^{N}\ddot{\tilde{w}}_k\sin k\pi\tilde{c}+\ddot{\tilde{a}}_3\,\tilde{c}+\ddot{\tilde{a}}_4\right]$$

$$+\frac{1}{4}\tilde{m}\tilde{r}_d{}^2\left[\sum_{k=1}^{N}\ddot{\tilde{w}}_k k\pi\cos k\pi\tilde{c}+\ddot{\tilde{a}}_3\right]+\tilde{m}_b\left(\ddot{\tilde{a}}_3+\ddot{\tilde{a}}_4\right)$$

$$+\sum_{k=1}^{N}\frac{2}{k\pi}\ddot{\tilde{w}}_k\left[\frac{1}{k\pi}\left(\sin k\pi\tilde{l}_1+\sin k\pi\tilde{l}_{12}\right)-\tilde{l}_1\cos k\pi\tilde{l}_1-\tilde{l}_{12}\cos k\pi\tilde{l}_{12}+(-1)^k\right]$$

$$+\frac{2}{3}\ddot{\tilde{a}}_3\left(\tilde{l}_1{}^3+\tilde{l}_{12}{}^3-1\right)-\ddot{\tilde{a}}_4\left(\tilde{l}_1{}^2-\tilde{l}_{12}{}^2+1\right)$$

$$+\frac{1}{4}\tilde{m}_c\,\tilde{r}_c{}^2\left(\sum_{k=1}^{N}k\pi\,\ddot{\tilde{w}}_k\cos k\pi\tilde{l}_{12}+\ddot{\tilde{a}}_3\right)+\tilde{m}_c\,\tilde{l}_{12}\left(\sum_{k=1}^{N}\ddot{\tilde{w}}_k\sin k\pi\tilde{l}_{12}+\ddot{\tilde{a}}_3\tilde{l}_{12}+\ddot{\tilde{a}}_4\right)$$

$$=2\Omega\left[\sum_{k=1}^{N}\dot{\tilde{v}}_k\frac{2}{k\pi}(-1)^k-\frac{2}{3}\dot{\tilde{a}}_1-\dot{\tilde{a}}_2\right]-\Omega^2\left[\sum_{k=1}^{N}\tilde{w}\frac{2}{k\pi}(-1)^k--\frac{2}{3}\tilde{a}_3-\tilde{a}_4\right]$$

$$+\lambda\left[\sum_{k=1}^{N}\tilde{v}_k\frac{2}{k\pi}(-1)^k-\frac{2}{3}\tilde{a}_1-\tilde{a}_2\right]-\tilde{m}\tilde{c}\lambda\left[\sum_{k=1}^{N}\tilde{v}_k\sin k\pi\tilde{c}+\tilde{a}_1 c+\tilde{a}_2\right]$$

$$-2\tilde{m}\tilde{c}\Omega\left[\sum_{k=1}^{N}\dot{\tilde{v}}_k\sin k\pi\tilde{c}+\dot{\tilde{a}}_1\,\tilde{c}+\dot{\tilde{a}}_2\right]+\tilde{m}\tilde{c}\Omega^2\left[\sum_{k=1}^{N}\tilde{w}_k\sin k\pi\tilde{c}+\tilde{a}_3\,\tilde{c}+\tilde{a}_4\right]$$

$$+\tilde{d}_e\left[\sum_{k=1}^{N}\dot{\tilde{w}}_k\frac{2}{k\pi}(-1)^k-\frac{2}{3}\dot{\tilde{a}}_3-\dot{\tilde{a}}_4\right]+\tilde{d}_e\,\Omega\left[\sum_{k=1}^{N}\tilde{v}_k\frac{2}{k\pi}(-1)^k-\frac{2}{3}\tilde{a}_1-\tilde{a}_2\right]$$

$$+\frac{1}{2}\tilde{\mu}\,\pi\cos\theta+\frac{\pi}{2}\tilde{m}\tilde{\mu}\,\tilde{c}\cos\theta+\tilde{m}\tilde{e}_d\,\tilde{c}\left[\Omega^2\sin\delta_d-\lambda\cos\delta_d\right]$$

$$-\frac{1}{4}\tilde{m}\tilde{r}_d{}^2\left[\sum_{k=1}^{N}\left(\Omega^2\,\tilde{w}_k+\lambda\,\tilde{v}_k\right)k\pi\cos k\pi\tilde{c}+\lambda\,\tilde{a}_1+\Omega^2\,\tilde{a}_3\right]$$

$$+\sum_{k=1}^{N}\frac{2k^3}{\pi}(-1)^k\left(\tilde{w}_k+\tilde{d}_i\,\dot{\tilde{w}}_k\right)$$

$$-\sum_{k=1}^{N}\frac{2}{k\pi}\left[\frac{1}{k\pi}\left(\sin k\pi\,\tilde{l}_1+\sin k\pi\,\tilde{l}_{12}\right)-\tilde{l}_1\cos k\pi\,\tilde{l}_1-\tilde{l}_{12}\cos k\pi\,\tilde{l}_{12}+(-1)^k\right]$$

$$*\left[\tilde{w}_k+\tilde{d}_i\dot{\tilde{w}}_k+2\Omega\dot{\tilde{v}}_k+\lambda\tilde{v}_k-\Omega^2\tilde{w}_k+\tilde{d}_e\left(\dot{\tilde{w}}_k+\Omega\tilde{v}_k\right)\right]$$

$$-\frac{2}{3}\left(\tilde{l}_1^{\,3}+\tilde{l}_{12}^{\,3}-1\right)\left[2\Omega\dot{\tilde{a}}_1+\lambda\tilde{a}_1-\Omega^2\tilde{a}_3+\tilde{d}_e\left(\dot{\tilde{a}}_3+\Omega\tilde{a}_1\right)\right]$$

$$+\left(\tilde{l}_1^{\,2}-\tilde{l}_{12}^{\,2}+1\right)\left[2\Omega\dot{\tilde{a}}_2+\lambda\tilde{a}_2-\Omega^2\tilde{a}_4+\tilde{d}_e\left(\dot{\tilde{a}}_4+\Omega\tilde{a}_2\right)-\frac{1}{2}\tilde{\mu}\pi\cos\theta\right]$$

$$-\tilde{m}_b\left[2\Omega\left(\dot{\tilde{a}}_1+\dot{\tilde{a}}_2\right)-\Omega^2\left(\tilde{a}_3+\tilde{a}_4\right)+\lambda\left(\tilde{a}_1+\tilde{a}_2\right)+\frac{\pi}{2}\tilde{\mu}\cos\theta\right]$$

$$-\frac{2}{\pi}\tilde{s}\left(\tilde{a}_3+\tilde{a}_4\right)-\frac{2}{\pi}\tilde{p}\left[\dot{\tilde{a}}_3+\dot{\tilde{a}}_4+\Omega\left(\tilde{a}_1+\tilde{a}_2\right)\right]$$

$$+2\sum_{k=1}^{N}\frac{k^2}{\pi^2}\left(\tilde{w}_k+\tilde{d}_i\dot{\tilde{w}}_k\right)\left(\sin k\pi\tilde{l}_1+\sin k\pi\tilde{l}_{12}\right)$$

$$-2\sum_{k=1}^{N}\frac{k3}{\pi^2}\left(\tilde{w}_k+\tilde{d}_i\dot{\tilde{w}}_k\right)\left(\tilde{l}_1\cos k\pi\tilde{l}_1+\tilde{l}_{12}\cos k\pi\tilde{l}_{12}\right)$$

$$-\frac{1}{4}\tilde{m}_c\tilde{r}_c^{\,2}\left[\sum_{k=1}^{N}k\pi\cos k\pi\tilde{l}_{12}\left(\Omega^2\tilde{w}_k+\lambda\tilde{v}_k\right)+\Omega^2\tilde{a}_3+\lambda\tilde{a}_1\right]$$

$$-\tilde{m}_c\tilde{l}_{12}\left[\tilde{l}_{12}\left(2\Omega\dot{\tilde{a}}_1+\lambda\tilde{a}_1-\Omega^2\tilde{a}_3\right)+2\Omega\dot{\tilde{a}}_2+\lambda\tilde{a}_2-\Omega^2\tilde{a}4+\frac{\pi}{2}\tilde{\mu}\cos\theta\right]$$

$$-\tilde{m}_c\tilde{l}_{12}\sum_{k=1}^{N}\sin k\pi\tilde{l}_{12}\left(2\Omega\dot{\tilde{v}}_k+\lambda\tilde{v}_k-\Omega^2\tilde{w}_k\right) \qquad (2.24.b)$$

$$\sum_{k=1}^{N} \ddot{\tilde{w}}_k \frac{2}{k\pi}\left[1-(-1)^k\right]+\ddot{\tilde{a}}_3+2\,\ddot{\tilde{a}}_4$$

$$+\tilde{m}\left[\sum_{k=1}^{N} \ddot{\tilde{w}}_k \sin k\pi\tilde{c}+\ddot{\tilde{a}}_3\,\tilde{c}+\ddot{\tilde{a}}_4\right]+\tilde{m}_b\left(\ddot{\tilde{a}}_3+2\,\ddot{\tilde{a}}_4\right)$$

$$-\sum_{k=1}^{N} \frac{2}{k\pi}\,\ddot{\tilde{w}}_k\left[1-\cos k\pi\,\tilde{l}_1+\cos k\pi\,\tilde{l}_{12}-(-1)^k\right]$$

$$-\left(\tilde{l}_1{}^2-\tilde{l}_{12}{}^2+1\right)\ddot{\tilde{a}}_3+2\left(\tilde{l}_1+\tilde{l}_2\right)\ddot{\tilde{a}}_4+\tilde{m}_c\left(\sum_{k=1}^{N} \ddot{\tilde{w}}_k \sin k\pi\,\tilde{l}_{12}+\ddot{\tilde{a}}_3\,\tilde{l}_{12}+\ddot{\tilde{a}}_4\right)$$

$$=-2\Omega\left\{\sum_{k=1}^{N} \dot{\tilde{v}}_k \frac{2}{k\pi}\left[1-(-1)^k\right]+\dot{\tilde{a}}_1+2\dot{\tilde{a}}_2\right\}$$

$$+\Omega^2\left\{\sum_{k=1}^{N} \tilde{w}_k \frac{2}{k\pi}\left[1-(-1)^k\right]+\tilde{a}_3+2\,\tilde{a}_4\right\}$$

$$-\lambda\left\{\sum_{k=1}^{N} \tilde{v}_k \frac{2}{k\pi}\left[1-(-1)^k\right]+\tilde{a}_1+2\,\tilde{a}_2\right\}$$

$$-\tilde{m}\lambda\left[\sum_{k=1}^{N} \tilde{v}_k \sin k\pi\tilde{c}+\tilde{a}_1\tilde{c}+\tilde{a}_2\right]-2\,\tilde{m}\Omega\left[\sum_{k=1}^{N} \dot{\tilde{v}}_k \sin k\pi\tilde{c}+\dot{\tilde{a}}_1\,\tilde{c}+\dot{\tilde{a}}_2\right]$$

$$+\tilde{m}\Omega^2\left[\sum_{k=1}^{N} \tilde{w}_k \sin k\pi\tilde{c}+\tilde{a}_3\,\tilde{c}+\tilde{a}_4\right]-\sum_{k=1}^{N} \frac{2k^3}{\pi}\left[1-(-1)^k\right]\left(\tilde{w}_k+\tilde{d}_i\dot{\tilde{w}}_k\right)$$

$$-\tilde{d}_e\left\{\sum_{k=1}^{N} \dot{\tilde{w}}_k \frac{2}{k\pi}\left[1-(-1)^k\right]+\dot{\tilde{a}}_3+2\dot{\tilde{a}}_4\right\}$$

$$-\tilde{d}_e\,\Omega\left\{\sum_{k=1}^{N} \tilde{v}_k \frac{2}{k\pi}\left[1-(-1)^k\right]+\tilde{a}_1+2\,\tilde{a}_2\right\}$$

$$+\pi\tilde{\mu}\cos\theta+\frac{\pi}{2}\tilde{m}\tilde{\mu}\cos\theta+\tilde{m}\tilde{e}_d\left[\Omega^2\sin\delta_d-\lambda\cos\delta_d\right]$$

$$+\sum_{k=1}^{N}\frac{2}{k\pi}\ddot{\tilde{v}}_k\left[1-\cos k\pi\tilde{l}_1+\cos k\pi\tilde{l}_{12}-(-1)^k\right]\left[k^4\left(\tilde{w}_k+\tilde{d}_i\dot{\tilde{w}}_k\right)\right.$$

$$\left.+2\Omega\dot{\tilde{v}}_k+\lambda\tilde{v}_k-\Omega^2\tilde{w}_k+\tilde{d}_e\left(\dot{\tilde{w}}_k+\Omega\tilde{v}_k\right)\right]$$

$$+\left(\tilde{l}_1-\tilde{l}_{12}+1\right)\left[2\Omega\dot{\tilde{a}}_1+\lambda\tilde{a}_1-\Omega^2\tilde{a}_3+\tilde{d}_e\left(\dot{\tilde{a}}_3+\Omega\tilde{a}_1\right)\right]$$

$$-2\left(\tilde{l}_1+\tilde{l}_2\right)\left[2\Omega\dot{\tilde{a}}_2+\lambda\tilde{a}_2-\Omega^2\tilde{a}_4+\tilde{d}_e\left(\dot{\tilde{a}}_4+\Omega\tilde{a}_2\right)-\frac{\pi}{2}\tilde{\mu}\cos\theta\right]$$

$$-\tilde{m}_b\left[2\Omega\left(\dot{\tilde{a}}_1+2\dot{\tilde{a}}_2\right)-\Omega^2\left(\tilde{a}_3+2\tilde{a}_4\right)+\lambda\left(\tilde{a}_1+2\tilde{a}_2\right)+\pi\tilde{\mu}\cos\theta\right]$$

$$-\frac{2}{\pi}\tilde{s}\left(\tilde{a}_3+2\tilde{a}_4\right)-\frac{2}{\pi}\tilde{p}\left[\dot{\tilde{a}}_3+2\dot{\tilde{a}}_4+\Omega\left(\tilde{a}_1+2\tilde{a}_2\right)\right]$$

$$-2\sum_{k=1}^{N}\frac{k^3}{\pi}\left(\tilde{w}_k+\tilde{d}_i\dot{\tilde{w}}_k\right)\left[-\cos k\pi\tilde{l}_1+\cos k\pi\tilde{l}_{12}\right]$$

$$-\tilde{m}_c\left[\tilde{l}_{12}\left(2\Omega\dot{\tilde{a}}_1+\lambda\tilde{a}_1-\Omega^2\tilde{a}_3\right)+2\Omega\dot{\tilde{a}}_2+\lambda\tilde{a}_2-\Omega^2\tilde{a}_4-\frac{\pi}{4}\tilde{\mu}\cos\theta\right]$$

$$-\tilde{m}_c\sum_{k=1}^{N}\sin k\pi\tilde{l}_{12}\left(2\Omega\dot{\tilde{v}}_k+\lambda\tilde{v}_k-\Omega^2\tilde{w}_k\right) \qquad (2.24.c)$$

Overdots now denote differentiation with respect to τ. Equations (2.23) - (2.24) are 2N+4 second-order ordinary differential equations, which will be solved by numerical integration.

A Fortran program for the IBM SP2 (Scalable Parallel Processor) was written to obtain the solution of the ordinary differential equations (ODE's). The DIVPAG subroutine with the Adams-Moulton method from IMSL (International Mathematical and Statistical Library) was used. It is applicable to first-order differential equations. Because of that, the second-order differential equations were transformed into first order differential equations as follows:

$$y_{2n-1} = \tilde{v}_n, \quad y_{2n} = \tilde{w}_n, \quad y_{2N+1} = \tilde{a}_1,$$

$$y_{2N+2} = \tilde{a}_2, \quad y_{2N+3} = \tilde{a}_3, \quad y_{2N+4} = \tilde{a}_4 \tag{2.25}$$

$$\dot{y}_{2n-1} = \frac{d\tilde{v}_n}{d\tau}, \quad \dot{y}_{2n} = \frac{d\tilde{w}_n}{d\tau}, \quad \dot{y}_{2N+1} = \frac{d\tilde{a}_1}{d\tau},$$

$$\dot{y}_{2N+2} = \frac{d\tilde{a}_2}{d\tau}, \quad \dot{y}_{2N+3} = \frac{d\tilde{a}_3}{d\tau}, \quad \dot{y}_{2N+4} = \frac{d\tilde{a}_4}{d\tau} \tag{2.26}$$

$$y_{M+2n-1} = \frac{d\tilde{v}_n}{d\tau}, \quad y_{M+2n} = \frac{d\tilde{w}_n}{d\tau}, \quad y_{M+2N+1} = \frac{d\tilde{a}_1}{d\tau},$$

$$y_{M+2N+2} = \frac{d\tilde{a}_2}{d\tau}, \quad y_{M+2N+3} = \frac{d\tilde{a}_3}{d\tau}, \quad y_{M+2N+4} = \frac{d\tilde{a}_4}{d\tau} \tag{2.27}$$

$$\dot{y}_{M+2n-1} = \frac{d^2\tilde{v}_n}{d\tau^2}, \quad \dot{y}_{M+2n} = \frac{d^2\tilde{w}_n}{d\tau^2}, \quad \dot{y}_{M+2N+1} = \frac{d^2\tilde{a}_1}{d\tau^2},$$

$$\dot{y}_{M+2N+2} = \frac{d^2\tilde{a}_2}{d\tau^2}, \quad \dot{y}_{M+2N+3} = \frac{d^2\tilde{a}_3}{d\tau^2}, \quad \dot{y}_{M+2N+4} = \frac{d^2\tilde{a}_4}{d\tau^2} \tag{2.28}$$

Hence

$$\dot{y}_{2n-1} = y_{M+2n-1}, \quad \dot{y}_{2n} = y_{M+2n}, \quad \dot{y}_{2N+1} = y_{M+2N+1},$$

$$\dot{y}_{2N+2} = y_{M+2N+2}, \quad \dot{y}_{2N+3} = y_{M+2N+3}, \quad \dot{y}_{2N+4} = y_{M+2N+4} \tag{2.29}$$

where

$M = 2N+4$

N = the highest mode considered

n = the number of the mode corresponding to the equation ranging from 1 to N

Therefore, the general formula can be written in the form

$$A\,\dot{y} = F(t,y) \qquad \text{or} \qquad \dot{y} = A^{-1}\,F(t,y) \tag{2.30}$$

where

A is a constant matrix of order 2Mx2M

A^{-1} is the inverse of the matrix A

y is a vector of order 2M

F(t,y) is a vector of order 2M

2.3. Critical Speeds

The shaft may have large deflections at or near certain shaft speeds, called critical speeds. In undamped systems, critical speeds occur when a vibration frequency is zero in the equations of motion, which gives an unstable condition. However, the system may become stable again when the speed increases past the critical speed. This phenomenon is called gyroscopic stabilization.

Critical speeds are computed for a steel rotor kit with data as follows:

Length of shaft $L = 30''$ (76.2 cm); Length of overhang $l_1 = l_2 = 6.5''$ (16.5 cm);

Radius of shaft $r_s = 1/2''$ (1.27 cm); Radius of disk $r_d = 4''$ (10.2 cm);

Radius of overhang mass $r_c = 2.16''$ (5.5 cm);

Weight of shaft $\mu gL = 6.7$ lb (30 N); Weight of disk $mg = 16$ lb (71 N);

Weight of bearing $m_b g = 2$ lb (8.9 N); Weight of overhang mass $m_c g = 9.9$ lb (44 N);

Young's modulus $E = 29 \times 10^6$ lb / in^2 (20×10^{10} N / m^2); Poisson' s ratio $\upsilon = 0.3$;

Density of shaft $\rho g = 0.283$ lb / in^3 (76,816 N / m^3); Crack depth $a = 0.2''$ (0.5 cm);

Crack location $b = 0.4L$; Stiffness of spring $s = 1300$ lb / in (227,660 N / m);

Eccentricity of disk $e_d = 0.04''$ (0.1 cm); Disk location $c = 0.5L$

Based on these data, the nondimensional quantities, to be called "standard data", can be obtained:

$$\tilde{r}_s = 0.0167, \quad \tilde{r}_d = 0.1333, \quad \tilde{r}_c = 0.0718,$$

$\tilde{e}_d = 0.001, \quad \delta_d = 0.75\pi, \quad a/2r_d = 0.2,$

$\tilde{\mu} = 2.755\text{x}10^{-5}, \quad \tilde{m} = 4.8, \quad \tilde{m}_b = 0.6, \quad \tilde{m}_c = 2.97,$

$\tilde{s} = 0.8, \quad \tilde{b} = 0.4, \quad \tilde{c} = 0.5, \quad \tilde{I}_1 = \tilde{I}_2 = 0.217$

The actual external damping, internal damping, and support damping are somewhat difficult to measure. For these quantities it is assumed that:

$\tilde{d}_e = 0.1, \quad \tilde{d}_i = 0.05, \quad \tilde{p} = 300$

which corresponds to the dimensional values

$d_e = 54.55 \text{ / sec}, \quad d_i = 9.165\text{x}10^{-5} \text{ sec}, \quad p = 900 \text{ lb / sec } (4{,}003 \text{ N / sec})$

The compliances c_{44} and c_{55} are related to the relative crack depth of the shaft. The nondimensional compliances are defined as follows:

$$\tilde{c}_{44} = \frac{EI}{L} c_{44}, \quad \tilde{c}_{55} = \frac{EI}{L} c_{55}$$

For the standard case, the compliances $\tilde{c}_{44}, \tilde{c}_{55}$ that correspond to the relative crack depth 0.2 are 0.00075 and 0.01055, respectively.

The relationships between nondimensional and dimensional angular velocity, angular acceleration, and time for the standard case are $\frac{d\theta}{dt} = 545.55\,\Omega \text{ rad / sec},$

$\frac{d^2\theta}{dt^2} = 2.976\text{x}10^{-5}\,\lambda \text{ rad / sec}^2, \quad t = 1.833\text{x}10^{-3}\,\tau \text{ sec}.$

For the uncracked shaft under constant angular velocity with flexible supports and neglecting external and internal damping, support damping, disk eccentricity, and the

effect of gravity, critical speeds were determined by exact and approximate methods. The exact method involves the solution of transverse vibrations of the shaft. In the approximate method, the approximate displacement functions with 5 modes of sine functions are used in the equations of motion. By assuming the angular velocity and the displacements are constant, the critical speeds are found by setting the determinant equal to zero. For the standard case, Table 2.1 gives first critical speeds for various conditions.

Table 2.1 Critical speeds

Case	$\tilde{m}$	$\tilde{m}_c$	$\tilde{s}$	$\tilde{I}_1$	$\tilde{I}_2$	Ω_{cr} exact	Ω_{cr} app.	% error
1	0	0	0.8	0	0	0.518	0.518	0
2	0	0	500	0	0	0.999	0.999	0
3	4.8	0	0.8	0	0	0.278	0.278	0
4	4.8	0	500	0	0	0.413	0.413	0
5	4.8	0	0.8	0.217	0.217	0.275	0.282	2.5
6	4.8	0	500	0.217	0.217	0.408	0.419	2.7
7	4.8	2.97	0.8	0.217	0.217	0.270	0.257	4.8
8	4.8	2.97	500	0.217	0.217	0.383	0.384	0.3

From this table, both methods give similar first critical speeds, with small differences. For the standard case of the shaft with or without overhang and with a disk at one end, case 3 and case 7 with $\tilde{s} = 0.8$ (flexible support) give similar first critical speeds, i.e., 0.278 and 0.270, respectively. In other cases with $\tilde{s} = 500$ (close to simply supported), case 4 without overhang has $\Omega_{cr} = 0.413$ and case 8 with overhang and a

disk at one end has $\Omega_{cr} = 0.383$.

For the uncracked shaft under constant angular velocity, including support damping, external and internal damping, and neglecting disk eccentricity and the effect of gravity, critical speeds were determined by approximate methods. For the case of the shaft without overhang, including $\tilde{p} = 300$, $\tilde{d}_e = 0.1$, and $\tilde{d}_i = 0.05$, the first critical speed Ω_{cr} for flexible support $\tilde{s} = 0.8$ is 0.413; on the other hand, for the case of the shaft with overhang and mass at one end, the first critical speed Ω_{cr} is 0.386. These values are similar to those of the case neglecting the dampings and with $\tilde{s} = 500$. In these cases, it seems the dampings give the same effect as the supports with high stiffness.

The first critical speeds that are mentioned above are not completely applicable, because they do not actually apply to a shaft with a breathing crack, unbalanced disk, and gravitational forces. However, for the standard case of the shaft with a crack, flexible supports, unbalanced disk, gravitational forces, and certain constant velocity, they agree with the numerical integration results, which give large deflections when the angular velocity is near these values. Therefore, these values are reasonable enough to be called the critical speeds for the problem considered here.

The time at which the angular velocity passes the critical speed is denoted τ_{cr} and will be called the "critical time". After passing τ_{cr}, the z-displacement becomes larger and reaches its maximum. The maximum z-displacement is called z_{max} and the time

corresponding to z_{max} is called τ_{max}.

2.4. Effects of Flexible Supports and Gyroscopic Moments

2.4.1. Introduction

In this section, the cracked shaft without overhang will be investigated. In this case, it is assumed that the overhang lengths at both ends l_1, l_2 and the mass m_c of the disk at the end of the overhang equal zero.

2.4.2. Convergence

The number of modes N of sine functions used in the approximate displacement functions (2.16.a) and (2.16.b) influences the accuracy of the result. Theoretically, if the number of flexural modes is infinite, one obtains the best result. For the considered case, the first mode gives the biggest influence compared to the others. This is shown in Fig. 2.4 for the standard case with acceleration $\lambda = 0.0005$, at $\tau = 900.4$. In this figure, the influence of each mode on the z-displacement at the disk location along the shaft is shown. It includes 5 flexural modes and two rigid body motions (rotation and translation). The influence of the even flexural modes is very small. The influence of the odd flexural modes decreases very fast for higher modes.

The resulting z_{max} for different values of N for the standard case is shown in

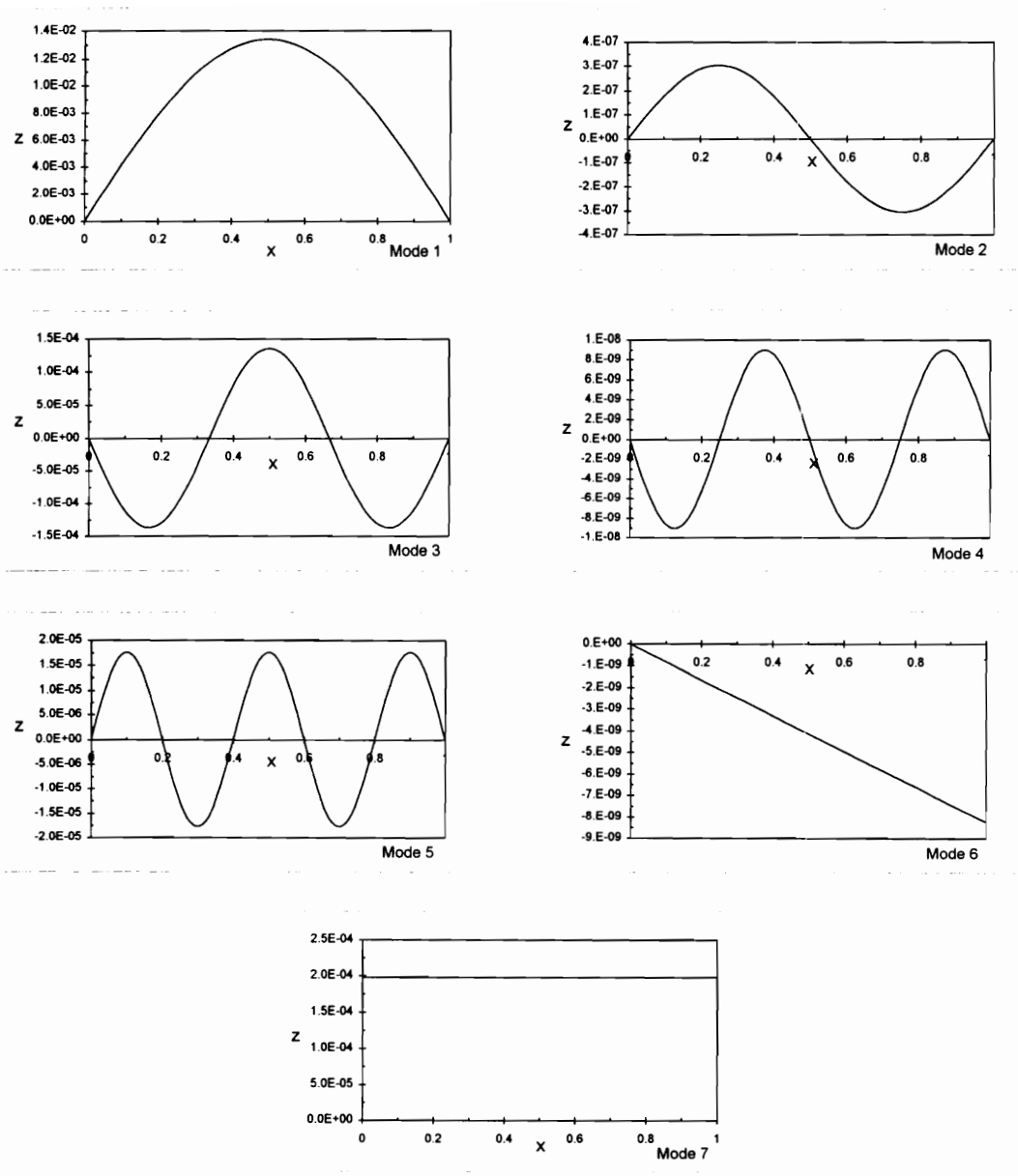

Fig. 2.4 Different Modes of z-displacement with Acceleration Rate
$\lambda = 0.0005$ at $\tau = 900.4$

Fig. 2.5 and Table 2.2. From this table, the difference of z_{max} between one flexural mode and 10 flexural modes is about 1.7%, and the difference between 5 modes and 10 modes is only 0.14%. Therefore, N=5 is assumed to give sufficiently accurate results, and will be used in the rest of this chapter.

Table 2.2 Relation between number of flexural modes and z_{max}

N	z_{max}
1	0.013622
2	0.013628
3	0.013808
4	0.013827
5	0.013833
6	0.013853
7	0.013842
8	0.013849
9	0.013851
10	0.013853

2.4.3. Acceleration and deceleration

The behavior of the cracked shaft with flexible and damped supports under constant acceleration and deceleration passing through the critical speed is investigated. For acceleration, the system starts from rest with $\theta = 0$, and the angular velocity Ω increases until it reaches 0.7. The angular rotation and velocity can be written as follows:

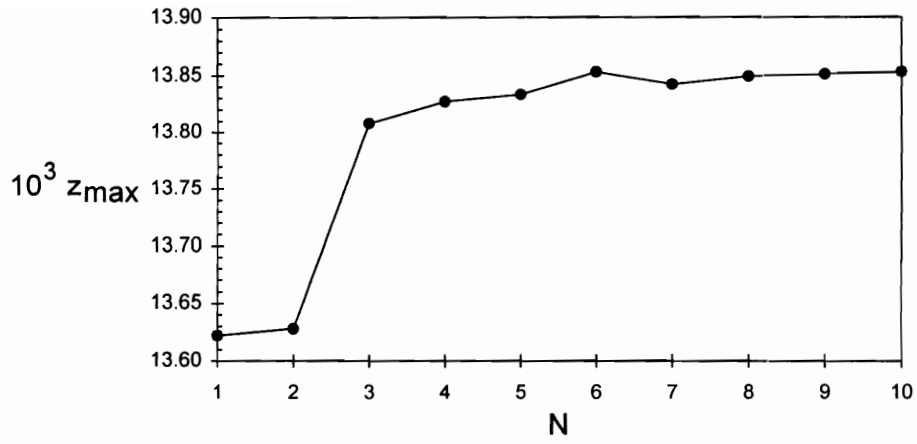

Fig. 2.5 Convergence

$$0 \le \tau \le T_1: \qquad \theta(\tau) = 0.5\ \lambda\ \tau^2, \qquad \Omega(\tau) = \lambda\,\tau$$

$$\tau \ge T_1: \qquad \theta(\tau) = 0.7\ \tau - 0.35\ T_1, \qquad \Omega(\tau) = 0.7 \tag{2.31}$$

where $T_1 = 0.7 / \lambda$ is the time when the angular velocity reaches 0.7 and Ω_0 is the initial angular velocity.

For deceleration, the angular velocity Ω is 0.7 initially and the initial conditions are zero except for $\tilde{v}_1 = \tilde{w}_1 = 0.001$. The formulation can be written as

$$0 \le \tau \le T_1: \qquad \theta(\tau) = 0.7\ \tau - \ 0.5\,\lambda\,\tau^2, \qquad \Omega(\tau) = 0.7 - \lambda\,\tau$$

$$\tau \ge T_1: \qquad \theta(\tau) = 0.35\ T_1, \qquad \Omega(\tau) = 0 \tag{2.32}$$

The angular velocity becomes zero at $\tau = T_1$. Four different rates of angular acceleration are considered in this study. The relation between the acceleration/deceleration rate and τ_{cr} is shown in Table 2.3.

Table 2.3 Relation between acceleration/deceleration rates and τ_{cr}

λ	T_1 / λ	τ_{cr}	
		Accel.	Decel.
0.001	700	413	287
0.0005	1400	826	574
0.00025	2800	1652	1148
0.00010	7000	4130	2870

Figures 2.6 - 2.9 show the time histories of the vertical displacement z and the radial displacement R at the disk location for the standard case under different acceleration rates, while Figs. 2.10 - 2.13 consider different deceleration rates. The solid line depicts a closed crack and the dashed line is for an open crack. For all cases, z reaches its maximum after passing the critical time τ_{cr}, and decreases quickly after that. For the uncracked shaft, the time history behavior is similar to that for the shaft with a breathing crack, but it has a smaller maximum value of z for this standard case. As the angular acceleration and deceleration rates decrease, the maximum value of z increases, as shown in Fig. 2.14. This occurs because there is a longer time to build up a larger displacement before the angular velocity reaches the critical speed.

2.4.4. Influence of support stiffness

The stiffness of the supports influences the behavior of the cracked rotating shaft. Based on the standard parameters including $\tilde{p} = 300$, and with $\lambda = 0.0005$ for acceleration, various support stiffnesses are investigated, from flexible supports to one that is close to a simple support. Figure 2.15 shows the relation between the stiffness of the supports and the maximum z-displacement of the disk. It is interesting that a support with small stiffness ($\tilde{s} = 0.5$) gives a relatively large z_{max} and that z_{max} decreases until $\tilde{s} = 15$. After that, increasing support stiffness gives a larger z_{max}. The difference between the smallest z_{max} (at $\tilde{s} = 15$) and the largest z_{max} (at $\tilde{s} = 500$) in Fig. 2.15 is about 7.25%.

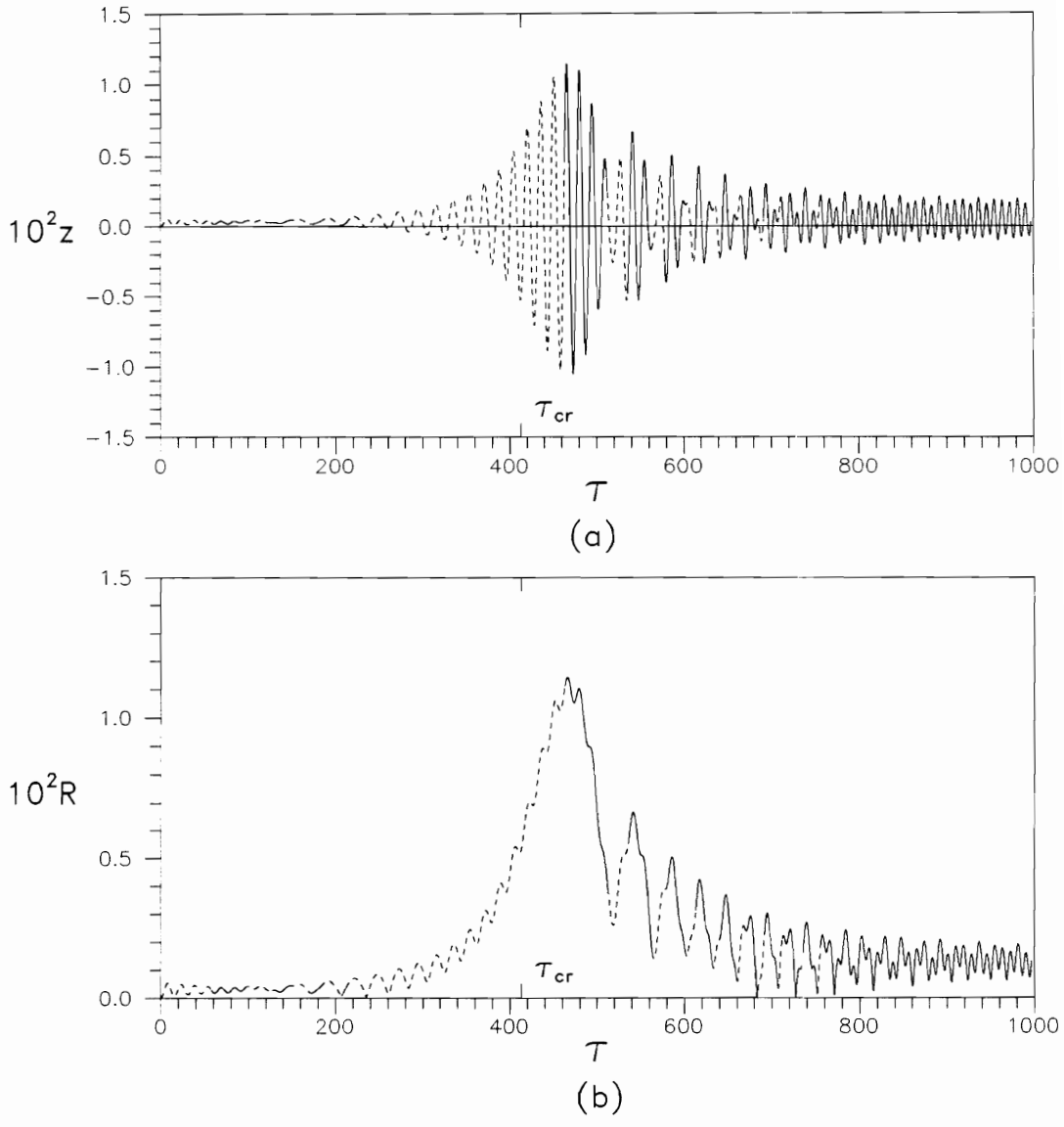

Fig. 2.6 Time Histories for Acceleration Rate λ=0.001

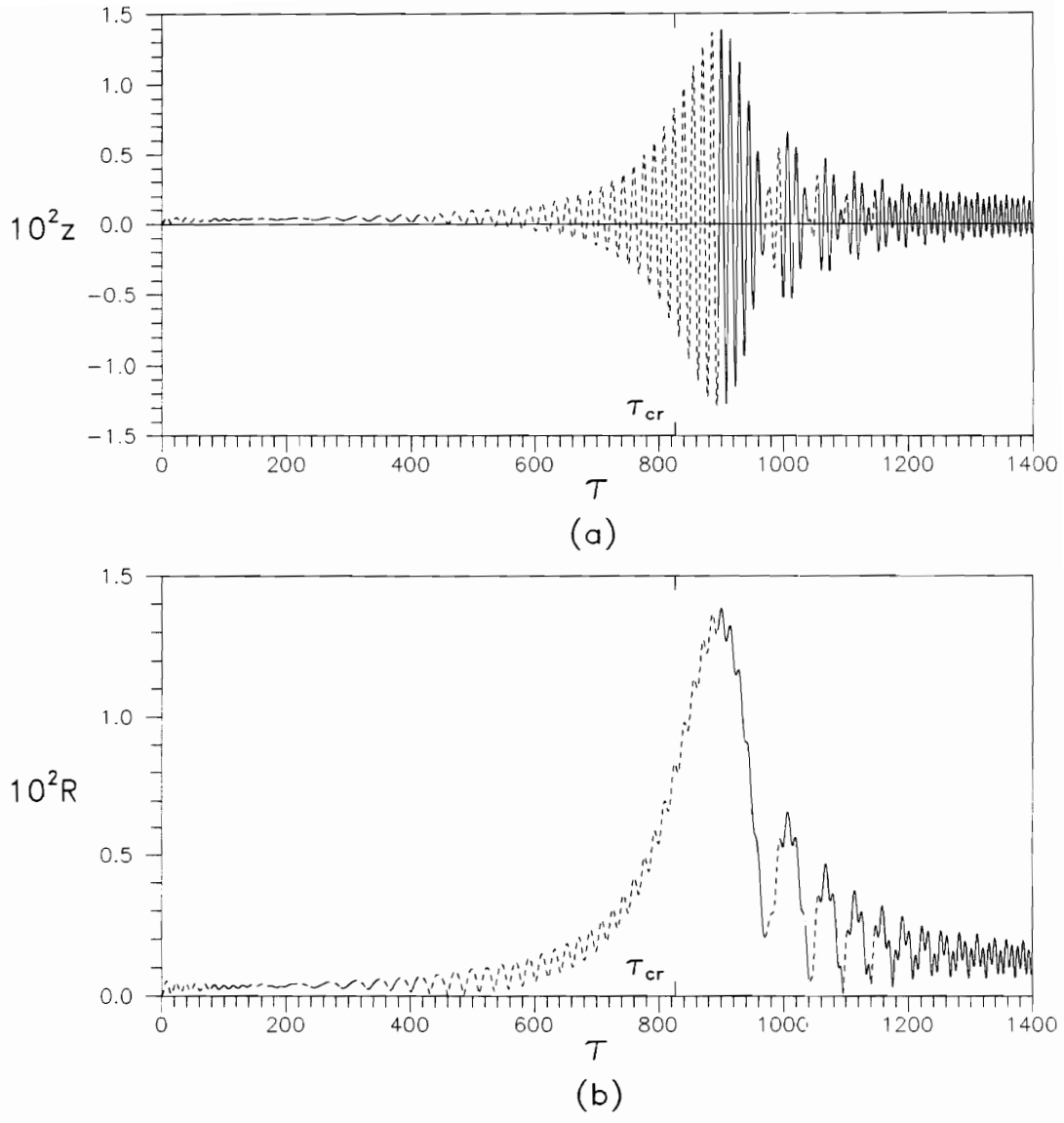

Fig. 2.7 Time Histories for Acceleration Rate λ=0.0005

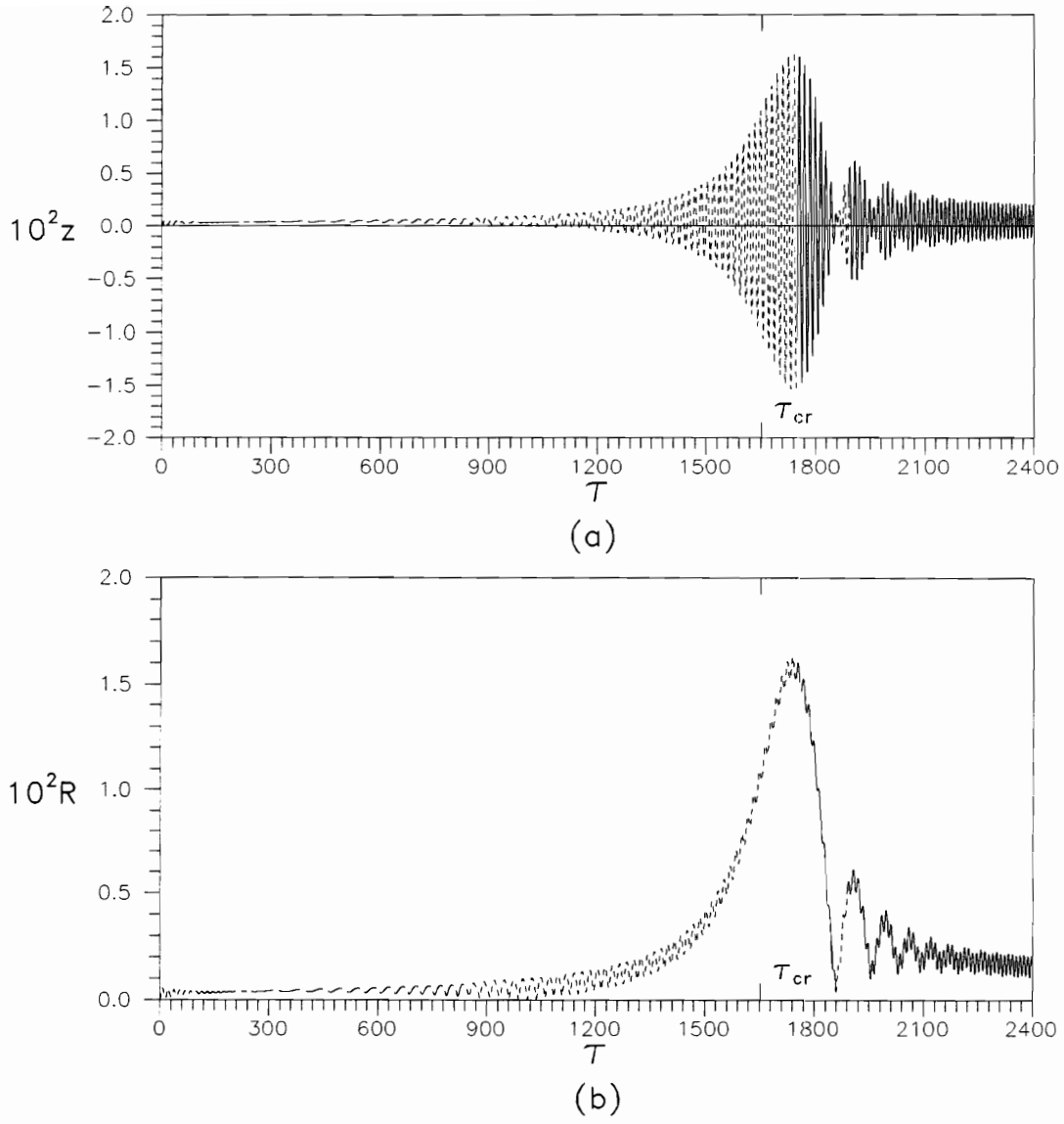

Fig. 2.8 Time Histories for Acceleration Rate λ=0.00025

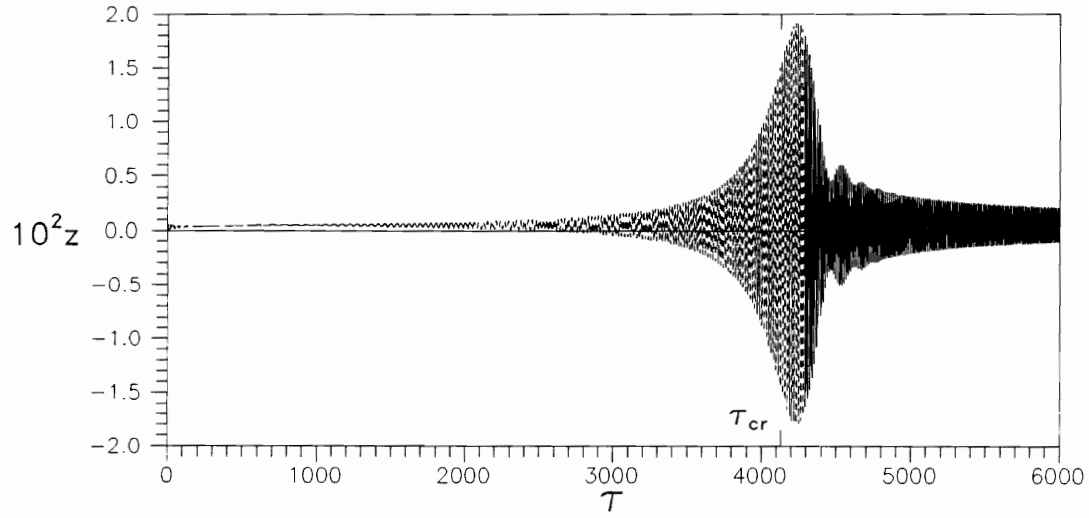

(a)

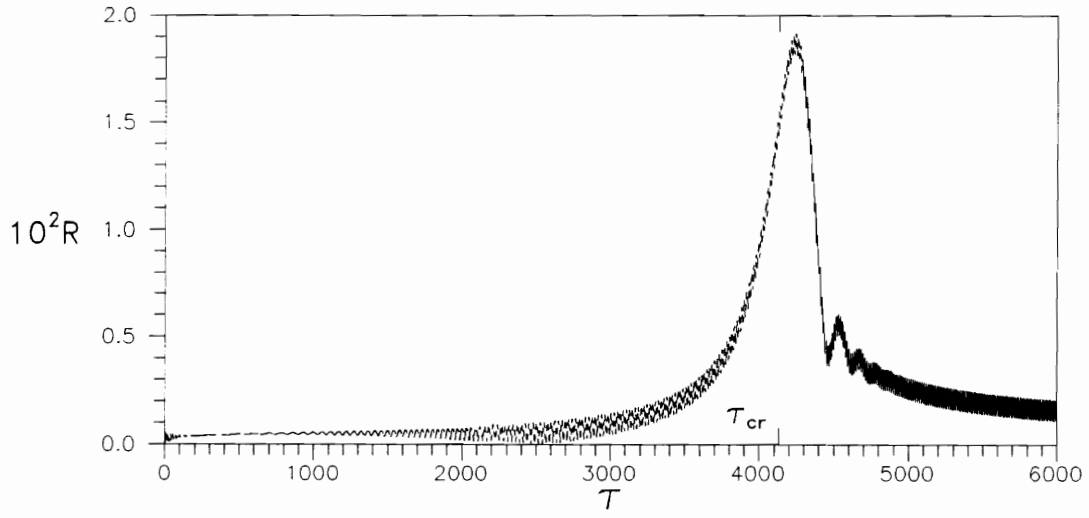

(b)

Fig. 2.9 Time Histories for Acceleration Rate λ=0.0001

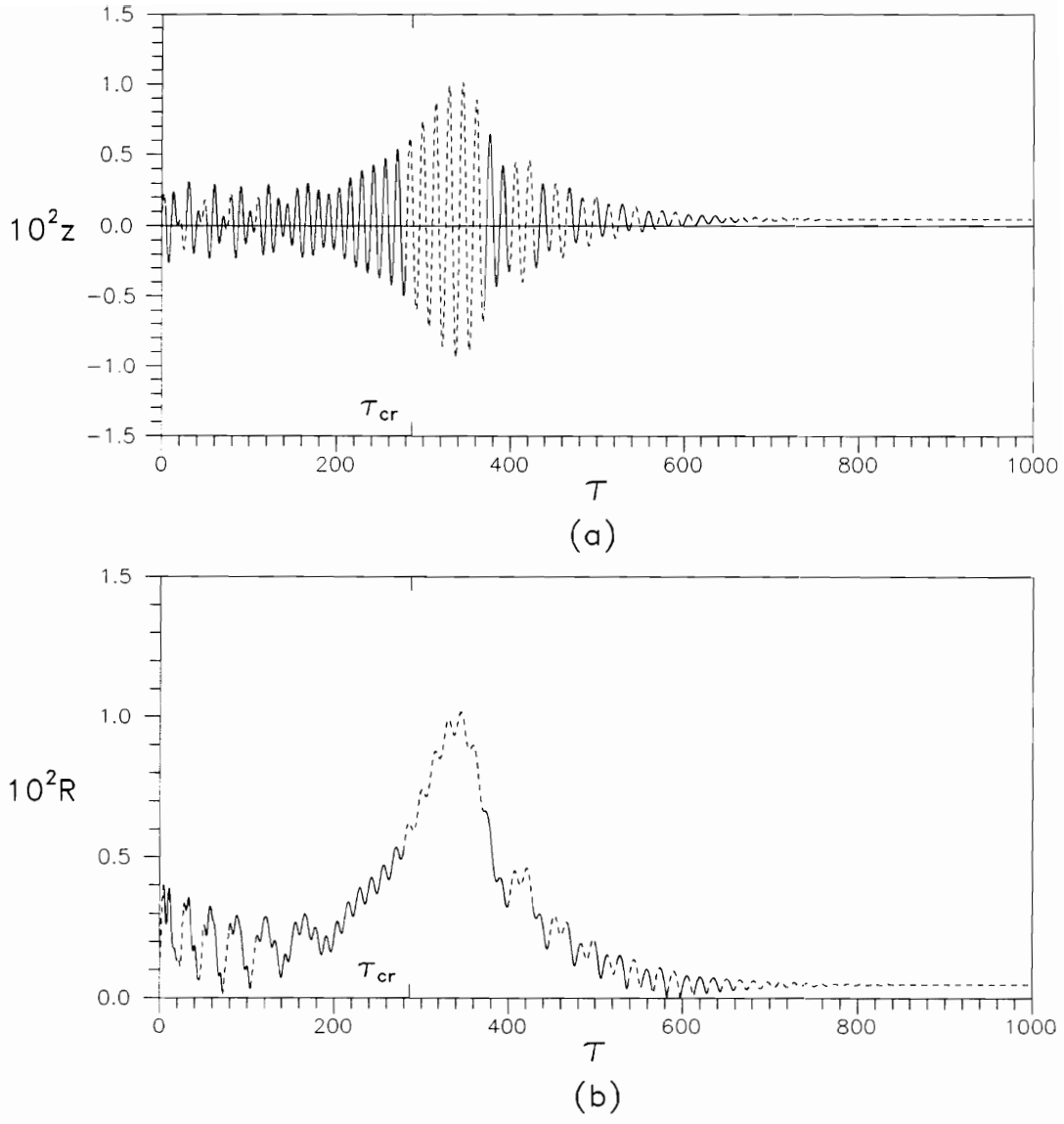

Fig. 2.10 Time Histories for Deceleration Rate λ=0.001

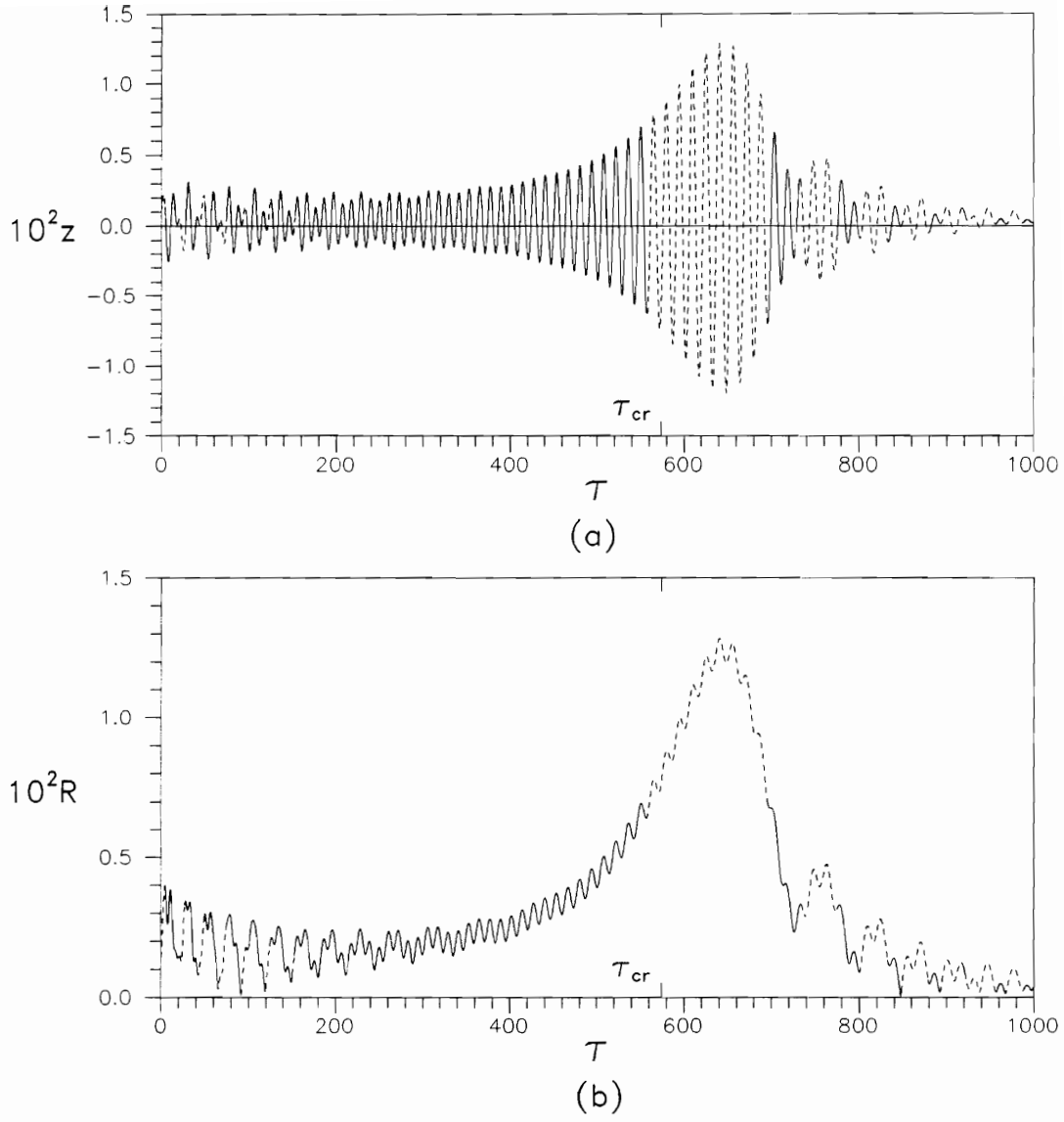

Fig. 2.11 Time Histories for Deceleration Rate λ=0.0005

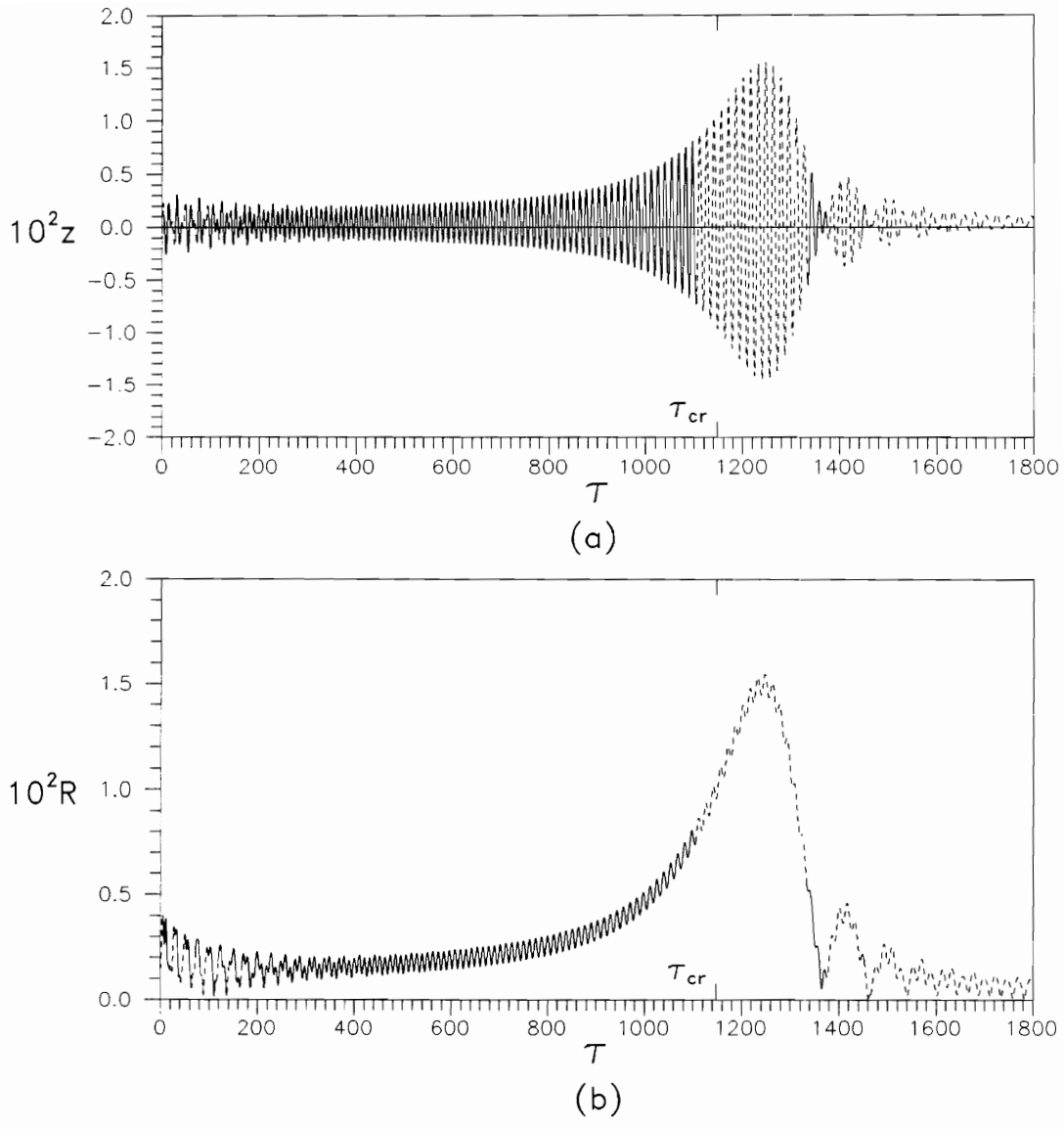

Fig. 2.12 Time Histories for Deceleration Rate λ=0.00025

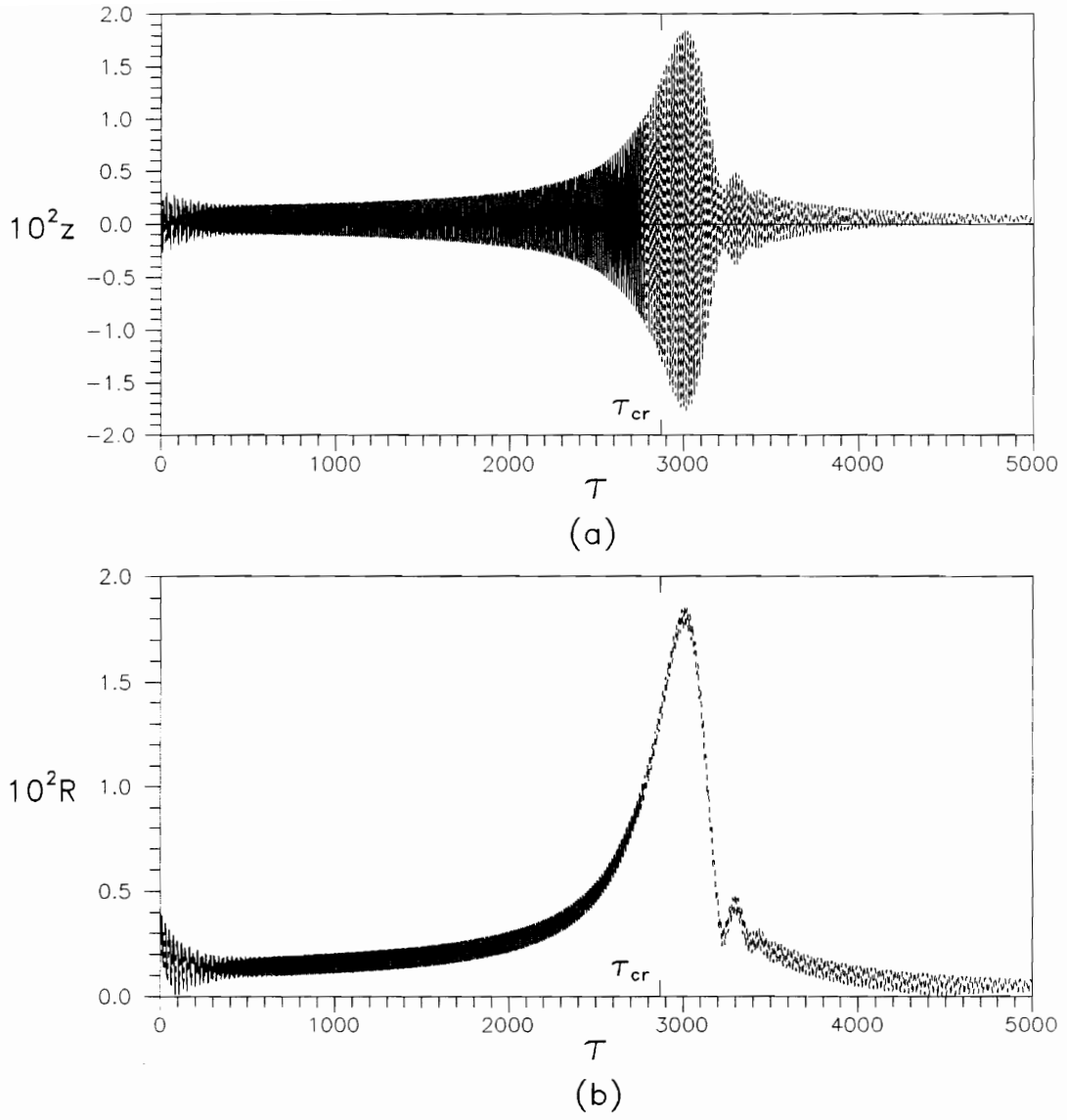

Fig. 2.13 Time Histories for Deceleration Rate λ=0.0001

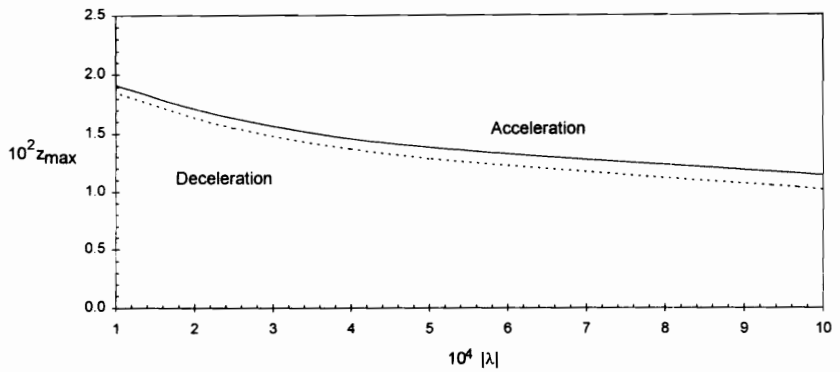

Fig. 2.14 Effects of Acceleration and Deceleration Rate on z_{max}

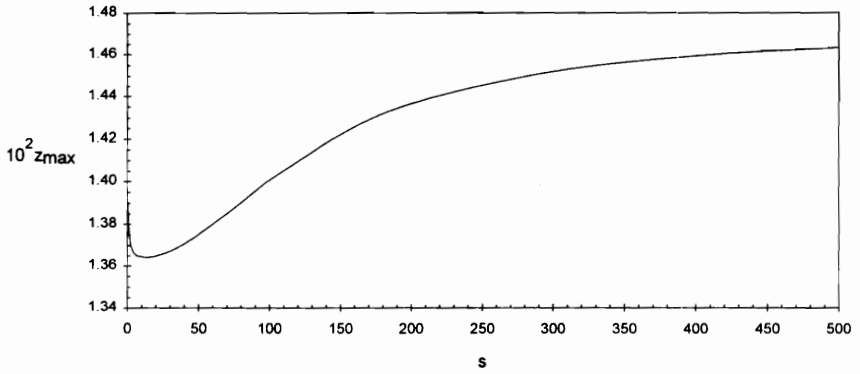

Fig. 2.15 Effect of Support Stiffness on z_{max}

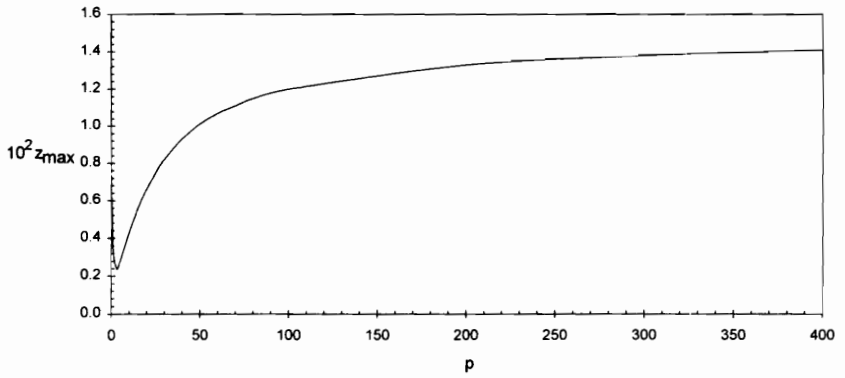

Fig. 2.16 Effect of Support Damping on z_{max}

The difference of z_{max} between $\tilde{s} = 0.5$ and $\tilde{s} = 15$ is about 1.9%. The vertical displacement z along the shaft looks almost the same as Mode 1 in Fig. 2.4. The rigid body motion decreases when the stiffness increases, and has a small influence on z.

2.4.5. Influence of support damping

In order to study the effect of support damping, z_{max} has been calculated for various values of support damping under the constant acceleration $\lambda = 0.0005$ with standard parameters, including $\tilde{s} = 0.8$. Figure 2.16 plots the result between support damping and the maximum value of z at the disk location. As $\tilde{p}$ is increased from $\tilde{p} = 0$ (undamped supports) till $\tilde{p} = 3$, z_{max} decreases; however, after that, increasing $\tilde{p}$ causes z_{max} to increase. The maximum z-displacement for $\tilde{p} = 0$ is about 3.2 times larger than for $\tilde{p} = 3$, and for $\tilde{p} = 3$ it is about 5.9 times smaller than for $\tilde{p} = 400$. Between $\tilde{p} = 300$ and $\tilde{p} = 400$, z_{max} does not change much; the difference is only 2.2%.

Figure 2.17 shows the behavior of z along the shaft with different support dampings, when τ is approximately τ_{max}. For the undamped case, the rigid body motion dominates the displacement. The rigid body motion decreases when support damping is applied, and has less effect on z for larger support damping.

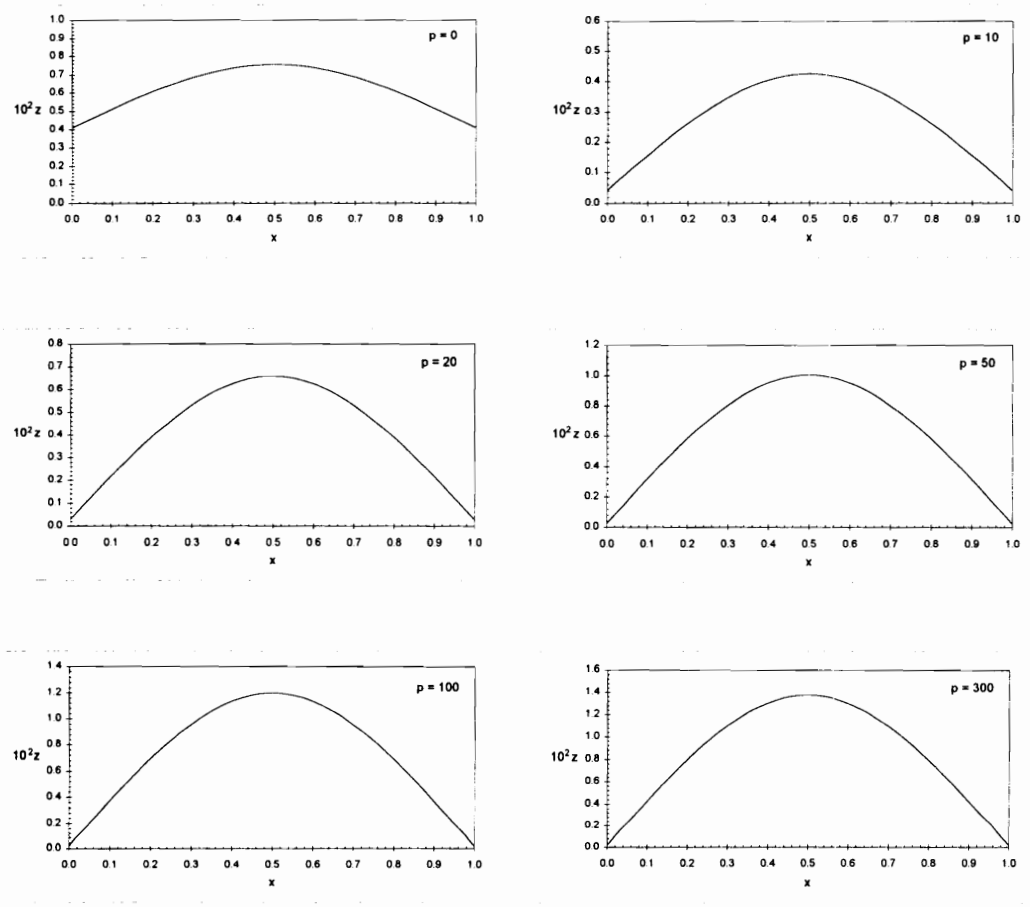

Fig. 2.17 Effect of Support Damping on z-displacement Along the Shaft

2.4.6. Influence of gyroscopic moments of disk

Gyroscopic effects of the disk have been included in the formulation. The location of the disk influences these gyroscopic effects. Based on this, an investigation is carried out for the cracked shaft under acceleration rate $\lambda = 0.0005$ and standard parameters, with different locations of the disk. The relation between the location of the disk and the maximum z-displacement at the center with and without gyroscopic effects is shown in Fig. 2.18. From that figure, it is clear that if the disk is at the center there is almost no effect from gyroscopic moments because the shaft is almost symmetric (although the crack at 0.4L makes it unsymmetric) and the initial conditions are symmetric. Then the motion is almost symmetric and the slope of the shaft at the center is almost zero. If the disk is far from the center, the effect becomes greater, but it still does not give too much difference here (about 2%).

2.4.7. Influence of disk eccentricity angle

The angle of disk eccentricity, δ_d, with respect to the crack face gives a promising result for detecting a crack on a rotating shaft with flexible and damped supports. As shown in Fig. 2.19, the relation between the disk eccentricity angle and the maximum z-displacement at the disk location for the standard case under constant acceleration $\lambda = 0.0005$ is different for a breathing crack, an open crack, and an uncracked shaft. For a rotating shaft with the disk eccentricity angle equal to zero, the three conditions of the shaft give almost the same result. For an uncracked shaft, the

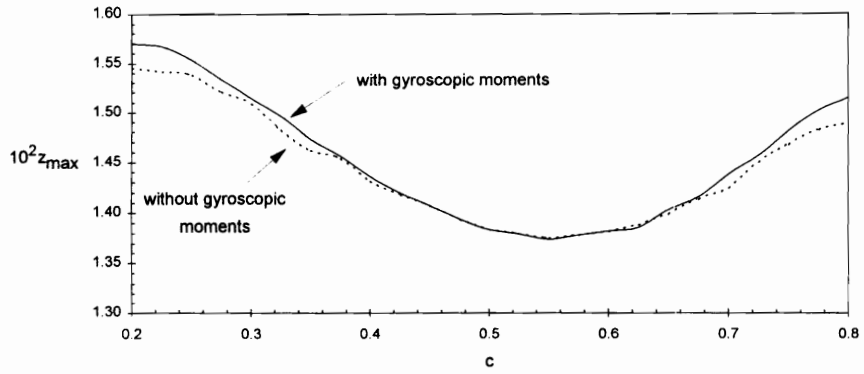

Fig. 2.18 Effects of Disk Location and Gyroscopic Moments on z_{max}

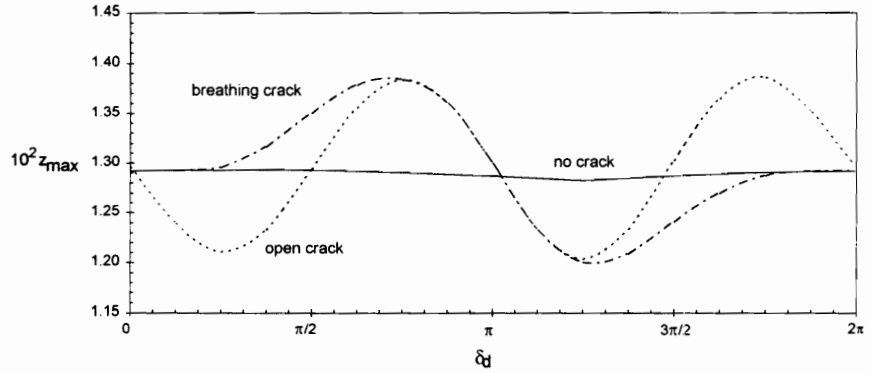

Fig. 2.19 Effect of Eccentricity Angle on z_{max}

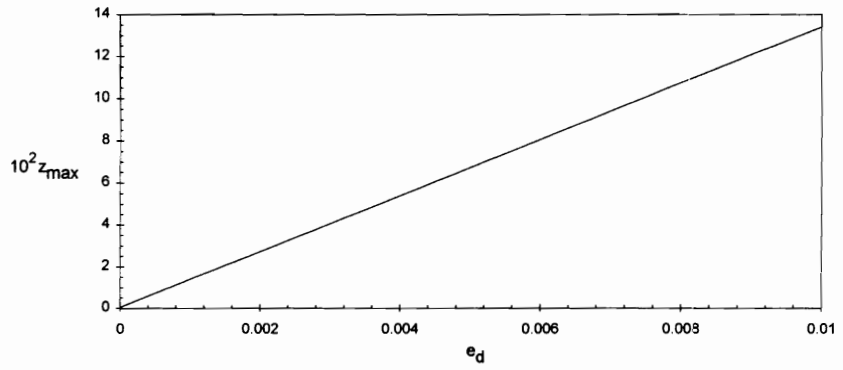

Fig. 2.20 Effect of Disk Eccentricity on z_{max}

variation of disk eccentricity angle does not have much effect on the maximum z-displacement. For the shaft with a breathing crack under different δ_d, the curve has one maximum and one minimum in Fig. 2.19. On the other hand, for the shaft with an open crack, the curve has two maxima and two minima. Compared to an uncracked shaft, the breathing cracked shaft and open cracked shaft sometimes have a smaller z_{max} and sometimes a larger z_{max}, depending on the disk eccentricity angle. When δ_d is between 0.75π and 1.25π, the open cracked shaft gives a similar result to the breathing cracked shaft. If various unbalanced weights can be added to the disk to cause certain eccentricity angles, the response might indicate the presence of crack.

However, various values of the disk eccentricity e_d with the standard case under constant acceleration $\lambda = 0.0005$ and a breathing crack do not give too much change. Increasing the disk eccentricity gives a higher maximum z-displacement proportionally, as shown in Fig. 2.20. This occurs because a larger disk eccentricity means a larger force on the rotating shaft and causes a larger displacement.

2.4.8. Influence of external and internal damping

The influence of the nondimensional external and internal damping coefficients, $\tilde{d}_e$ and $\tilde{d}_i$, is investigated, based on the standard parameters under constant acceleration $\lambda = 0.0005$ with different combinations of external and internal damping. Figures 2.21 - 2.24 show time histories with various values of external damping and constant internal

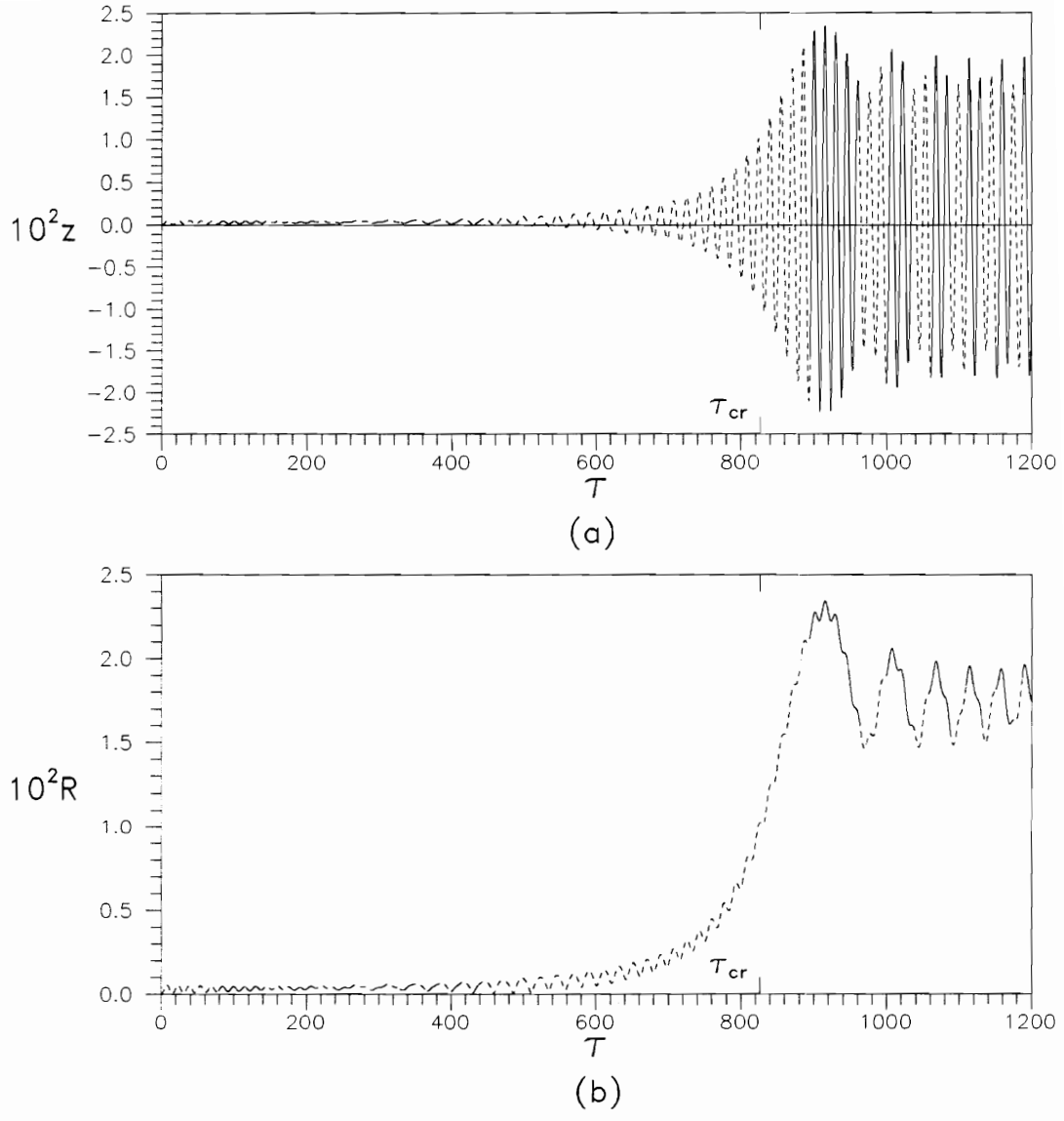

Fig. 2.21 Time Histories for d_e=0, d_i=0.05

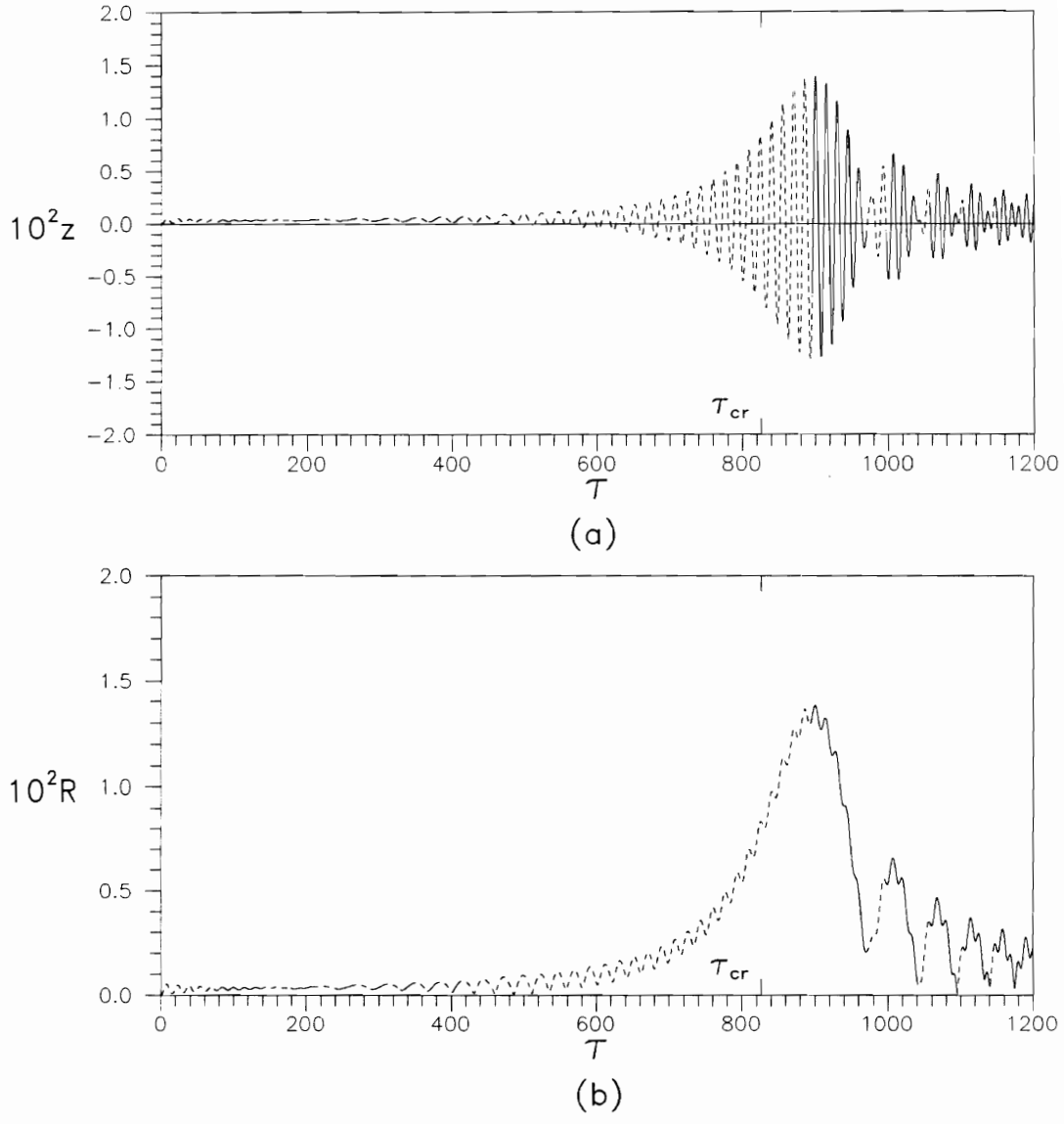

Fig. 2.22 Time Histories for d_e=0.1, d_i=0.05

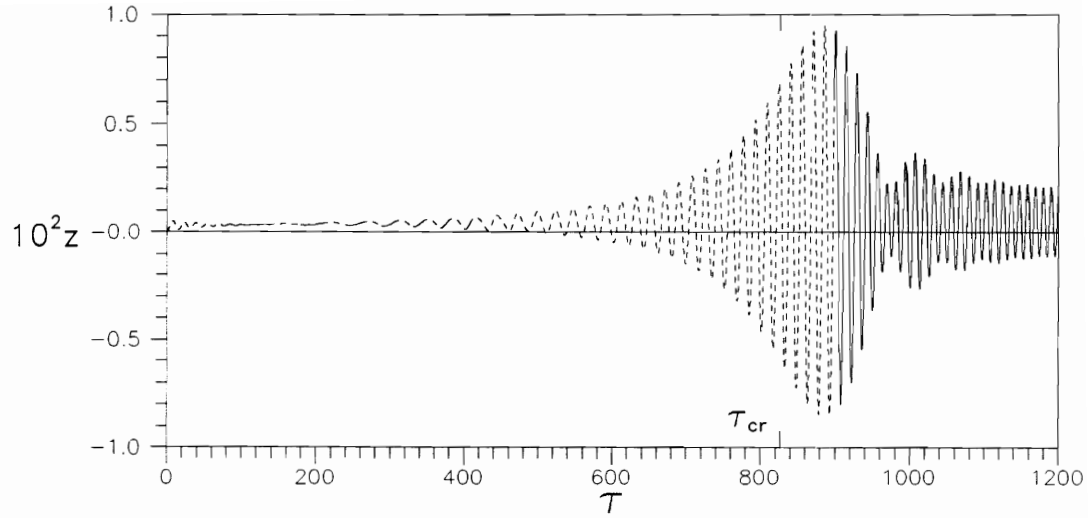

(a)

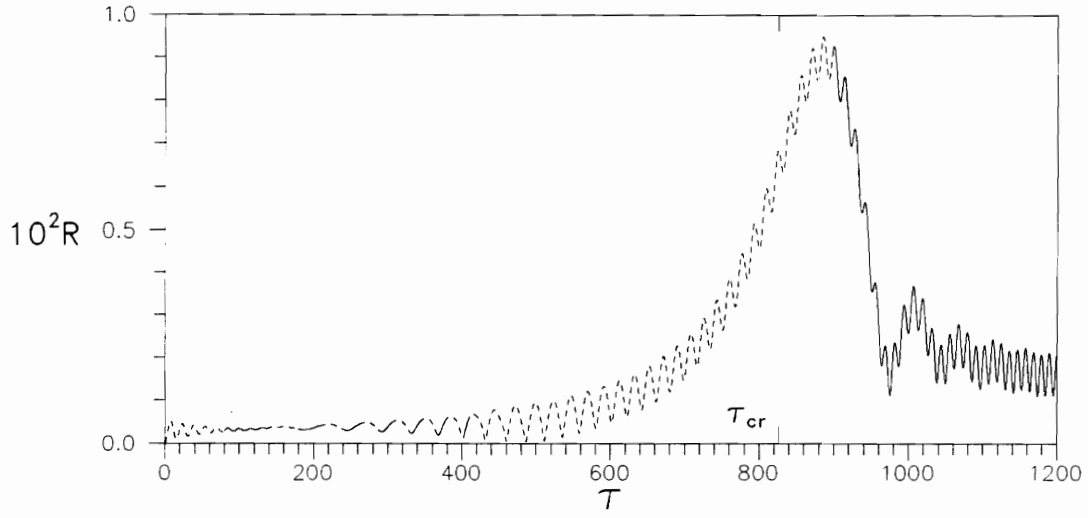

(b)

Fig. 2.23 Time Histories for d_e=0.2, d_i=0.05

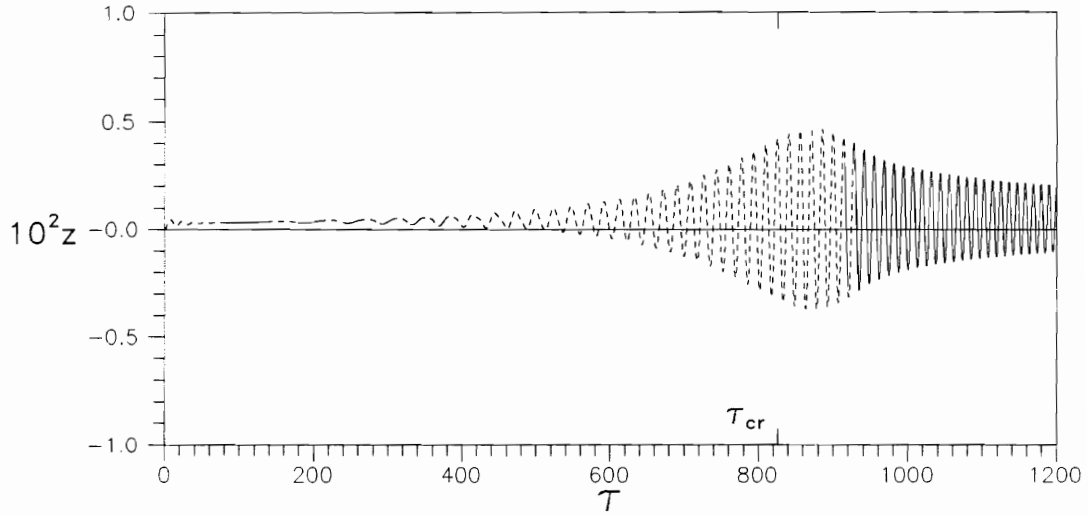

(a)

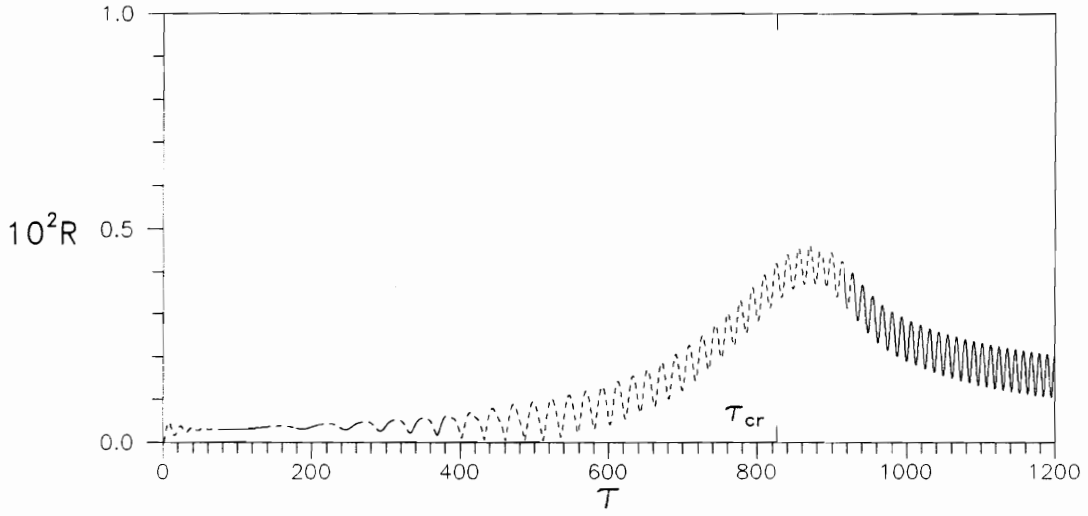

(b)

Fig. 2.24 Time Histories for d_e=0.5, d_i=0.05

damping ($\tilde{d}_i = 0.05$). Figures 2.25 - 2.28 give time histories with various values of external damping but without internal damping. From these figures, it is clear that increasing external damping tends to make the system more stable.

Time histories for various internal damping coefficients with constant external damping ($\tilde{d}_e = 0.1$) are presented in Figs. 2.26, 2.29 - 2.32. The system becomes unstable when $\tilde{d}_i$ reaches 0.4, and the response tends to increase (Figs. 2.31 and 2.32 for $\tau > 1000$).

2.5. Effect of Overhangs with Mass at One End

2.5.1. Introduction

This section concentrates on the cracked rotating shaft with overhang and mass at one end of the overhang. Figures 2.33 and 2.34 show the time histories of the cracked shaft with overhang under acceleration and deceleration $\lambda = 0.0005$, respectively. They show the vertical displacement z and the radial displacement R at the disk location for the standard case with a breathing crack. The figures are similar to the ones without overhang (Figs. 2.7 and 2.11), but the maximum z-displacements are smaller. This occurs because the critical speed for the case with overhang is smaller than for the case without overhang; thus, the critical time τ_{cr} is reached sooner. In this case, there is less time for the shaft to build up energy before the maximum z-displacement is attained.

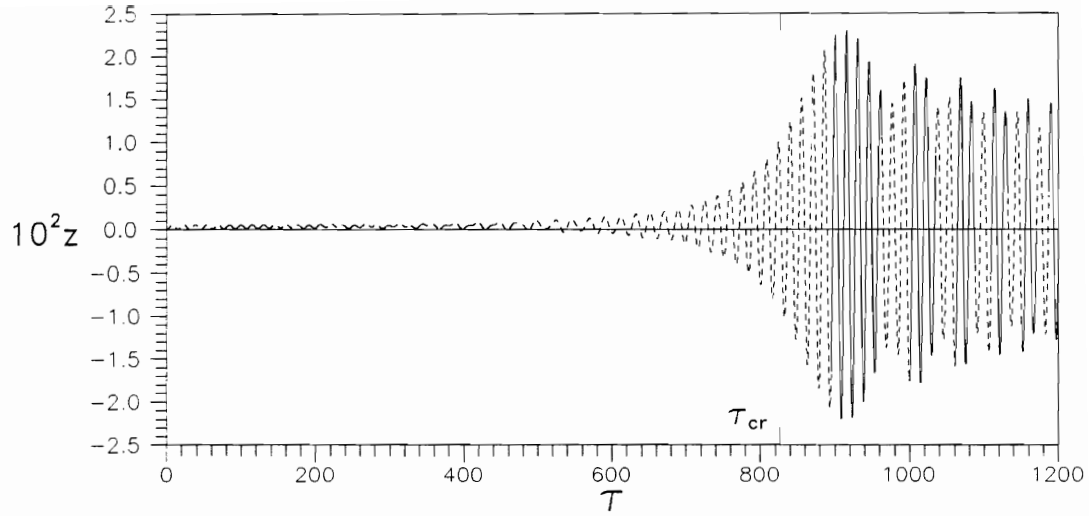

(a)

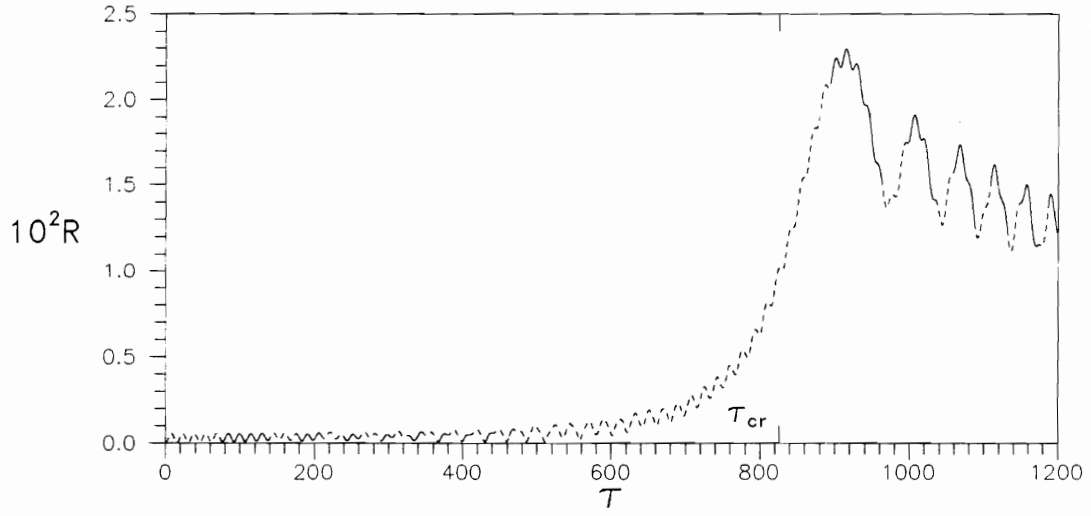

(b)

Fig. 2.25 Time Histories for $d_e=0$, $d_i=0$

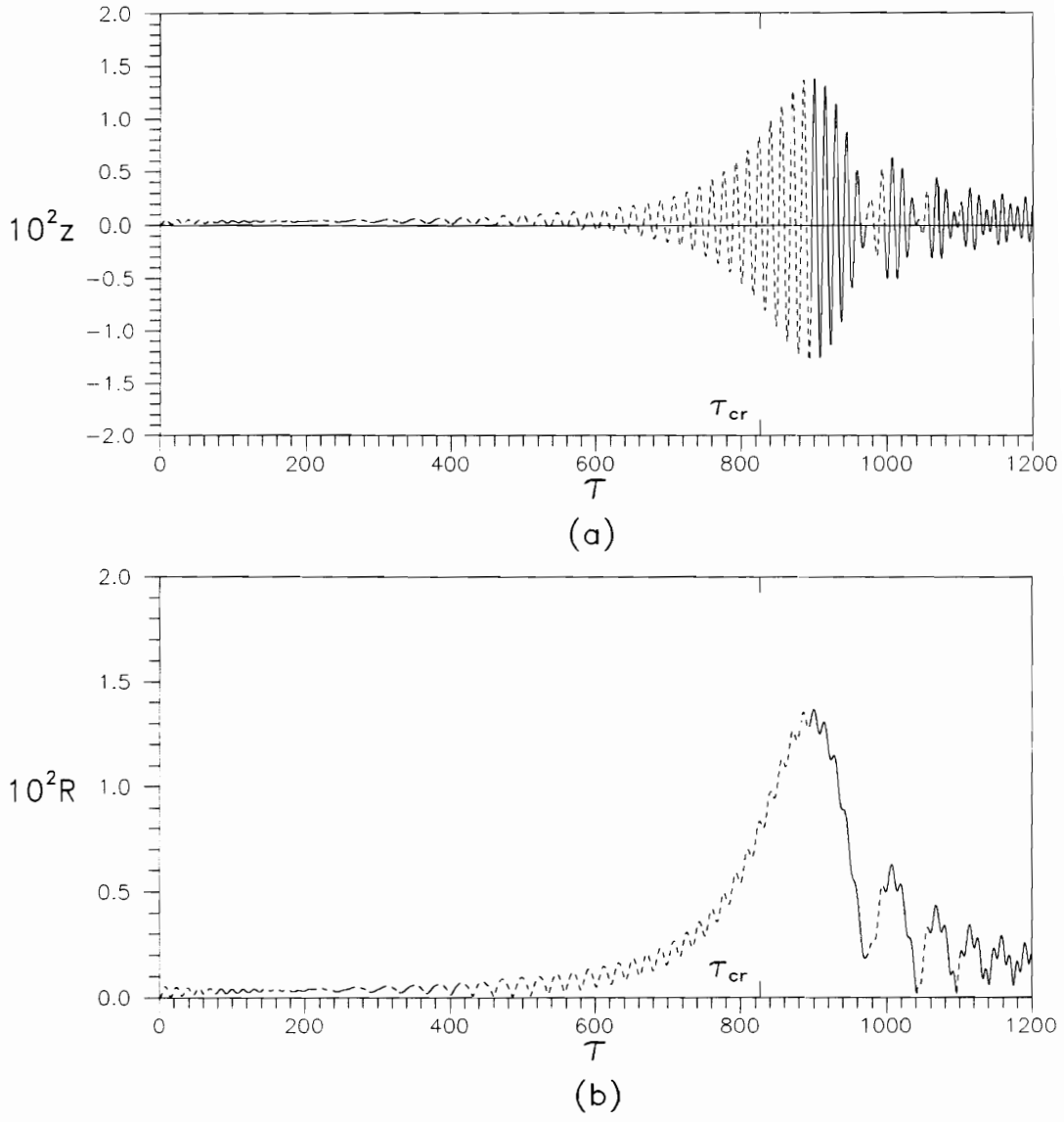

Fig. 2.26 Time Histories for d_e=0.1, d_i=0

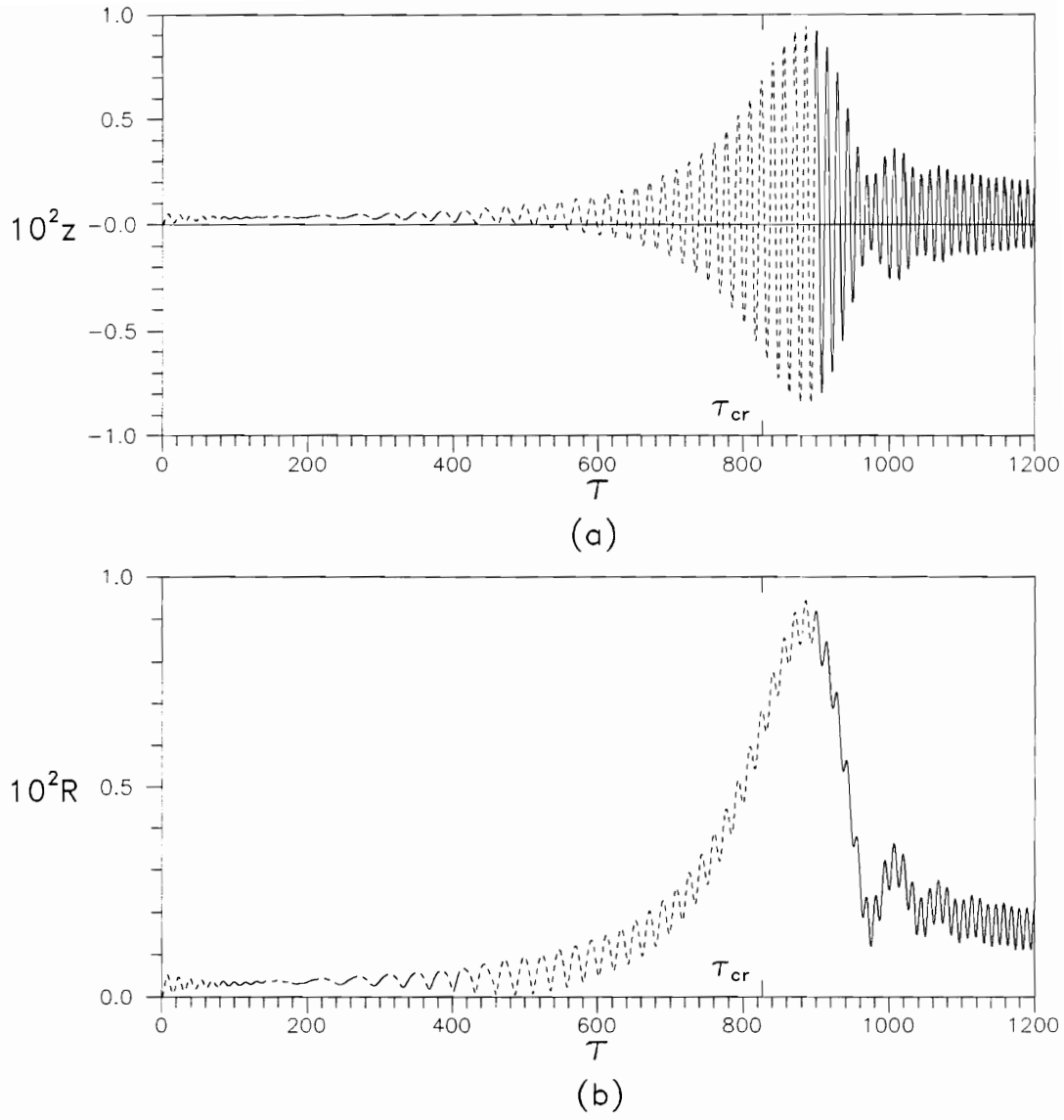

Fig. 2.27 Time Histories for d_e=0.2, d_i=0

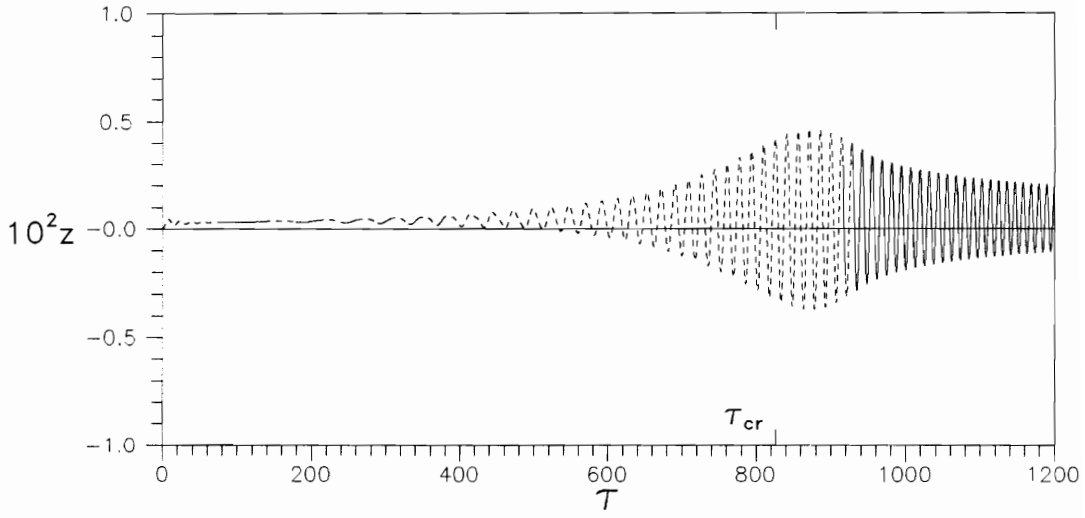

(a)

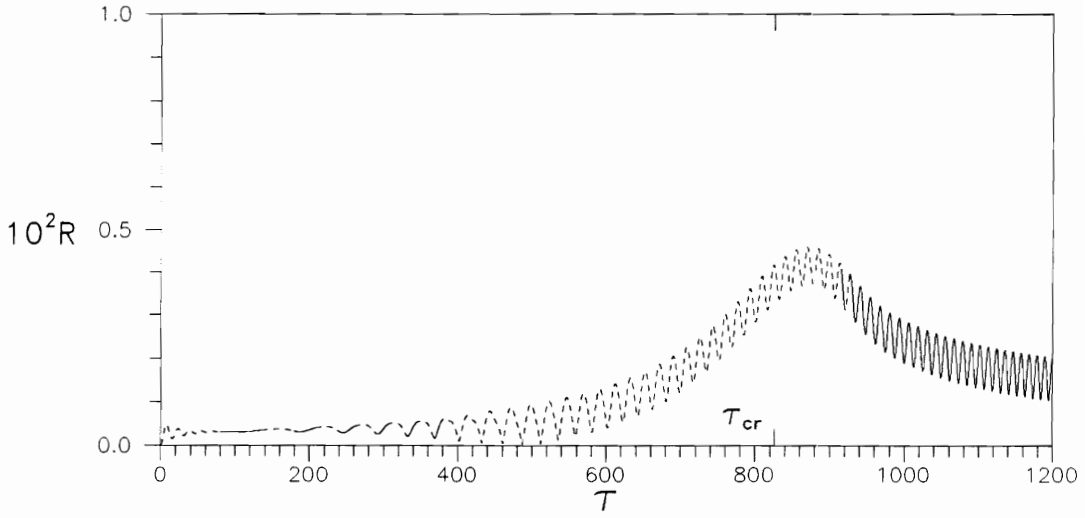

(b)

Fig. 2.28 Time Histories for d_e=0.5, d_i=0

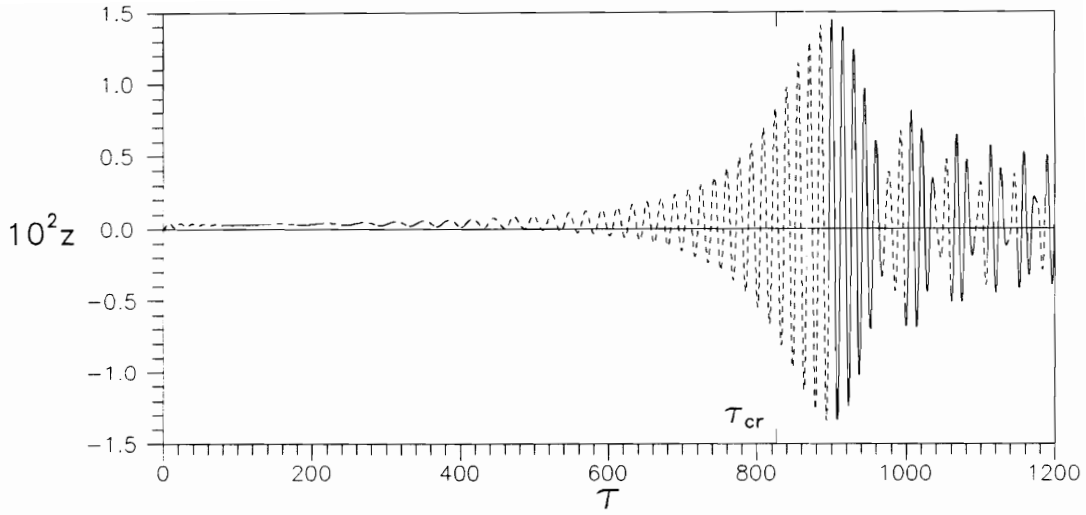

(a)

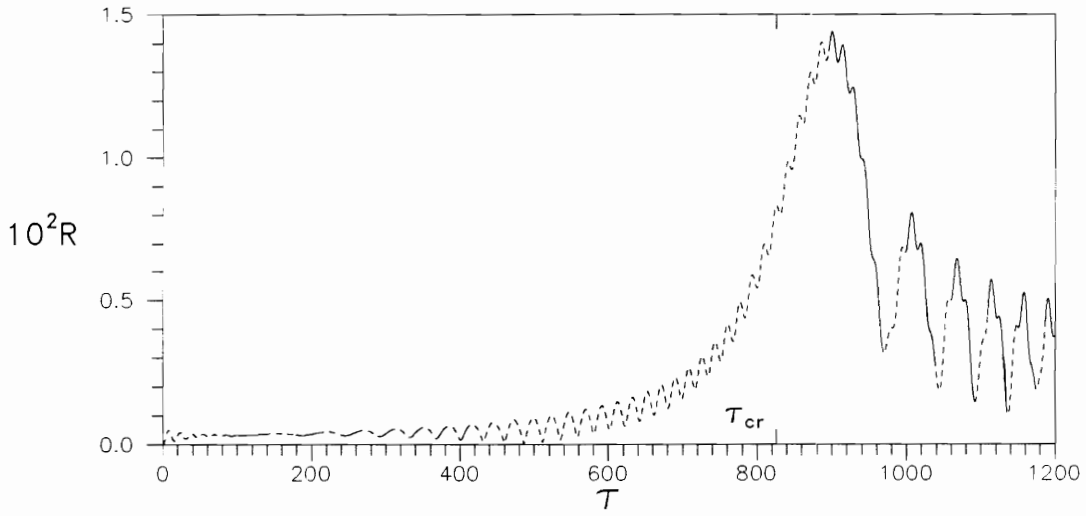

(b)

Fig. 2.29 Time Histories for d_e=0.1, d_i=0.25

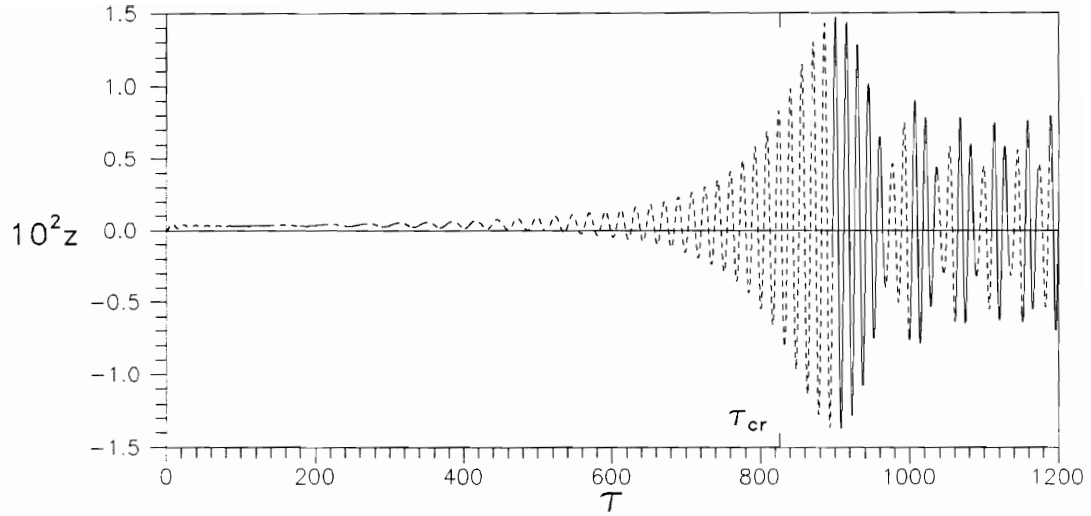

(a)

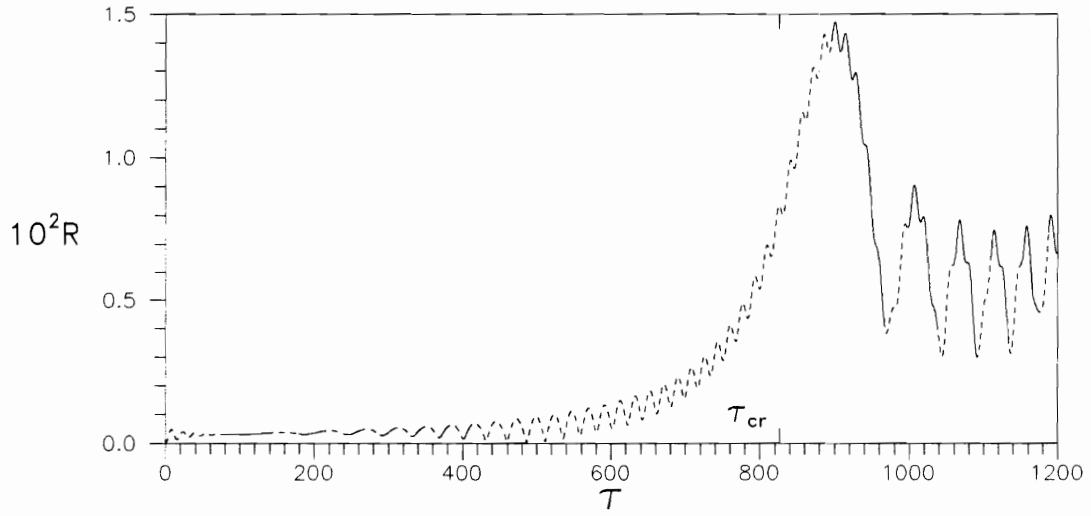

(b)

Fig. 2.30 Time Histories for d_e=0.1, d_i=0.35

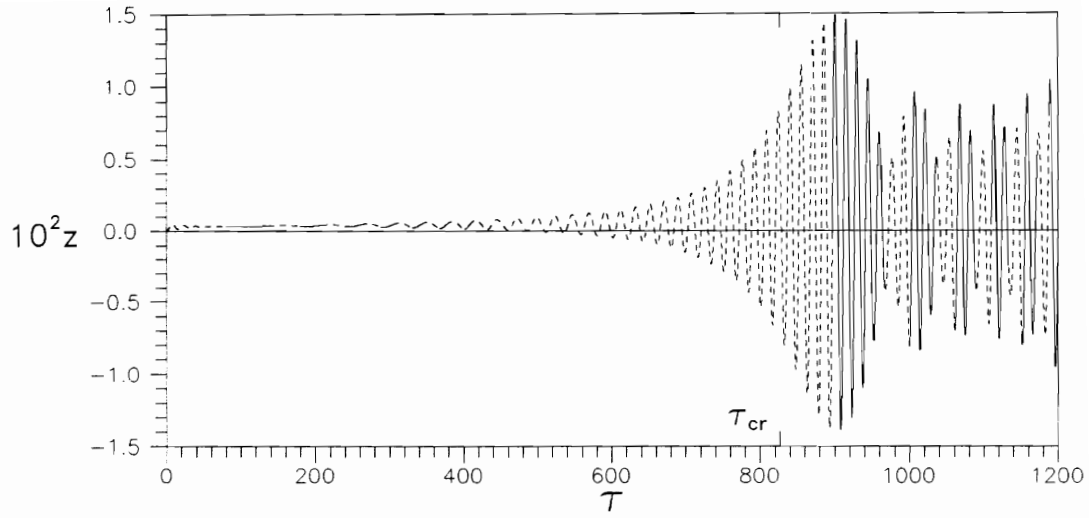

(a)

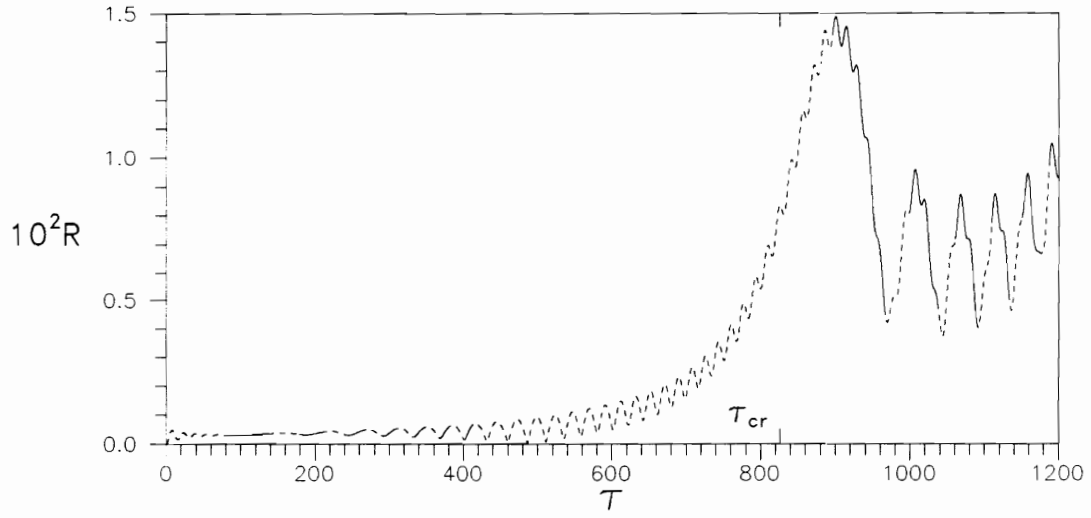

(b)

Fig. 2.31 Time Histories for d_e=0.1, d_i=0.40

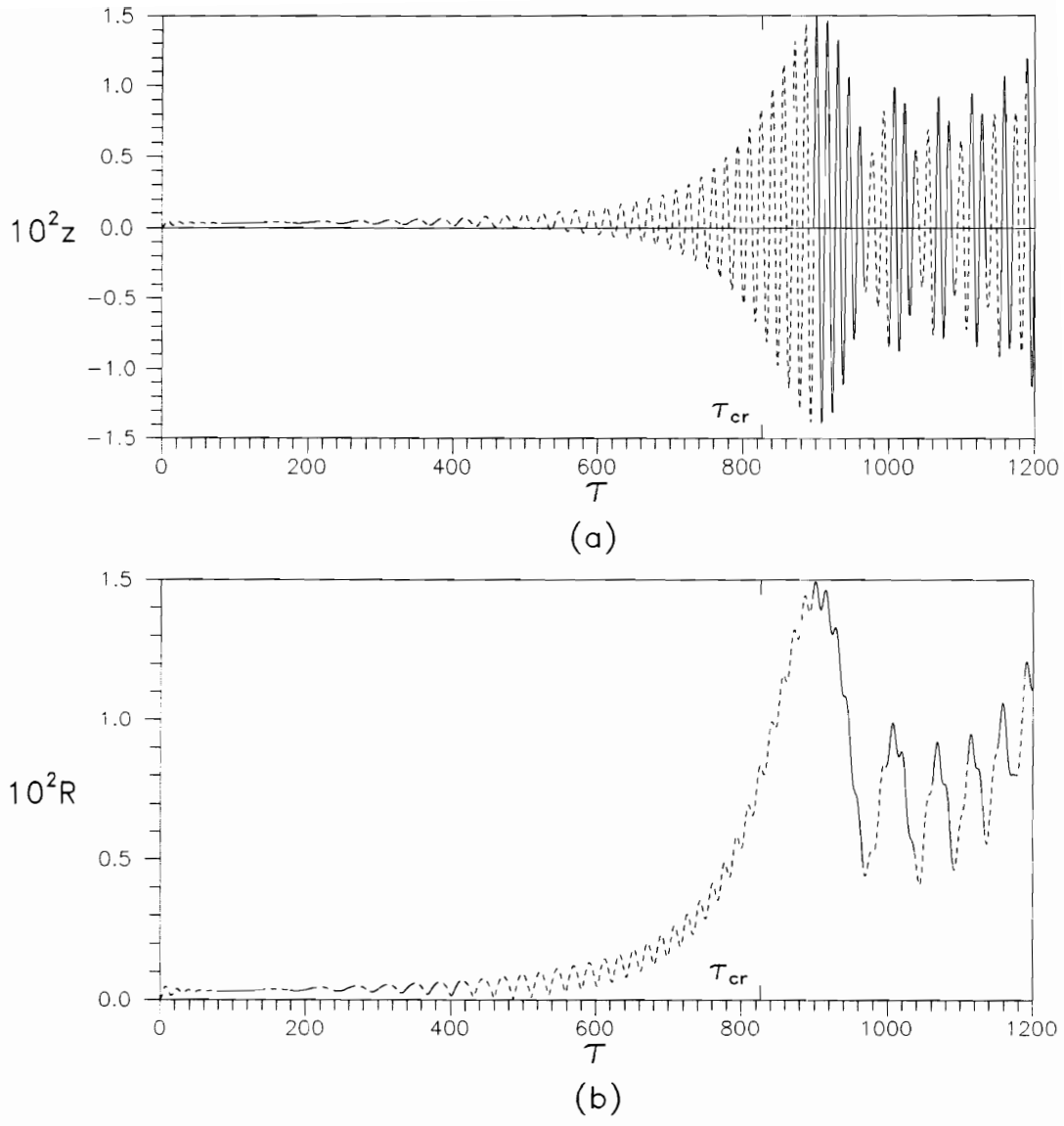

Fig. 2.32 Time Histories for d_e=0.1, d_i=0.425

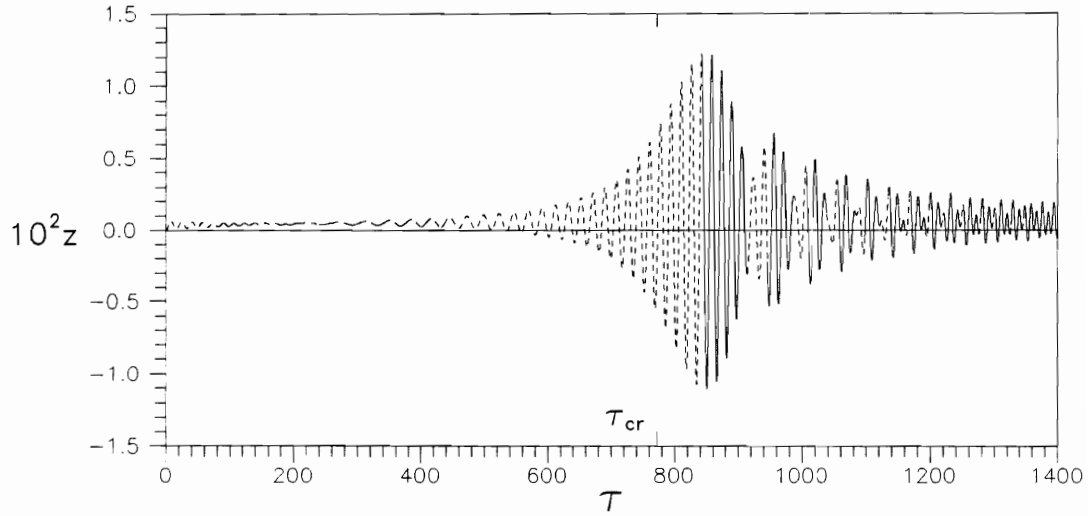

(a)

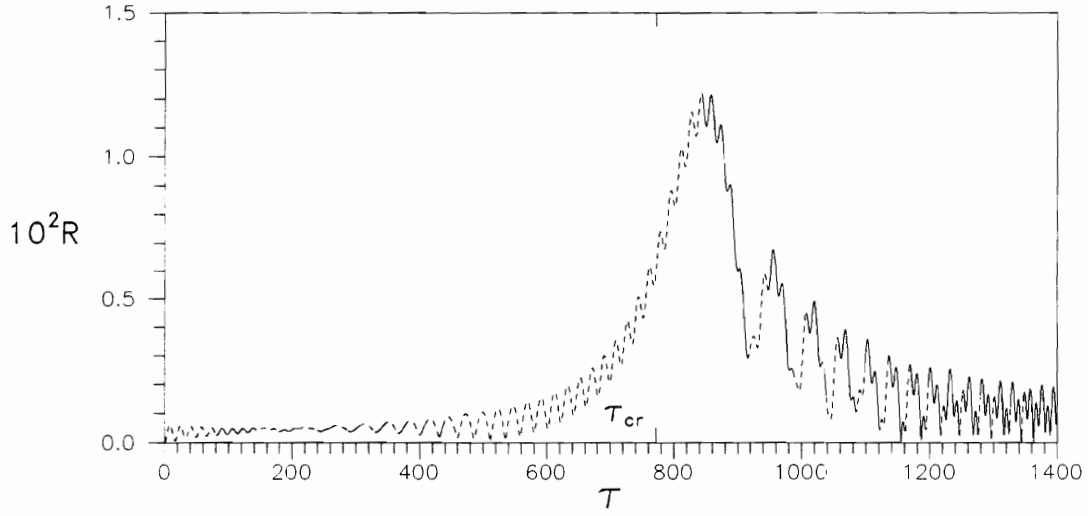

(b)

Fig. 2.33 Time Histories of Overhung Shaft with Acceleration Rate λ=0.0005

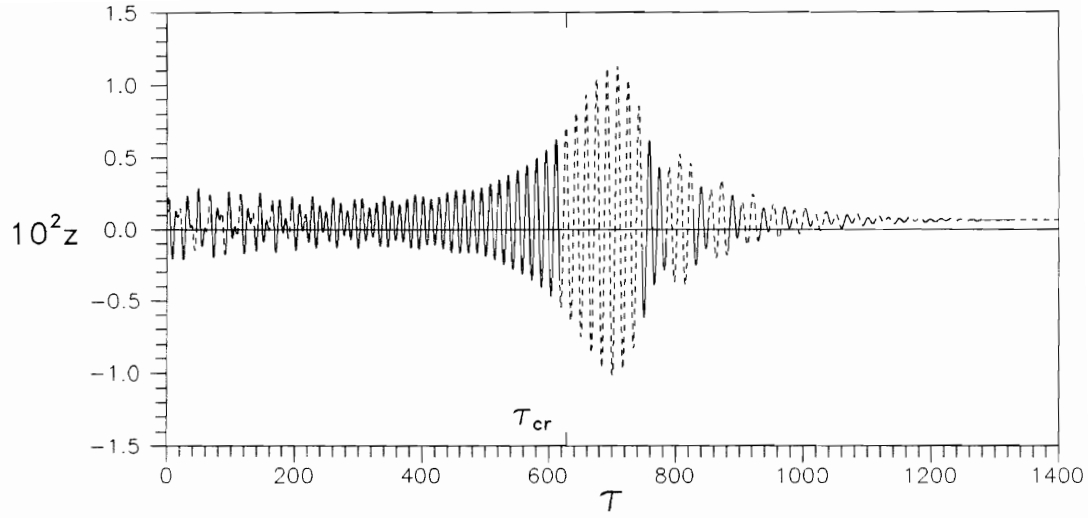

(a)

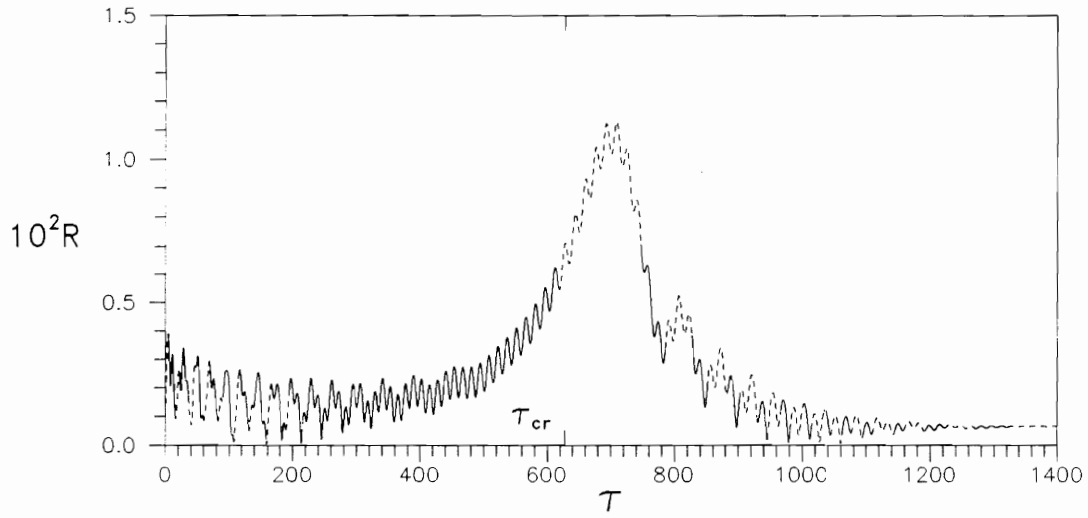

(b)

Fig. 2.34 Time Histories of Overhung Shaft with Deceleration Rate λ=0.0005

2.5.2. Influence of lengths of overhangs

The lengths of the overhangs influence the behavior of the cracked rotating shaft. Based on the standard parameters with a breathing crack, mass at one end, and $\lambda = 0.0005$ for the constant acceleration, various equal lengths of the overhangs are investigated. The time histories are similar to Fig. 2.7.

Figure 2.35 shows the relationship between the lengths of the overhangs $(l_1 = l_2)$ and the maximum z-displacement at the disk. An increase in the overhang length causes a decrease in the maximum z-displacement. When the length of each overhang is between 0 and 0.05, the maximum z-displacement is almost the same (constant). The difference between the largest z_{max} $(l_1 = l_2 = 0)$ and the smallest z_{max} $(l_1 = l_2 = 0.25)$ in Fig. 2.35 is about 15.7%.

2.5.3. Influence of mass of disk at the end of the overhang

In order to study the effect of the mass of the disk at the end of the overhang, the maximum z-displacement has been calculated for various values of disk mass under the constant acceleration $\lambda = 0.005$ with standard parameters and a breathing crack. Figure 2.36 plots the result between the mass of the overhung disk and the maximum value of z at the disk location $\tilde{c} = 0.5$. Similar to the effect of the length of the overhang, an increase in the mass of the overhung disk causes a decrease in the maximum z-displacement.

Figure 2.37 shows the vertical displacement at $\tau = 842.6$ over the whole length of the shaft with different values of the mass of the overhung disk. It is clear that with a heavier mass the vertical displacement becomes smaller.

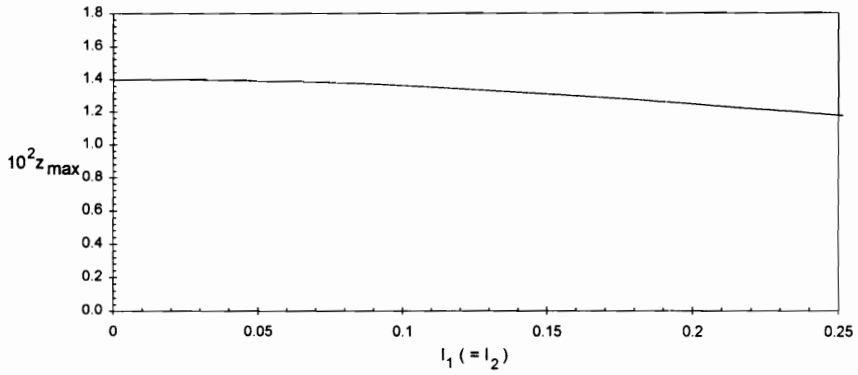

Fig. 2.35 Effect of Equal Overhang Lengths on z_{max}

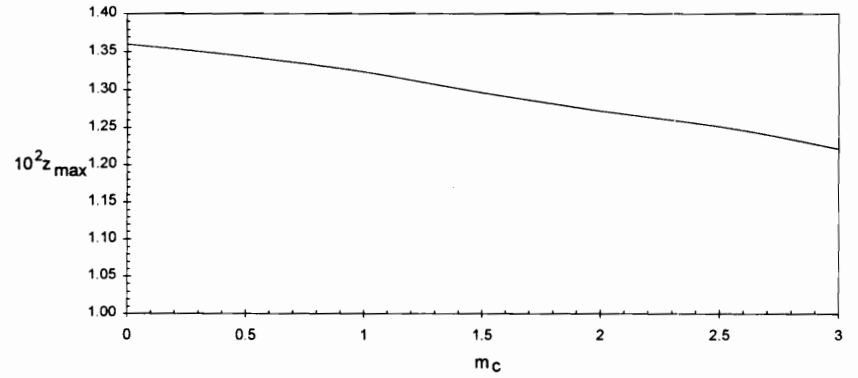

Fig. 2.36 Effect of Mass of Overhung Disk on z_{max}

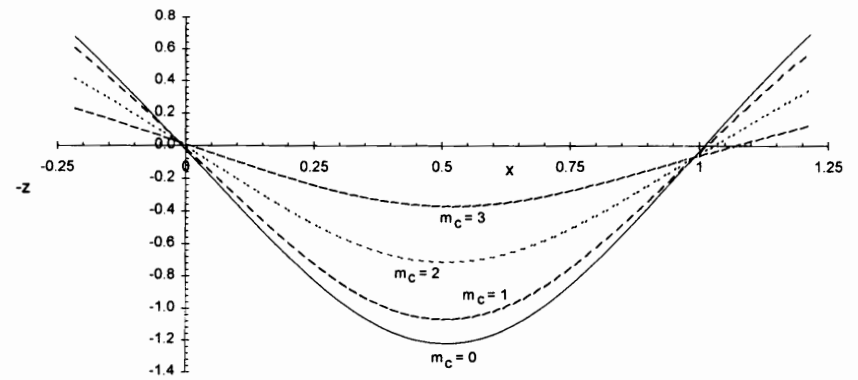

Fig. 2.37 Effect of Mass of Overhung Disk on z-displacement Along the Shaft

CHAPTER 3

GENERAL FORMULATION FOR NONIDEAL MOTOR

3.1. Introduction

In the analysis of vibration behavior, it is usually assumed that the motor (energy source) has unlimited power, and it is called an ideal motor or an ideal energy source. With this assumption, the coupling effect of the system and the motor is neglected.

If the power of the motor is limited, it is called a nonideal motor or a source with limited energy supply. In this case, the interaction between the motor and the rotating shaft must be included in the equations of motion to represent the behavior of the system. The torque depends on the operational frequency. In a resonance condition, the rate of increase of motor frequency decreases, because the motor has to supply a higher torque to maintain this condition (Rajac and Evan-Iwanowski 1976). The effect of a limited power supply, called the Sommerfeld effect, makes a nonideal motor in the resonance region slow down, followed by a rapid increase in the motor frequency which may cause a discontinuity (jump) in the motion (Evan-Iwanowski 1976).

The maximum amplitude of non-stationary vibration passing through a critical speed with a limited power supply (nonideal motor) may be greater than that of an ideal system (with constant acceleration) (Iwatsubo et al. 1972). The relation between the

natural frequencies of the shaft and the motor characteristic influences the amplitude of vibration during start-up (Iwatsubo et al. 1986). Peeken et al. (1980) considered a coupled electrical and mechanical system and used digital simulation. The torsional response in shaft systems was calculated with the help of a mathematical model of the machine. Iwatsubo et al. (1986) also mentioned that torsional vibration should be evaluated in relation to the dynamic behavior of the electrical system.

In this section, systems with a nonideal motor will be considered. The dynamic behavior of a cracked rotating shaft passing through a critical speed during run-up and coast-down will be investigated. The angular velocity will be a variable, because for a nonideal motor it is not specified.

The physical model is the same as in Chapter 2 (Figs. 2.1-2.3), but in this case $\dot{\theta}(t)$ is not specified. From the previous investigation, the gyroscopic effect does not have much influence on the dynamic behavior of the shaft. Therefore, in this study with a nonideal motor, the gyroscopic effect is neglected. The flexible, damped supports and the overhang with a mass at the end are still included. The shaft with a breathing crack is investigated, including the eccentricity of the disk, gravitational forces, and internal and external damping.

3.2. Analysis

In the system with the nonideal motor, there are three unknown variables, i.e., two transverse displacements v(x,t) and w(x,t), and the angular velocity $\dot{\theta}(t)$. The equations of motion and boundary conditions are derived by Hamilton's Principle. The v- and w-equations of motion are the same as eq. (2.14) without I_d and I_p terms. The additional $\dot{\theta}$ – equation of motion $\left(GE_\theta = 0\right)$ is as follows (see derivation in Appendix C):

"$\dot{\theta}$ – equation ":

$$
\begin{aligned}
GE_\theta \equiv \int_{-l_1}^{L+l_2} \Big\{ & \mu\left[v_{tt}w - vw_{tt} - 2\dot{\theta}\left(vv_t + ww_t\right) - \ddot{\theta}\left(w^2 + v^2\right)\right] \\
& + m\delta(x-c)\left[v_{tt}\left(w + e_d\sin\delta_d\right) - w_{tt}\left(v + e_d\cos\delta_d\right) - 2\dot{\theta}\,w_t\left(w + e_d\sin\delta_d\right)\right. \\
& \left. - 2\dot{\theta}\,v_t\left(v + e_d\cos\delta_d\right) - \ddot{\theta}\left(w + e_d\sin\delta_d\right)^2 - \ddot{\theta}\left(v + e_d\cos\delta_d\right)^2\right] \\
& - I_p\,\ddot{\theta}\delta(x-c) + \mu g\,v\cos\theta - \mu g\,w\sin\theta - d_e\,\mu\dot{\theta}\left(r_1^{\,2} + r_2^{\,2}\right) \\
& + m\delta(x-c)\left[g\cos\theta\left(v + e_d\cos\delta_d\right) - g\sin\theta\left(w + e_d\sin\delta_d\right)\right]\Big\}dx + \bar{\kappa} = 0 \quad (3.1)
\end{aligned}
$$

The additional boundary conditions are as follows (see derivation in Appendix C):

At $x = 0, L$:

$$
BC_1 \equiv m_b\left[wv_{tt} - vw_{tt} - 2\dot{\theta}\left(ww_t + vv_t\right) - \ddot{\theta}\left(w^2 + v^2\right)\right]
$$

$$- m_b\, g\left(v\cos\theta - w\sin\theta\right) = 0 \tag{3.2.a}$$

At $x = L + l_2$:

$$BC_2 \equiv m_c\left[wv_{tt} - vw_{tt} - 2\dot{\theta}\left(ww_t + vv_t\right) - \ddot{\theta}\left(w^2 + v^2\right)\right]$$

$$- I_{pc}\,\ddot{\theta} - m_c\, g\left(v\cos\theta - w\sin\theta\right) = 0 \tag{3.2.b}$$

Here $\bar{\kappa}$ is the torque of the motor and is a function of the angular velocity. It is always positive and is assumed to be a linearly decreasing function, i.e.,

$$\bar{\kappa} = \bar{\upsilon}_0 - \bar{\upsilon}_1\dot{\theta} \tag{3.3}$$

where:

$\bar{\upsilon}_0$ is the initial motor torque

$\bar{\upsilon}_1$ is the gradient motor torque

Between eqs. (3.1) and (2.14), there are two common terms, i.e., $\left[\mu + m\delta\left(x - c\right)\right]v_{tt}$ and $\left[\mu + m\delta\left(x - c\right)\right]w_{tt}$. By substituting these common terms from eq. (2.14) into eq. (3.1), eq. (3.1) is simplified as follows:

$$GE_\theta \equiv \int_{-l_1}^{L+l_2}\Big\{ EI\left(v\,w_{xxxx} - w\,v_{xxxx} + d_i v\,w_{txxxx} - d_i w\,v_{txxxxx}\right)$$

$$+ d_e\,\mu\left[v\,w_t - w\,v_t + \dot{\theta}\,v^2 + \dot{\theta}\,w^2 - \dot{\theta}\left(r_1{}^2 + r_2{}^2\right)\right]$$

$$-\Lambda\left[\delta'\left(x - b_+\right) - \delta'\left(x - b_-\right)\right]\frac{(EI)^2}{\varepsilon}\,c_{44}\left(wv_{xx} + d_i wv_{txx}\right)\Big|_{x=b}$$

$$-\Lambda\left[\delta'(x-b_+)-\delta'(x-b_-)\right]\frac{(EI)^2}{\varepsilon}c_{55}\left(vw_{xx}+d_i vw_{txx}\right)\Big|_{x=b}$$

$$+me_d\,\delta(x-c)\Big[\sin\delta_d\left(-\ddot{\theta}w-\dot{\theta}^2v-2\dot{\theta}w_t+v_{tt}\right)-e_d\ddot{\theta}+g\cos(\theta+\delta_d)$$

$$+\cos\delta_d\left(-\ddot{\theta}v+\dot{\theta}^2w-2\dot{\theta}v_t-w_{tt}\right)\Big]-I_p\,\ddot{\theta}\,\delta(x-c)\Big\}dx+\bar{\kappa}=0 \quad (3.4)$$

By linearizing eq. (3.4), the $\dot{\theta}$ – equation of motion becomes

$$GE_\theta \equiv \int_{-l_1}^{L+l_2}-\left(I_p+me_d^{\,2}\right)\delta(x-c)\ddot{\theta}-d_e\,\mu\,\dot{\theta}\left(r_1^{\,2}+r_2^{\,2}\right)$$

$$+me_d\,\delta(x-c)\Big[\sin\delta_d\left(v_{tt}-2\dot{\theta}w_t-\dot{\theta}^2v-\ddot{\theta}w\right)+g\cos(\theta+\delta_d)$$

$$-\cos\delta_d\left(w_{tt}+2\dot{\theta}v_t-\dot{\theta}^2w+\ddot{\theta}v\right)\Big]\Big\}dx+\bar{\kappa}=0 \quad (3.5)$$

With the simplified $\dot{\theta}$ – equation of motion (eq. 3.5) and linearized boundary conditions (eq. 3.2), the following equation is obtained:

$$\int_{-l_1}^{L+l_2}\Big\{-\left(I_p+me_d^{\,2}\right)\delta(x-c)\ddot{\theta}-d_e\,\mu\,\dot{\theta}\left(r_1^{\,2}+r_2^{\,2}\right)$$

$$+me_d\,\delta(x-c)\Big[\sin\delta_d\left(v_{tt}-2\dot{\theta}w_t-\dot{\theta}^2v-\ddot{\theta}w\right)+g\cos(\theta+\delta_d)$$

$$-\cos\delta_d\left(w_{tt}+2\dot{\theta}v_t-\dot{\theta}^2w+\ddot{\theta}v\right)\Big]\Big\}dx$$

$$-m_b\, g\left(v\cos\theta - w\sin\theta\right)\Big|_{x=0} - m_b\, g\left(v\cos\theta - w\sin\theta\right)\Big|_{x=L}$$

$$-\left[I_{pc}\,\ddot{\theta} + m_c\, g\left(v\cos\theta - w\sin\theta\right)\right]\Big|_{x=L+l_2} + \bar{\kappa} = 0 \tag{3.6}$$

Then, by applying the approximate displacement functions from eqs. (2.16), eq. (3.6) becomes

$$-\left(I_p + m e_d^{\,2}\right)\ddot{\theta} - d_e\,\mu\dot{\theta}\left(r_1^{\,2} + r_2^{\,2}\right)\left(L + l_1 + l_2\right)$$

$$+ m e_d \sin\delta_d \left[\sum_{k=1}^{N} \ddot{v}_k \sin\frac{k\pi c}{L} + \ddot{a}_1 c + \ddot{a}_2 - 2\dot{\theta}\left(\sum_{k=1}^{N} \dot{w}_k \sin\sin\frac{k\pi c}{L} + \dot{a}_3 c + \dot{a}_4\right)\right.$$

$$\left. - \dot{\theta}^2\left(\sum_{k=1}^{N} v_k \sin\frac{k\pi c}{L} + a_1 c + a_2\right) - \ddot{\theta}\left(\sum_{k=1}^{N} w_k \sin\frac{k\pi c}{L} + a_3 c + a_4\right)\right]$$

$$- m e_d \cos\delta_d \left[\sum_{k=1}^{N} \ddot{w}_k \sin\frac{k\pi c}{L} + \ddot{a}_3 c + \ddot{a}_4 + 2\dot{\theta}\left(\sum_{k=1}^{N} \dot{v}_k \sin\sin\frac{k\pi c}{L} + \dot{a}_1 c + \dot{a}_2\right)\right.$$

$$\left. - \dot{\theta}^2\left(\sum_{k=1}^{N} w_k \sin\frac{k\pi c}{L} + a_3 c + a_4\right) + \ddot{\theta}\left(\sum_{k=1}^{N} v_k \sin\frac{k\pi c}{L} + a_1 c + a_2\right)\right]$$

$$- m_b\, g\left[\cos\theta\left(2a_2 + a_1 L\right) - \sin\theta\left(2a_4 + a_3 L\right)\right]$$

$$- m_c\, g\cos\theta\left(\sum_{k=1}^{N} v_k \sin\frac{k\pi\left(L + l_2\right)}{L} + a_1\left(L + l_2\right) + a_2\right)$$

$$+ m_c\, g\sin\theta\left(\sum_{k=1}^{N} w_k \sin\frac{k\pi\left(L + l_2\right)}{L} + a_3\left(L + l_2\right) + a_4\right)$$

$$+ m e_d\, g\cos\left(\theta + \delta_d\right) - I_{pc}\,\ddot{\theta} + \bar{\upsilon}_0 - \bar{\upsilon}_1\dot{\theta} = 0 \tag{3.7}$$

Using eq. (2.21) and additional nondimensionalized quantities, i.e., $\upsilon_0 = \frac{2L}{\pi^4 EI}\bar{\upsilon}_0$ and $\upsilon_1 = \frac{2}{\pi^2 L}\sqrt{\frac{1}{EI\mu}}\bar{\upsilon}_1$, eq. (3.7) becomes a non-dimensionalized equation as follows:

$$\left(0.5\,\tilde{m}\tilde{r}_d^{\,2} + 0.5\,\tilde{m}_c\tilde{r}_c^{\,2} + \tilde{m}\tilde{e}_d^{\,2}\right)\ddot{\theta}$$

$$-\tilde{m}\tilde{e}_d \sin\delta_d\left[\sum_{k=1}^{N}\ddot{\tilde{v}}_k \sin k\pi\tilde{c} + \ddot{\tilde{a}}_1 c + \ddot{\tilde{a}}_2 - \ddot{\theta}\left(\sum_{k=1}^{N}\tilde{w}_k \sin k\pi\tilde{c} + \tilde{a}_3 c + \tilde{a}_4\right)\right]$$

$$+\tilde{m}\tilde{e}_d \cos\delta_d\left[\sum_{k=1}^{N}\ddot{\tilde{w}}_k \sin k\pi\tilde{c} + \ddot{\tilde{a}}_3 c + \ddot{\tilde{a}}_4 - \ddot{\theta}\left(\sum_{k=1}^{N}\tilde{v}_k \sin k\pi\tilde{c} + \tilde{a}_1 c + \tilde{a}_2\right)\right]$$

$$=-\tilde{m}\tilde{e}_d \sin\delta_d\left[2\dot{\theta}\left(\sum_{k=1}^{N}\dot{\tilde{w}}_k \sin k\pi c + \dot{\tilde{a}}_3\tilde{c} + \dot{\tilde{a}}_4\right) + \dot{\theta}^2\left(\sum_{k=1}^{N}\tilde{v}_k \sin k\pi c + \tilde{a}_1\tilde{c} + \tilde{a}_2\right)\right]$$

$$-\tilde{m}\tilde{e}_d \cos\delta_d\left[2\dot{\theta}\left(\sum_{k=1}^{N}\dot{\tilde{v}}_k \sin k\pi c + \dot{\tilde{a}}_1\tilde{c} + \dot{\tilde{a}}_2\right) - \dot{\theta}^2\left(\sum_{k=1}^{N}\tilde{w}_k \sin k\pi c + \tilde{a}_3\tilde{c} + \tilde{a}_4\right)\right]$$

$$-\frac{\pi}{2}\tilde{m}_b\tilde{\mu}\left[\cos\theta\left(\tilde{a}_1 + 2\tilde{a}_2\right) - \sin\theta\left(\tilde{a}_3 + 2\tilde{a}_4\right)\right]$$

$$-\frac{\pi}{2}\tilde{m}_c\tilde{\mu}\cos\theta\left(\sum_{k=1}^{N}\tilde{v}_k \sin k\pi\tilde{l}_{12} + \tilde{a}_1\tilde{l}_{12} + \tilde{a}_2\right)$$

$$+\frac{\pi}{2}\tilde{m}_c\tilde{\mu}\sin\theta\left(\sum_{k=1}^{N}\tilde{w}_k \sin k\pi\tilde{l}_{12} + \tilde{a}_3\tilde{l}_{12} + \tilde{a}_4\right)$$

$$+\frac{\pi}{2}\tilde{m}\tilde{e}_d\tilde{\mu}\cos\left(\theta+\delta_d\right) - \tilde{d}_e\tilde{r}_s^{\,2}\dot{\theta}\left(\tilde{l}_1^{\,2} + \tilde{l}_{12}^{\,2}\right) + \upsilon_0 - \upsilon_1\dot{\theta} \qquad (3.8)$$

Therefore, the system has 2N+5 second order ordinary differential equations, eqs. (3.8), (2.23), and (2.24). Overdots denote differentiation with respect to τ. These second order ODE's will be solved by numerical integration, similar to the ones in Chapter 2 and transformed to first-order ODE's with M now equal to 2N+5 (see eqs. (2.25) - (2.30)).

3.3. Stationary Case

In order to understand the relationship between the motor characteristic and the displacement of the rotating shaft, the stationary case is analyzed now. In this section, the angular velocity $\dot{\theta}$ and the displacements $\tilde{v}$, $\tilde{w}$ are assumed to be constant as follows:

$$\dot{\theta} = \Omega; \quad \tilde{v} = v_0; \quad \tilde{w} = w_0 \tag{3.9}$$

Therefore the derivatives of $\tilde{v}$, $\tilde{w}$, and $\dot{\theta}$ with respect to τ are zero. Also, the resulting stationary radial amplitude is given by

$$R_0 = \sqrt{v_0^2 + w_0^2} \tag{3.10}$$

Then eqs. (2.23)-(2.24) with the assumption of constant $\tilde{v}_k$, $\tilde{w}_k$, $\tilde{a}_1$, $\tilde{a}_2$, $\tilde{a}_3$, $\tilde{a}_4$, and $\dot{\theta}$ are solved, based on the standard case. The eccentricity of the disk, internal and external damping, flexible and damped supports, overhung shaft, and mass at the end of the overhang are included. However, the crack and the gravitational forces are neglected. From the solutions, the motor characteristic $\kappa(\dot{\theta})$ is calculated by equation

(3.8). The peaks of the stationary radial amplitude R_0 (when plotted versus Ω) are related to the first critical speeds.

Figure 3.1.a shows the relation between the angular velocity Ω and the stationary radial amplitude R_0, and Fig. 3.1.b shows the relation between the angular velocity Ω and the motor characteristic $\kappa(\dot{\theta})$ at the disk location $\tilde{c} = 0.5$ for the standard case. The "first critical speed" occurs at $\Omega_{cr} = 0.39$. Other cases with different stiffnesses at the supports give similar results, with relatively small differences.

The influence of support damping on the stationary case is shown in Fig. 3.2, based on the standard data and the disk location $\tilde{c} = 0.5$. In this figure, the result of the standard case with support damping $\tilde{p} = 300$ is compared with other support dampings. From this figure, an increase in the support damping causes an increase in the stationary radial amplitude and the motor characteristic. This is due to the fact that the motion tends to involve more flexure and less rigid body translation. After reaching higher support dampings, the values of the stationary radial amplitude and the motor characteristic are similar. The first critical speed for all cases with different support dampings is the same: $\Omega_{cr} = 0.39$.

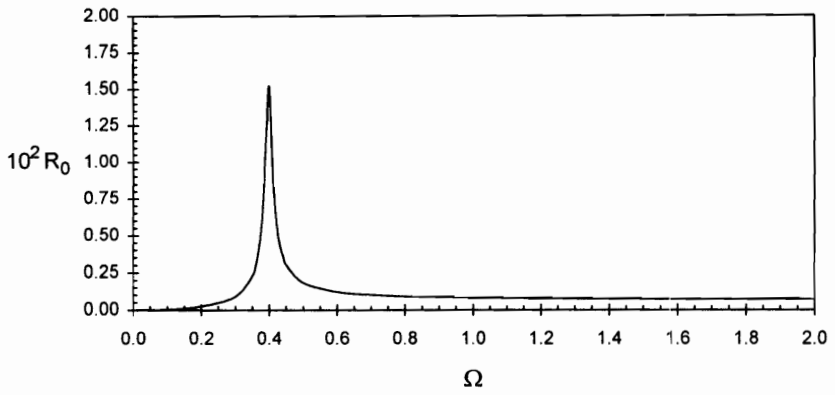

(a)

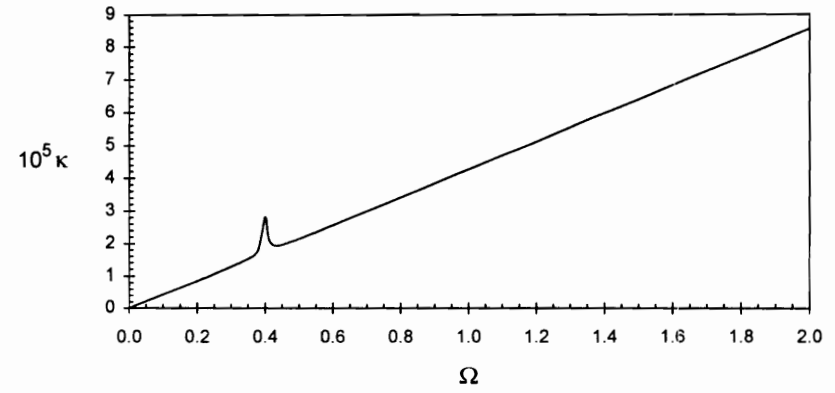

(b)

Fig. 3.1 Stationary Conditions for Standard Case

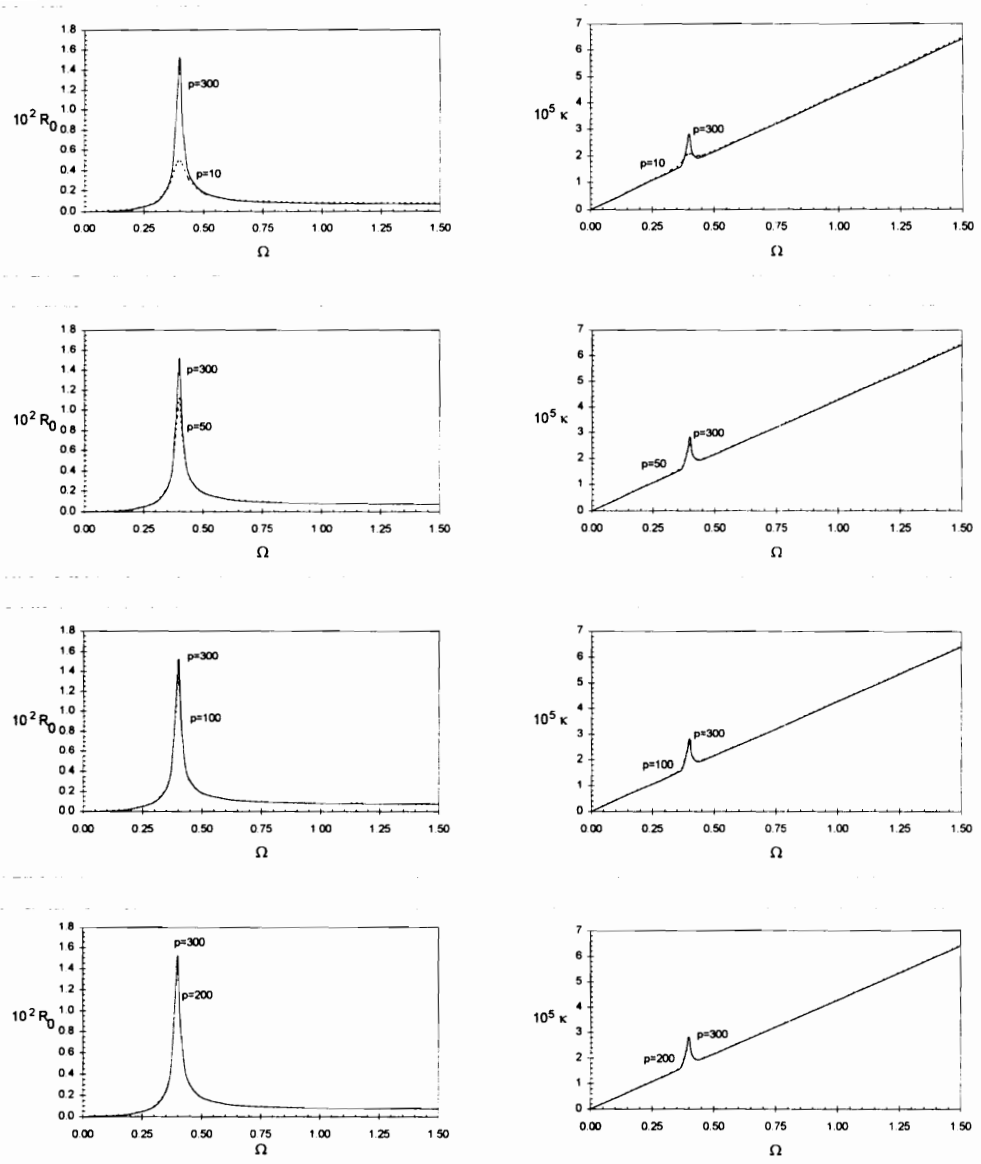

Fig. 3.2 Effect of Support Damping under Stationary Conditions

3.4. Nonstationary Case

3.4.1. Introduction

The dynamic behavior of the cracked rotating shaft is analyzed during run-up and coast-down passing through the critical speed. For the run-up case, the choice of the motor characteristic $\left(\kappa(\dot{\theta}) = \upsilon_0 - \upsilon_1\dot{\theta}\right)$ is based on the results from the stationary case. The linear motor characteristic will meet the shaft characteristic at a certain angular velocity, called the stationary angular velocity Ω_{st}. By choosing this angular velocity Ω_{st} from the stationary case, the corresponding motor characteristic $\kappa(\Omega_{st})$ is known; then, with that value and a specified initial motor torque υ_0, the gradient motor torque υ_1 is determined by eq. (3.6). These values of υ_0 and υ_1 will be the inputs for the nonstationary case. In the nonstationary case during run-up, the angular velocity of the shaft will increase and approach the stationary angular velocity.

During coast-down, the motor torque is assumed to be zero $\left(\kappa(\dot{\theta}) = 0\right)$. Therefore, following some initial conditions, the shaft will rotate freely with decreasing angular velocity that will approach zero.

3.4.2. Influence of motor characteristic

The motor characteristic influences the nonstationary behavior of the rotating shaft. Figure 3.3 shows different linear motor characteristics for the nonstationary case with the standard case. All motor characteristics are decreasing linearly until reaching the

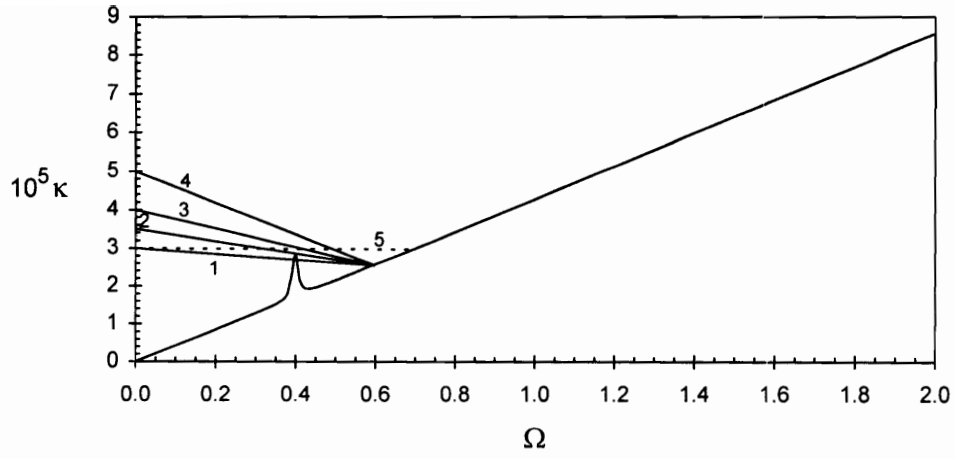

Fig. 3.3 Motor Characteristics

stationary angular velocity Ω_{st}; the differences are in the initial torque υ_0 and the gradient torque υ_1 (Table 3.1).

Table 3.1 Motor characteristic

Case no.	$\kappa(\Omega_{st})$	ν_0	ν_1	Ω_{st}
1	2.54E-5	0.00003	7.68E-6	0.6
2	2.54E-5	0.000035	1.6E-5	0.6
3	2.54E-5	0.00004	2.43E-5	0.6
4	2.54E-5	0.00005	4.10E-5	0.6
5	2.97E-5	0.00003	4E-7	0.7

In Figure 3.4, for case no. 1 (Table 3.1) during run-up, with the initial motor characteristic $\upsilon_0 = 0.00003$ and the stationary angular velocity $\Omega_{st} = 0.6$, the shaft speed comes close to, but does not pass, the critical speed $\Omega_{cr} = 0.39$. As depicted in Fig. 3.4.b, the angular acceleration of the shaft slows down when the speed is near the critical speed, and the speed becomes almost constant. This is called the Sommerfeld effect. Due to this effect, the shaft has an almost constant large displacement. In this case, the crack is open most of the time.

Figure 3.5, with initial motor characteristic $\upsilon_0 = 0.000035$ and the stationary angular velocity $\Omega_{st} = 0.6$ (case no. 2), shows that the shaft passes the critical speed during run-up. When the shaft reaches the critical speed, the angular acceleration slows down for a certain time (with the angular velocity almost constant) and then increases. At the same time, the displacement becomes large and reaches its maximum. While the angular velocity increases after slowing down, the displacement decreases very fast and

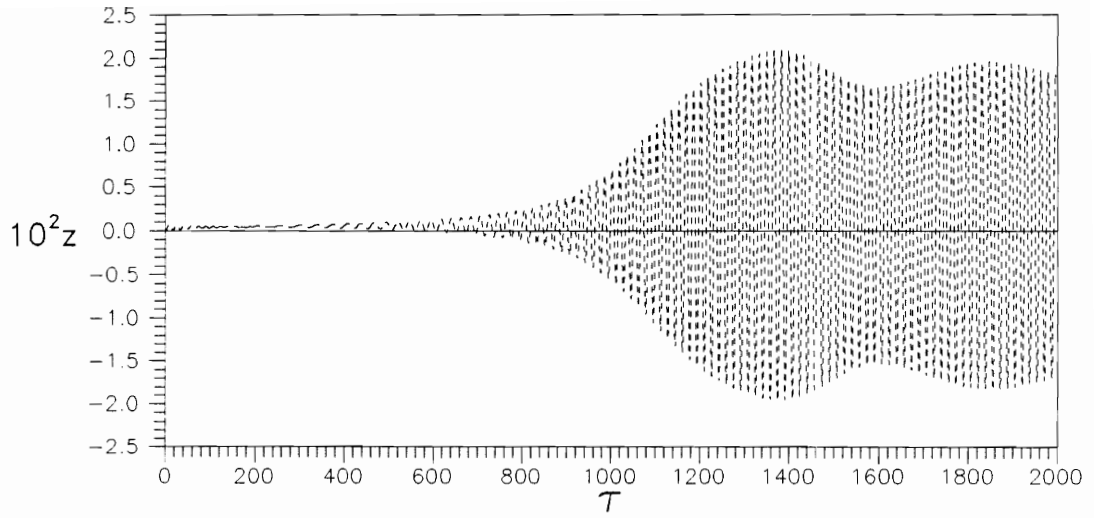

(a)

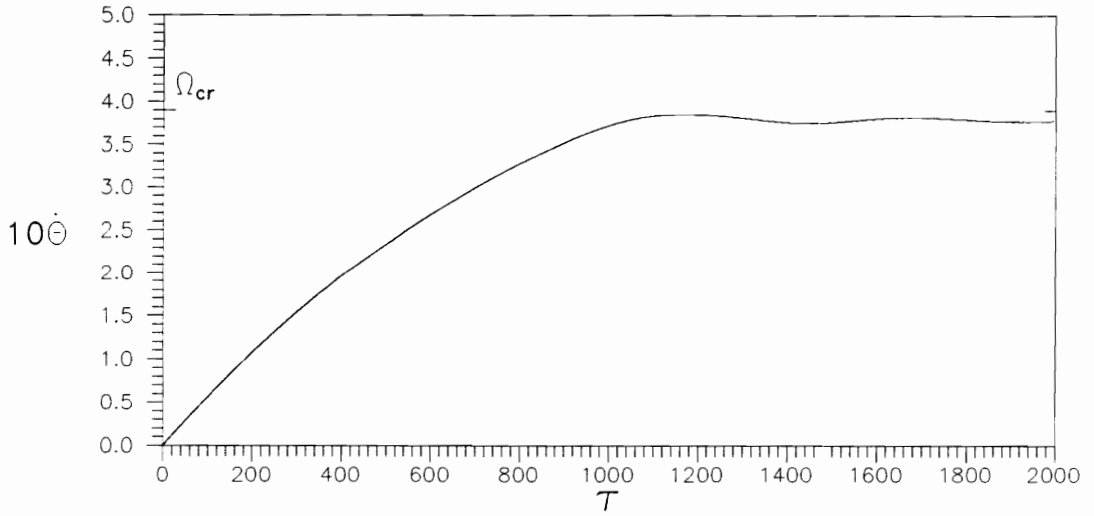

(b)

Fig. 3.4 Run-up Time Histories with υ_0=0.00003, υ_1=7.7x10^{-6}

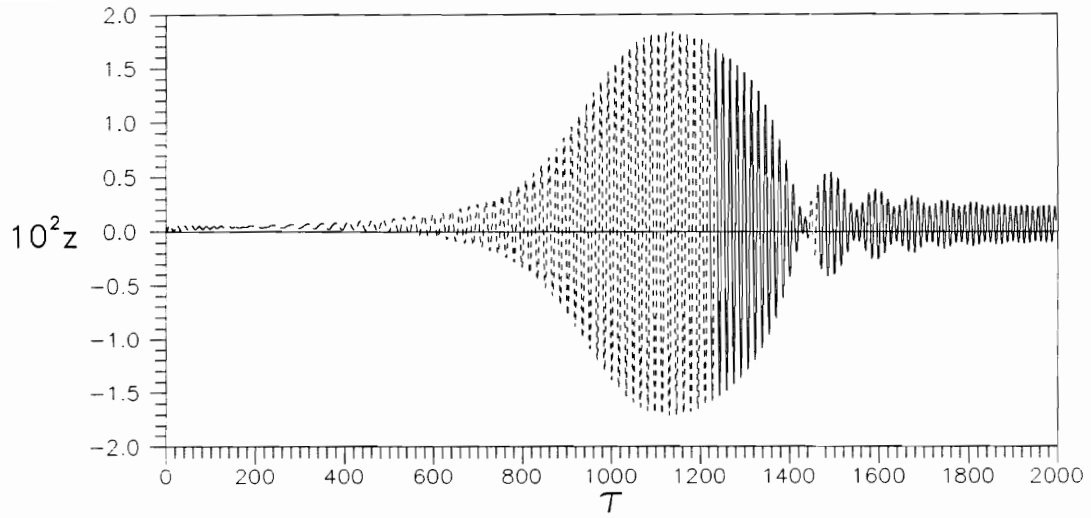

(a)

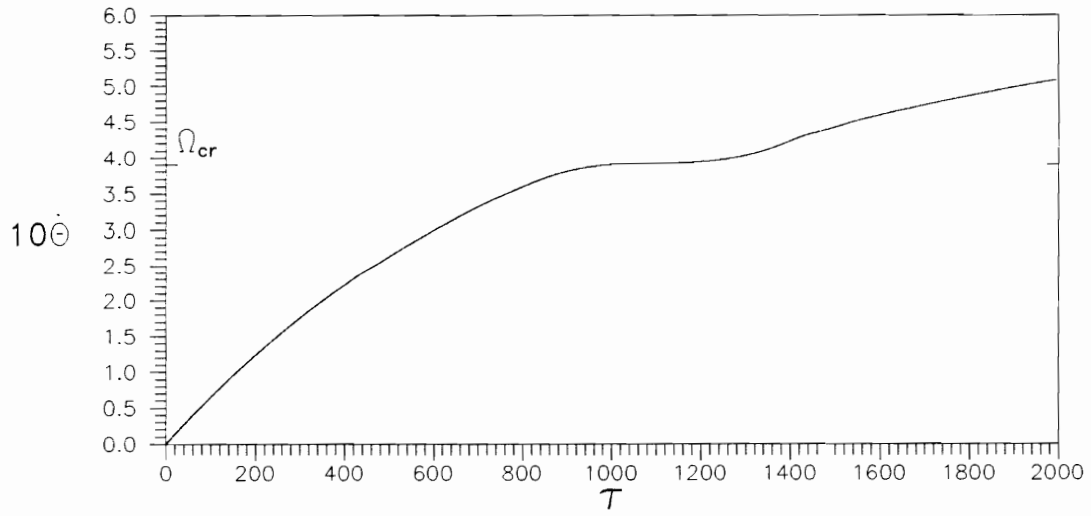

(b)

Fig. 3.5 Run−up Time Histories with υ_0=0.000035, υ_1=1.6x10^{-5}

approaches a stationary condition. Similar to the system with an ideal motor for the acceleration, the crack is open most of the time until reaching the maximum and then is closed for a while. After that, there is a breathing condition and when the stationary condition is approached the crack is closed most of the time.

With initial motor characteristic $\upsilon_0 = 0.00004$ and the stationary angular velocity $\Omega_{st} = 0.6$ (case no. 3), Fig. 3.6 shows the time histories of the z-displacement and the angular velocity of the shaft during run-up. In this case, the critical speed is passed faster than in the previous one; therefore the maximum z-displacement is reached sooner and is smaller. The Sommerfeld effect lasts for less time compared to Figs. 3.4 and 3.5.

In Fig. 3.7, case no. 4, the initial motor characteristic is larger than the one in Fig. 3.6 with the same stationary angular velocity. This gives much less time to pass the critical speed, and a smaller Sommerfeld effect. The maximum displacement occurs after the shaft passes the critical speed. Because the time to reach the maximum is smaller, the maximum z-displacement becomes smaller. This phenomenon is similar to that for the case with an ideal motor as depicted in Fig. 2.14 during constant acceleration.

Figure 3.8 has a different stationary angular velocity, i.e., $\Omega_{st} = 0.7$, and the same initial motor characteristic as in case no. 1 (Fig. 3.4) with $\upsilon_0 = 0.00003$. In this case the motor characteristic near the peak in Fig. 3.3 is larger than the one for case no.1, and this allows the shaft to pass the critical speed. The Sommerfeld effect occurs for a while, and the displacement reaches its maximum. After that, different from Fig. 3.4, the angular velocity increases and the displacement decreases.

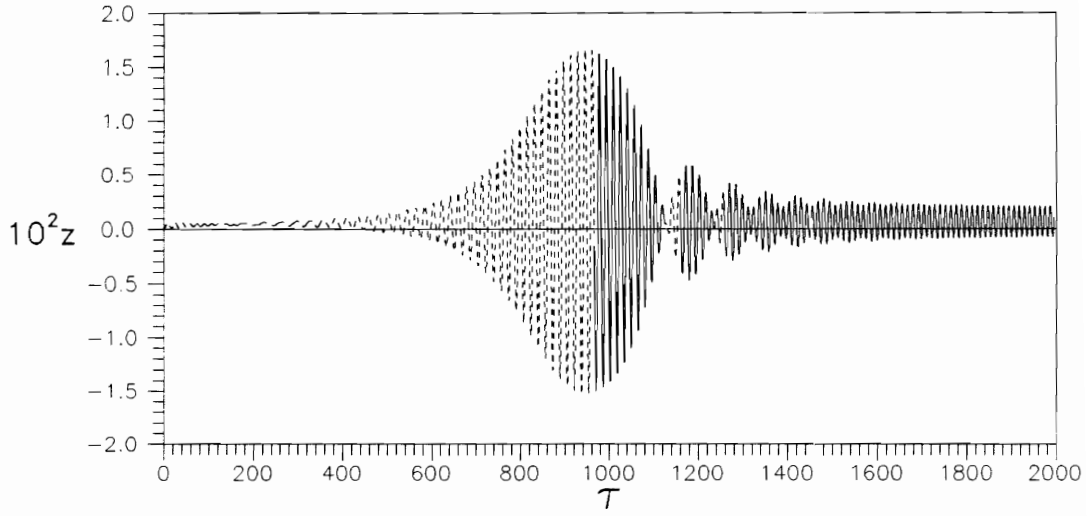

(a)

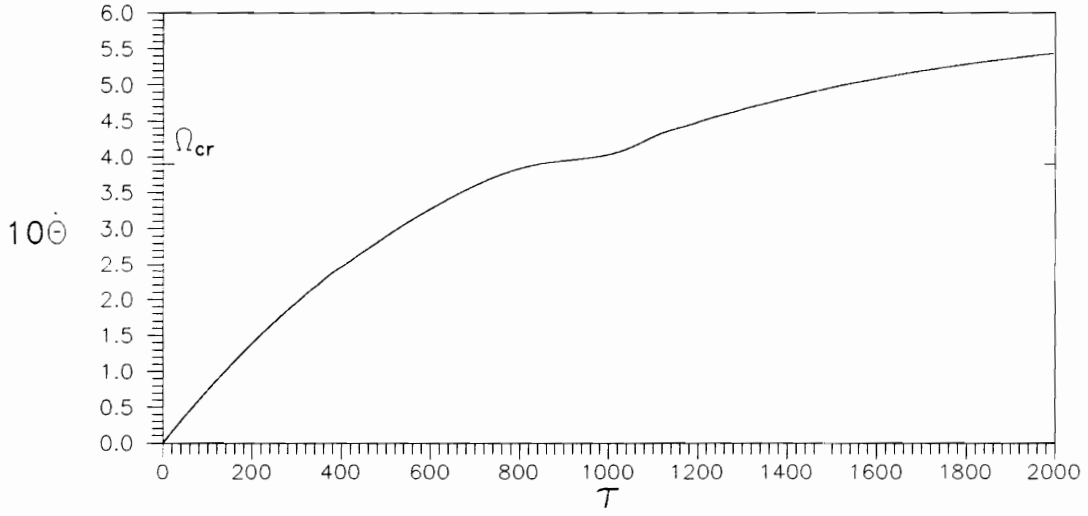

(b)

Fig. 3.6 Run−up Time Histories with υ_0=0.00004, υ_1=2.4x10^{-5}

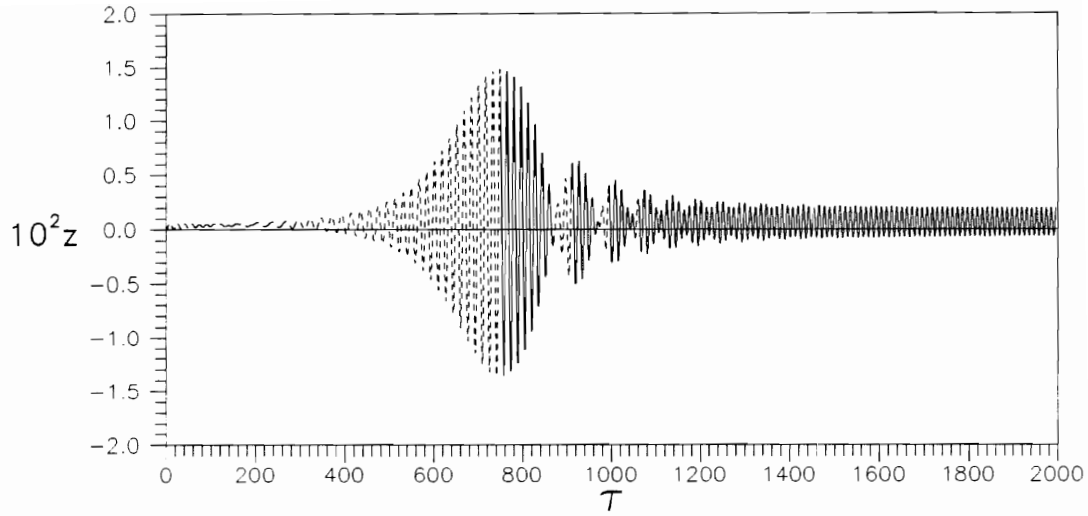

(a)

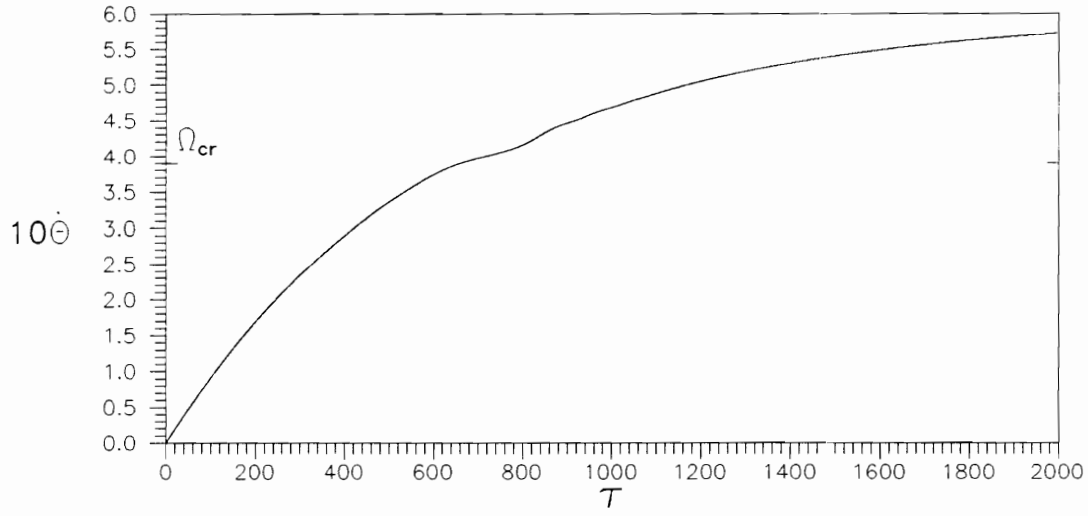

(b)

Fig. 3.7 Run-up Time Histories with υ_0=0.00005, υ_1=4.1x10^{-5}

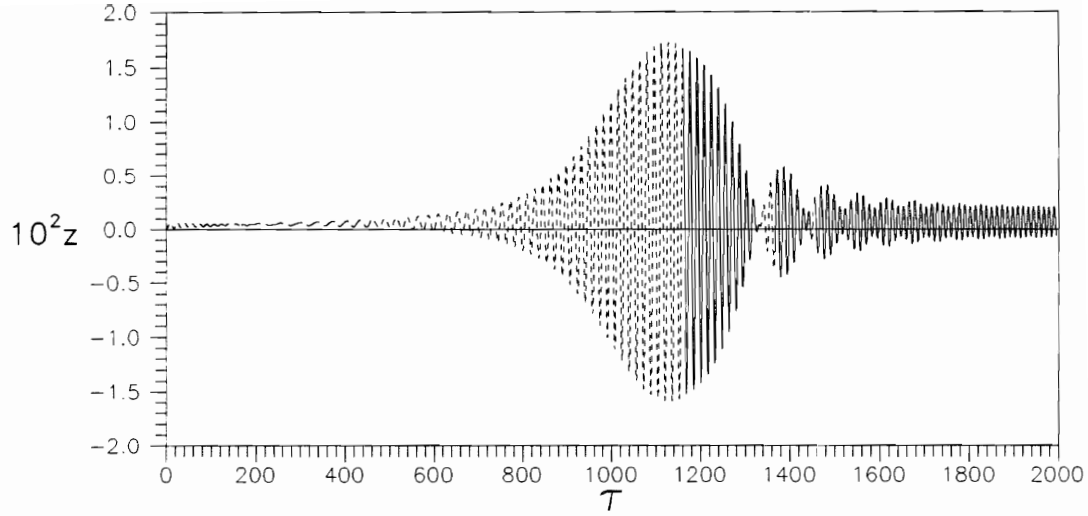

(a)

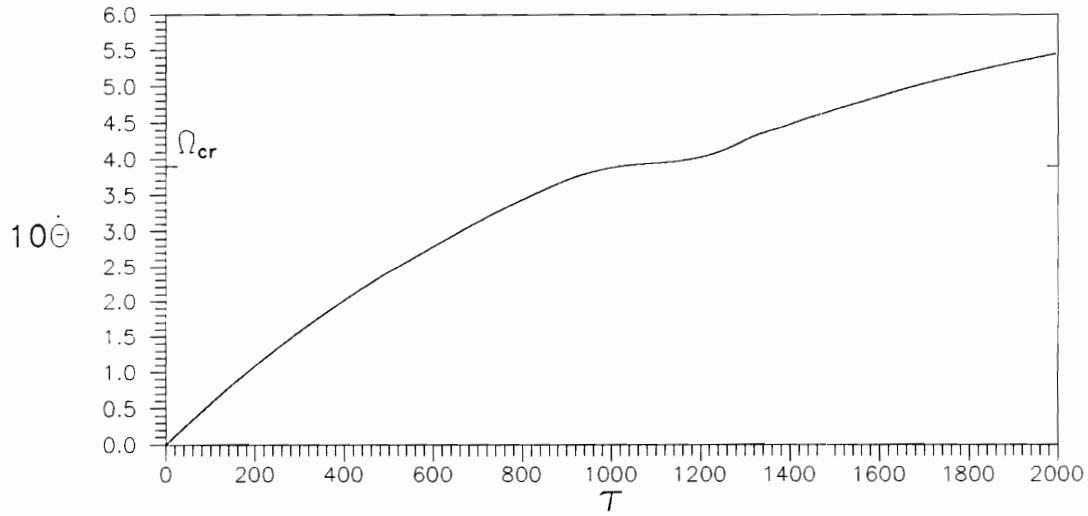

(b)

Fig. 3.8 Run−up Time Histories with υ_0=0.00003, υ_1=4x10^{-7}

In conclusion, if the motor characteristic is closer to the peak (Fig. 3.3), the Sommerfeld effect acts for a longer time. On the opposite side, when the motor characteristic is larger when passing the peak, the critical time is passed faster, the maximum z-displacement becomes smaller, and the Sommerfeld effect lasts for less time. The crack condition during run-up passing the critical speed has the same behavior as for the case of constant acceleration with an ideal motor.

The nonstationary behavior of the cracked rotating shaft during coast-down with different initial conditions is shown in Figs. 3.9 - 3.12 based on the standard data with a breathing crack and zero motor torque. The initial conditions for Figs. 3.9 and 3.10 are taken from the stationary condition of the shaft during run-up (Figs. 3.6 and 3.7). The initial conditions for Fig. 3.11 and 3.12 have the same initial displacements as for Fig. 3.9 but different initial angular velocities: $\dot{\theta}_{\text{initial}} = 0.7$ and 0.8, respectively.

From Figs. 3.9-3.12, the time histories of the z-displacement and the angular velocity have similar behavior but with different initial conditions and times to reach the critical speed. For Figs. 3.9 and 3.10 the displacement starts from a stationary condition because the initial conditions are taken from the stationary values of the run-up case (Figs. 3.6 and 3.7, respectively). On the other hand, the displacement for Figs. 3.11 and 3.12 has some transient behavior initially, because the initial conditions are modified from the stationary conditions of the run-up case (Fig. 3.6) by changing the initial angular velocity with 0.7 and 0.8 to make the resonance conditions at a later time. It is clear from

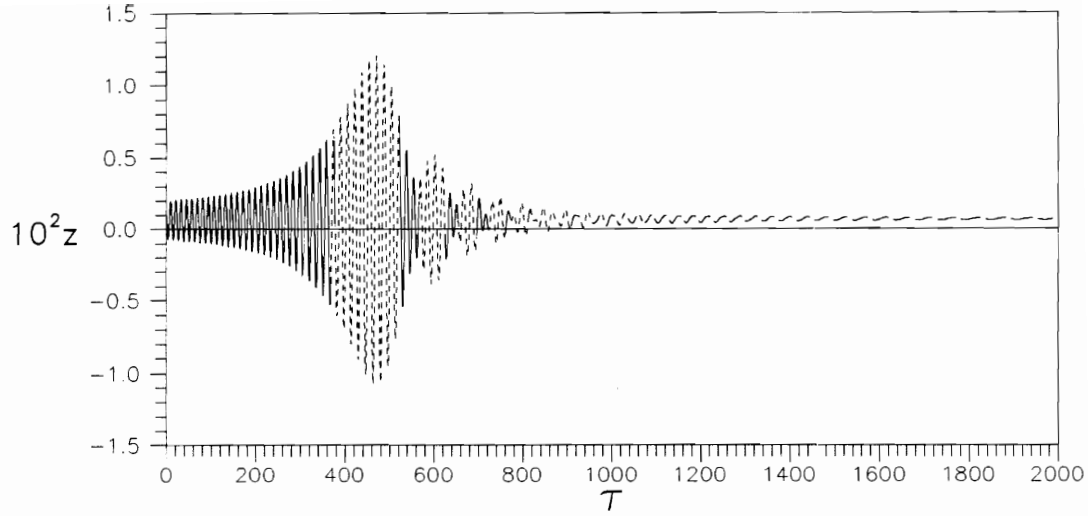

(a)

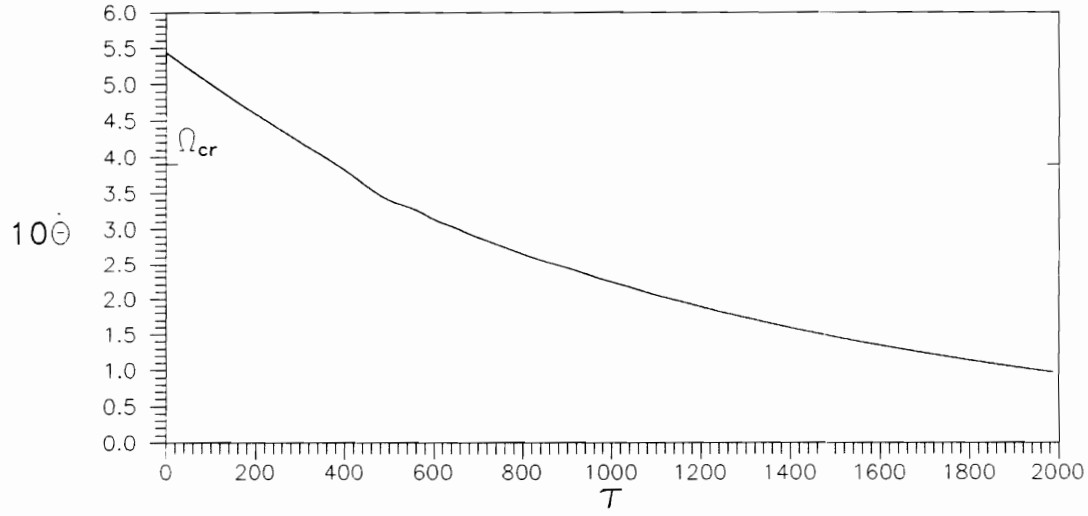

(b)

Fig. 3.9 Coast-down Time Histories with $\dot{\Theta}_{initial}=0.54$

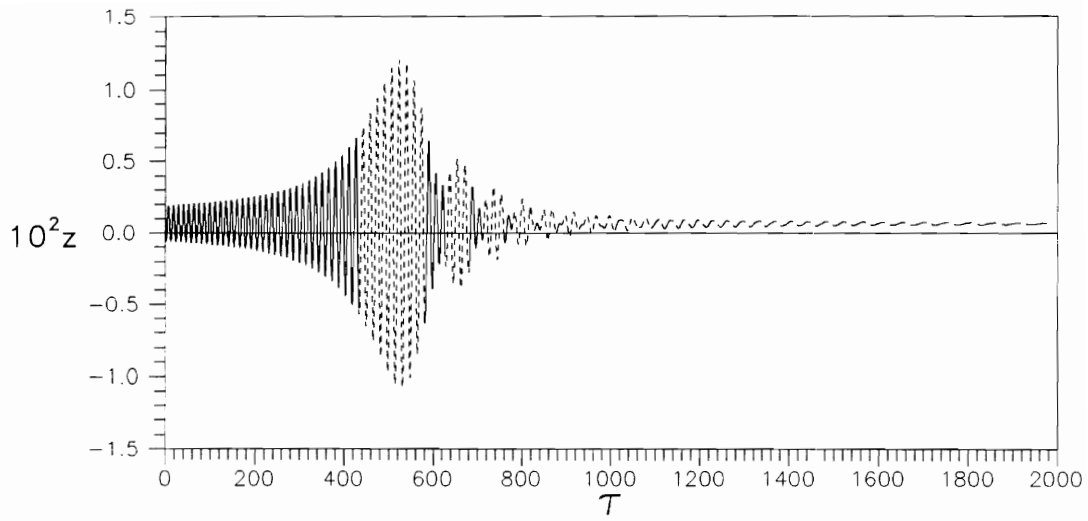

(a)

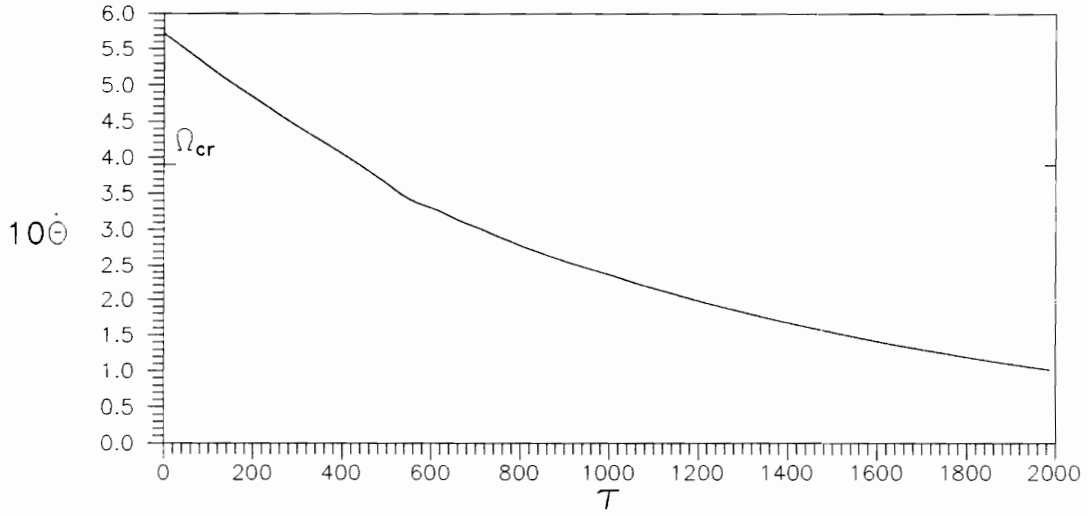

(b)

Fig. 3.10 Coast-down Time Histories with $\dot{\Theta}_{initial}=0.57$

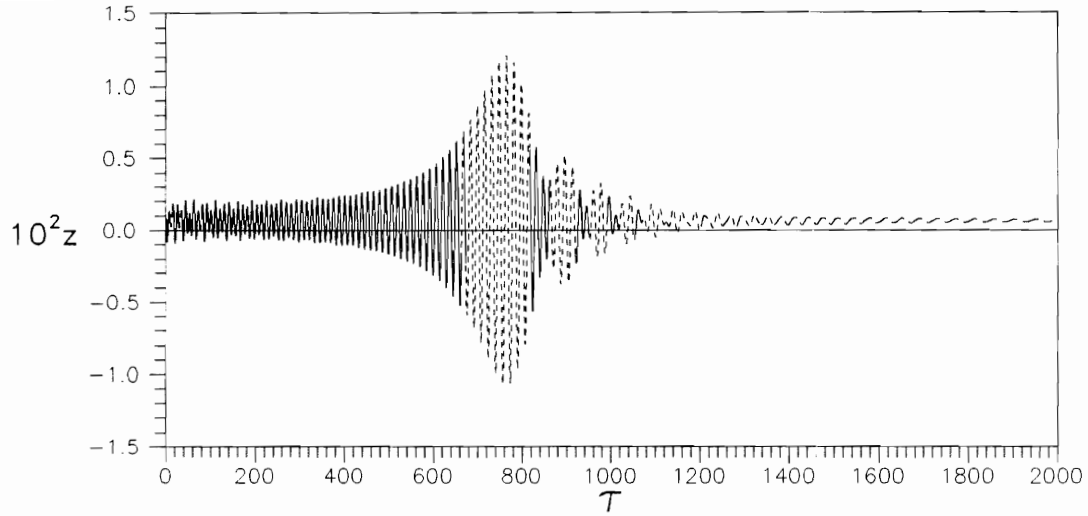

(a)

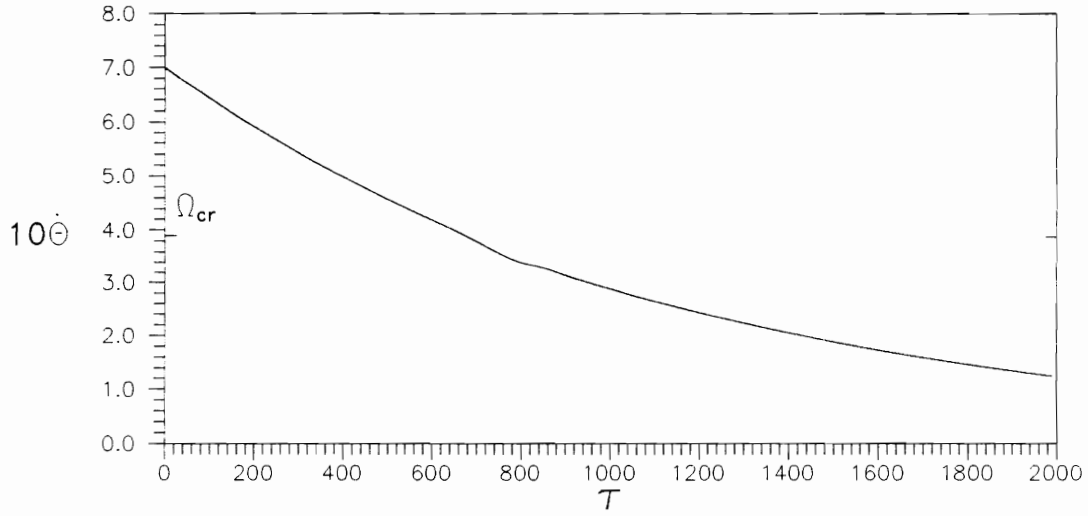

(b)

Fig. 3.11 Coast-down Time Histories with $\dot{\Theta}_{initial}=0.7$

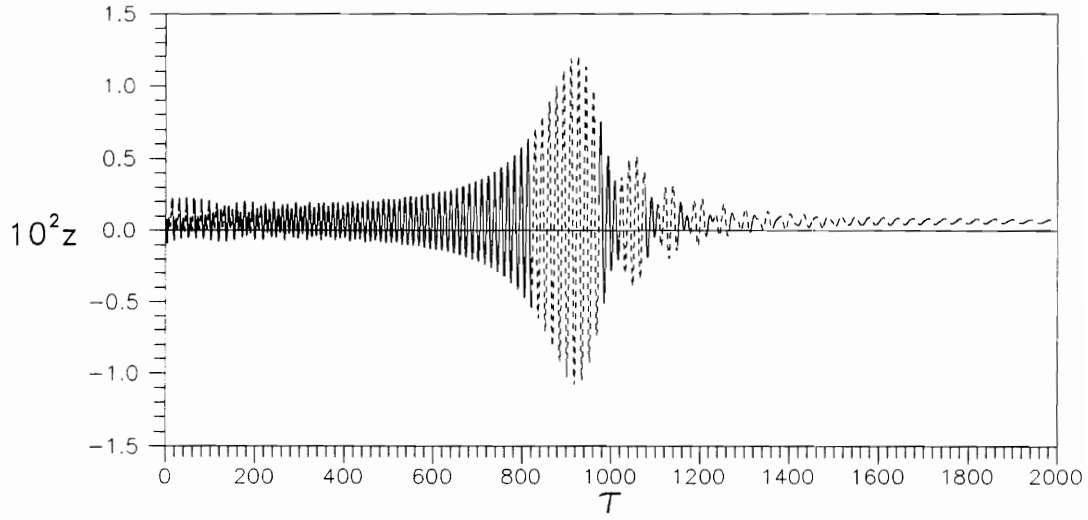

(a)

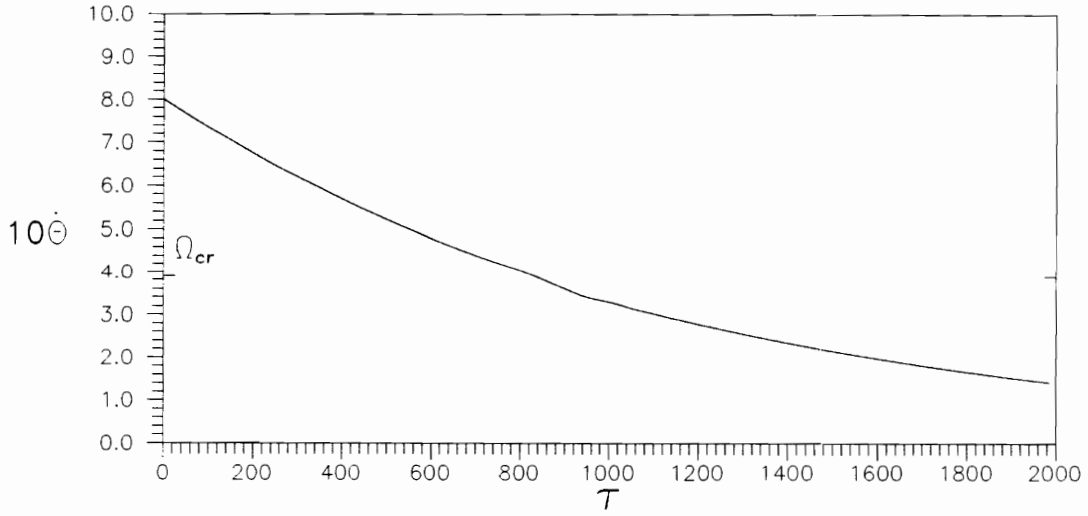

(b)

Fig. 3.12 Coast-down Time Histories with $\dot{\Theta}_{initial}=0.8$

these two figures with larger initial angular velocity that the critical speed is passed at a later time. However, the characteristics of the angular velocity time history are similar.

The Sommerfeld effect in Figs. 3.9-3.12 is hardly seen. The maximum z-displacement occurs after the shaft passes the critical speed. Similar to the behavior of the cracked shaft with an ideal motor torque during deceleration, usually the crack is closed until the amplitude increases, and then becomes open for a while as the maximum displacement is passed. After that, there is a breathing condition and the shaft is open again at the stationary condition.

3.4.3. Influence of support stiffness

The influence of different support stiffnesses on the nonstationary behavior of the shaft is investigated, based on the standard case during run-up with the initial motor characteristic $\upsilon_0 = 0.00004$ and the stationary angular velocity $\Omega_{st} = 0.6$ (Fig. 3.6). The support stiffness $\tilde{s}$ varies from 0.8 to 100. The time histories of the z- displacement and the angular velocity for different support stiffnesses are almost identical to those in Fig. 3.6. The differences in the z-displacement and the angular velocity are relatively small. A similar behavior also occurs during coast-down.

3.4.4. Influence of support damping

The effect of the support damping during run-up is investigated, based on the standard case with the motor characteristic $\upsilon_0 = 0.00004$ and the stationary angular

velocity $\Omega_{st} = 0.6$ (Fig. 3.6). Compared to the amplitude results of the stationary condition with different support dampings (Fig. 3.2), in the nonstationary case the z-displacement for different support dampings has the same behavior. From Figs. 3.13, 3.14, 3.15, and 3.6 with the support dampings $\tilde{p} = 10,\ 50,\ 100$, and 300, respectively, the maximum z-displacement during run-up becomes smaller when the support damping increases. The time histories of the angular velocity are almost the same, only for small support damping $\tilde{p} = 10$ (Fig. 3.13) the Sommerfeld effect lasts longer than for the other cases.

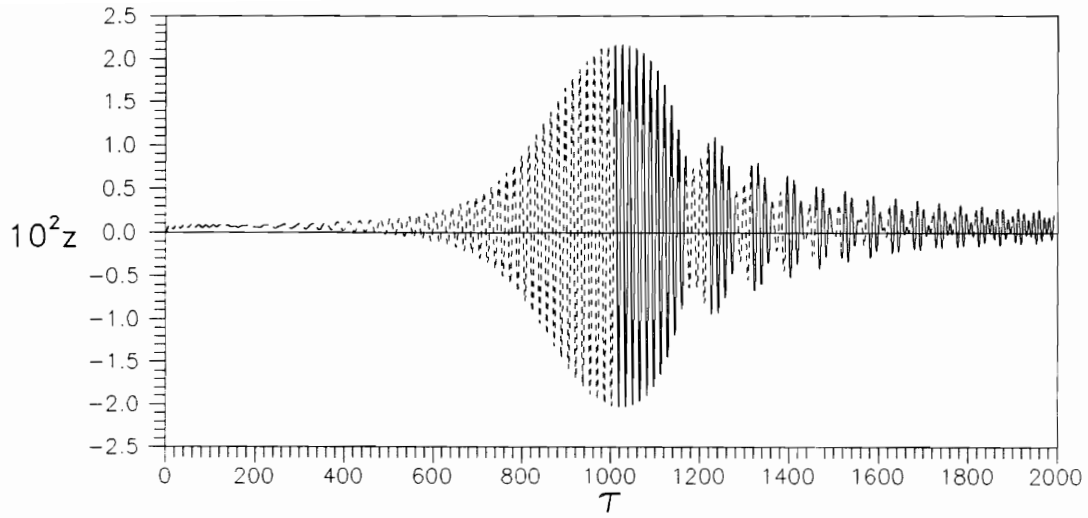

(a)

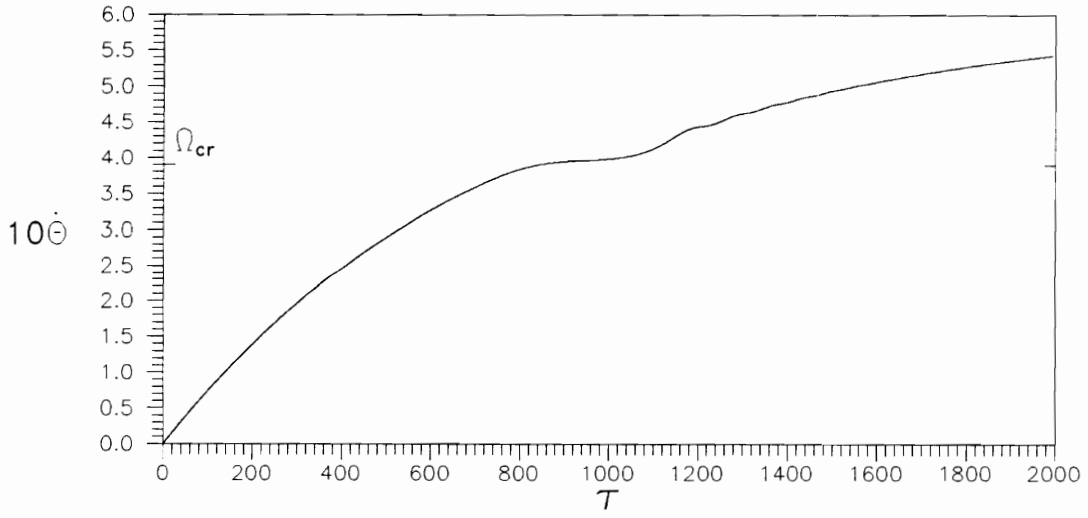

(b)

Fig. 3.13 Run-up Time Histories with p=10

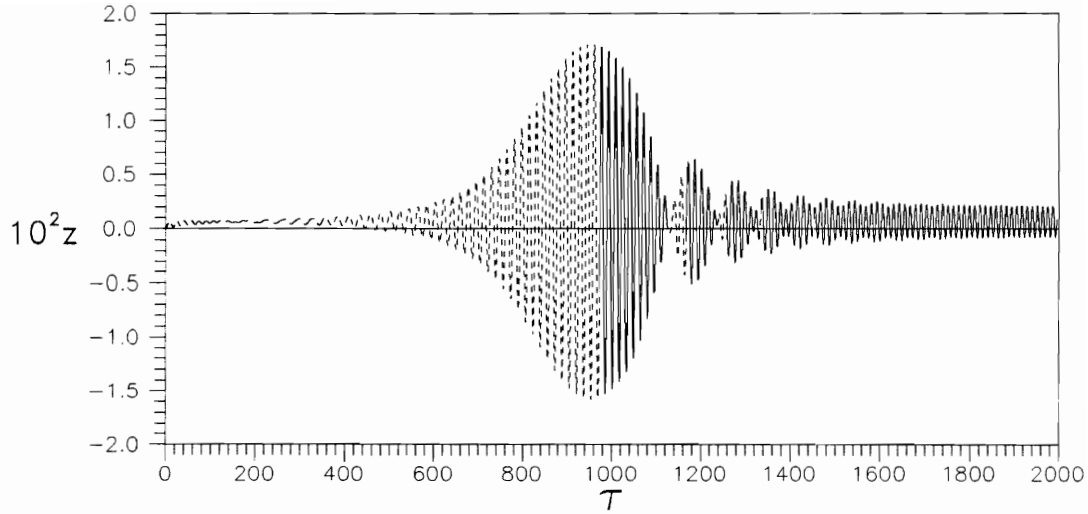

(a)

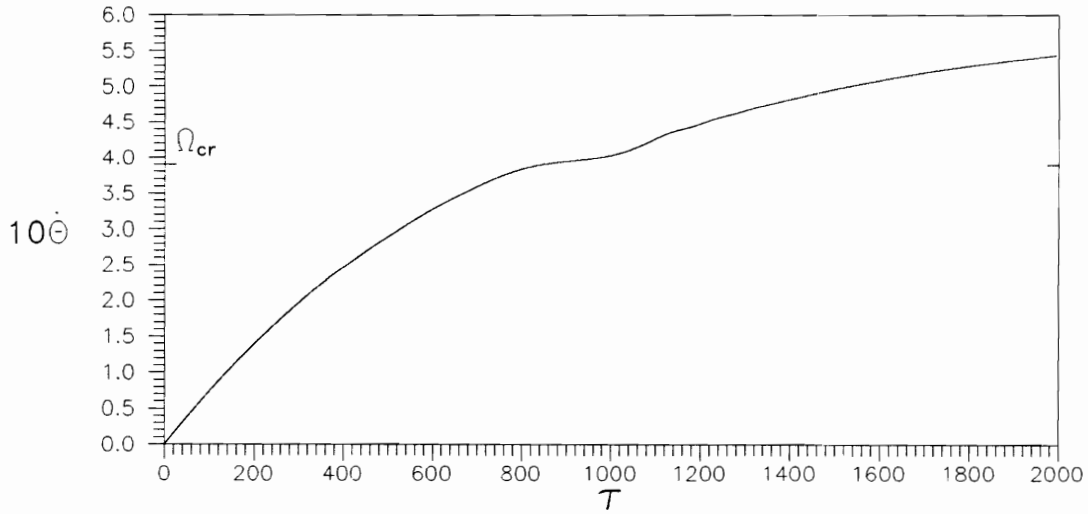

(b)

Fig. 3.14 Run−up Time Histories with p=50

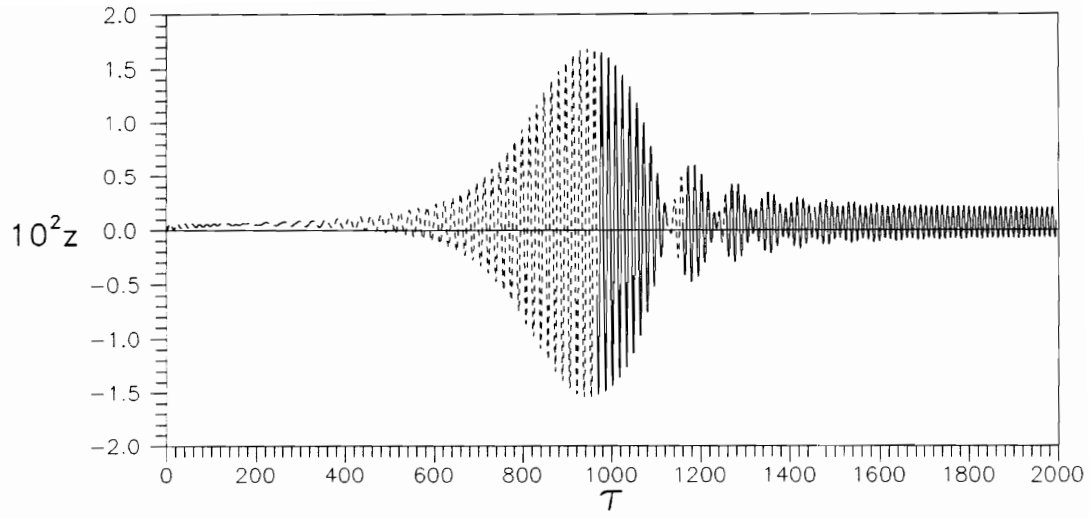

(a)

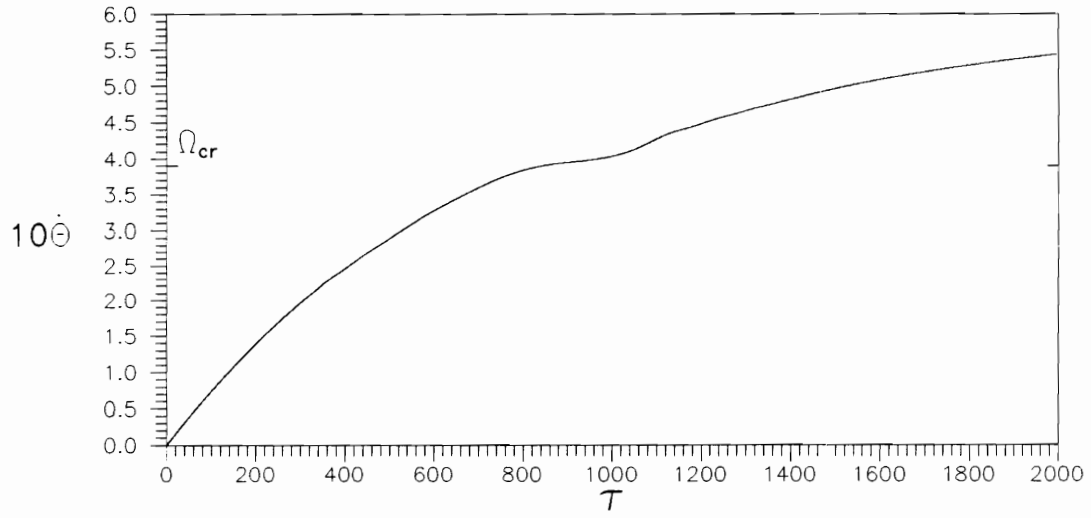

(b)

Fig. 3.15 Run−up Time Histories with p=100

CHAPTER 4

VIBRATION SUPPRESSION WITH THE USE OF AN INTERNAL FLEXIBLE CONSTRAINT

4.1. Physical Model

The displacement of a cracked rotating shaft passing through a critical speed becomes large, as seen in the previous chapters. In order to suppress this displacement, one can try to prevent the shaft from passing a critical speed by causing modifications while the shaft is rotating.

In this study, in order to suppress the vibration, the system stiffness is modified by adding an internal flexible support for a certain amount of time. By adding an internal support, the stiffness of the system will increase and the critical time will become larger than that of the original system without it. This additional support should be easily applied to the shaft while the shaft is still rotating. Thus, the stiffness of the system can be modified during rotation of the shaft by activating or deactivating the additional support so that the actual angular velocity of the shaft never coincides with a resonant frequency.

The influence of the ideal and the nonideal motor on the vibration suppression by

adding the internal support is investigated. For the ideal motor, the angular velocity is specified, but for the nonideal motor it is not specified.

The horizontal shaft is depicted in Fig. 4.1. The shaft is circular with the length L, radius r_s, diameter d_s, mass per unit length μ, Young's modulus E, shear modulus G, Poisson's ratio ν, and cross-sectional moment of inertia $I = 0.25\,\pi\,r_s^4$. The shaft has a transverse crack at $x = b$ and a disk at $x = c$. Both supports are simply supported. The additional internal support is flexible with stiffness s_i and is located at $x = x_i$. It can be activated or deactivated.

The coordinate systems as depicted in Fig. 2.2 are still used. The geometry of the cross section with a crack and the geometry of the disk are the same as in Figs. 2.2 and 2.3. In this study, longitudinal displacement, shear deformation, and gyroscopic moments are not included. The eccentricity of the disk, gravitational forces, and internal and external damping are taken into account.

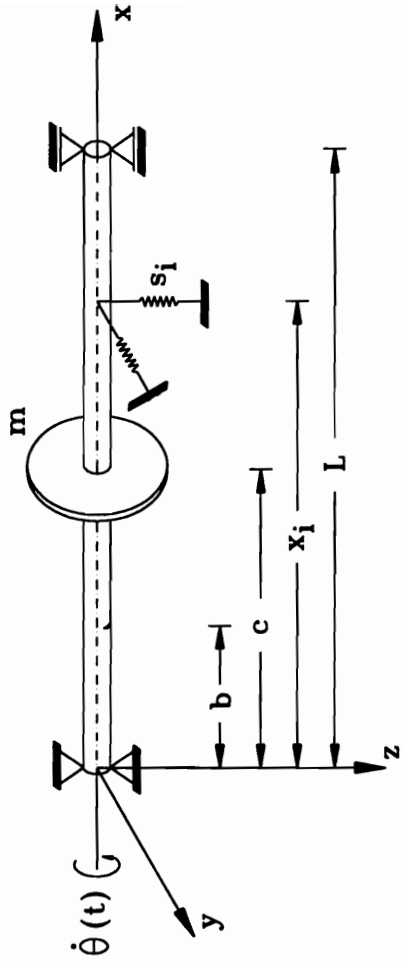

Fig. 4.1 Geometry of Simply Supported Shaft with Disk and Internal Support

4.2. Ideal Motor

4.2.1. Introduction

Vibration suppression of the cracked rotating shaft with an ideal motor is examined during acceleration and deceleration in this section. With the ideal motor, the energy supply is unlimited and the angular velocity is specified.

During rotation the stiffness of the system will be changed by activating the internal support. This switching will occur in the neighborhood of resonance, just before and sometimes after passing the critical speed.

4.2.2. Analysis

The equations of motion and boundary conditions are derived by Hamilton's Principle with the assumption that there is an additional internal support on the shaft whose stiffness can be varied from zero to a large stiffness similar to a simple support. A zero internal support stiffness means the shaft has no internal support.

Following Hamilton's Principle (eq. 2.15), the governing equation now is as follows:

$$\int_{t_0}^{t_1}\int_{0}^{L}\Big\langle \left[\mu + m\delta(x-c)\right]\Big\{\left[-v_{tt} + 2\dot{\theta}w_t + \ddot{\theta}w + \dot{\theta}^2 v\right]\delta v$$

$$+\left[-w_{tt} - 2\dot{\theta}v_t - \ddot{\theta}v + \dot{\theta}^2 w\right]\delta w\Big\} + me_d\delta(x-c)\Big\{\left[\ddot{\theta}\sin\delta_d + \dot{\theta}^2\cos\delta_d\right]\delta v$$

$$+\left[-\ddot{\theta}\cos\delta_d + \dot{\theta}^2 \sin\delta_d\right]\delta w\Big\} - \Big\{EI\, v_{xxxx} - \left[\mu + m\delta(x-c)\right]g\sin\theta\Big\}\delta v$$

$$-\Big\{EI\, w_{xxxx} - \left[\mu + m\delta(x-c)\right]g\cos\theta\Big\}\delta w + \left[-d_e\mu\left(v_t - \dot{\theta}w\right) - d_i EI\, v_{txxxx}\right]\delta v$$

$$+\left[-d_e\mu\left(w_t + \dot{\theta}\, v\right) - d_i EI\, w_{txxxx}\right]\delta w - \Lambda\left(M_\zeta + m_\zeta\right)\left[\delta'(x-b_+) - \delta'(x-b_-)\right]\delta v$$

$$+\Lambda\left(M_\eta + m_\eta\right)\left[\delta'(x-b_+) - \delta'(x-b_-)\right]\delta w\Big\rangle dx\, dt - \int_{t_0}^{t_1}\left(s_i\, v\delta v + s_i\, w\delta w\right)dt\Big|_{x=x_i}$$

$$-\int_{t_0}^{t_1}\left[EI\, v_{xx}\,\delta v_x - EI\, v_{xxx}\,\delta v + EI\, w_{xx}\,\delta w_x - EI\, w_{xxx}\,\delta w\right]dt\Big|_0^{x_i^-}$$

$$-\int_{t_0}^{t_1}\left[EI\, v_{xx}\,\delta v_x - EI\, v_{xxx}\,\delta v + EI\, w_{xx}\,\delta w_x - EI\, w_{xxx}\,\delta w\right]dt\Big|_{x_i^+}^{L}$$

$$-\int_{t_0}^{t_1} d_i\left[EI\, v_{txx}\,\delta v_x - EI\, v_{txxx}\,\delta v + EI\, w_{txx}\,\delta w_x - EI\, w_{txxx}\,\delta w\right]dt\Big|_0^{x_i^-}$$

$$-\int_{t_0}^{t_1} d_i\left[EI\, v_{txx}\,\delta v_x - EI\, v_{txxx}\,\delta v + EI\, w_{txx}\,\delta w_x - EI\, w_{txxx}\,\delta w\right]dt\Big|_{x_i^+}^{L} = 0 \quad (4.1)$$

Then the equations of motion can be written as $H_v = 0$ and $H_w = 0$, where

$$H_v \equiv \left[\mu + m\delta(x-c)\right]\left[-v_{tt} + 2\dot{\theta}\, w_t + \ddot{\theta}\, w + \dot{\theta}^2 v\right]$$

$$+ me_d\delta(x-c)\left[\ddot{\theta}\sin\delta_d + \dot{\theta}^2\cos\delta_d\right] - EI\, v_{xxxx} + \left[\mu + m\delta(x-c)\right]g\sin\theta$$

$$-d_e\mu\left(v_t-\dot{\theta}w\right)-d_iEI\,v_{txxxx}-\Lambda\left(M_\zeta+m_\zeta\right)\left[\delta'\left(x-b_+\right)-\delta'\left(x-b_-\right)\right]=0$$

(4.2.a)

$$H_w\equiv\left[\mu+m\delta\left(x-c\right)\right]\left[-w_{tt}-2\dot{\theta}v_t-\ddot{\theta}v+\dot{\theta}^2w\right]$$

$$+me_d\delta\left(x-c\right)\left[-\ddot{\theta}\cos\delta_d+\dot{\theta}^2\sin\delta_d\right]-EI\,w_{xxxx}+\left[\mu+m\delta\left(x-c\right)\right]g\cos\theta$$

$$-d_e\mu\left(w_t+\dot{\theta}v\right)-d_iEI\,w_{txxxx}+\Lambda\left(M_\eta+m_\eta\right)\left[\delta'\left(x-b_+\right)-\delta'\left(x-b_-\right)\right]=0$$

(4.2.b)

and the boundary conditions are

At $x = 0, L$

$$EI\left(v_{xx}+d_i\,v_{txx}\right)=0,\quad EI\left(w_{xx}+d_i\,w_{txx}\right)=0,\quad v=0,\quad w=0 \qquad (4.3.a)$$

At $x = x_i$

$$EI\left(v_{xx}+d_i\,v_{txx}\right)\Big|_{x=x_i^+}-EI\left(v_{xx}+d_i\,v_{txx}\right)\Big|_{x=x_i^-}=0$$

$$EI\left(w_{xx}+d_i\,w_{txx}\right)\Big|_{x=x_i^+}-EI\left(w_{xx}+d_i\,w_{txx}\right)\Big|_{x=x_i^-}=0$$

$$EI\left(v_{xxx}+d_i\,v_{txxx}\right)\Big|_{x=x_i^+}-EI\left(v_{xxx}+d_i\,v_{txxx}\right)\Big|_{x=x_i^-}+s_iv=0$$

$$EI\left(w_{xxx}+d_i\,w_{txxx}\right)\Big|_{x=x_i^+}-EI\left(w_{xxx}+d_i\,w_{txxx}\right)\Big|_{x=x_i^-}+s_iw=0 \qquad (4.3.b)$$

The supports are simply supported; therefore, there is no rigid body translation or inclination of the shaft. Then the approximate displacement functions become

$$v = \sum_{k=1}^{N} v_k \sin\frac{k\pi x}{L} \tag{4.4.a}$$

$$w = \sum_{k=1}^{N} w_k \sin\frac{k\pi x}{L} \tag{4.4.b}$$

The boundary conditions at the supports $x = 0, L$ are satisfied, but the boundary conditions at $x = x_i$ are not satisfied. The Extended Galerkin Method is still used to eliminate the spatial dependence. Then, the equations become

$$\int_0^L H_v \sin\frac{n\pi x}{L} dx + s_i \sum_{k=1}^{N} v_k \sin\frac{k\pi x_i}{L} \sin\frac{n\pi x_i}{L} = 0 \tag{4.5.a}$$

$$\int_0^L H_w \sin\frac{n\pi x}{L} dx + s_i \sum_{k=1}^{N} w_k \sin\frac{k\pi x_i}{L} \sin\frac{n\pi x_i}{L} = 0 \tag{4.5.b}$$

By using the nondimensionalized quantities from eq. (2.21) and the additional ones defined by

$$\tilde{s}_i = \frac{L^3}{\pi^3 EI} s_i, \quad \tilde{x}_i = \frac{x_i}{L} \tag{4.6}$$

eq. (4.5) becomes

$$\ddot{\tilde{v}}_n + \tilde{m} \sin n\pi\tilde{c} \sum_{k=1}^{N} \ddot{\tilde{v}}_k \sin k\pi\tilde{c} =$$

$$-n^4 \tilde{v}_n + 2\dot{\theta}\dot{\tilde{w}}_n + \ddot{\theta}\tilde{w}_n + \dot{\theta}^2 \tilde{v}_n + \tilde{m} \sin n\pi\tilde{c} \sum_{k=1}^{N} \left(2\dot{\theta}\dot{\tilde{w}}_k + \ddot{\theta}\tilde{w}_k + \dot{\theta}^2 \tilde{v}_k\right) \sin k\pi\tilde{c}$$

$$-\tilde{d}_e\left(\ddot{\tilde{v}}_n - \dot{\theta}\dot{\tilde{w}}_n\right) - \tilde{d}_i\ddot{\tilde{v}}_n n^4 + 2\Lambda\,\tilde{c}_{44}\,n^2 \sin n\pi\tilde{b} \sum_{k=1}^{N} k^2\left(\tilde{v}_k + \tilde{d}_i\dot{\tilde{v}}_k\right)\sin k\pi\tilde{b}$$

$$+\left\{\frac{1}{n}\left[1-(-1)^n\right] + \tilde{m}\frac{\pi}{2}\sin n\pi\tilde{c}\right\}\tilde{\mu}\sin\theta + \tilde{m}\tilde{e}_d \sin n\pi\tilde{c}\left(\ddot{\theta}\sin\delta_d + \dot{\theta}^2\cos\delta_d\right)$$

$$-\frac{2}{\pi}\,\tilde{s}_i \sum_{k=1}^{N}\tilde{v}_k \sin k\pi\tilde{x}_i \sin n\pi\tilde{x}_i \qquad (4.7.a)$$

$$\ddot{\tilde{w}}_n + \tilde{m}\sin n\pi\tilde{c} \sum_{k=1}^{N}\ddot{\tilde{w}}_k \sin k\pi\tilde{c} =$$

$$-n^4\tilde{w}_n - 2\dot{\theta}\dot{\tilde{v}}_n - \ddot{\theta}\tilde{v}_n + \dot{\theta}^2\tilde{w}_n - \tilde{m}\sin n\pi\tilde{c}\sum_{k=1}^{N}\left(2\dot{\theta}\dot{\tilde{v}}_k - \ddot{\theta}\tilde{v}_k - \dot{\theta}^2\tilde{w}_k\right)\sin k\pi\tilde{c}$$

$$-\tilde{d}_e\left(\ddot{\tilde{w}}_n + \dot{\theta}\tilde{v}_n\right) - \tilde{d}_i\ddot{\tilde{w}}_n n^4 + 2\Lambda\,\tilde{c}_{55}\,n^2 \sin n\pi\tilde{b} \sum_{k=1}^{N} k^2\left(\tilde{w}_k + \tilde{d}_i\dot{\tilde{w}}_k\right)\sin k\pi\tilde{b}$$

$$+\left\{\frac{1}{n}\left[1-(-1)^n\right] + \tilde{m}\frac{\pi}{2}\sin n\pi\tilde{c}\right\}\tilde{\mu}\cos\theta + \tilde{m}\tilde{e}_d \sin n\pi\tilde{c}\left(\ddot{\theta}\cos\delta_d + \dot{\theta}^2\sin\delta_d\right)$$

$$-\frac{2}{\pi}\,\tilde{s}_i \sum_{k=1}^{N}\tilde{w}_k \sin k\pi\tilde{x}_i \sin n\pi\tilde{x}_i \qquad (4.7.b)$$

There are 2N second-order ordinary differential equations which are solved by numerical integration as in the previous chapters. The "standard data" from Chapter 2 are used, with N chosen to be five.

4.2.3. Stationary case

In order to study the characteristics of the shaft with and without an additional internal support, the stationary case is investigated first. In this case, the crack and the gravitational forces are neglected. The forces come from the eccentricity of the disk. For the stationary condition, the angular velocity $\dot{\theta}(t)$ and displacements $v(t), w(t)$ are assumed to be constant, as in eqs. (3.9) and (3.10). By using these constant values of $\dot{\theta}$, v, and w, and using eq. (4.7), the resonance condition of the shaft with and without internal support is known. The influence of the internal support is shown in the last term of eqs. (4.7.a-b).

Figure 4.2 shows the stationary result based on the standard case for different conditions, i.e., the shaft without internal support ($\tilde{s}_i = 0$) and the shaft with internal support with support stiffness $\tilde{s}_i = 10$ at location $\tilde{x}_i = 0.7$. The response is measured at $\tilde{x} = 0.5$, the same as the disk location $\tilde{c} = 0.5$. The first critical speed Ω_{cr} for the shaft without internal support ($\tilde{s}_i = 0$) is 0.41, and for the shaft with this internal support it is 0.80.

In this example, by adding an internal support the stiffness of the system becomes larger and causes a larger critical speed compared to the original system (shaft without internal support). Therefore, the vibration suppression can be done by preventing the shaft speed from coinciding with a critical speed. In order to pass the critical speed of the original system, the best way is to activate the internal support near the resonance condition and deactivate it shortly after passing the resonance condition. The critical

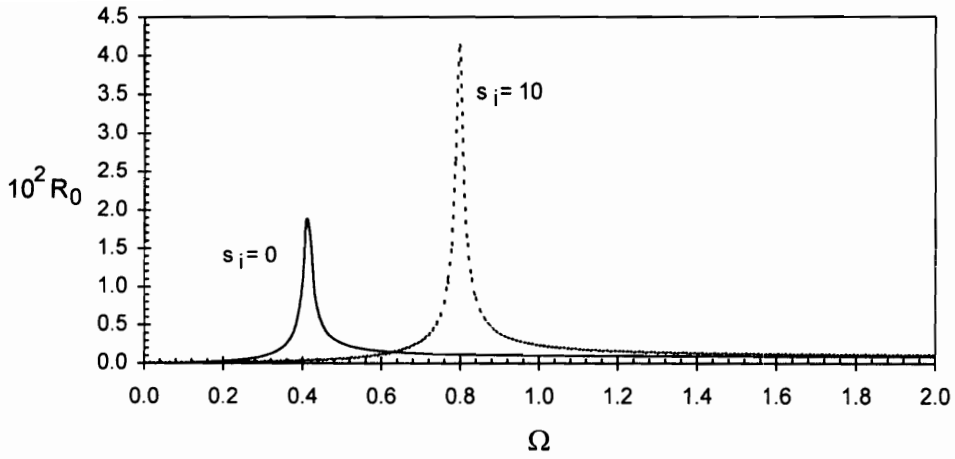

Fig. 4.2 Stationary Response Versus Angular Velocity, with and without Internal Support

speed of the system with internal support will not be passed also, because the system has already returned to the original one.

The influence of the eccentricity of the disk on the stationary case is investigated based on the standard data. Figures 4.3.a-c show the influence of the disk eccentricity with different internal support stiffnesses at $\tilde{x}_i = 0.7$. The results are examined at the location $\tilde{x} = 0.7$. The maximum stationary amplitude increases when the eccentricity of the disk increases. Also, increasing the internal support stiffness from $\tilde{s}_i = 0$ to $\tilde{s}_i = 10$ tends to make the maximum stationary amplitude increase. Critical speeds for different disk eccentricities but for the same internal support stiffness are essentially the same in Fig. 4.3.

The case treated in Fig. 4.3.c is examined further in Fig. 4.4. Figures 4.4.a-c show the relation between the angular velocity Ω and the stationary amplitude R_0 measured at different locations, i.e., at $\tilde{x} = 0.7$, 0.5, and 0.3, respectively. Also, the internal support siffness is varied more, i.e., between 0 and 500. The standard data with the disk eccentricity $\tilde{e}_d = 0.001$ and location of the internal support at $\tilde{x}_i = 0.7$ are used. In Fig. 4.4.a at $\tilde{x} = 0.7$, the maximum stationary amplitude after $\tilde{s}_i \approx 10$ tends to decrease as the internal support stiffness increases. This occurs because the internal support is located at $\tilde{x}_i = 0.7$ also. When the internal support becomes stiff, it will act like a simple support and make the displacement at that location small. In the same figure, the stationary amplitudes R_0 for $0 < \tilde{s}_i \leq 20$ are larger than the stationary

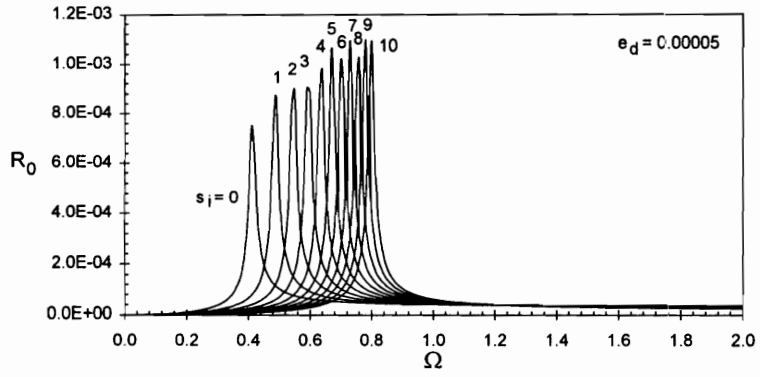

(a)

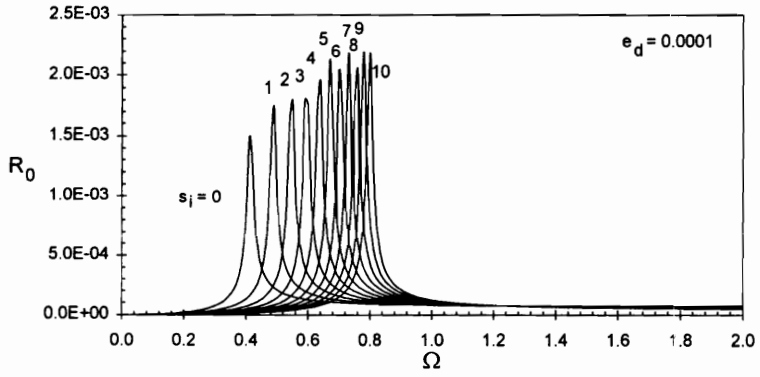

(b)

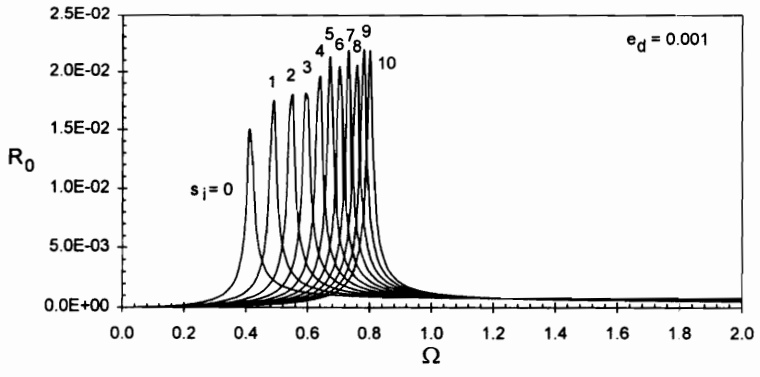

(c)

Fig. 4.3 Influence of Disk Eccentricity and Internal Support Stiffness

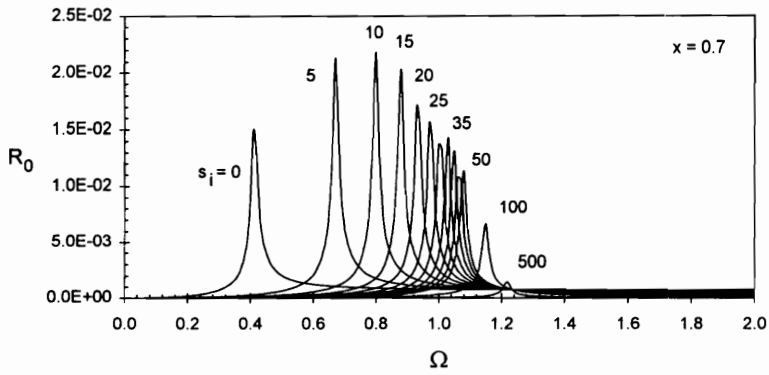

(a)

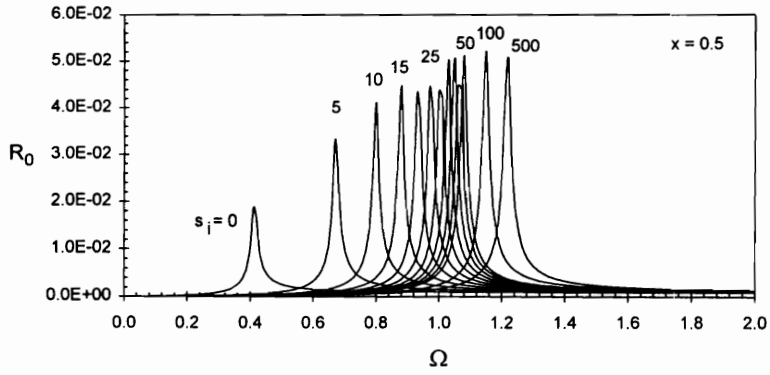

(b)

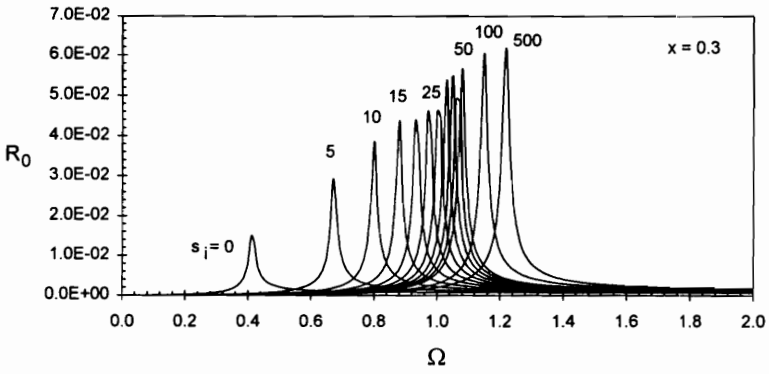

(c)

Fig. 4.4 Influence of Internal Support Stiffness on Response at Different Locations on the Shaft

amplitude R_0 for the shaft without internal support ($\tilde{s}_i = 0$).

While the maximum stationary amplitude at $\tilde{x} = 0.7$ decreases when the internal support stiffness increases beyond $\tilde{s}_i \approx 10$, the maximum stationary amplitude at $\tilde{x} = 0.5$ (Fig. 4.4.b) as well as at $\tilde{x} = 0.3$ (Fig. 4.4.c) tends to increase. Because the internal support becomes like a simple support for large stiffness, it causes the stationary amplitude between $\tilde{x} = 0$ and $\tilde{x} = 0.7$ to become larger. The stationary amplitude for a shaft without an internal support is large at $\tilde{x} = 0.5$ and has the same value at $\tilde{x} = 0.7$ as at $\tilde{x} = 0.3$, due to the symmetry condition (the crack is neglected here). The resonance frequencies in Figs. 4.4.a, b, and c are always the same for the same internal support stiffness.

Figure 4.5 shows the vertical displacement along the shaft for the standard case with internal support stiffnesses $\tilde{s}_i = 0, 5, 10,$ and 100 at $\tilde{x}_i = 0.7$ at the resonance condition as seen in Fig. 4.4. The force from the eccentricity ($e_d \times \Omega^2$) is not the same for each curve. An increasing internal support stiffness has an increasing resonance frequency and an increasing force in Fig. 4.5. The vertical displacement can become larger or smaller at a fixed location as $\tilde{s}_i$ increases.

Without internal support the vertical displacement along the shaft is symmetric with maximum at $\tilde{x} = 0.5$. With large internal support stiffnesses $\tilde{s}_i = 25$ and 100 the vertical displacement at $\tilde{x} = 0.7$ (at the location of the internal support, Fig. 4.5) becomes small and the maximum vertical displacement moves to the left. But for small internal

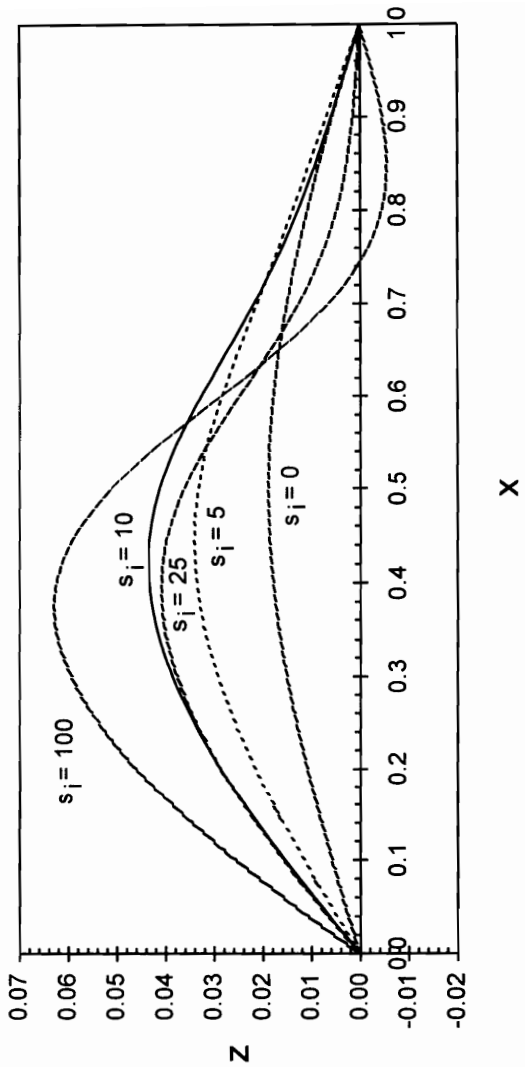

Fig. 4.5 Influence of Internal Support Stiffness on Displacement Along the Shaft at Resonance

support stiffnesses $\tilde{s}_i = 5$ and 10, the vertical displacement at the location of the internal support (Fig. 4.5) is larger than that without internal support.

4.2.4. Nonstationary case

The critical speed for the simply supported shaft without internal support is 0.41. In order to suppress the vibration, the activation of the internal support has to be done before reaching that critical speed, the support, and can be removed after passing the critical speed.

In order to examine the amount of the suppression, the original system without internal support is investigated under acceleration and deceleration conditions. Figures 4.6.a-b show constant acceleration and deceleration rates, respectively. The angular velocity and the angle of rotation for acceleration are defined as follows:

$$0 \le \tau \le T_1: \qquad \theta(\tau) = 0.5\lambda\tau^2, \qquad \Omega(\tau) = \lambda\tau \tag{4.8.a}$$

$$\tau > T_1: \qquad \theta(\tau) = 0.8\tau - 0.4T_1, \qquad \Omega(\tau) = 0.8 \tag{4.8.b}$$

where $T_1 = 0.8/\lambda$, and λ is the acceleration rate. The initial conditions are zero, so that the system starts from rest and the angular velocity increases until it reaches $\Omega = 0.8$.

For deceleration, the angular velocity and angle of rotation are defined by

$$0 \le \tau \le T_1: \qquad \theta(\tau) = 0.8\tau - 0.5\lambda\tau^2, \qquad \Omega(\tau) = 0.8 - \lambda\tau \tag{4.9.a}$$

$$\tau > T_1: \qquad \theta(\tau) = 0.4T_1, \qquad \Omega(\tau) = 0 \tag{4.9.b}$$

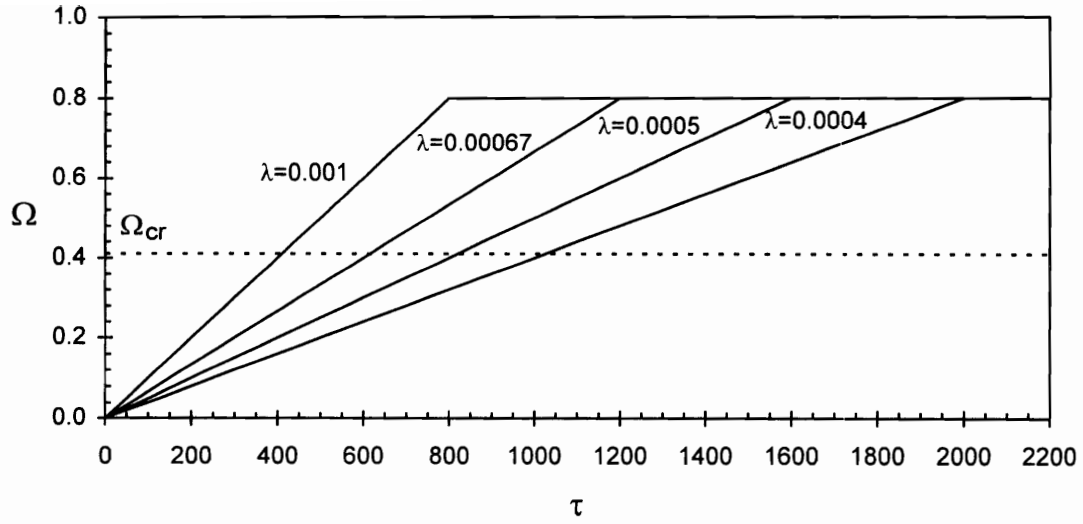

(a) Acceleration

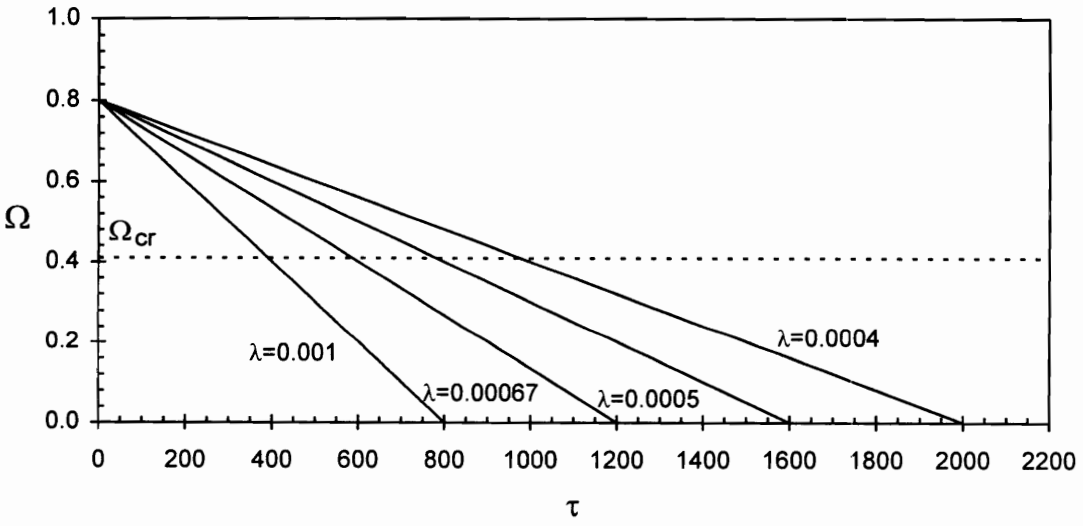

(b) Deceleration

Fig. 4.6 Acceleration and Deceleration Rates

The initial displacement is taken from the stationary condition of the corresponding acceleration case, and the initial angular velocity is 0.8. The angular velocity becomes zero at $\tau = T_1$. Figures 4.6.a-b show the acceleration and deceleration rates 0.001, 0.00067, 0.0005, and 0.0004.

The time histories of the cracked rotating shaft with no internal support based on the standard data are shown in Figs. 4.7.a-d and 4.8.a-d for these acceleration and deceleration rates. The vertical displacement at the disk location is plotted. As the acceleration and deceleration rates decrease, the critical time increases and the resonance occurs later.

The suppression of the dynamic response of the shaft is accomplished by changing the system stiffness, i.e., adding or deleting the internal support. The switching could be done one time, or it could be done several times while the shaft is rotating. A single switching time is called τ_{si} and two switching times are called τ_{si1} and τ_{si2}. In the next part, both types of switching will be investigated.

For one switching time, in the acceleration case the shaft is initially at rest and the internal support is active from the start. Then the internal support is deactivated after the system passes the critical speed. On the other hand, in the deceleration case, in the beginning the shaft is rotating at a speed greater than the first critical speed and the internal support is inactive. Then, just before reaching the critical speed, the internal support is activated.

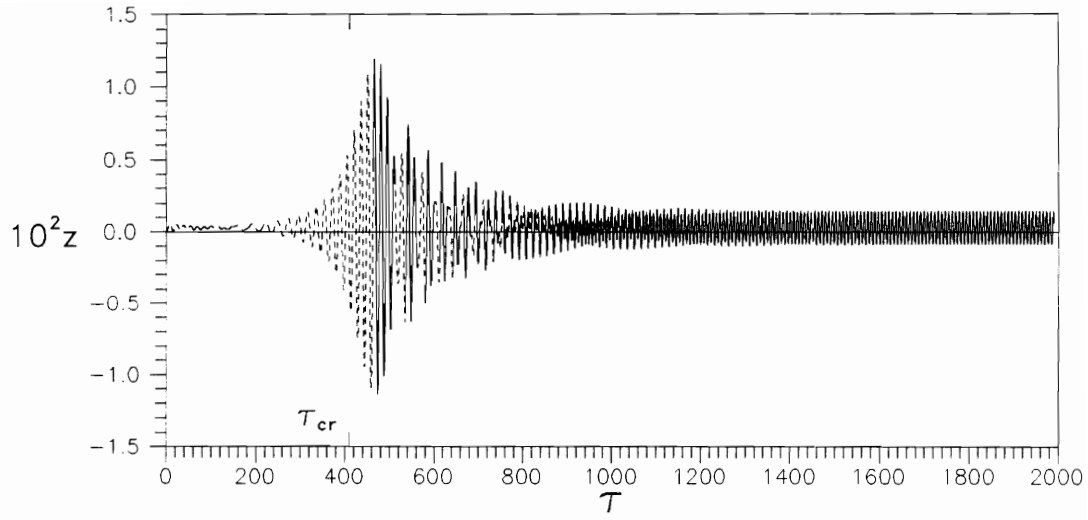

Fig. 4.7.a Time History for Acceleration Rate λ=0.001

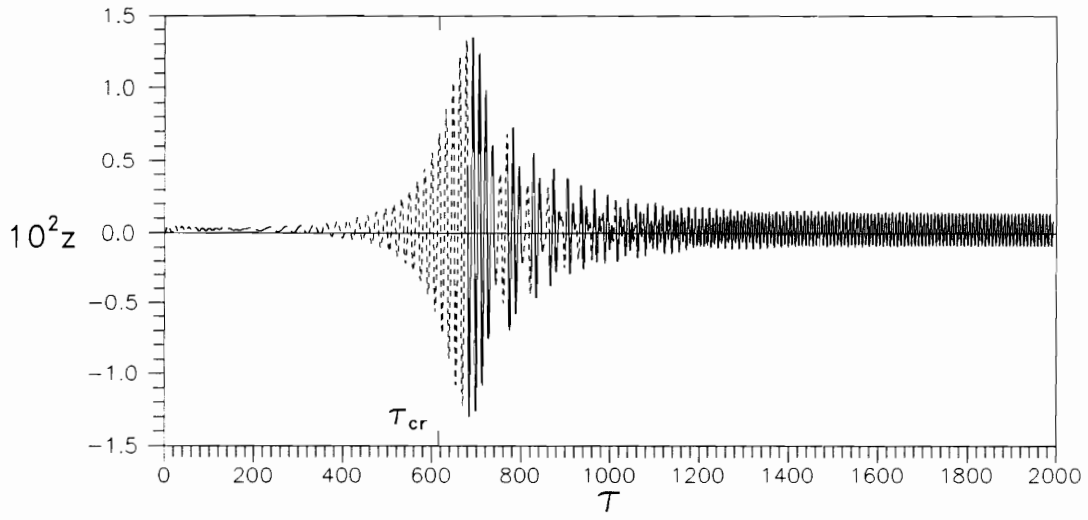

Fig. 4.7.b Time History for Acceleration Rate λ=0.00067

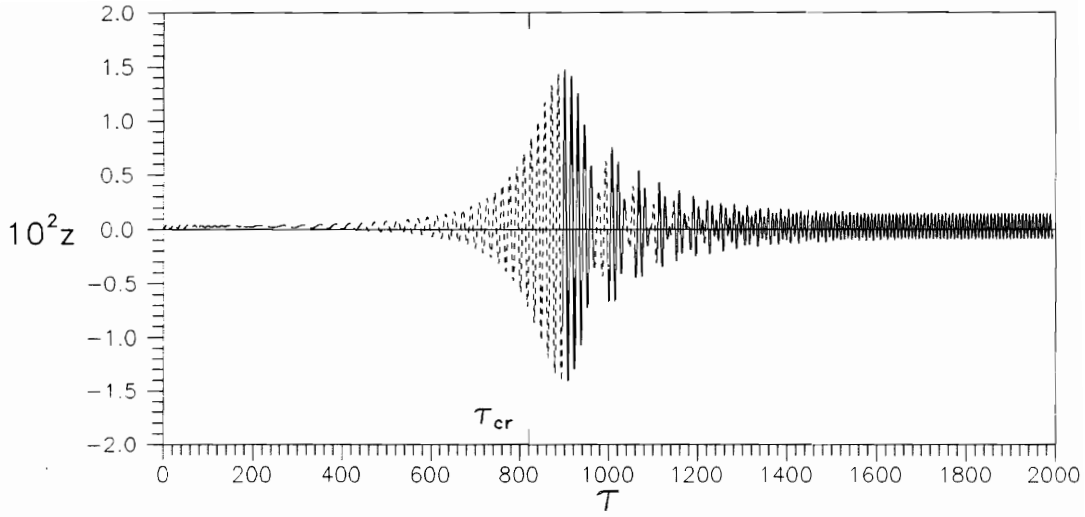

Fig. 4.7.c Time History for Acceleration Rate λ=0.0005

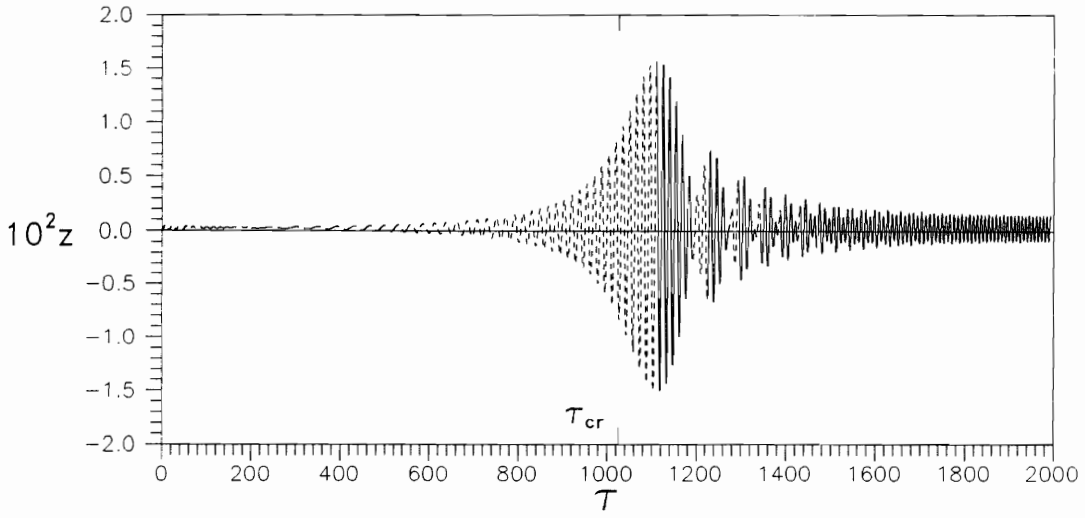

Fig. 4.7.d Time History for Acceleration Rate λ=0.0004

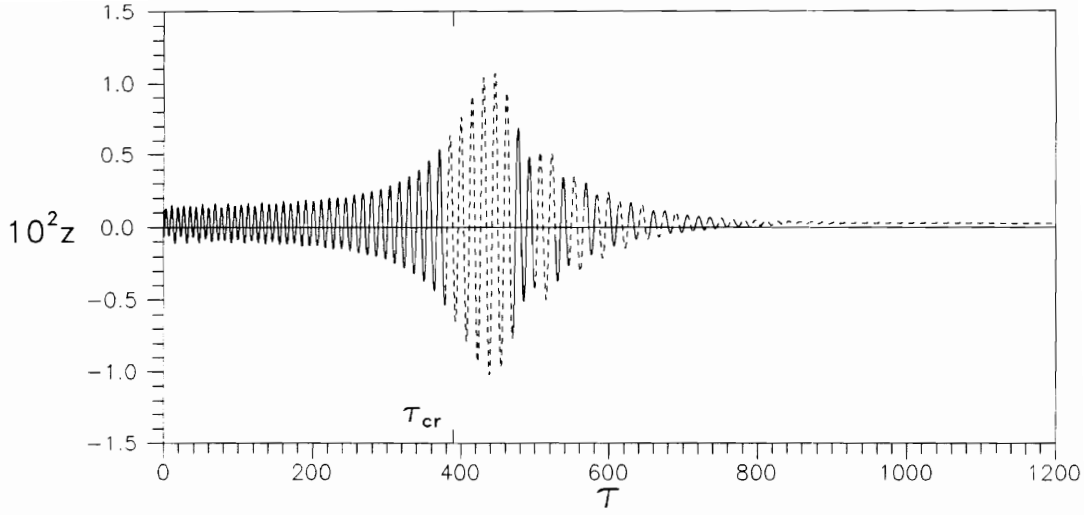

Fig. 4.8.a Time History for Deceleration Rate λ=0.001

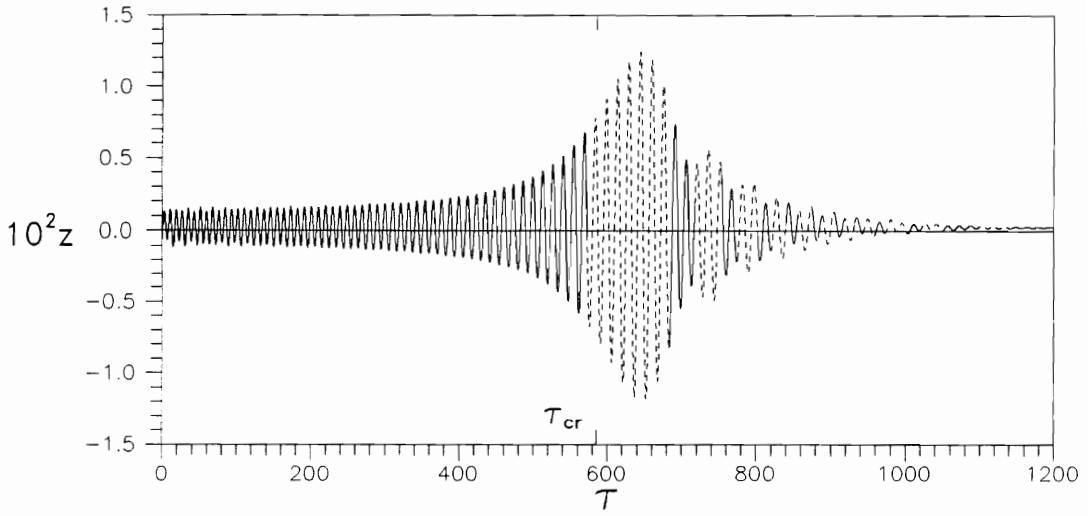

Fig. 4.8.b Time History for Deceleration Rate λ=0.00067

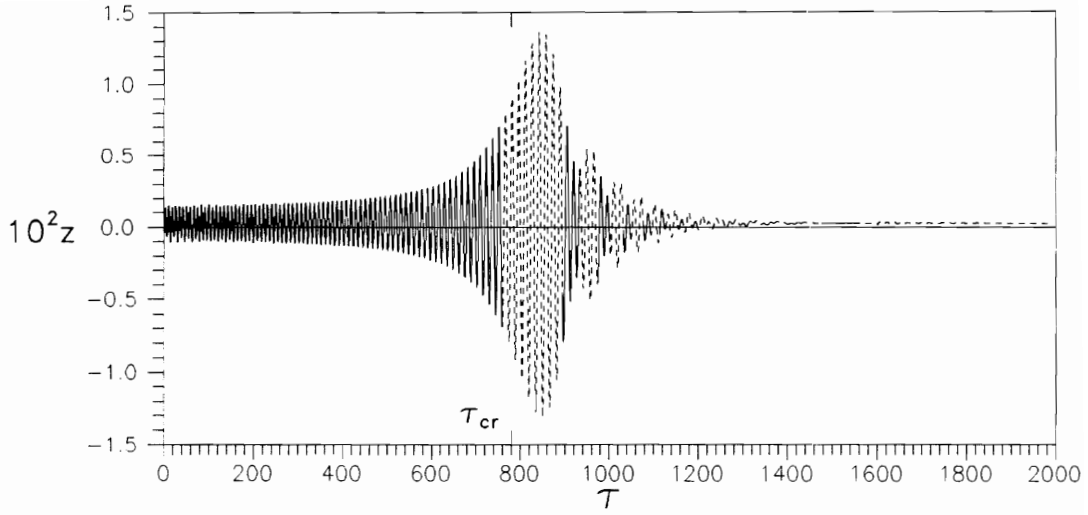

Fig. 4.8.c Time History for Deceleration Rate λ=0.0005

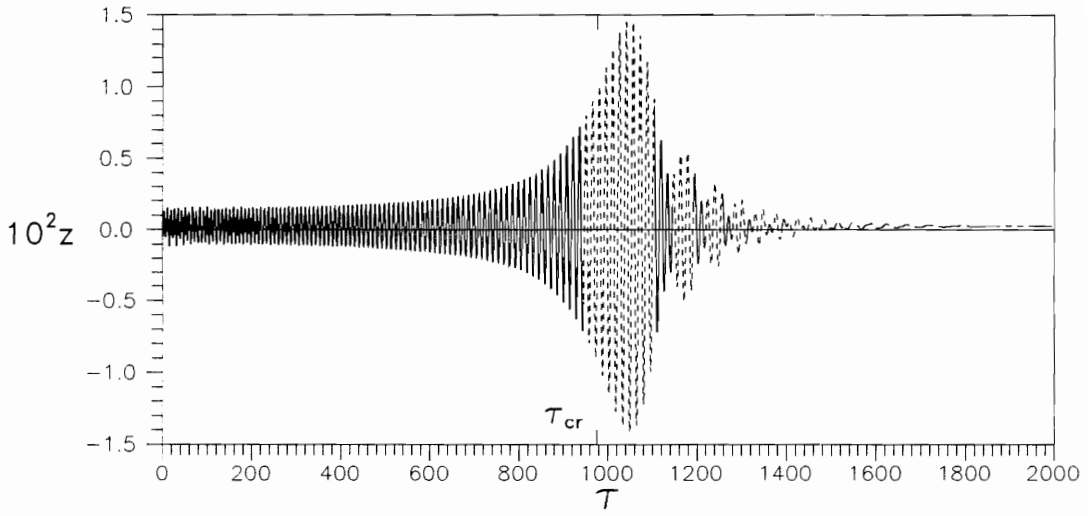

Fig. 4.8.d Time History for Deceleration Rate λ=0.0004

For two switching times, in the acceleration or deceleration case the first switching is made before passing the critical speed of the original system, to have the internal support active, and the second switching is made after passing the critical speed to have the internal support inactive. By doing this, the critical speed of the original system is passed, and the critical speed of the system with the internal support is too high to be passed.

One switching time

Figures 4.9.a-d show the time histories of the z-displacement corresponding to Figs. 4.7.a-d for the acceleration case with one switching time to suppress the response. In Fig. 4.9, at first the systems are running with the internal support $\tilde{s}_i = 10$ at $\tilde{x}_i = 0.7$ (for all cases) and, after reaching the switching time, the internal support is deactivated and the system returns to the original one without internal support. Because the critical speed of the original system has been passed, the displacement does not become large after τ_{si}. The jump at the switching time occurs due to transient motion caused by the switching stiffness. Table 4.1 gives the results of the suppression for the different cases in Figs. 4.7.a-d and Figs. 4.9.a-d.

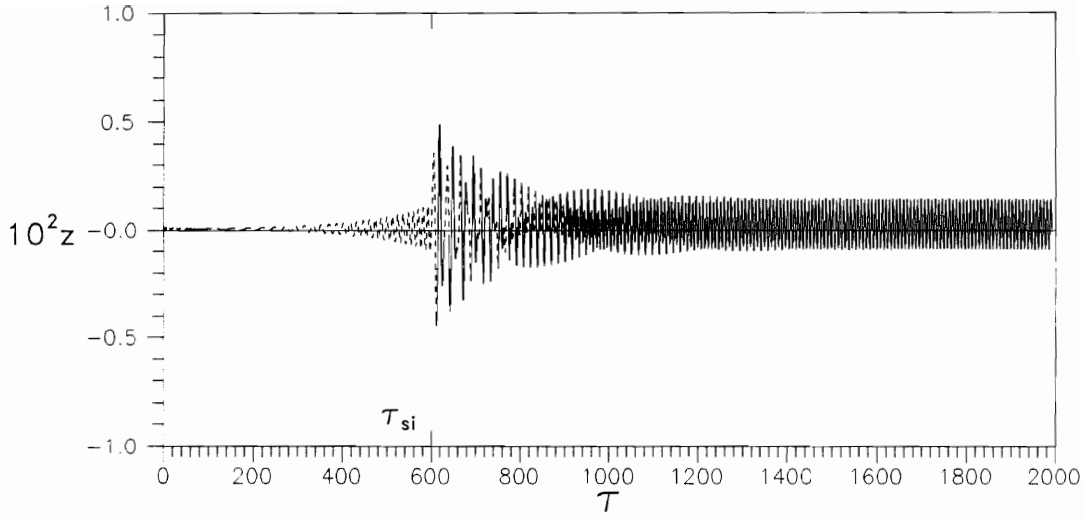

Fig. 4.9.a Switching Stiffness with Acceleration Rate λ=0.001

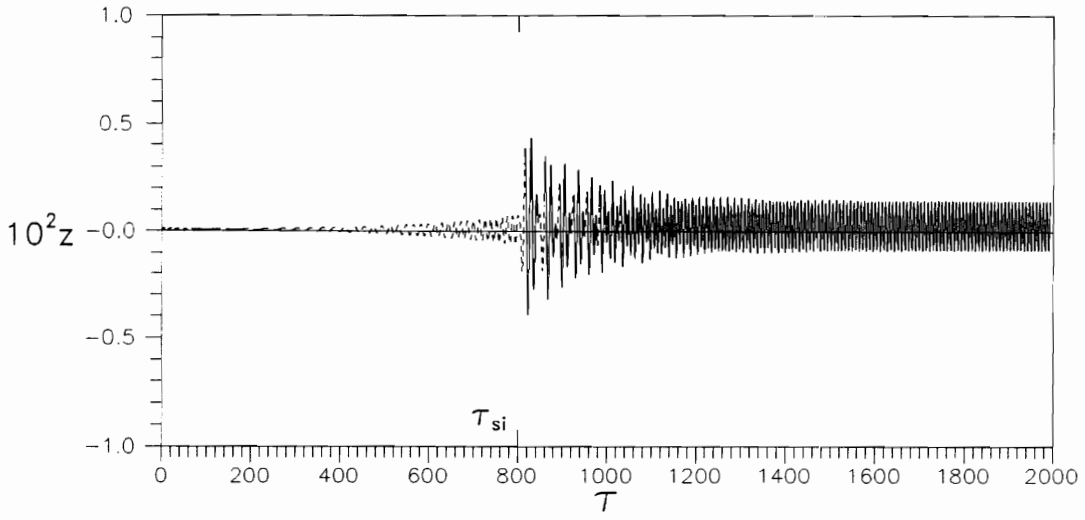

Fig. 4.9.b Switching Stiffness with Acceleration Rate λ=0.00067

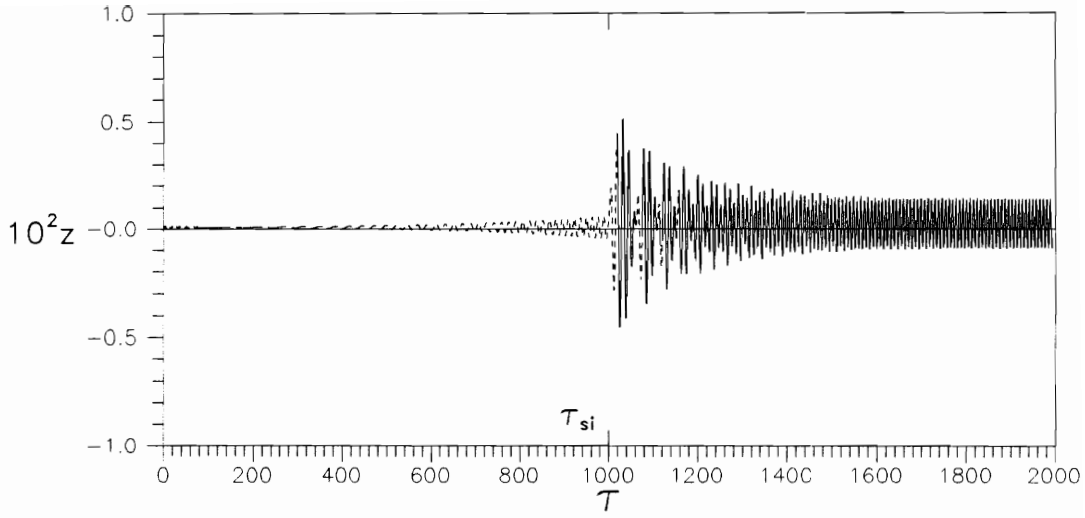

Fig. 4.9.c Switching Stiffness with Acceleration Rate λ=0.0005

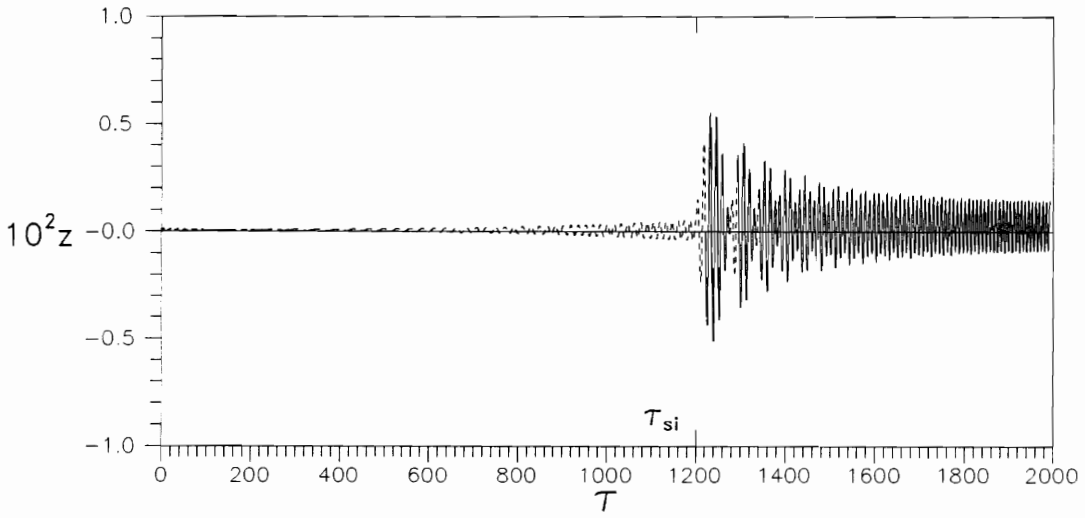

Fig. 4.9.d Switching Stiffness with Acceleration Rate λ=0.0004

Table 4.1 Maximum vertical displacement for the acceleration cases

Accel. λ	τ_{si}	z_{max} without internal support	z_{max} with switching	% reduction
0.001	600	0.0119	0.0049	59.0
0.00067	800	0.0135	0.0043	68.1
0.0005	1000	0.0147	0.0051	65.1
0.0004	1200	0.0157	0.0055	64.7

From Table 4.1 for the acceleration cases, the reduction of the maximum vertical displacement is larger than 50%.

Figures 4.10.a-d show the time histories of the z-displacement for the deceleration cases with deceleration rates 0.001, 0.00067, 0.0005, and 0.0004, respectively, corresponding to Figs. 4.8.a-d. At first the shaft is running without an internal support until close to the corresponding resonance condition and then the internal support is activated, with stiffness $\tilde{s}_i = 10$ at $\tilde{x}_i = 0.7$. After switching, the shaft is left with the internal support active. It is not necessary to switch again to the original system because the shaft motion decreases and approaches zero. Similar to the acceleration cases, there is no large displacement any more due to resonance but there is still transient motion due to the switching. Table 4.2 lists the results.

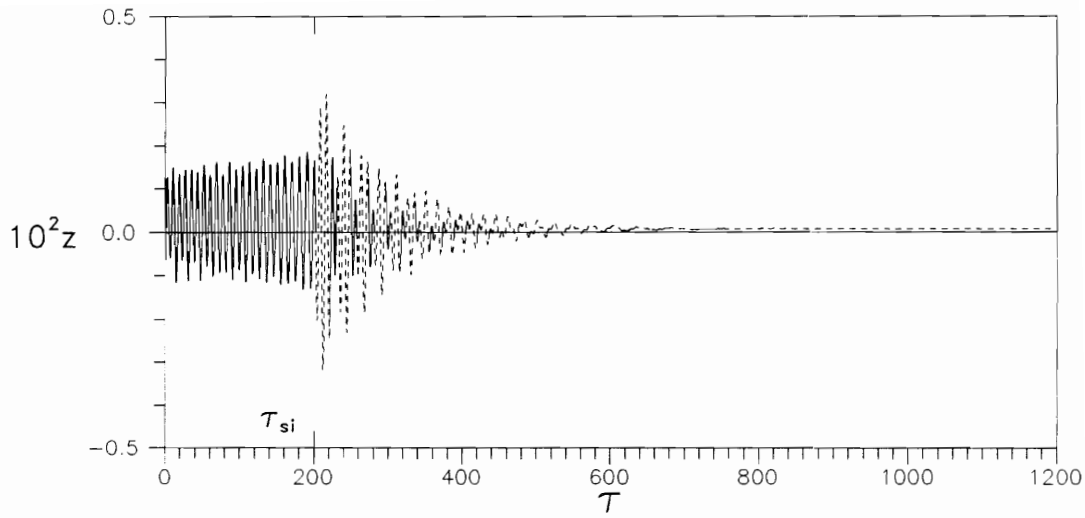

Fig. 4.10.a Switching Stiffness with Deceleration Rate λ=0.001

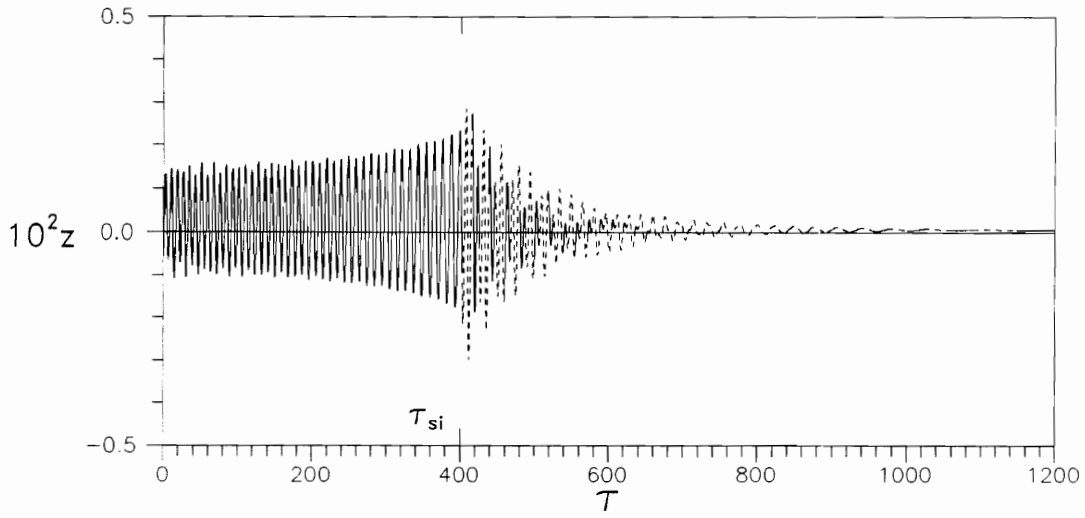

Fig. 4.10.b Switching Stiffness with Deceleration Rate λ=0.00067

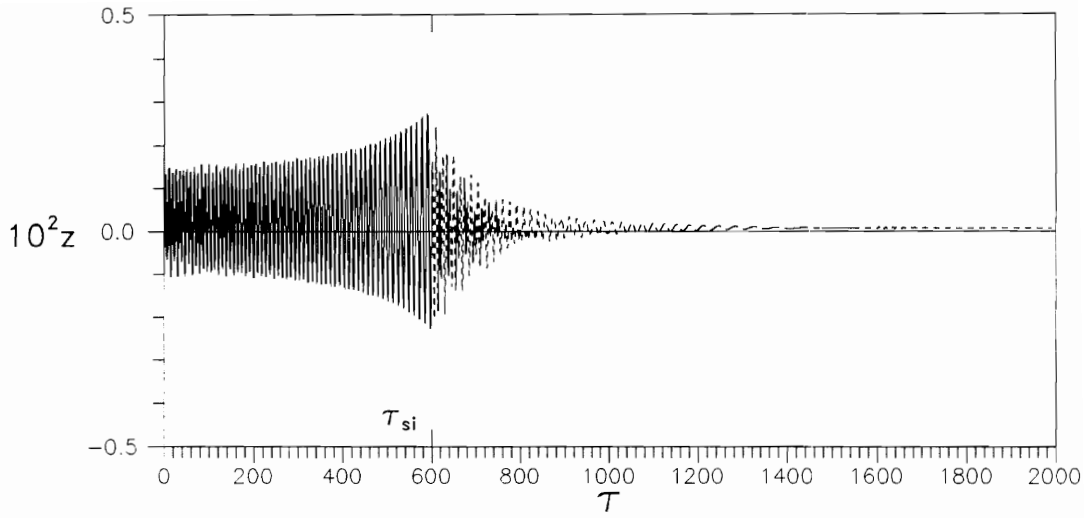

Fig. 4.10.c Switching Stiffness with Deceleration Rate λ=0.0005

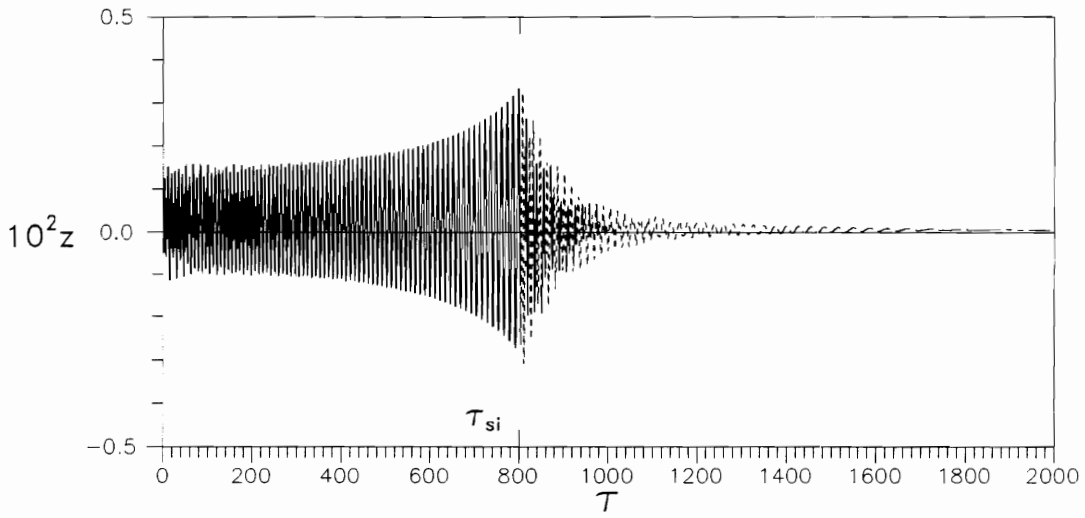

Fig. 4.10.d Switching Stiffness with Deceleration Rate λ=0.0004

Table 4.2 Maximum vertical displacement for the deceleration cases

Decel. λ	τ_{si}	z_{max} without internal support	z_{max} with switching	% reduction
0.001	200	0.0107	0.0032	70.2
0.00067	400	0.0124	0.0030	76.0
0.0005	600	0.0136	0.0027	79.8
0.0004	800	0.0145	0.0033	82.5

The reduction for these deceleration cases is larger than that for the acceleration cases, and is greater than 70%.

Two switching times

In Figs. 4.11.a-d, for the same acceleration cases as in Figs. 4.9.a-d, the switching occurs before and after the resonance frequency of the original system (without an internal support) is passed. Before the first switching time τ_{si1} the shaft is rotating without an internal support, then between τ_{si1} and the second switching time τ_{si2} the internal support is active. Finally, after τ_{si2} the internal support is inactive and the system returns to the original one. Table 4.3 gives the results, including the two switching times used.

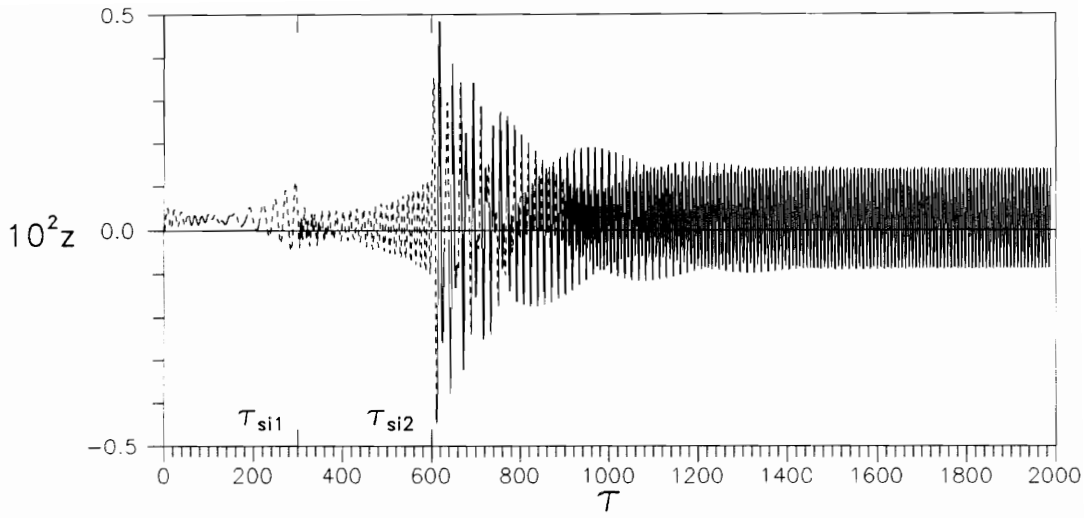

Fig. 4.11.a Two Switching Times with Acceleration Rate λ=0.001

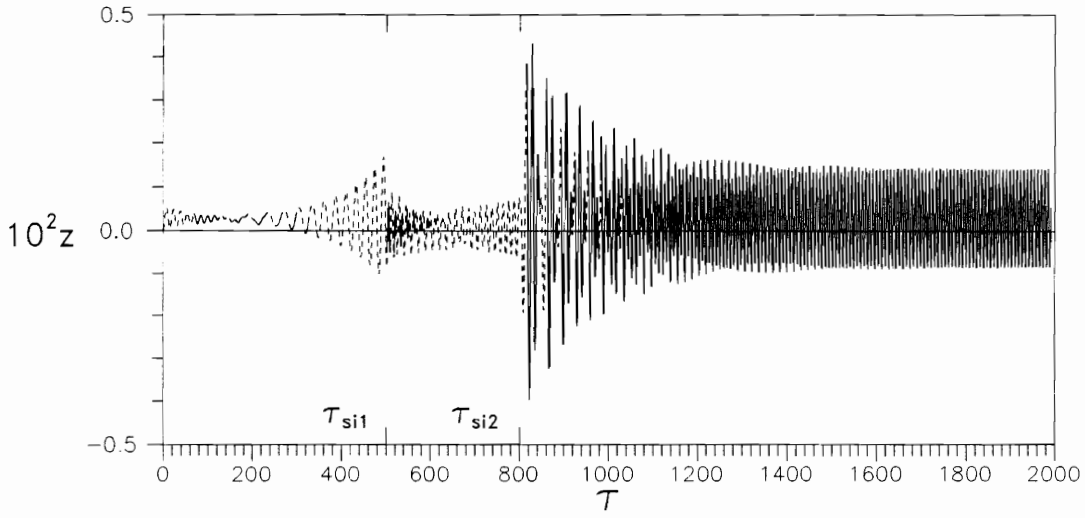

Fig. 4.11.b Two Switching Times with Acceleration Rate λ=0.00067

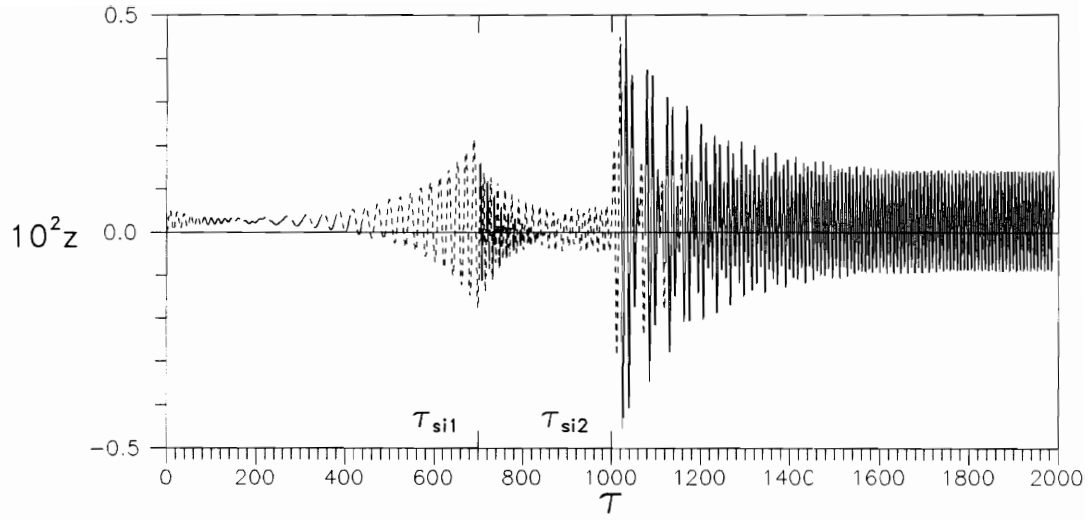

Fig. 4.11.c Two Switching Times with Acceleration Rate λ=0.0005

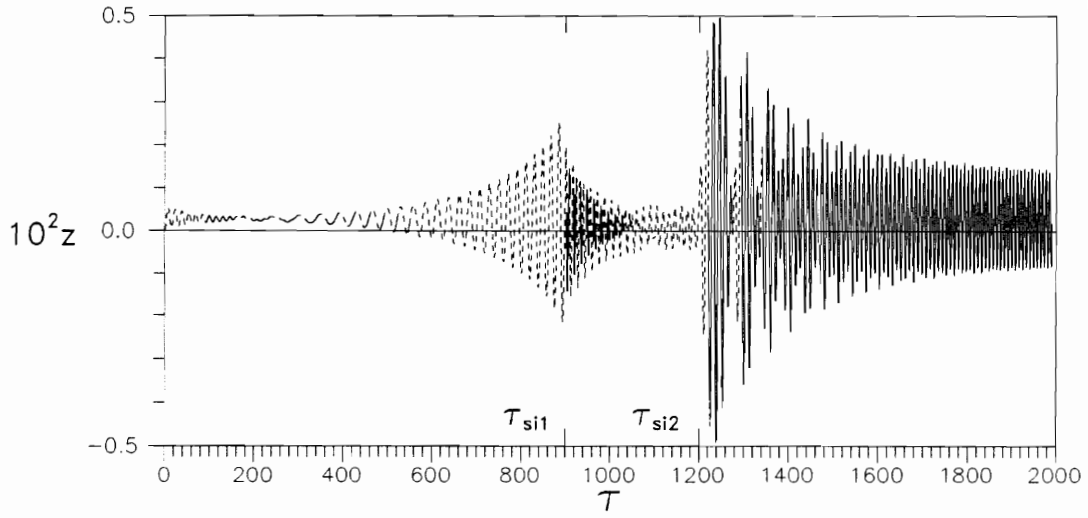

Fig. 4.11.d Two Switching Times with Acceleration Rate λ=0.0004

Table 4.3 Maximum vertical displacement with two switching times

Accel. λ	τ_{si1}	τ_{si2}	z_{max} without internal support	z_{max} with switching	% reduction
0.001	300	600	0.0119	0.0049	59.2
0.00067	500	800	0.0135	0.0043	68.0
0.0005	700	1000	0.0147	0.0051	65.1
0.0004	900	1200	0.0157	0.0056	64.3

At the first switching time there are transient motions but they are small compared to the transient motions at the second switching time. The maximum z-displacements occur during the transient motions following the second switching and are similar to those in Figs. 4.9.a-d with one switching, because the second switching times τ_{si2} are the same as τ_{si} in Fig. 4.9. The transient displacements depend on the initial conditions at the switching time, and if the initial conditions are similar, the transient motion will be similar also. In these two-switching-time cases, the duration when the internal support is active is less than that for the one-switching-time cases.

Two switching times for deceleration cases are shown in Figs. 4.12.a-d with different deceleration rates corresponding to Figs. 4.10.a-d. The switching is done similarly to the acceleration cases. Therefore, between the first switching time τ_{si1} and the second switching time τ_{si2} the internal support with stiffness $\tilde{s}_i = 10$ at $\tilde{x}_i = 0.7$ is active. Table 4.4 gives the results for deceleration with two switching times.

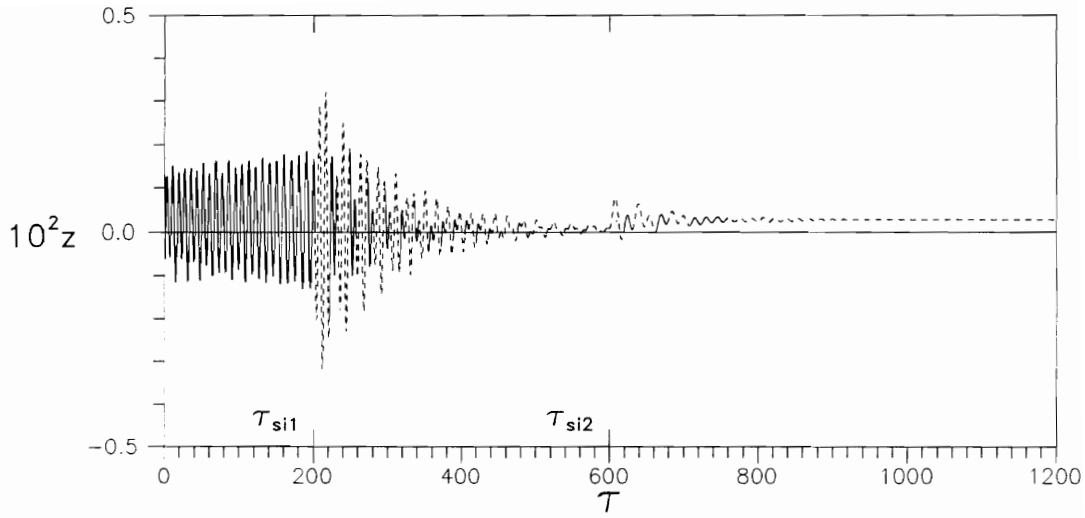

Fig. 4.12.a Two Switching Times with Deceleration Rate λ=0.001

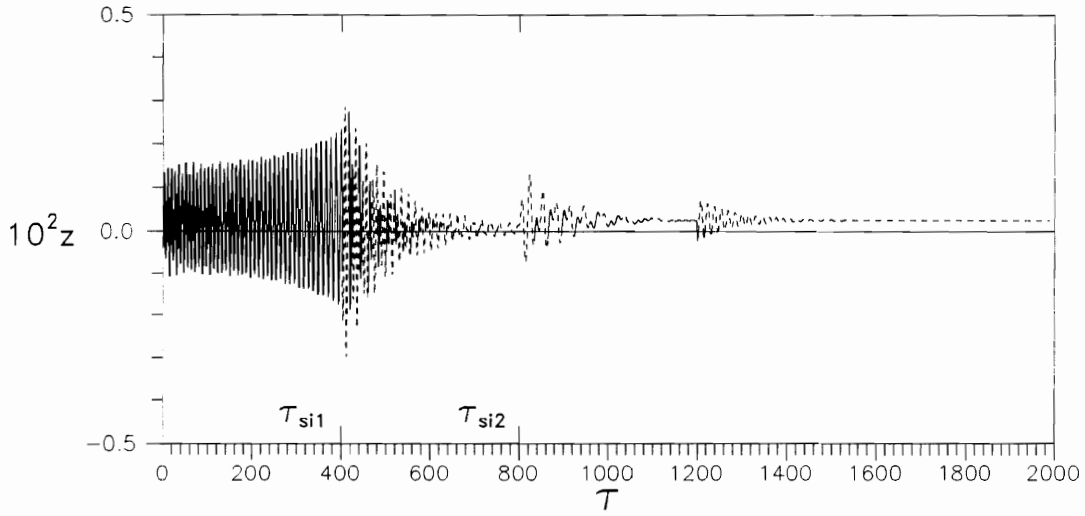

Fig. 4.12.b Two Switching Times with Deceleration Rate λ=0.00067

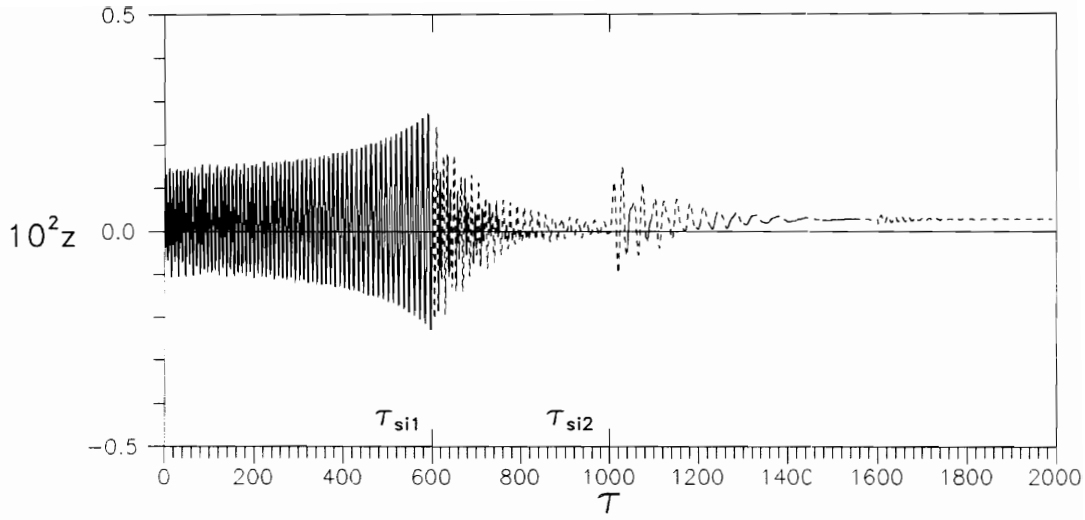

Fig. 4.12.c Two Switching Times with Deceleration Rate λ=0.0005

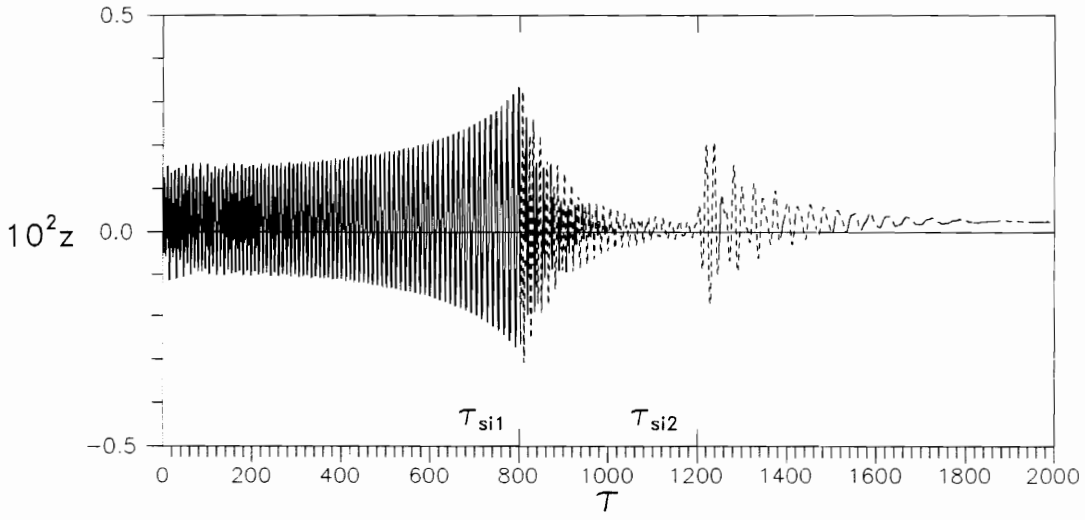

Fig. 4.12.d Two Switching Times with Deceleration Rate λ=0.0004

Table 4.4 Maximum vertical displacement with two switching times

Decel. λ	τ_{si1}	τ_{si2}	z_{max} without internal support	z_{max} with switching	% reduction
0.001	200	600	0.0107	0.0032	70.2
0.00067	400	800	0.0124	0.0030	76.0
0.0005	600	1000	0.0136	0.0027	79.8
0.0004	800	1200	0.0145	0.0033	82.5

The results are exactly the same as in Table 4.2 due to the same conditions where the maximum z-displacements occur, which is just after the first switching time. The second switching time does not give a larger transient displacement because the displacement is already small then. There is a third transient motion when the angular velocity becomes zero. It is seen clearly at $\tau = 1200$ in Fig. 4.12.b, and occurs at $\tau = 800$, 1600, and 2000 in Figs. 4.12.a, c, and d, respectively. For deceleration cases it is better to switch only one time before the resonance and let the system decrease with the internal support after that, to avoid transient motion when the support is deactivated.

4.3. Nonideal Motor

4.3.1. Introduction

The physical model of the cracked rotating shaft is the same as in the previous section with an ideal motor (Fig. 4.1). However, because the motor is nonideal, the energy supply is limited and there is interaction between the system and the motor. The

angular velocity $\dot{\theta}(\tau)$ is an unknown variable and is determined together with the displacements $\tilde{v}_n(\tau)$, $\tilde{w}_n(\tau)$. An internal support is added to suppress the vibration near resonance, the same as for the shaft with an ideal motor.

4.3.2. Analysis

Basically, the equations of motion and boundaries for the displacements $\tilde{v}_n(\tau)$, $\tilde{w}_n(\tau)$ are the same as the ones with an ideal motor. But, for a nonideal motor, the angular velocity $\dot{\theta}(\tau)$ is an unknown also. The derivation of the torque equation of motion is similar to that in chapter 3 with the corresponding physical model in Fig. 4.1.

The complete nondimensionalized equations of motion are as follows:

$$\ddot{\tilde{v}}_n + \tilde{m}\sin n\pi\tilde{c}\sum_{k=1}^{N}\left(\ddot{\tilde{v}}_k - \ddot{\theta}\tilde{w}_k\right)\sin k\pi\tilde{c} - \ddot{\theta}\tilde{w}_n - \tilde{m}\tilde{e}_d\ddot{\theta}\sin n\pi\tilde{c}\sin\delta_d =$$

$$-n^4\tilde{v}_n + 2\dot{\theta}\dot{\tilde{w}}_n + \dot{\theta}^2\tilde{v}_n + \tilde{m}\sin n\pi\tilde{c}\sum_{k=1}^{N}\left(2\dot{\theta}\dot{\tilde{w}}_k + \dot{\theta}^2\tilde{v}_k\right)\sin k\pi\tilde{c}$$

$$-\tilde{d}_e\left(\ddot{\tilde{v}}_n - \dot{\theta}\tilde{w}_n\right) - \tilde{d}_i\ddot{\tilde{v}}_n n^4 + 2\Lambda\tilde{c}_{44}n^2\sin n\pi\tilde{b}\sum_{k=1}^{N}k^2\left(\tilde{v}_k + \tilde{d}_i\dot{\tilde{v}}_k\right)\sin k\pi\tilde{b}$$

$$+\left\{\frac{1}{n}\left[1-(-1)^n\right] + \tilde{m}\frac{\pi}{2}\sin n\pi\tilde{c}\right\}\tilde{\mu}\sin\theta + \tilde{m}\tilde{e}_d\dot{\theta}^2\sin n\pi\tilde{c}\cos\delta_d$$

$$-\frac{2}{\pi}\tilde{s}_i\sum_{k=1}^{N}\tilde{v}_k\sin k\pi\tilde{x}_i\sin n\pi\tilde{x}_i, \qquad (4.9.a)$$

$$\ddot{\tilde{w}}_n + \tilde{m}\sin n\pi\tilde{c}\sum_{k=1}^{N}\left(\ddot{\tilde{w}}_k + \ddot{\theta}\tilde{v}_k\right)\sin k\pi\tilde{c} + \ddot{\theta}\tilde{v}_n + \tilde{m}\tilde{e}_d\ddot{\theta}\sin n\pi\tilde{c}\cos\delta_d =$$

$$-n^4\tilde{w}_n - 2\dot{\theta}\dot{\tilde{v}}_n + \dot{\theta}^2\tilde{w}_n - \tilde{m}\sin n\pi\tilde{c}\sum_{k=1}^{N}\left(2\dot{\theta}\dot{\tilde{v}}_k - \dot{\theta}^2\tilde{w}_k\right)\sin k\pi\tilde{c}$$

$$-\tilde{d}_e\left(\ddot{\tilde{w}}_n + \dot{\theta}\tilde{v}_n\right) - \tilde{d}_i\dot{\tilde{w}}_n n^4 + 2\Lambda\tilde{c}_{55}n^2\sin n\pi\tilde{b}\sum_{k=1}^{N}k^2\left(\tilde{w}_k + \tilde{d}_i\dot{\tilde{w}}_k\right)\sin k\pi\tilde{b}$$

$$+\left\{\frac{1}{n}\left[1-(-1)^n\right] + \tilde{m}\frac{\pi}{2}\sin n\pi\tilde{c}\right\}\tilde{\mu}\cos\theta + \tilde{m}\tilde{e}_d\dot{\theta}^2\sin n\pi\tilde{c}\sin\delta_d$$

$$-\frac{2}{\pi}\tilde{s}_i\sum_{k=1}^{N}\tilde{w}_k\sin k\pi\tilde{x}_i\sin n\pi\tilde{x}_i, \qquad (4.9.b)$$

$$\left(\frac{1}{2}\tilde{m}\tilde{r}_d{}^2 + \tilde{m}\tilde{e}_d{}^2\right)\ddot{\theta} - \tilde{m}\tilde{e}_d\sin\delta_d\left[\sum_{k=1}^{N}\left(\ddot{\tilde{v}}_k - \ddot{\theta}\tilde{w}_k\right)\sin k\pi\tilde{c}\right]$$

$$+\tilde{m}\tilde{e}_d\cos\delta_d\left[\sum_{k=1}^{N}\left(\ddot{\tilde{w}}_k - \ddot{\theta}\tilde{v}_k\right)\sin k\pi\tilde{c}\right] =$$

$$-\tilde{m}\tilde{e}_d\sin\delta_d\sum_{k=1}^{N}\left(\dot{\theta}^2\tilde{v}_k + 2\dot{\theta}\dot{\tilde{w}}_k\right)\sin k\pi\tilde{c}$$

$$+\tilde{m}\tilde{e}_d\cos\delta_d\sum_{k=1}^{N}\left(\dot{\theta}^2\tilde{w}_k - 2\dot{\theta}\dot{\tilde{v}}_k\right)\sin k\pi\tilde{c} + \frac{\pi}{2}\tilde{m}\tilde{e}_d\tilde{\mu}\cos\left(\theta+\delta_d\right)$$

$$-\tilde{d}_e\tilde{r}_s{}^2\dot{\theta} + \upsilon_0 - \upsilon_1\dot{\theta} \qquad (4.9.c)$$

Now there are 2N+1 second-order equations of motion.

4.3.3. Stationary case

During the stationary operation the angular velocity $\dot{\theta}(\tau)$ and the displacements $\tilde{v}_n(\tau), \tilde{w}_n(\tau)$ are assumed to be constant by using eqs. (3.9) and (3.10). After solving eqs. 4.9.a-b with constant Ω, v_0, and w_0, the motor characteristic $\kappa = \upsilon_0 - \upsilon_1\dot{\theta}$ is then obtained from eq. 4.9.c. The crack and the gravitational forces are neglected.

Figures 4.13.a-d show the relation between the stationary amplitude R_0 at the disk location $\tilde{c} = 0.5$ and the constant angular velocity Ω for the shaft without internal support ($\tilde{s}_i = 0$) and for the shaft with different internal support stiffnesses ($\tilde{s}_i = 1, 5, 10, 25$) at $\tilde{x}_i = 0.7$. For the same cases as in Figs. 4.13.a-d, Figs. 4.13.e-h show the relation between the motor characteristic κ and the constant angular velocity Ω. They are obtained by putting all terms in eq. 4.9.c except $\upsilon_0 - \upsilon_1\dot{\theta}$ or the left side and plotting this left side when $\dot{\theta} = \Omega = \text{constant}$. The increasing of the internal support stiffness causes the resonance frequencies for the shaft with and without internal support to move farther apart. The effect of switching is better if the two resonance conditions are not too close together. Also, it is not necessary to have a stiff internal support. Figures 4.13.e-h are useful to predict the driving torque of the motor for the nonstationary case. If one chooses the stationary angular velocity Ω_{st}, the corresponding motor characteristic $\kappa(\Omega_{st})$, and the initial torque υ_0, the gradient motor torque υ_1 is then determined. Using υ_0 and υ_1, the driving torque κ for the nonstationary case is obtained from the following equation:

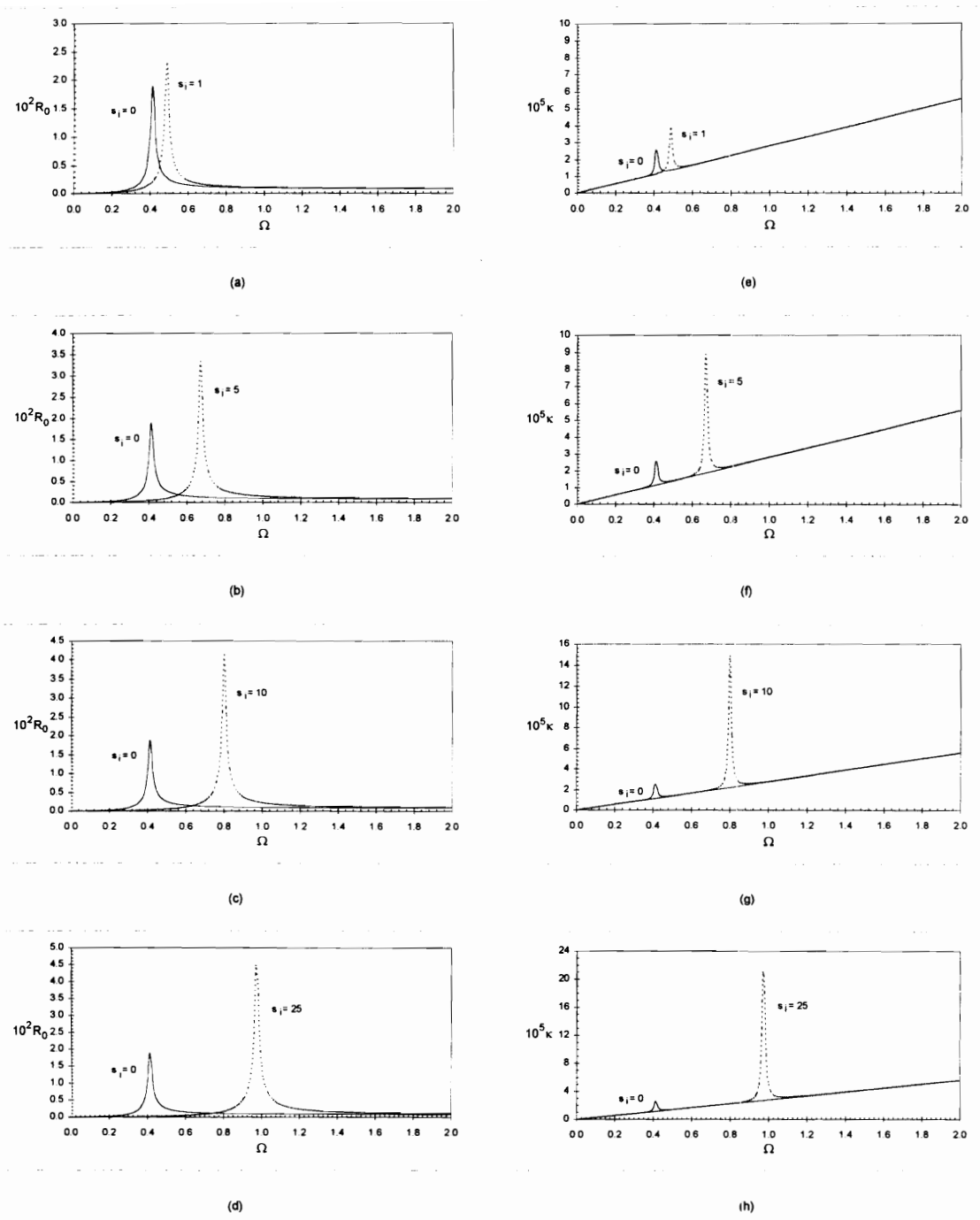

Fig. 4.13 Stationary Results for Nonideal Motor with and without Internal Support

$$\kappa = \upsilon_0 - \upsilon_1 \dot{\theta} \tag{4.10}$$

4.3.4. Influence of switching type

The stiffness can be changed suddenly or gradually. Adding the internal support directly causes a sudden change in the system stiffness, whereas adding the internal support gradually causes a gradual change in the system stiffness. For a gradual change, the length of time to reach the new stiffness can be selected.

The stiffness of the internal support can be varied. Based on the stationary condition in Fig. 4.13, the additional support stiffness $\tilde{s}_i$ is chosen to be 10 for the standard case. The system's fundamental critical speed is not too close to the critical speed of the original system. The critical speed of the shaft without an internal support is 0.41, and the critical speed of the shaft with an internal support at $\tilde{x}_i = 0.7$ with stiffness $\tilde{s}_i = 10$ is 0.8.

For run-up cases, the driving torque is determined from the stationary condition. Figure 4.14 shows the stationary condition from Fig. 4.13.c and Fig. 4.13.g with the linear motor characteristic. The initial torque υ_0 is 0.00006 and the stationary angular velocity Ω_{st} after run-up is 0.6. Based on this driving torque and the standard data, the nonstationary results for the shaft with and without internal support are given in Figs. 4.15 and 4.16. In Fig. 4.15, the shaft passes the critical speed at $\Omega = 0.41$ and the vertical displacement becomes large. The Sommerfeld effect occurs, as the shaft remains stuck near the resonance condition for a while. Then, the angular velocity increases and

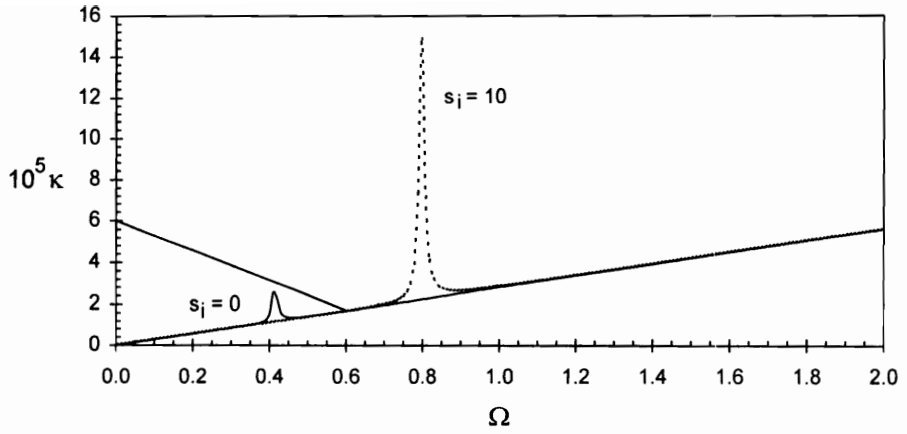

Fig. 4.14 Driving Torque for Run-up Case

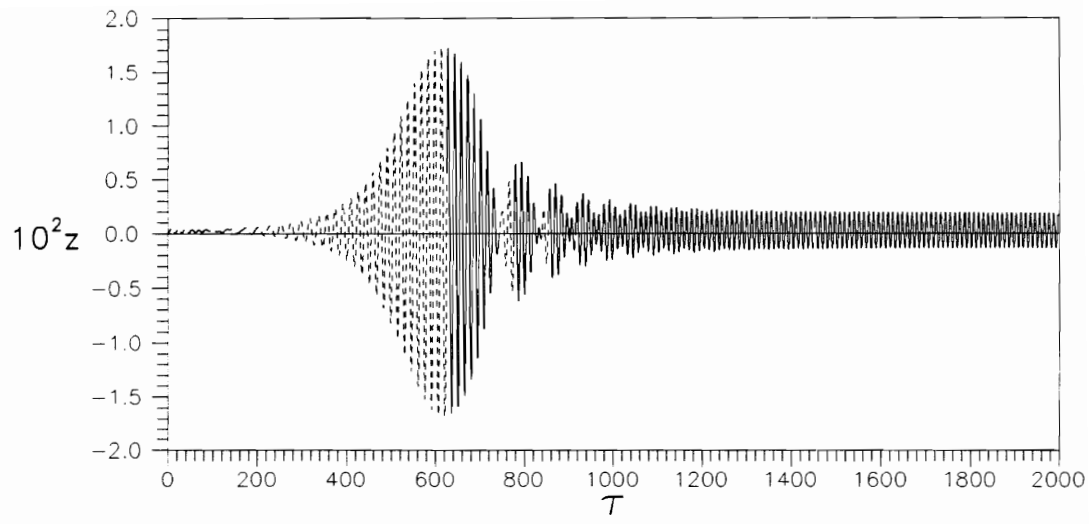

(a)

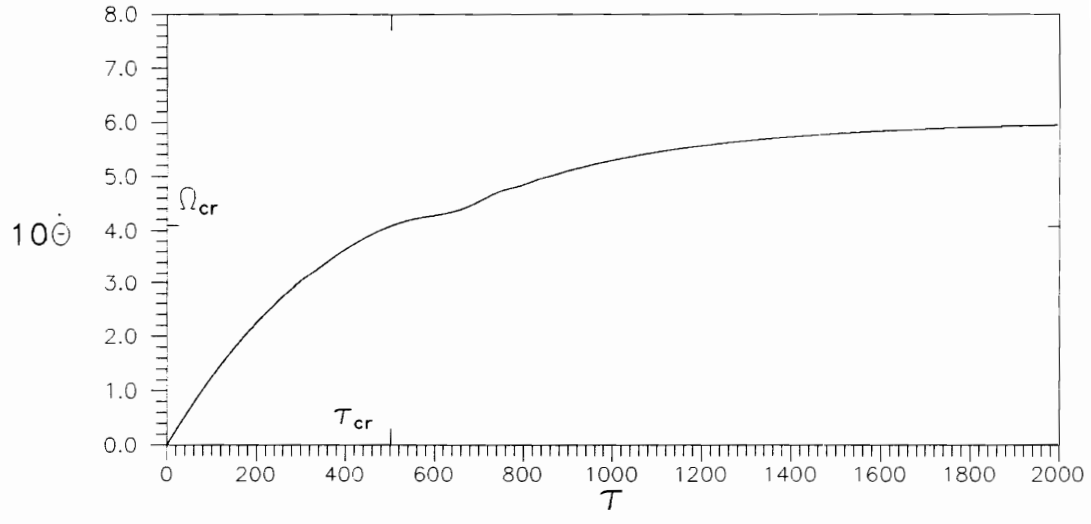

(b)

Fig. 4.15 Time Histories of Shaft without Internal Support

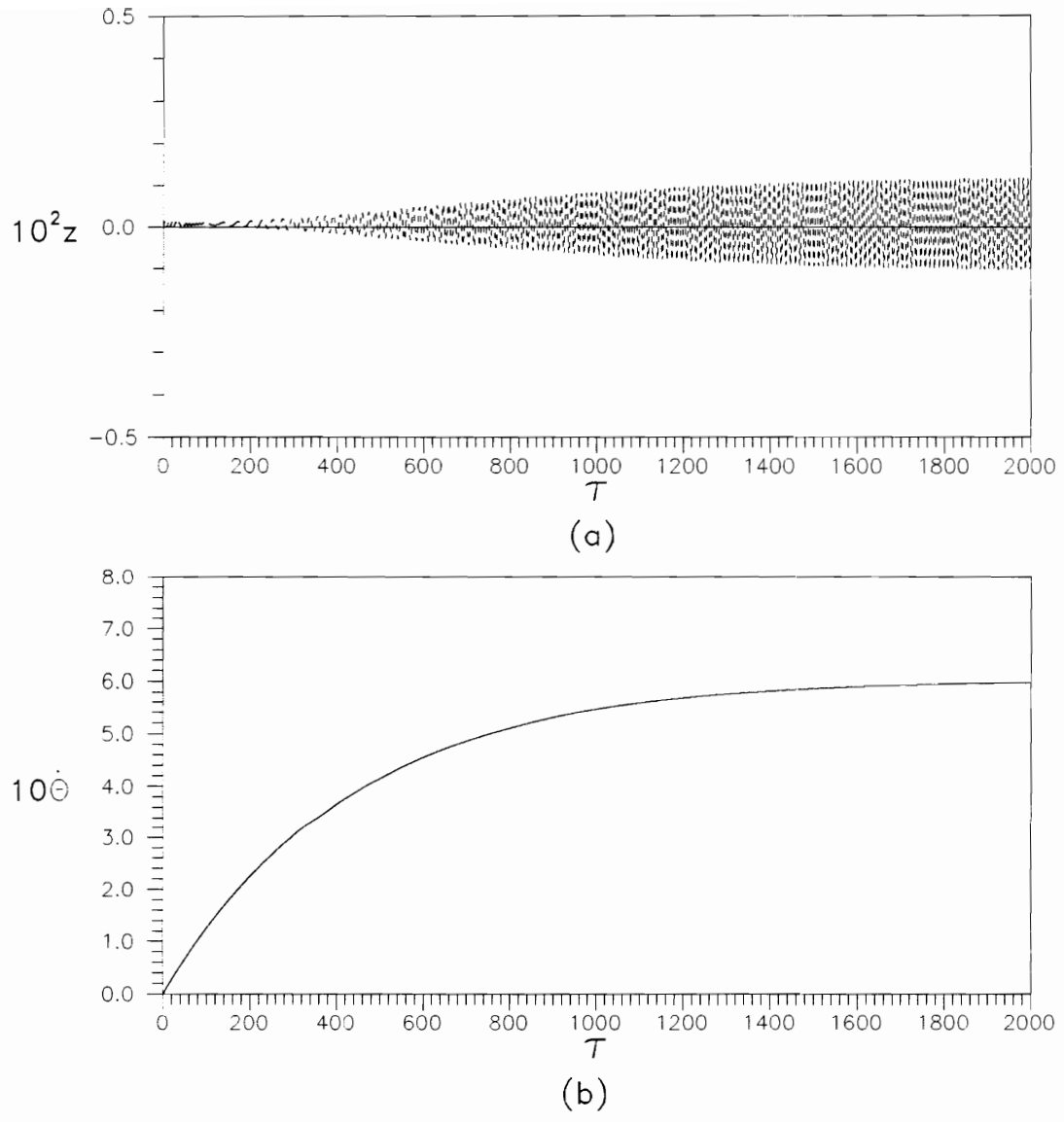

Fig. 4.16 Time Histories of Shaft with Internal Support, s_i=10

approaches the stationary angular velocity $\Omega_{st} = 0.6$. On the other hand, for the shaft with internal support stiffness $\tilde{s}_i = 10$ (Fig. 4.16), the shaft does not pass the critical speed because the driving torque is limited to the stationary angular velocity $\Omega_{st} = 0.6$, whereas the critical speed is $\Omega_{cr} = 0.8$. In this case, no large displacement occurs.

First, a sudden switching of stiffness will be examined. The shaft starts rotating with the additional internal support ($\tilde{s}_i = 10$) until it passes the critical speed, and then the internal support is suddenly deactivated. In Fig. 4.17, the internal support is deactivated at the switching time $\tau_{si} = 700$. This case corresponds to Figs. 4.15 and 4.16 based on the standard data. The comparison of the maximum z-displacement at the disk location in Fig. 4.17 with that in Fig. 4.15 (the shaft without internal support) shows a 66.1% reduction. The maximum z-displacement in the switching case (Fig. 4.17) is caused by the transient condition due to the stiffness switching, and is not due to passing the critical speed. In Fig. 4.17 there is no Sommerfeld effect any more. After passing the transient motion, the shaft approaches the stationary condition.

Two cases of gradually removing the internal support are shown in Figs. 4.18 and 4.19 for the same system as in Fig. 4.17. In Fig. 4.18 the switching starts at $\tau_{si} = 700$ with $\tilde{s}_i = 10$, and the internal support stiffness is reduced linearly until $\tilde{s}_i = 0$ at $\tau = 800$. In Fig. 4.19, the switching starts at $\tau_{si} = 700$ and the stiffness decreases linearly until it finally reaches $\tilde{s}_i = 0$ at $\tau = 900$. In Fig. 4.18 the reduction in maximum displacement (relative to the shaft without internal support) is 52.9% compared to a

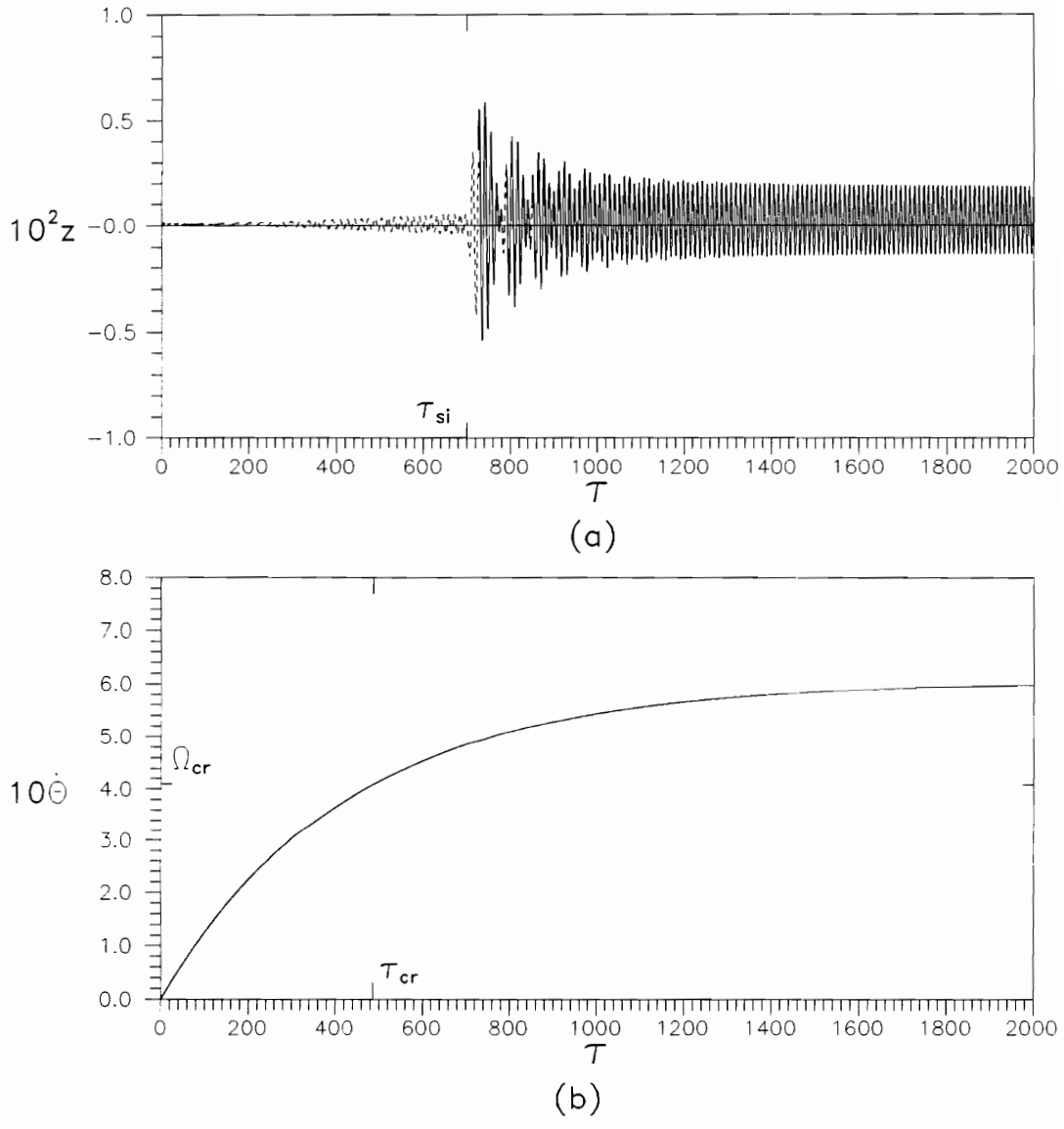

Fig. 4.17 Sudden Stiffness Switching

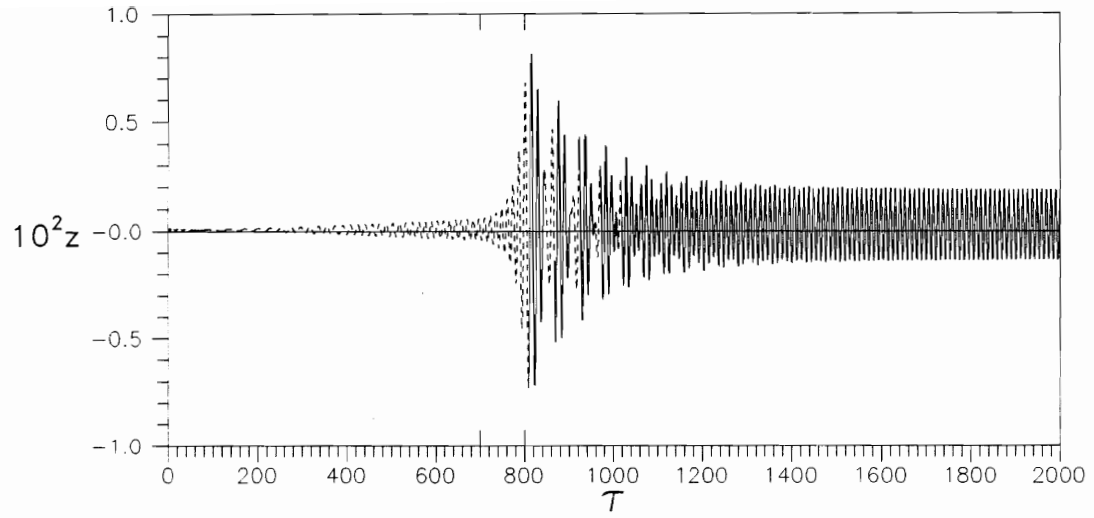

Fig. 4.18 Gradual Stiffness Switching from τ=700 until τ=800

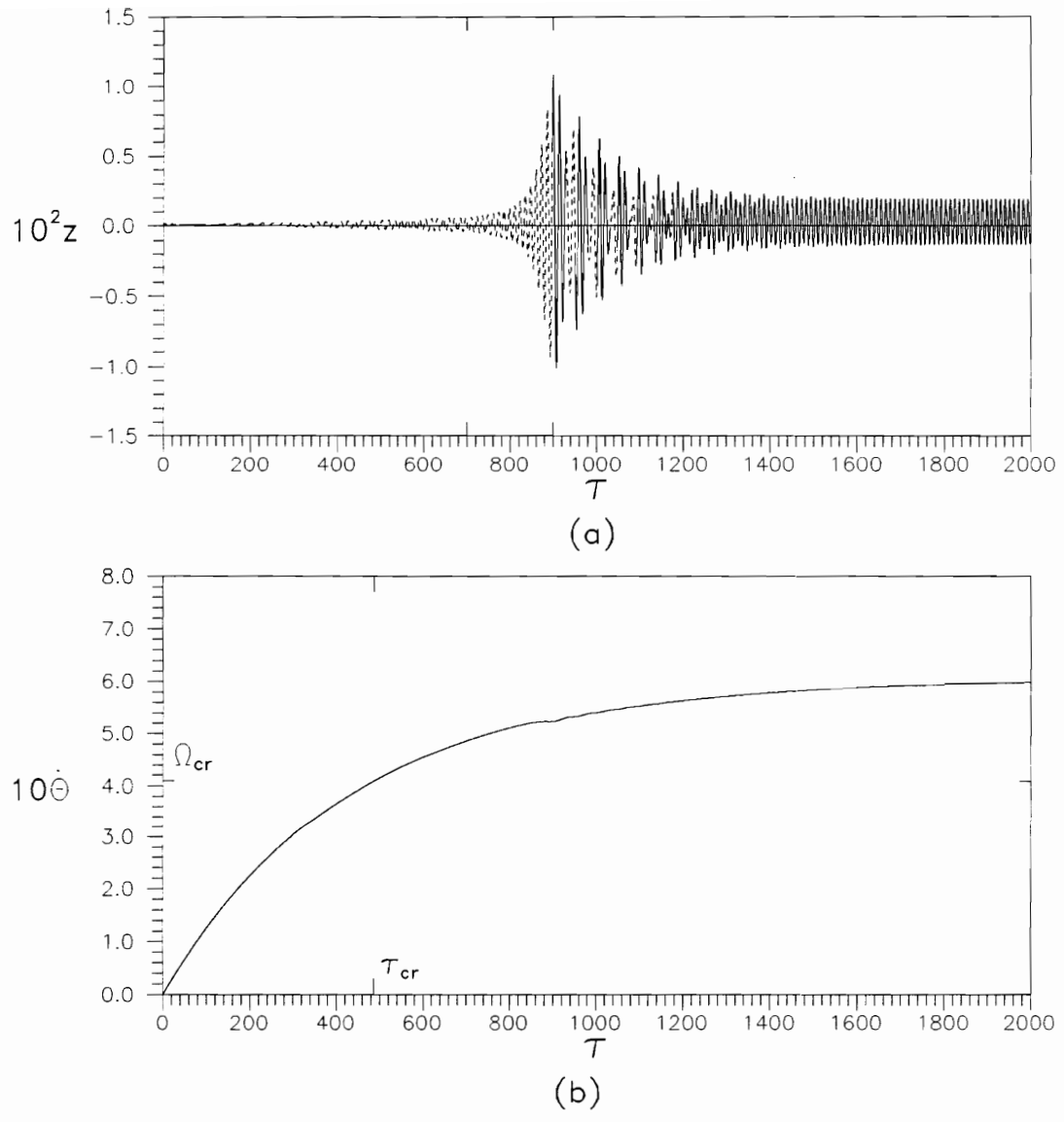

Fig. 4.19 Gradual Stiffness Switching from τ=700 until τ=900

37.4% reduction in Fig. 4.19. Both cases have less reduction than the case of a sudden change in stiffness (Fig. 4.17). This occurs because for gradually changing stiffness the shaft displacement has time to build up, and if the time to change is longer, the shaft can reach a larger displacement. The angular velocity of the shaft still increases while the stiffness changes, which causes more force to be applied to the shaft until the internal support stiffness reaches zero. Therefore, if the time to change is longer, the displacement increases, and the initial condition for the transition motion becomes large also. In conclusion, for the run-up case, it is better if the internal support is removed suddenly.

In Figure 4.17 in the case of a sudden change of stiffness, the internal support is activated for a long time, i.e., the critical speed of the original system has been passed. This may not be desirable. Now assume that the support is active only for a short time, by letting the shaft without internal support rotate until the speed is near the critical speed, then adding the internal support till the critical speed of the original system is passed, and then removing the internal support. The result is shown in Fig. 4.20 with the first switching time at $\tau_{si1} = 400$ and the second one at $\tau_{si2} = 700$ under the same driving torque and standard data as in Fig. 4.17. The displacement reduction is 66.2%, which is similar to that for the case of only one switching time at $\tau_{si} = 700$ since the second switching time is exactly the same. Therefore the initial conditions of the transient motions are similar. The second switching in Fig. 4.20 gives a larger transient motion than the first switching, because at the first switching the stiffness changes from a smaller one to a bigger one, but for the second switching it is the opposite. After the

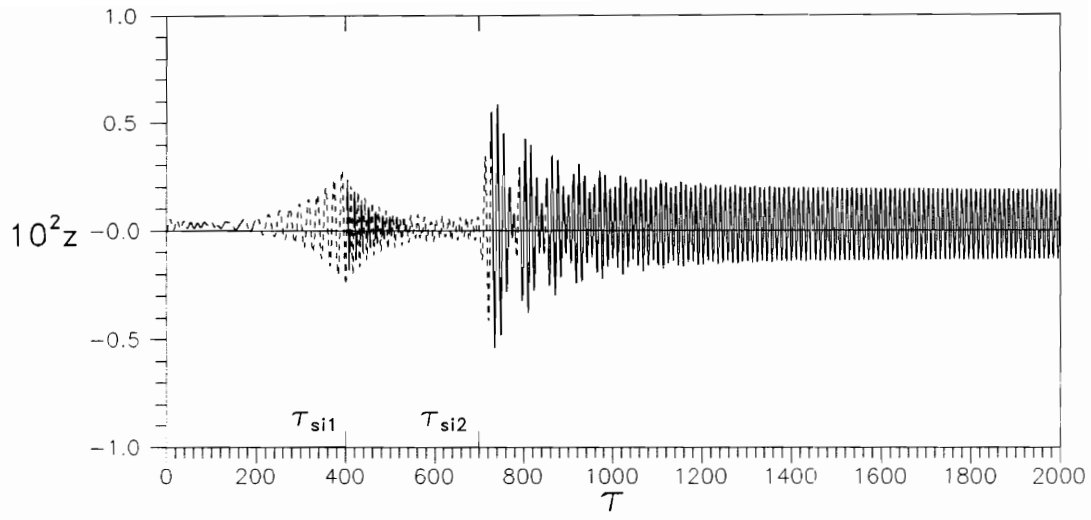

(a)

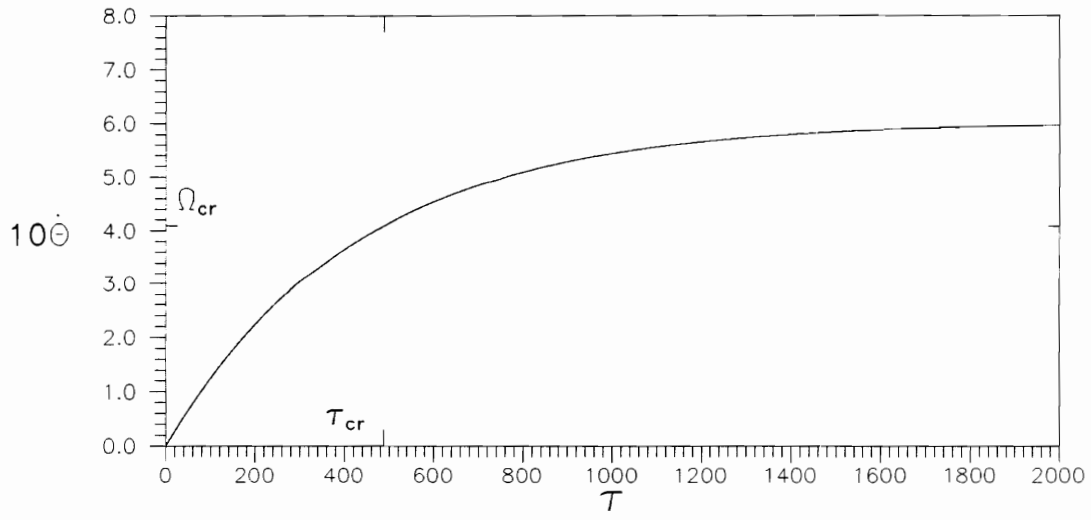

(b)

Fig. 4.20 Two Switching Times During Run-up

second transient motion, the shaft approaches the stationary condition similar to the previous cases.

The influence of the times of stiffness switching is investigated for cases similar to Fig. 4.20, with initial driving torque $\upsilon_0 = 0.00006$, stationary angular velocity $\Omega_{st} = 0.6$, and the standard data. The stiffness of the additional internal support is $\tilde{s}_i = 10$. Table 4.5 gives the difference in the displacement reduction due to the different switching times.

Table 4.5 Influence of switching times on displacement reduction

Case no.	τ_{si1}	τ_{si2}	% Reduction
1	400	700	66.2
2	400	800	69.7
3	400	900	71.7
4	400	1000	76.8
5	400	1100	71.1
6	300	700	66.2
7	300	800	69.4

Cases no. 2-7 have similar time histories of the z-displacement and the angular velocity as case no.1 (Fig. 4.20). The displacement reduction for all cases is greater than 65%. Case no. 1 and case no. 6 have the same reduction because they have the same second switching time. The effect of switching times on the percentage reduction does not seem to have a regular pattern.

For coast-down, the case with initial conditions from the stationary condition of the run-up case (Fig. 4.15) and the standard data, but without a driving torque, is

investigated. Results are shown in Fig. 4.21 with no internal support. The displacement decreases quickly after the maximum value is reached, and the angular velocity slowly approaches zero. The Sommerfeld effect is hardly seen.

The stiffness switching for coast-down is shown in Fig. 4.22 under the same conditions as for Fig. 4.21. The shaft is rotating without an internal support until the switching time $\tau_{si} = 300$; then, the internal support with stiffness $\tilde{s}_i = 10$ at $\tilde{x}_i = 0.7$ is activated and remains active until the shaft stops rotating. As shown in Fig. 4.22, the angular velocity at the time of switching is about 0.5, above the critical speed $\Omega_{cr} = 0.41$. The displacement reduction is 78.2%. The transient motion does not have a large amplitude in this case; the motion has almost the same maximum displacement as the displacement just before the switching time, and decreases very fast toward zero.

The influence of a gradual linear switching of the stiffness during coast down is investigated in Figs. 4.23 and 4.24. These cases are similar to Fig. 4.22 with different durations of the stiffness switching. In Fig. 4.23 the duration is from $\tau = 300$ until $\tau = 400$, and in Fig. 4.24 from $\tau = 300$ until $\tau = 500$. Similar to the run-up cases with gradual switching, the longer time for switching leads to a larger transient motion. The displacement reductions are 61.6% and 51.8 %, respectively.

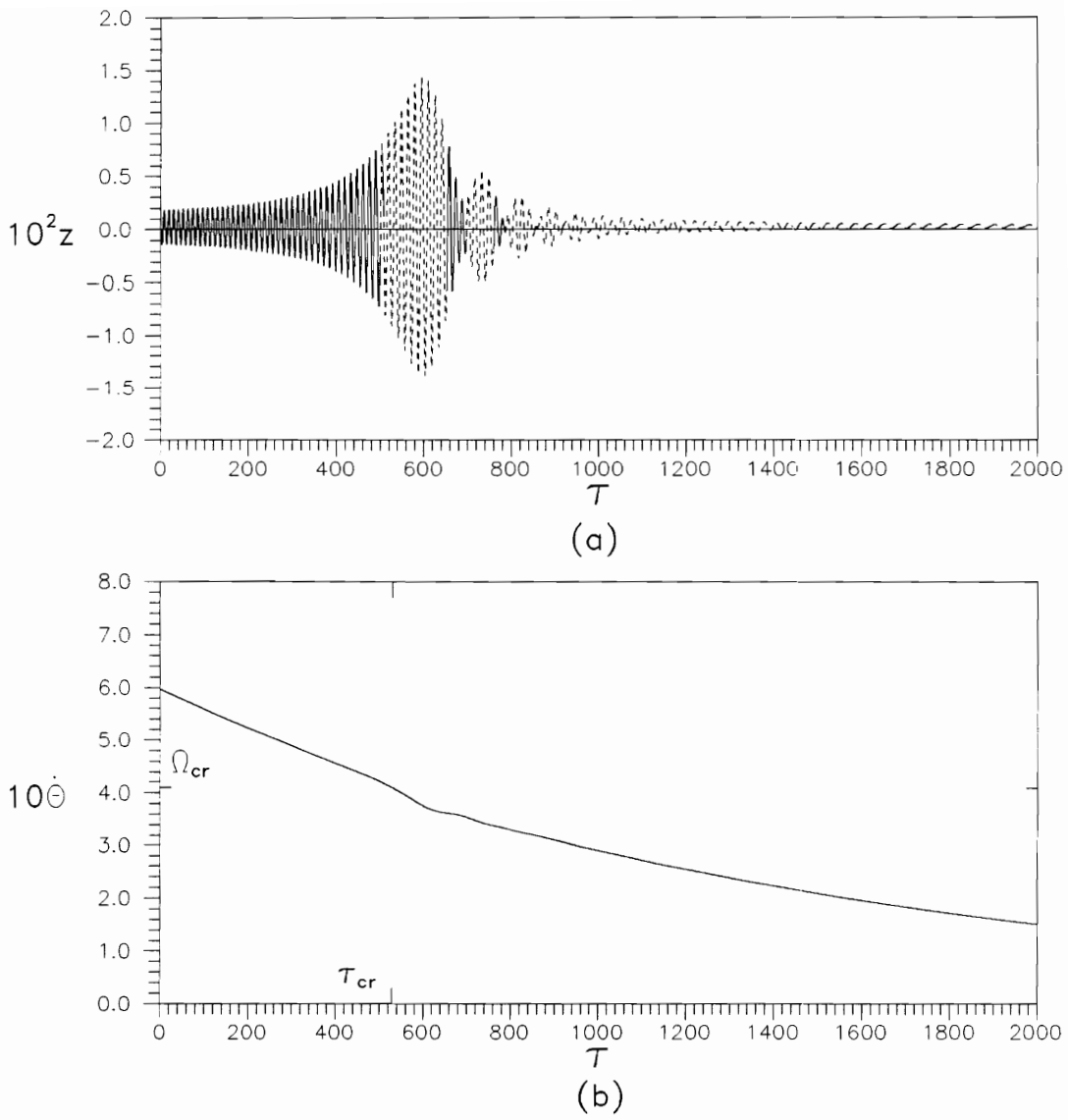

Fig. 4.21 Time Histories of Shaft without Internal Support During Coast-down

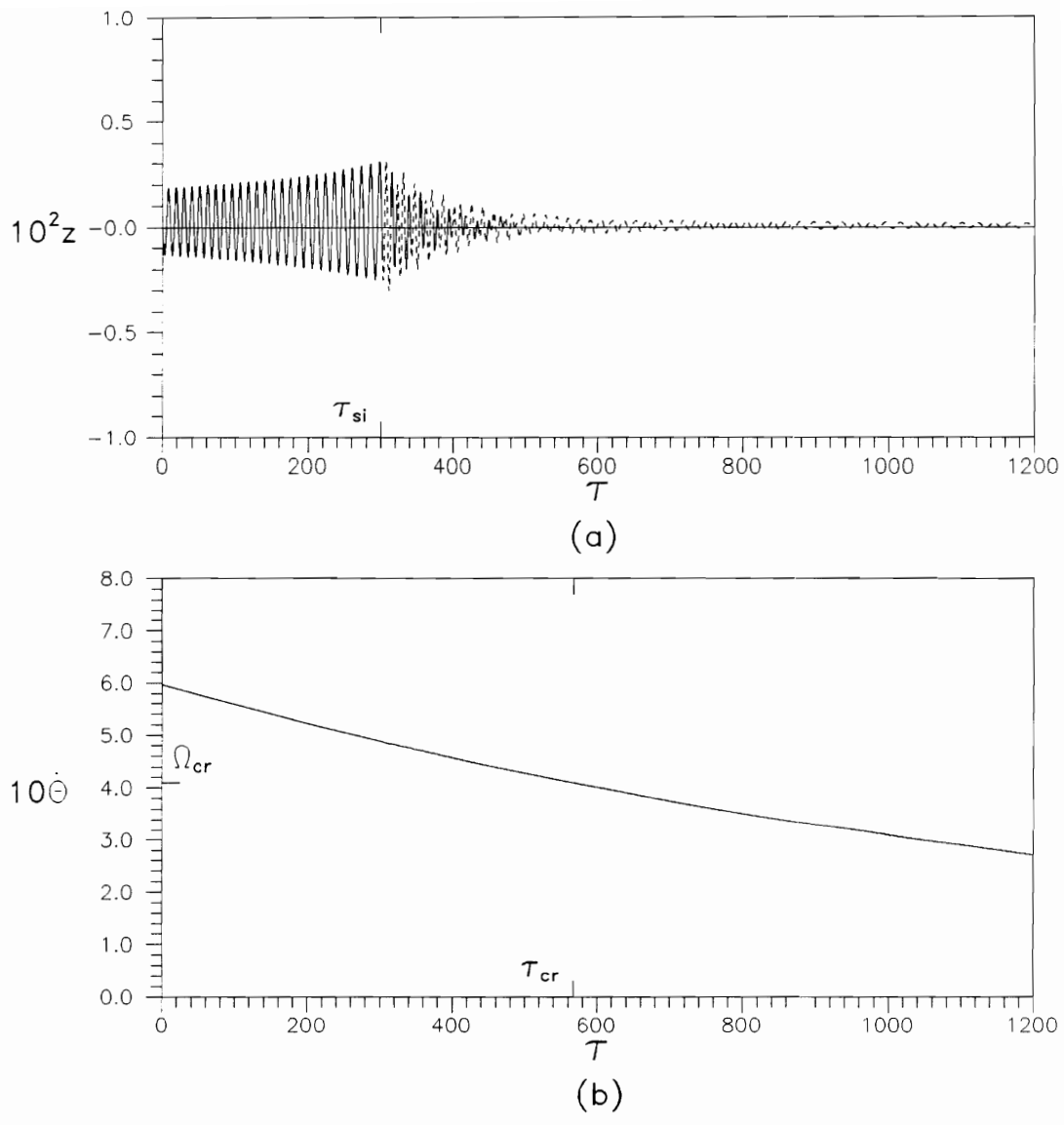

Fig. 4.22 Switching Stiffness During Coast-down

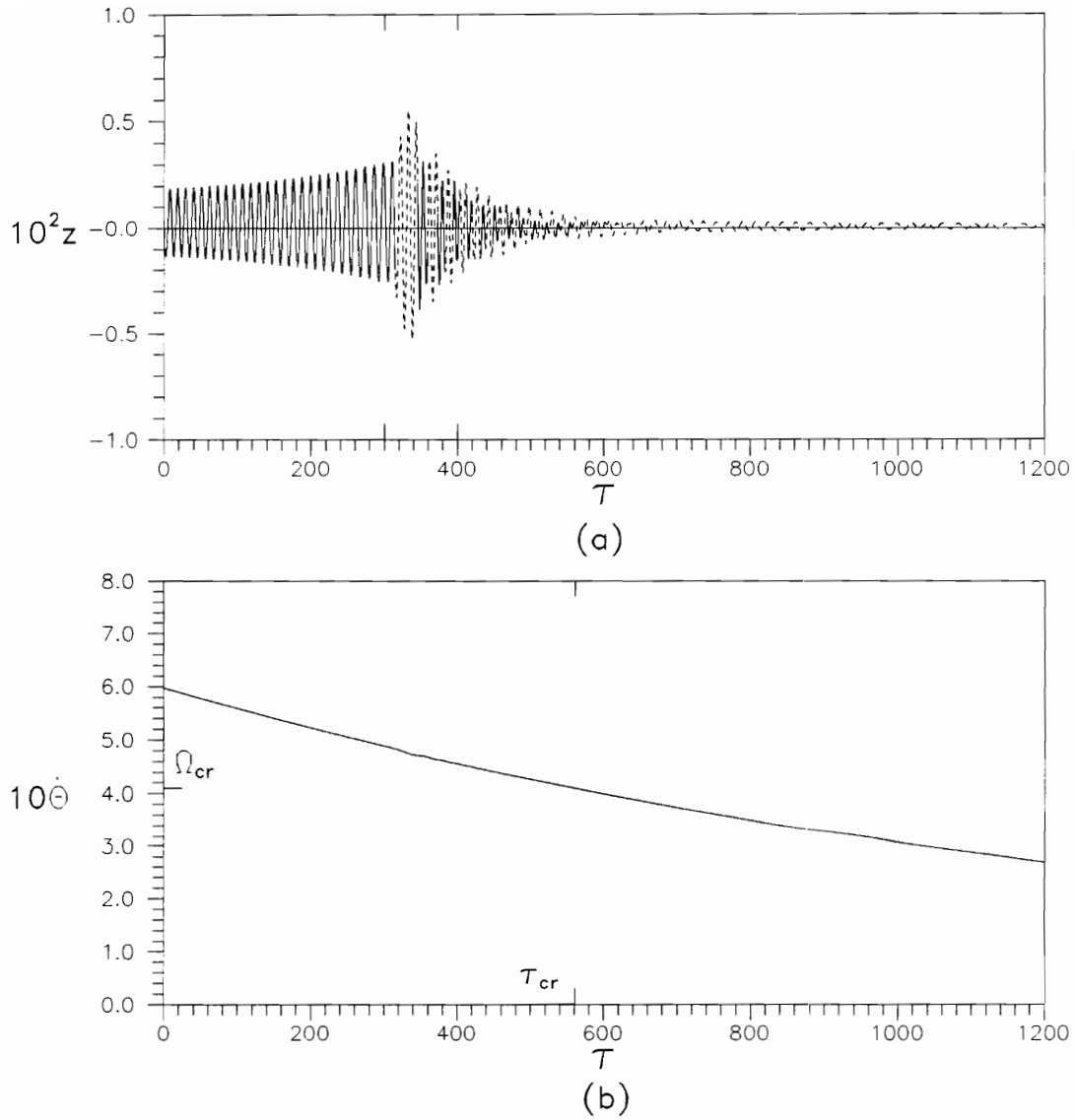

Fig. 4.23 Gradual Stiffness Switching During Coast-down, from τ=300 until τ=400

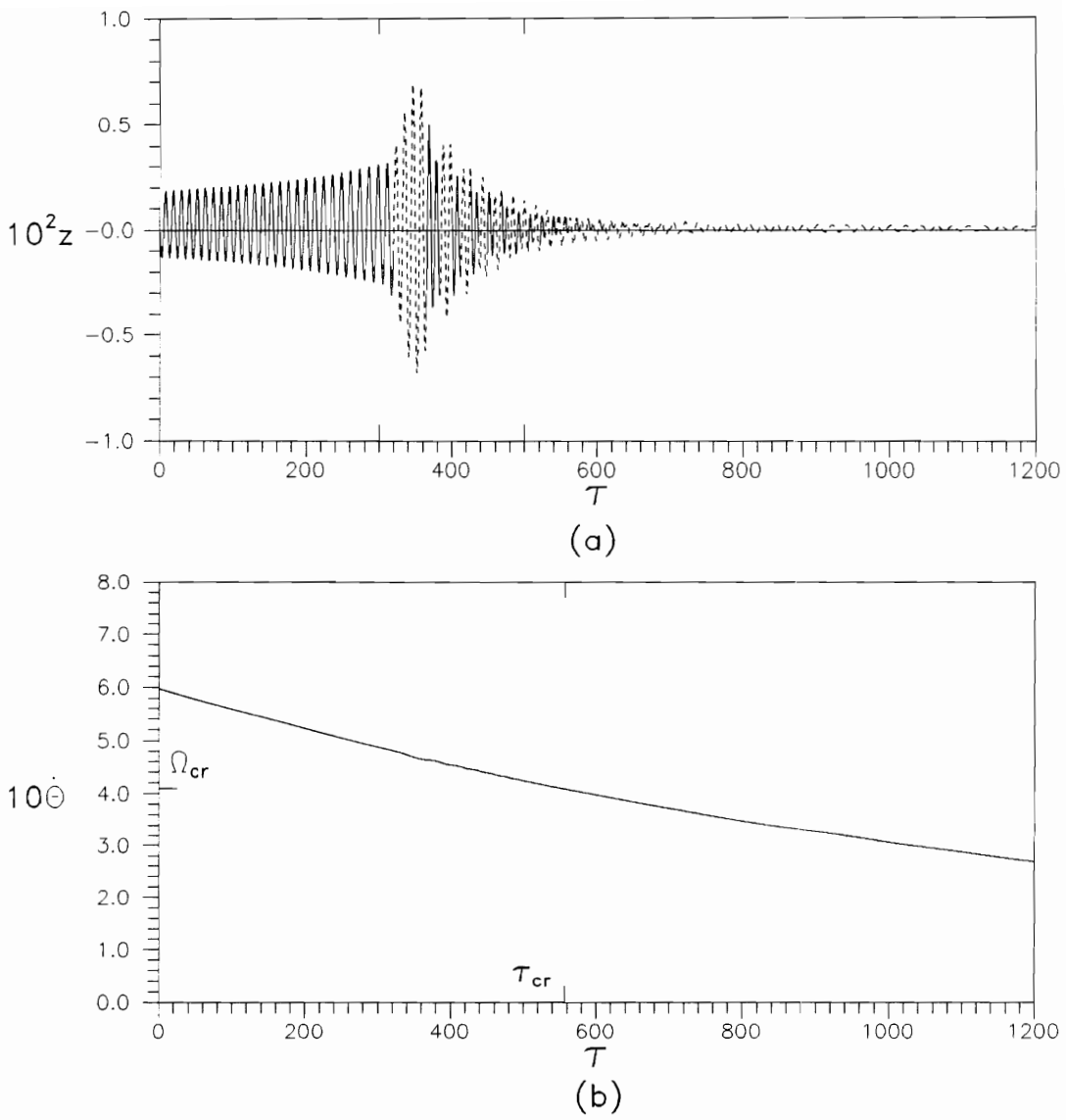

Fig. 4.24 Gradual Stiffness Switching During Coast-down, from τ=300 until τ=500

4.3.5. Influence of the motor characteristic

Changes in the driving torque characteristic cause different interactions between the displacement and the torque. In this section, different constant and linear driving torques will be investigated.

Figure 4.25 shows the three constant driving torques to be considered, with $\upsilon_1 = 0$ and $\upsilon_0 = 0.000025,\ 0.000028,\ 0.00003\,0$. The corresponding nonstationary time histories are shown in Figs. 4.26, 4.27, and 4.28, respectively, based on the standard data. In Fig. 4.26, after the shaft speed is near the critical speed, the angular velocity does not increase (due to insufficient power) and remains stuck at the resonance condition. Therefore, a large displacement occurs as the angular velocity remains near the resonance frequency. This is a dangerous condition for the rotating shaft.

However, for slightly higher constant driving torque ($\upsilon_0 = 0.000028$) than the previous one, the shaft can pass the critical speed (Fig. 4.27). It still has a Sommerfeld effect, but not for long. For the case with a higher constant driving torque ($\upsilon_0 = 0.000030$, Fig. 4.28) the angular velocity increases faster than in the previous ones. Together with this faster increase in the angular velocity, the maximum z-displacement decreases when the constant driving torque increases.

Now, to suppress the vibration, the system stiffness is switched by adding an internal flexible support for a certain time, i.e., for the critical time range when the shaft would pass the critical speed. Figure 4.29 gives the time histories of the z-displacement and the angular velocity under the constant driving torque with initial torque

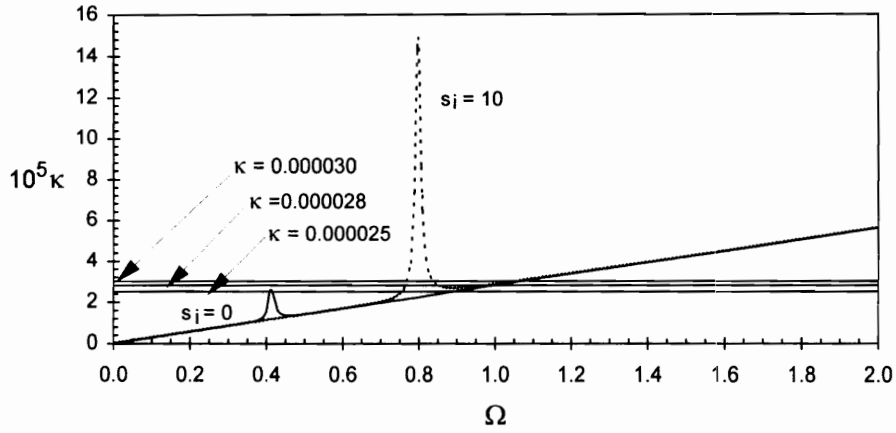

Fig. 4.25 Constant Driving Torque

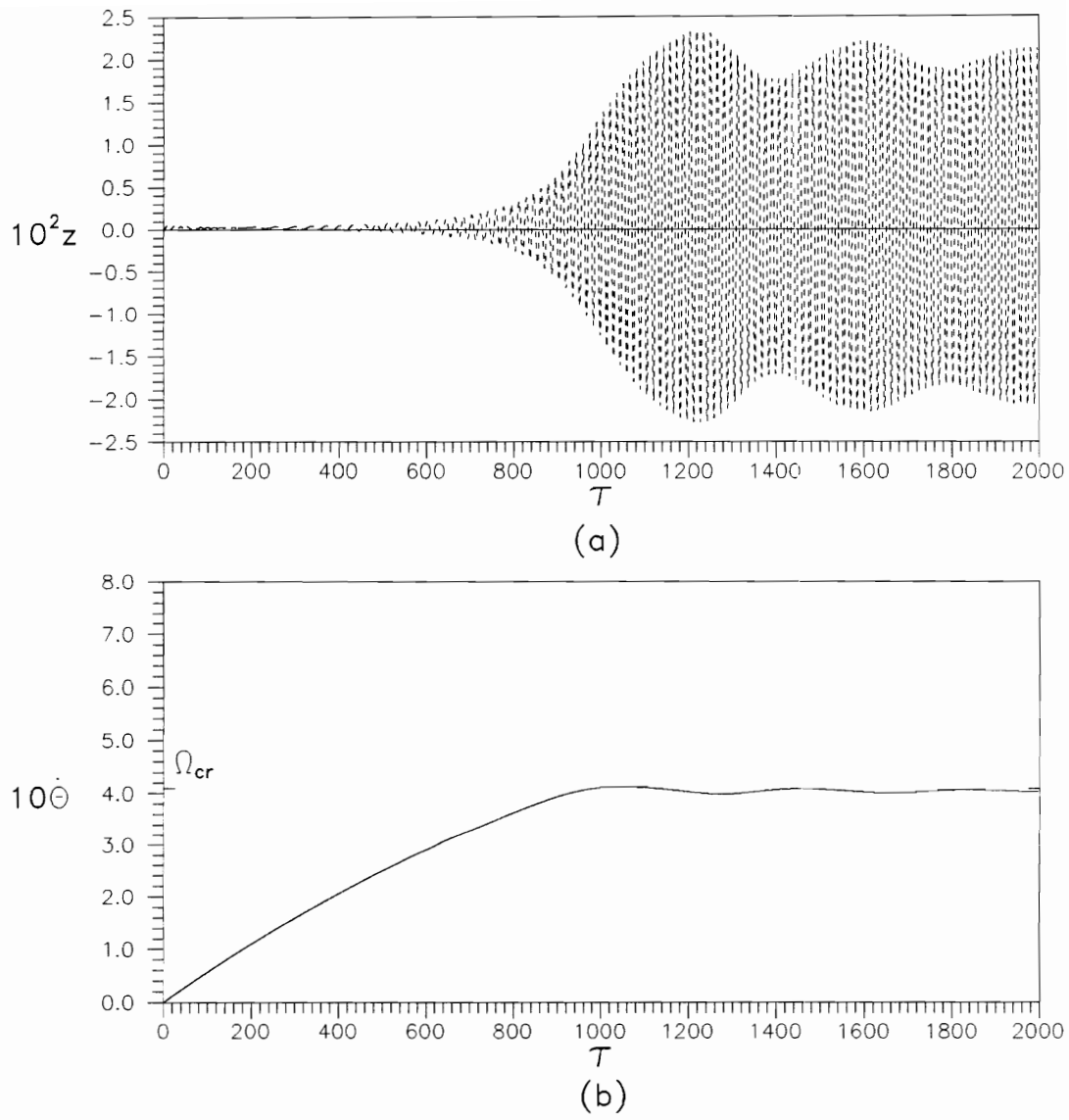

Fig. 4.26 Time Histories under Constant Driving Torque; υ_0=0.000025

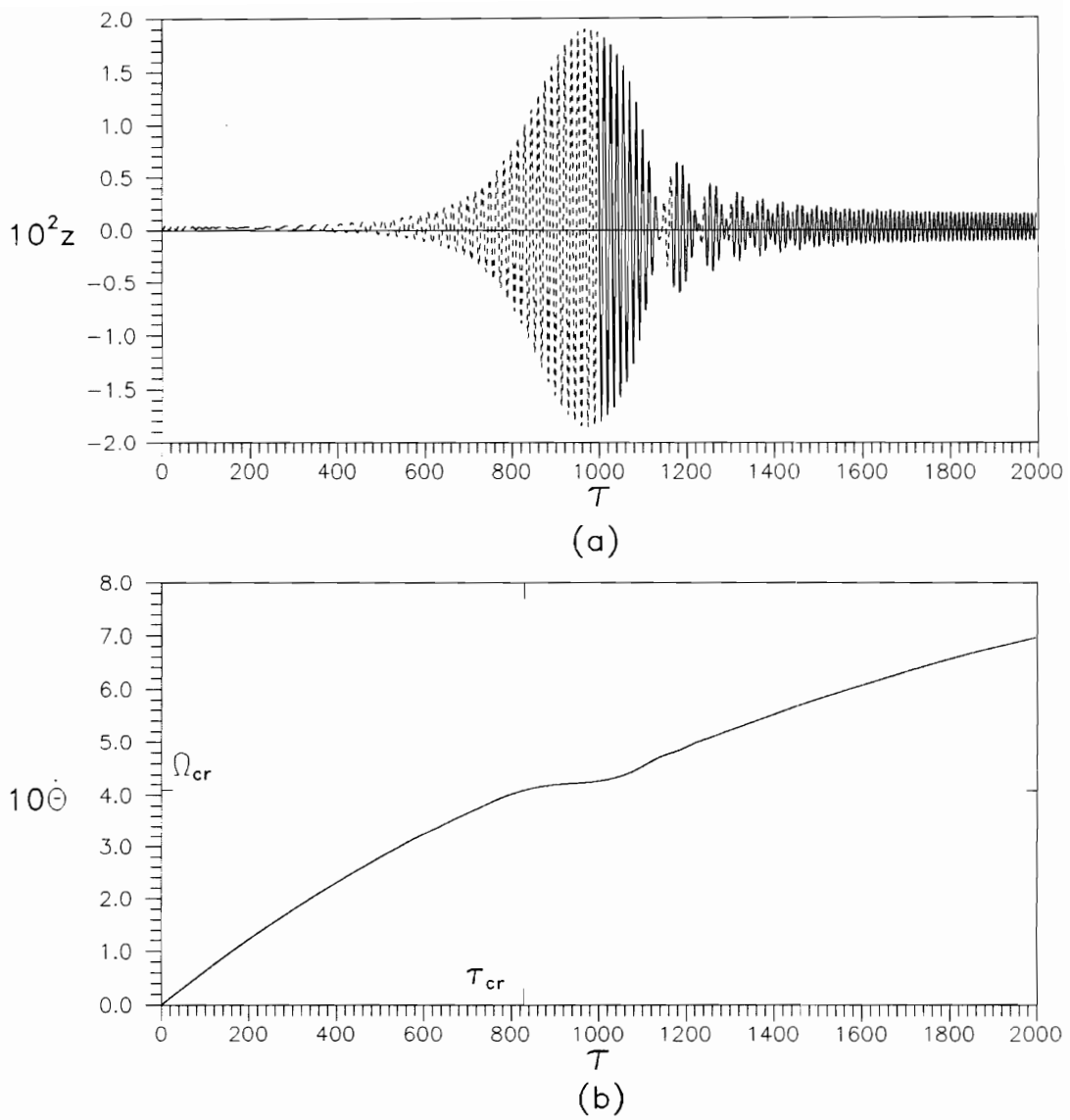

Fig. 4.27 Time Histories under Constant Driving Torque; υ_0=0.000028

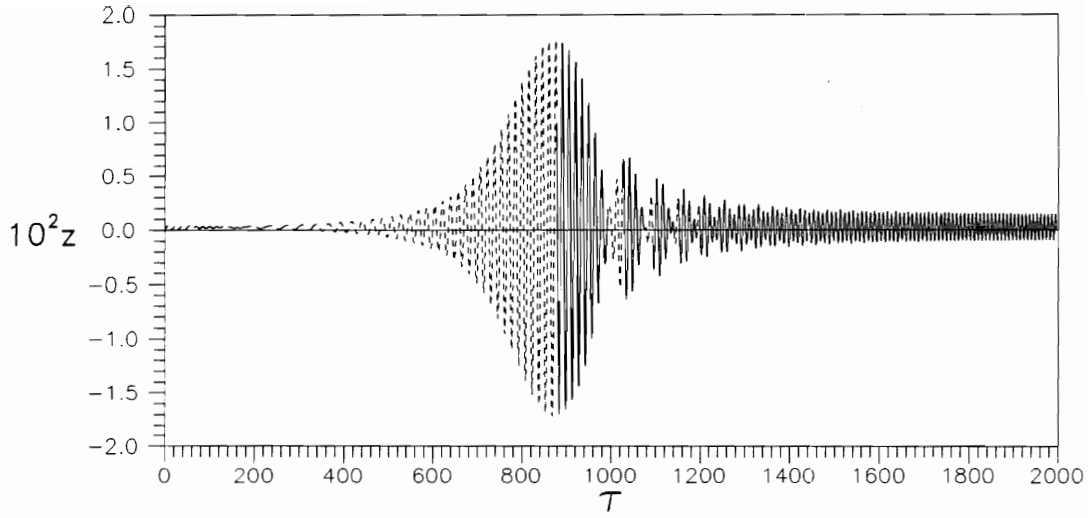

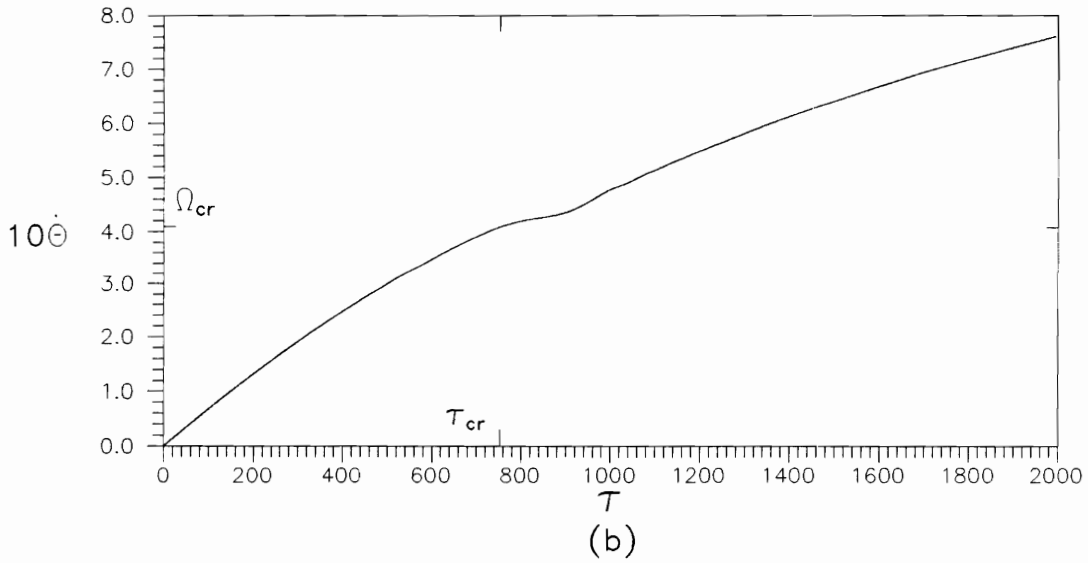

Fig. 4.28 Time Histories under Constant Driving Torque; υ_0=0.000030

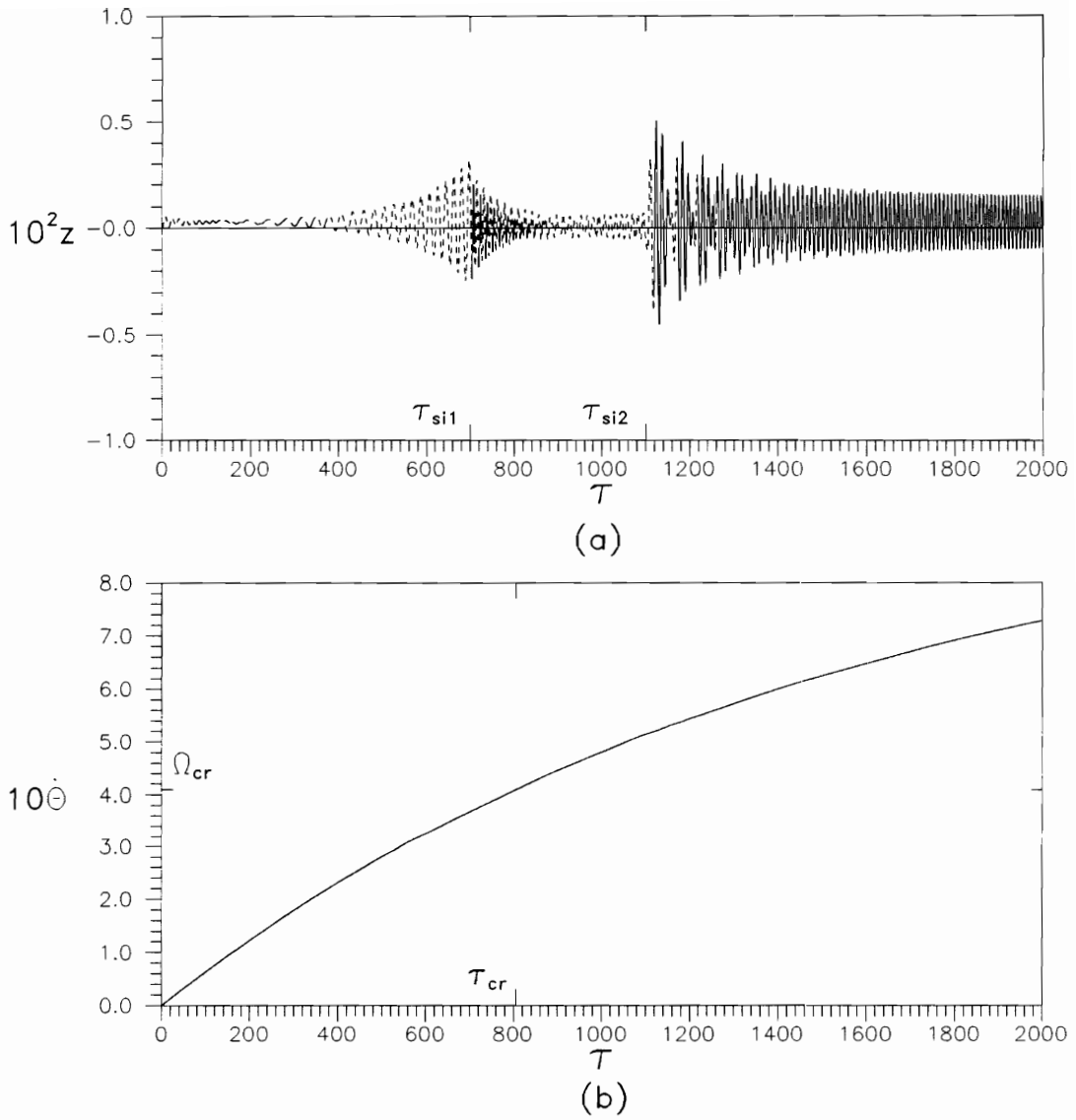

Fig. 4.29 Switching Stiffness under Constant Driving Torque; υ_0=0.000028

$\upsilon_0 = 0.000028$ and standard data with the switching stiffness. Between the first switching time at $\tau_{si1} = 700$ and the second one at $\tau_{si2} = 1100$, an internal support with stiffness $\tilde{s}_i = 10$ at $\tilde{x}_i = 0.7$ is active. Other cases with constant driving torque but different switching times give similar results, as listed in Table 4.6.

Table 4.6 Reduction under constant driving torque

Constant torque υ_0	τ_{si1}	τ_{si2}	% Reduction
0.000025	800	1400	80.0
0.000028	700	1100	73.6
0.000030	600	1000	72.1

The reduction is large, especially for the first case.

Now linear driving torques are considered. First, the stationary angular velocity Ω_{st} is held constant at 0.6. Figure 4.30 shows three different initial torques $\upsilon_0 = 0.00005, 0.00006, 0.00007$ and the same standard data. The nonstationary results are shown in Figs. 4.31, 4.15, and 4.32, respectively. With small initial driving torque $\upsilon_0 = 0.00005$, the Sommerfeld effect lasts longer than for the others and the maximum displacement is the largest. This is similar to the acceleration cases: with slower acceleration rate, the displacement becomes larger. The switching stiffness for the case with initial torque $\upsilon_0 = 0.00006$ is shown in Fig. 4.20. For other driving torques, the switching stiffness cases are carried out similarly to Fig. 4.20 by adding the internal support $\tilde{s}_i = 10$ between the first switching time and the second switching time. The time histories of the z-displacement and the angular velocity for $\upsilon_0 = 0.00005, 0.00007$

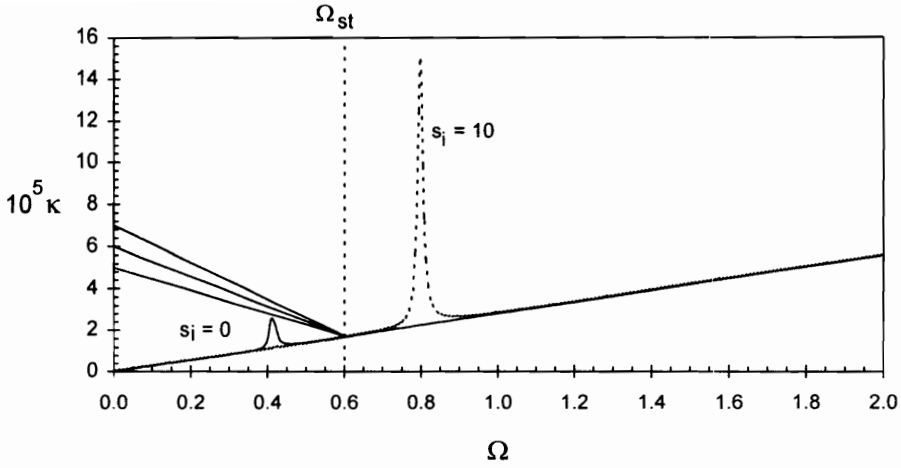

Fig. 4.30 Linear Driving Torque with $\Omega_{st} = 0.6$

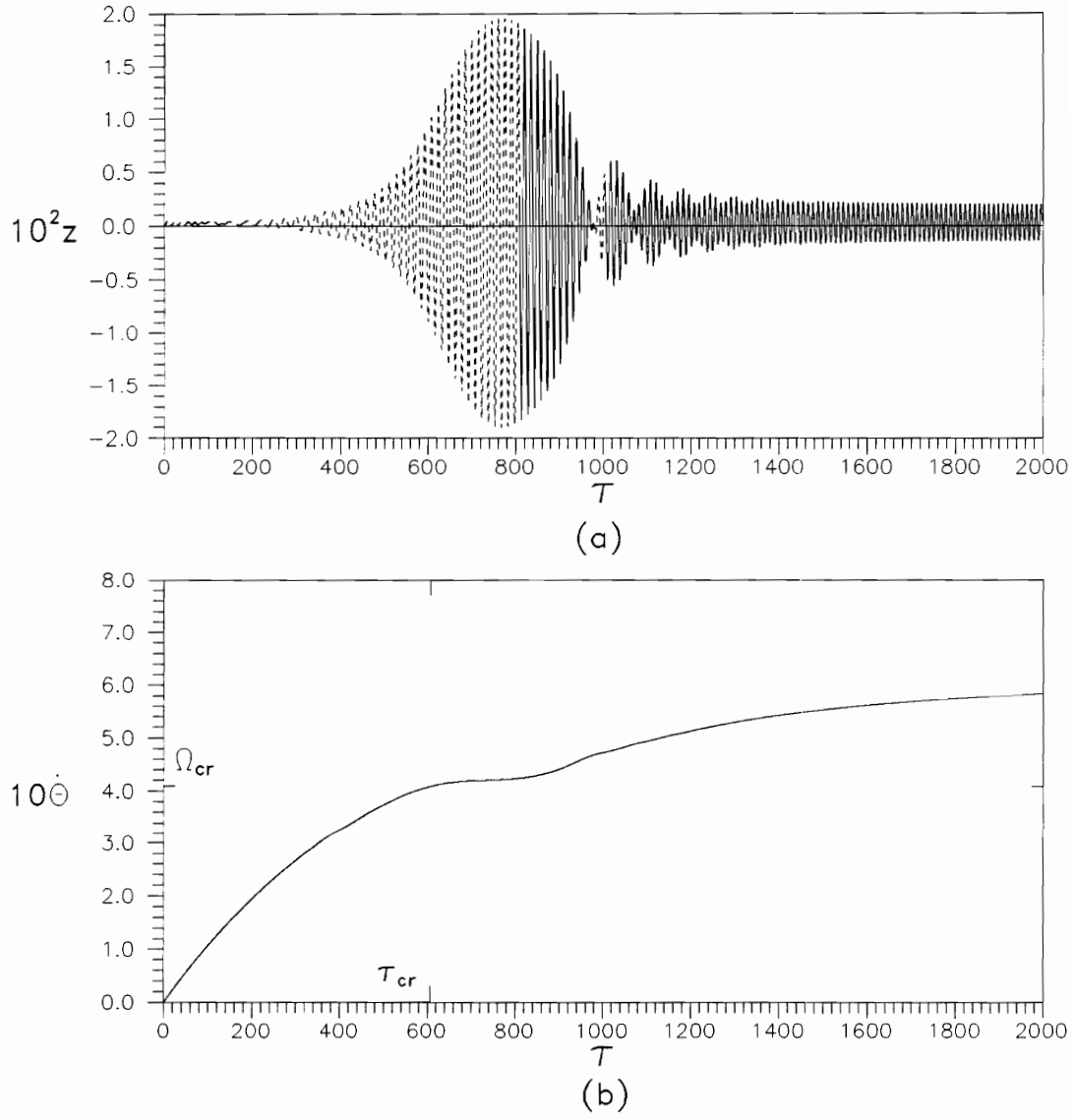

Fig. 4.31 Time Histories During Run-up with v_0=0.00005 and Ω_{st}=0.6

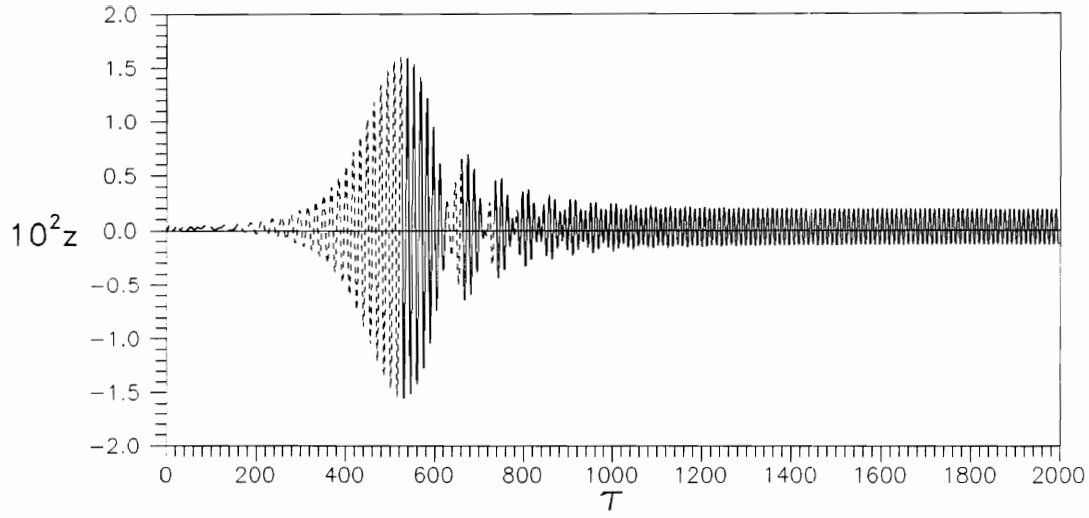

(a)

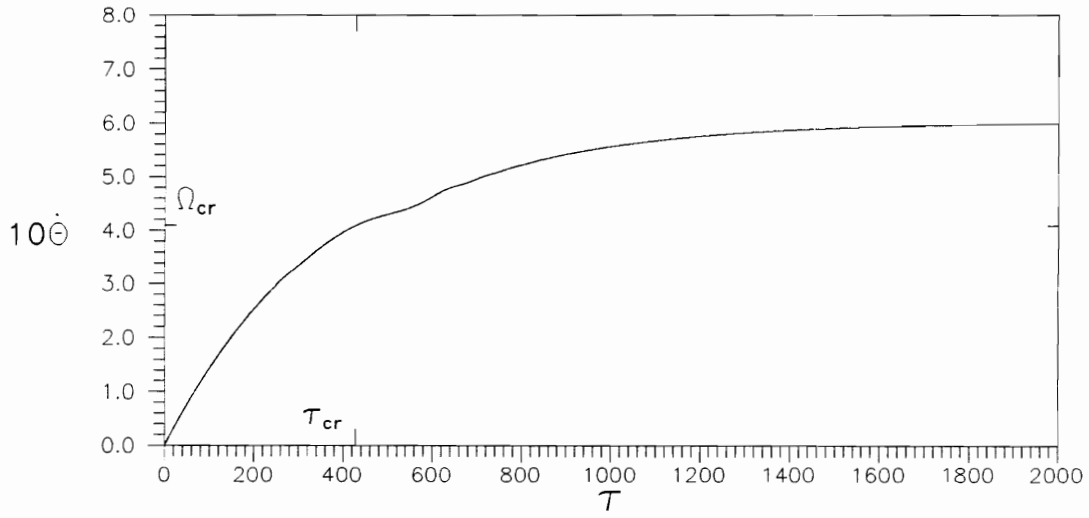

(b)

Fig. 4.32 Time Histories During Run−up with υ_0=0.00007 and Ω_{st}=0.6

with the switching stiffness are similar to Fig. 4.20. Table 4.7 gives the results of displacement reduction for different linear driving torques.

Table 4.7 Displacement reduction with different linear driving torques

υ_0	υ_1	τ_{si1}	τ_{si2}	% Reduction
0.00005	0.000055	500	1000	75.1
0.00006	0.000071	400	700	66.2
0.00007	0.000088	300	600	63.5

Now, the initial driving torque υ_0 is held fixed at 0.00014 (Fig. 4.33). Three run-up cases are treated, with $10^4\upsilon_1 = 2.5,\ 2.3,\ 2.0$, corresponding stationary angular velocities $\Omega_{st} = 0.5,\ 0.55,\ 0.60$, and the standard data. The time histories of the z-displacement and the angular velocity without an internal support are similar to the ones in Fig. 4.15. The critical speeds with the new driving torques occur much earlier than in Fig. 4.15 because the initial driving torque is larger. Each case approaches a different stationary angular velocity, and there is enough power so that the Sommerfeld effect is hardly seen for these three cases. The vibration suppression is done by adding an internal support with stiffness $\tilde{s}_i = 10$ at $\tilde{x}_i = 0.7$ between the first switching time $\tau_{si1} = 200,\ 200,\ 150$ and the second switching time $\tau_{si2} = 500,\ 400,\ 400$, respectively, corresponding to three run-up cases. These switching times are chosen depending on the z-displacement time histories of the corresponding original system. The angular velocities at the time of switching are about 0.37, 0.38, and 0.34, respectively. The critical speed of the original

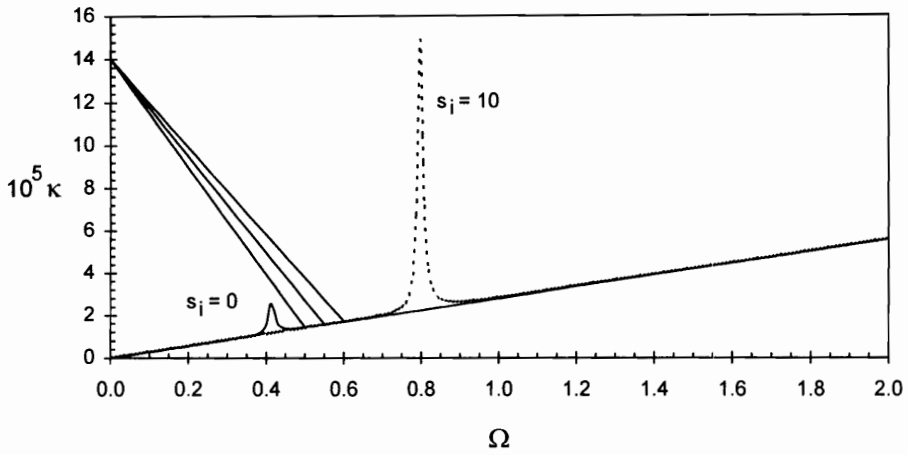

Fig. 4.33 Linear Driving Torques
with Initial Driving Torque υ_0=0.0001

system is $\Omega_{cr} = 0.41$. The displacement reductions for these three cases are 59.2%, 58.2%, and 62.1%, respectively.

4.3.6. Influence of initial conditions for coast-down

The initial conditions for coast-down (with zero driving torque) influence the interaction between the displacement and the angular velocity. From the previous case in Fig. 4.21 with initial conditions from the stationary condition of the run-up case, other cases with the same data and the same initial conditions except for different initial angular velocities, i.e., $\dot{\theta}_{initial} = 0.7,\ 0.8,\ 0.9$, respectively, give similar figures to Fig. 4.21 which has initial angular velocity $\dot{\theta}_{initial} = 0.6$. The main difference is that the time needed to pass the critical speed becomes longer when the initial angular velocity increases. Also, since the initial conditions are not the stationary conditions, for the new cases there are small transient motions in the beginning.

For switching cases similar to Fig. 4.22, the three cases above are investigated. The additional internal support with $\tilde{s}_i = 10$ at $\tilde{x}_i = 0.7$ is activated at the switching times $\tau_{si} = 500,\ 700,\ 900$, respectively, and remains active until the motion stops. The displacement reductions are 81.1%, 81.0%, 78.7%, respectively.

4.3.7. Influence of internal support stiffness

In the previous cases (after Fig. 4.5) the additional internal support stiffness was $\tilde{s}_i = 10$. In this section the influence of the internal support stiffness is investigated. Figure 4.34 depicts the stationary condition of the motor characteristic for comparisons between the system with internal support stiffnesses $\tilde{s}_i = 5, 10, 25$ and the system without internal support. The same driving torque and stationary angular velocity are taken for all three conditions. The initial driving torque υ_0 is 0.0001 and the stationary angular velocity Ω_{st} is 0.55. With this driving torque, the nonstationary condition for the shaft without internal support is shown in Fig. 4.35. The critical speed is reached quickly, because the angular velocity increases quickly. The angular velocity approaches the stationary condition $\Omega = 0.55$.

The vibration suppression is carried out by adding an internal support with different stiffnesses $\tilde{s}_i = 5, 10, 25$ at $\tilde{x}_i = 0.7$ between the first switching time $\tau_{si1} = 250$ and the second switching time $\tau_{si2} = 500$ for all three cases. The resulting time histories of the z-displacement and the angular velocity are shown in Figs. 4.36, 4.37, and 4.38, respectively. These three figures show similar features in the angular velocity and small differences in the z-displacement. Between the first and the second switching times, the displacement decreases when the internal support stiffness increases. This influences the initial conditions at the second switching time, but only has a small effect on the subsequent transient motion. The reductions of the three cases are similar, i.e., 59.5%, 62.4%, and 63.3%, respectively. The case with the smallest internal support

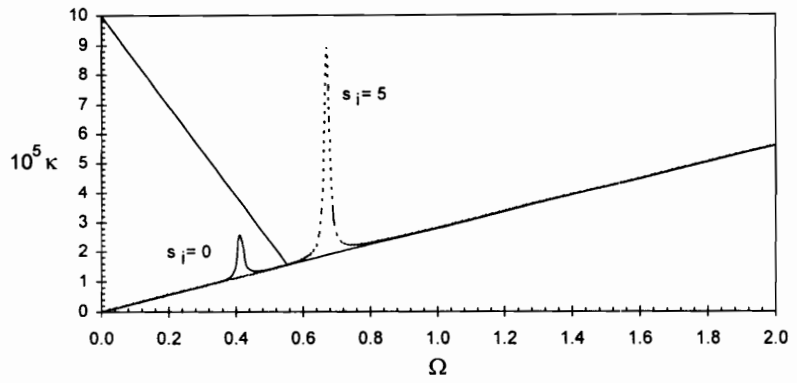

(a)

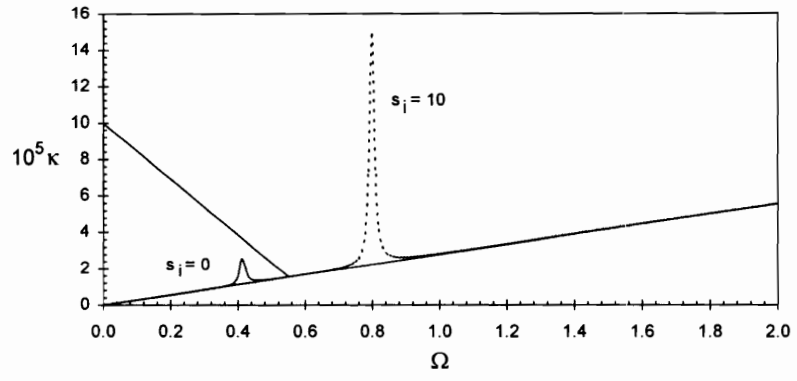

(b)

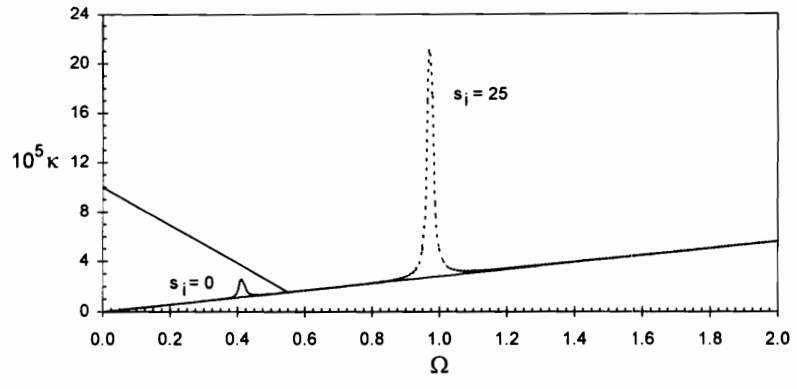

(c)

Fig. 4.34 Motor Characteristic with Different Internal Support Stiffness

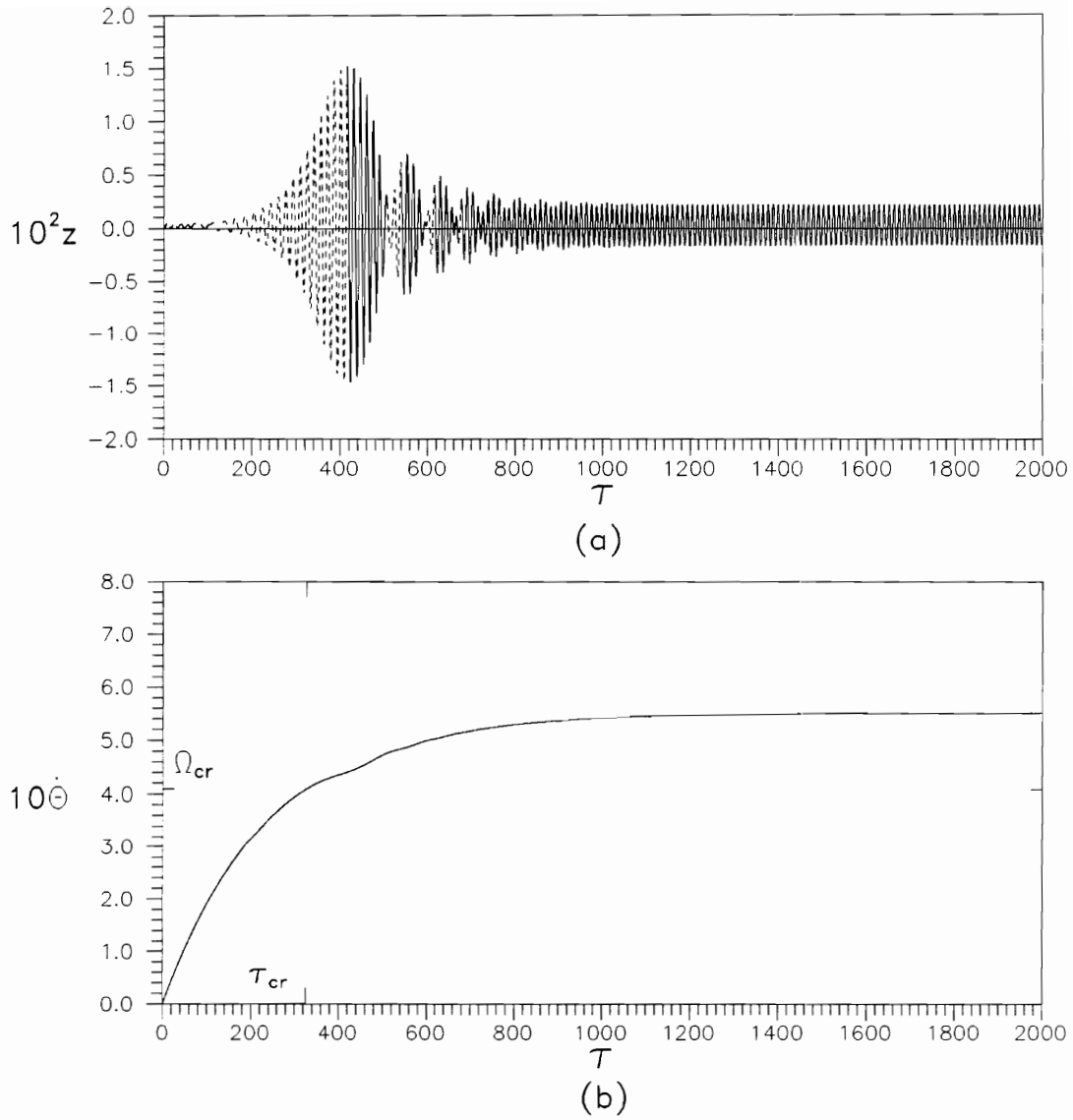

Fig. 4.35 Time Histories During Run-up with υ_0=0.0001 and Ω_{st}=0.55

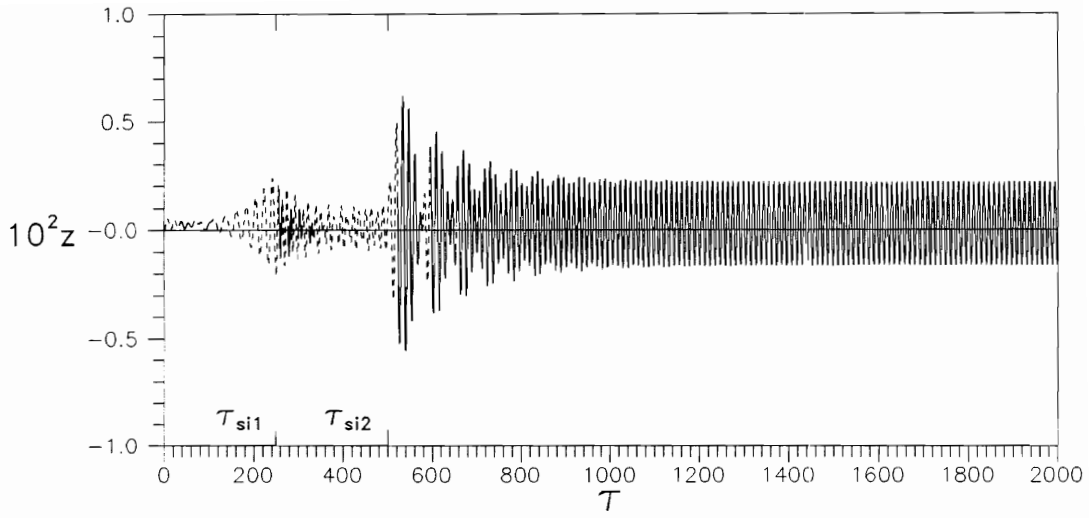

Fig. 4.36 Switching Stiffness with s_i=5

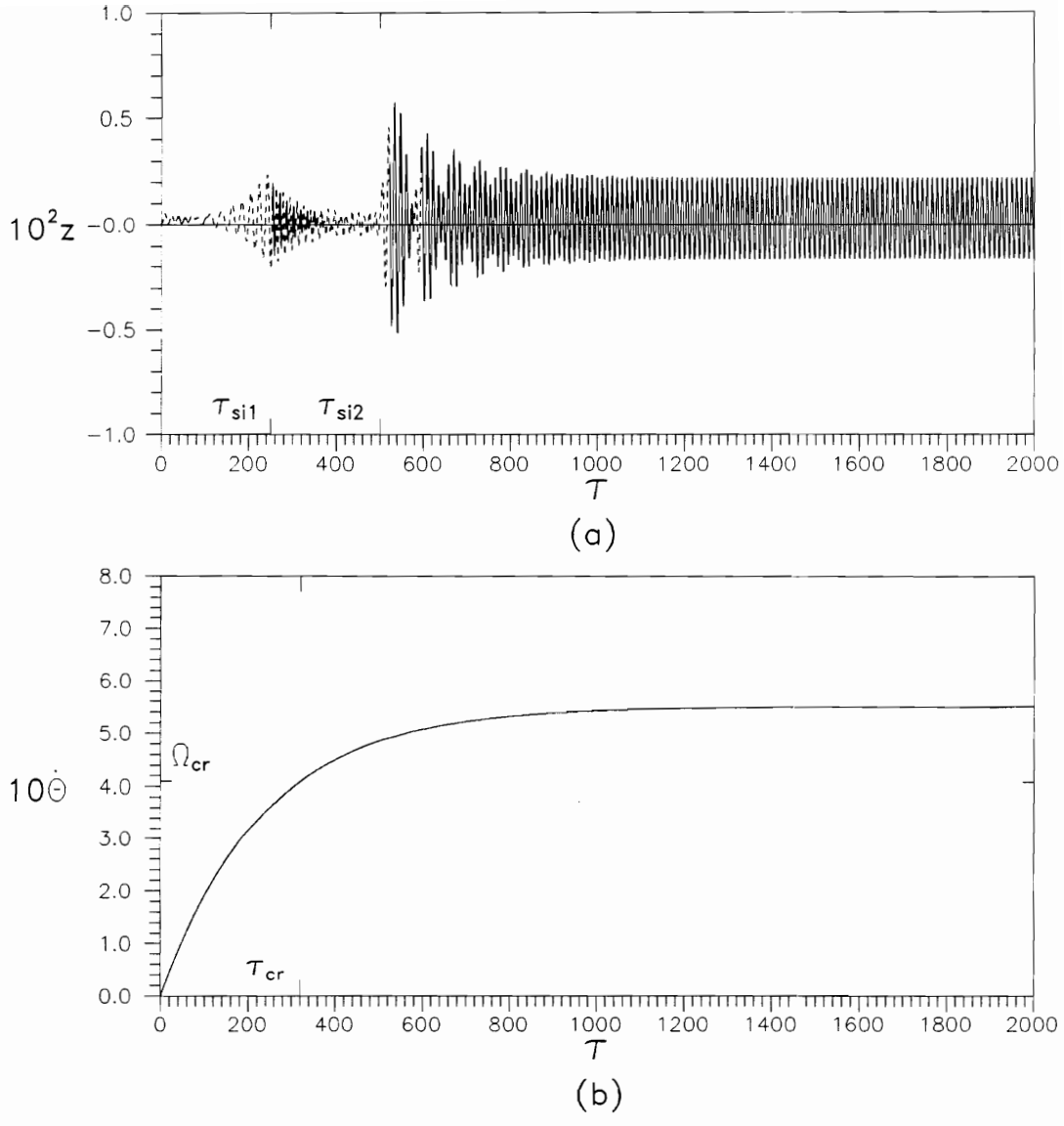

Fig. 4.37 Switching Stiffness with s_i=10

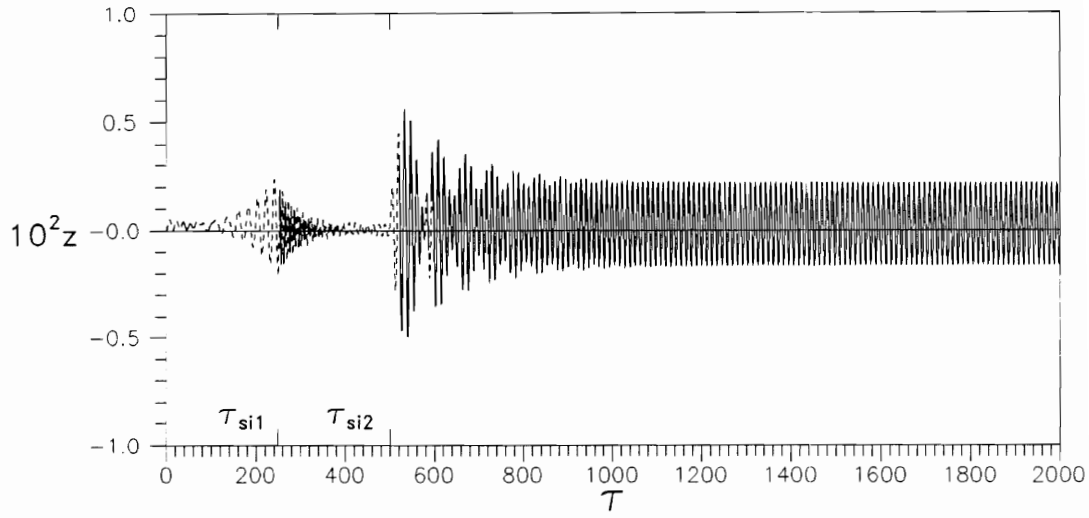

(a)

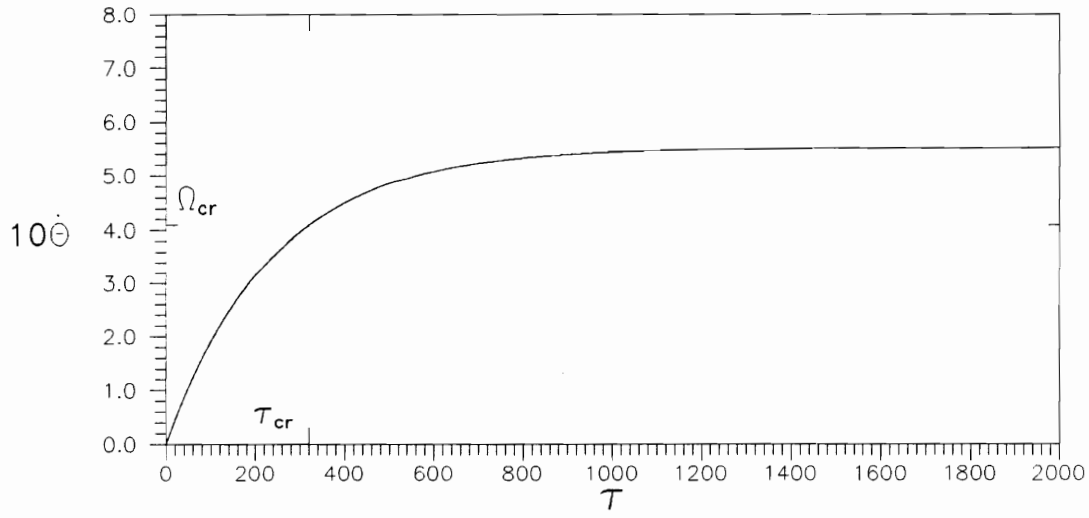

(b)

Fig. 4.38 Switching Stiffness with s_i=25

stiffness has a slightly lower displacement reduction compared to the others, because the initial displacement is slightly higher at τ_{si2}.

4.3.8. Influence of internal support location

The previous cases always have the additional internal support location at $\tilde{x}_i = 0.7$. Now, the influence of the location of the additional internal support is examined with $\tilde{x}_i = 0.2, 0.3, 0.4, 0.5, 0.6, 0.7,$ and 0.8. Also, locations $\tilde{x} = 0.1$ and 0.9 are very close to the supports and are not considered. Based on Fig. 4.15 for the shaft without internal support under the initial driving torque $\upsilon_0 = 0.00006$ and the stationary angular velocity $\Omega_{st} = 0.6$, the influence of the internal support location on the displacement reduction is studied. The internal support with stiffness $\tilde{s}_i = 10$ is active between the first switching time $\tau_{si1} = 400$ and the second switching time $\tau_{si2} = 700$. The time histories are similar to Fig. 4.20 with small differences in the time histories of the z-displacement between the switching times. If the internal support location moves closer to the disk location, the maximum displacement decreases (similar to the influence of a larger internal support stiffness). The resulting displacement reduction is 63.6%, 66.5%, 67.2%, 67.1%, 67.0%, 66.2%, 63.5%, respectively, for the six locations. The results are not symmetric because there is a breathing crack at the location $\tilde{b} = 0.4$. However, the difference is very small.

4.3.9. Influence of the external damping

Figures 4.39, 4.40, 4.15, and 4.41 show the time histories of the z-displacement and the angular velocity with the same initial driving torque $\upsilon_0 = 0.00006$ and stationary angular velocity $\Omega_{st} = 0.6$, and different external dampings, i.e., $\tilde{d}_e = 0.05,\ 0.075,\ 0.1,$ and 0.15, respectively. For the case with external damping $\tilde{d}_e = 0.05$, the maximum z-displacement is largest and the subsequent z-displacement decreases most slowly. Increasing the external damping causes the maximum z-displacement to decrease and the angular velocity to increase more slowly. For the case with external damping $\tilde{d}_e = 0.15$ the interaction between the system and the motor (Sommerfeld effect) is seen more clearly than for the others. The displacement reductions by adding the internal support with stiffness $\tilde{s}_i = 10$ at $\tilde{x}_i = 0.7$ between the first switching time $\tau_{si1} = 400$ and the second switching time $\tau_{si2} = 700$ are 77.8%, 73.7%, 66.2%, 65.6%, respectively. The time histories for the switching case are similar to those in Fig. 4.20 for all these damping values.

4.3.10. Influence of restoring torque

The application of an internal support may resist rotation of the shaft, as well as deflection. The influence of such a restoring torque when the internal support is applied is investigated in this section. It is assumed that the restoring torque $\kappa_b(\dot{\theta})$ reduces the motor torque $\kappa(\dot{\theta})$ by a certain percentage, so that it can be formulated as follows:

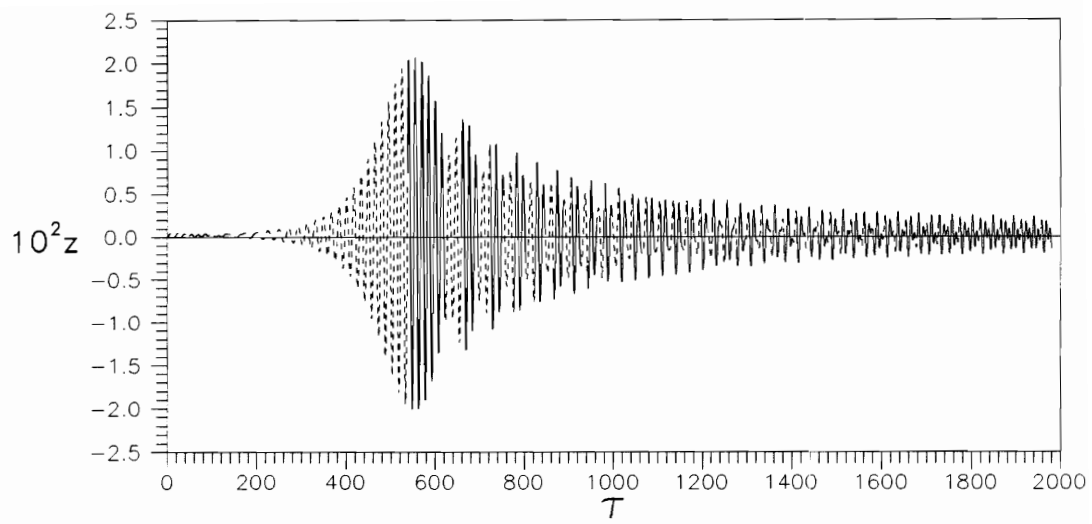

(a)

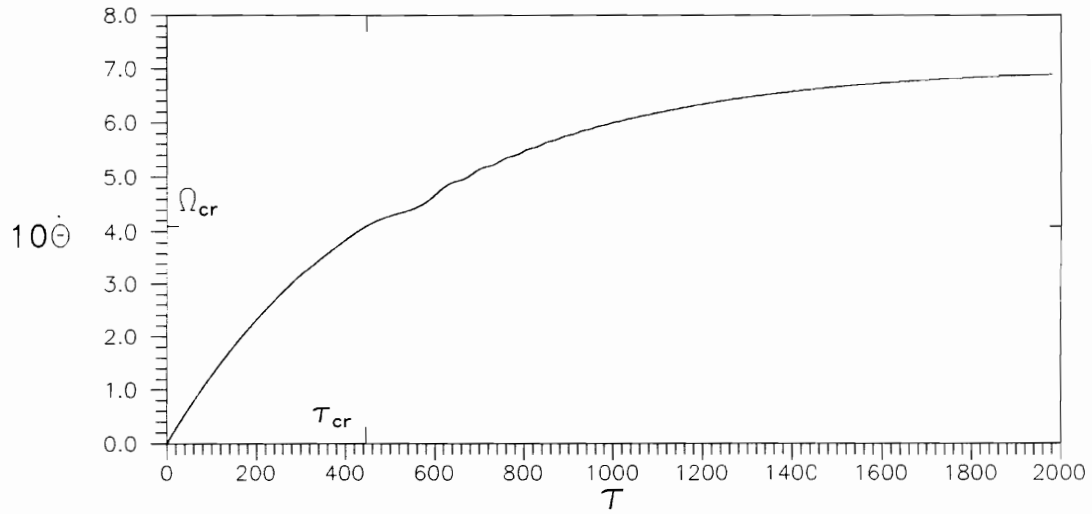

(b)

Fig. 4.39 Time Histories During Run-up for d_e=0.05

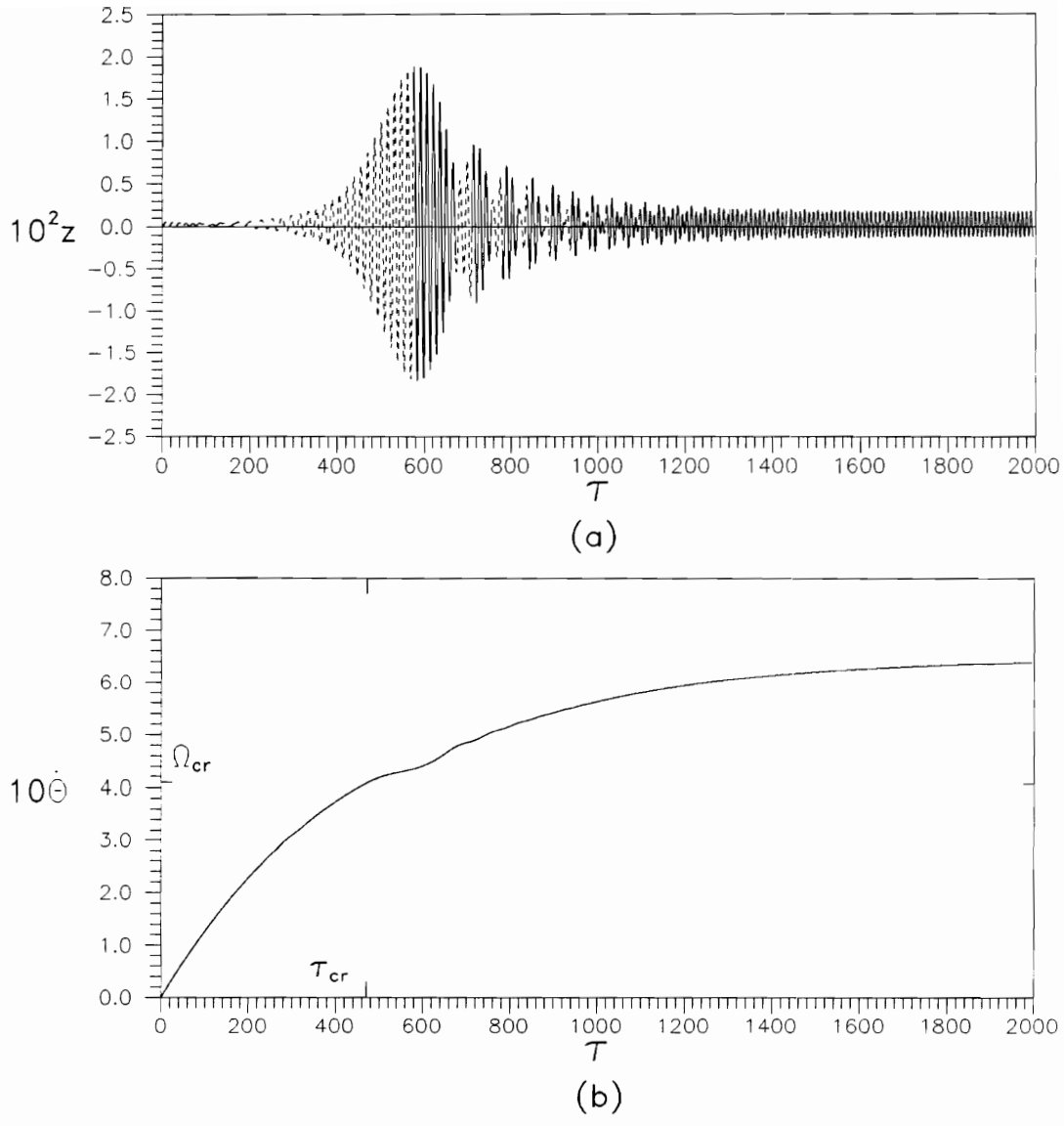

Fig. 4.40 Time Histories During Run−up for d_e=0.075

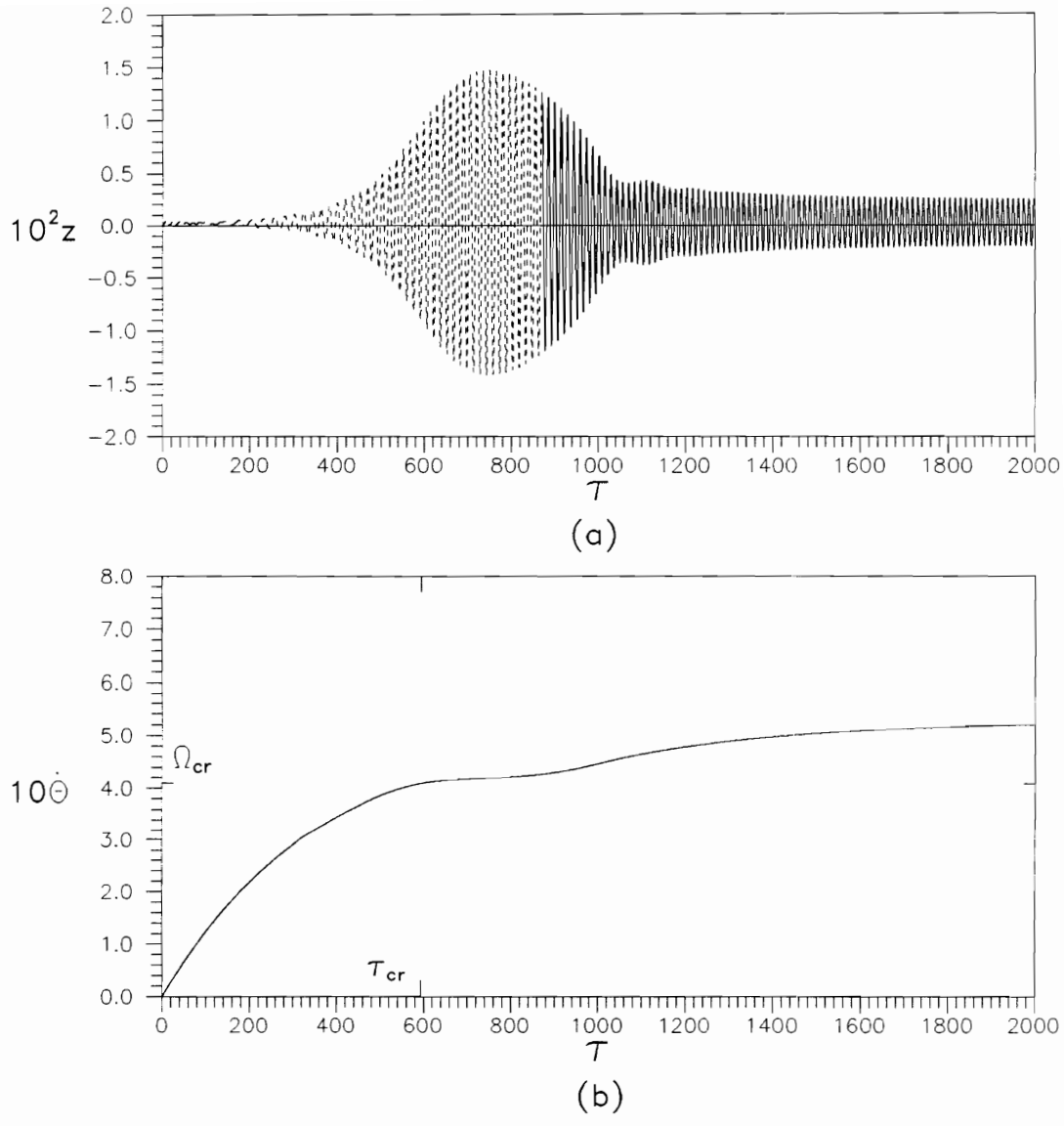

Fig. 4.41 Time Histories During Run−up for d_e=0.15

$$\kappa_b(\dot{\theta}) = \alpha\ \kappa(\dot{\theta}) = \alpha\left(\upsilon_0 - \upsilon_1\dot{\theta}\right) \tag{4.11}$$

Then, the total motor torque (including the restoring torque) becomes

$$\kappa(\dot{\theta}) - \kappa_b(\dot{\theta}) = (1-\alpha)\ \kappa(\dot{\theta}) \tag{4.12}$$

Cases similar to Fig. 4.20, with initial driving torque $\upsilon_0 = 0.00006$, stationary angular velocity, and the standard data, are investigated with different restoring torques, i.e., with $\alpha = 0.10$, 0.15, 0.20, 0.25, 0.30, and 0.35. The internal support is applied between $\tau_{si1} = 400$ and $\tau_{si1} = 700$ for all these cases. Figure 4.42 shows the angular velocity and z-displacement time histories for the case $\alpha = 0.20$. The other cases give similar time histories to Fig. 4.42. Increasing the restoring torque causes the angular velocity to increase more slowly. The results of the displacement reduction compared to the case without internal support (Fig. 4.15) are 63.6%, 61.0%, 58.1%, 56.0%, 52.6%, and 46.5%, respectively. From the previous result (Fig. 4.20), the reduction of the z-displacement without restoring torque is 66.2%. From these results, increasing restoring torque gives a smaller z-displacement reduction.

The influence of different switching times for the previous case with motor torque reduction $\alpha = 0.20$ is studied now. The second switching times are taken as $\tau_{si2} = 700$, 800, 900, 1000, 1100, and 1200, and the first switching time is the same for all cases, i.e., $\tau_{si1} = 400$. The z-displacement reductions become 58.1%, 64.5%, 67.9%, 70.0% , 71.7%, 71.9%, respectively. When the second switching time occurs later, the angular velocity at the second switching time is farther from the critical speed, the resulting transient motion is smaller, and the reduction of the z-displacement is larger.

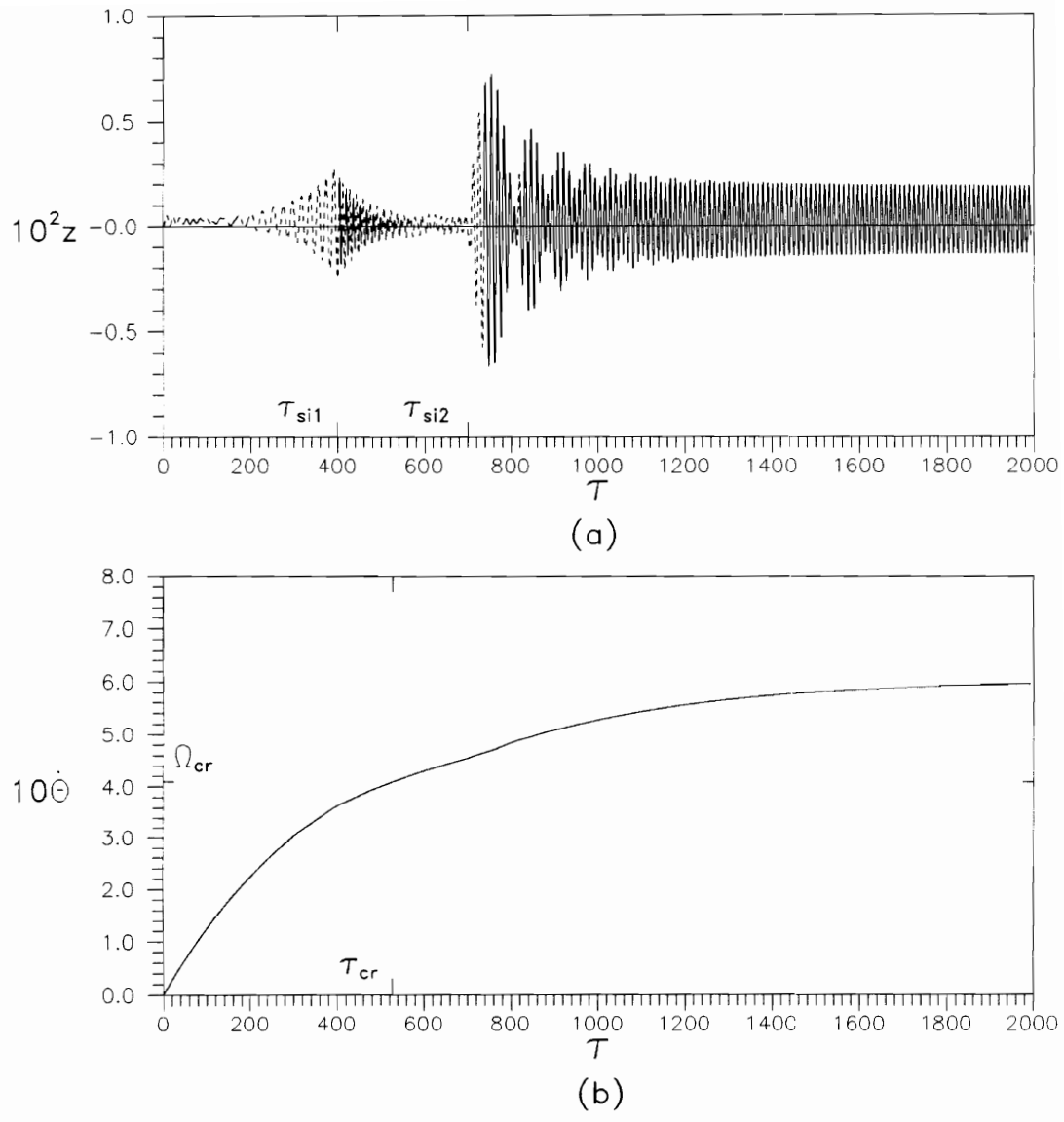

Fig. 4.42 Time Histories with Restoring Torque Factor α=0.2

4.3.11. Switching based on angular velocity

In the previous sections, the switching was activated at a certain time and for a certain duration near the critical time. In this section, the internal support activation is based on the angular velocity of the shaft assuming that the critical speed of the system is known, the internal support is activated between an angular velocity Ω_1 before the critical speed and an angular velocity Ω_2 after the critical speed, which are chosen as follows:

$$\Omega_1 = (1-\beta)\,\Omega_{cr} \tag{4.13}$$

$$\Omega_2 = (1+\beta)\,\Omega_{cr} \tag{4.14}$$

where β is a range factor.

Based on the standard data with initial driving torque $\upsilon_0 = 0.00006$ and stationary angular velocity $\Omega_{st} = 0.6$, cases with switching stiffness are investigated. The additional internal support with stiffness $\tilde{s}_i = 10$ is located at $\tilde{x}_i = 0.7$. Cases with different range factors are examined, i.e., with $\beta =$ 0.10, 0.125, 0.15, 0.175, and 0.20. Figure 4.44 shows the time histories of the z-displacement and the angular velocity of the shaft with an internal support that is active when the angular velocity is between 85% of the critical speed and 115% of the critical speed ($\beta =$ 0.15). The displacement reduction compared to that without internal support (Fig. 4.15) is 63.1%. This result is similar to the case in Fig. 4.20 where the internal support is active between $\tau_{si1} = 400$ and $\tau_{si2} = 700$ and the reduction is 66.2%.

The displacement reductions for the above cases (with different value of β) are 57.5%, 61.5%, 63.1%, 68.0%, 68.0%, respectively. From the results, there is a tendency to get more displacement reduction if the range factor is larger. This tendency is also shown for different switching times (Table 4.5), where the initial switching time is always the same and the final switching time is increased.

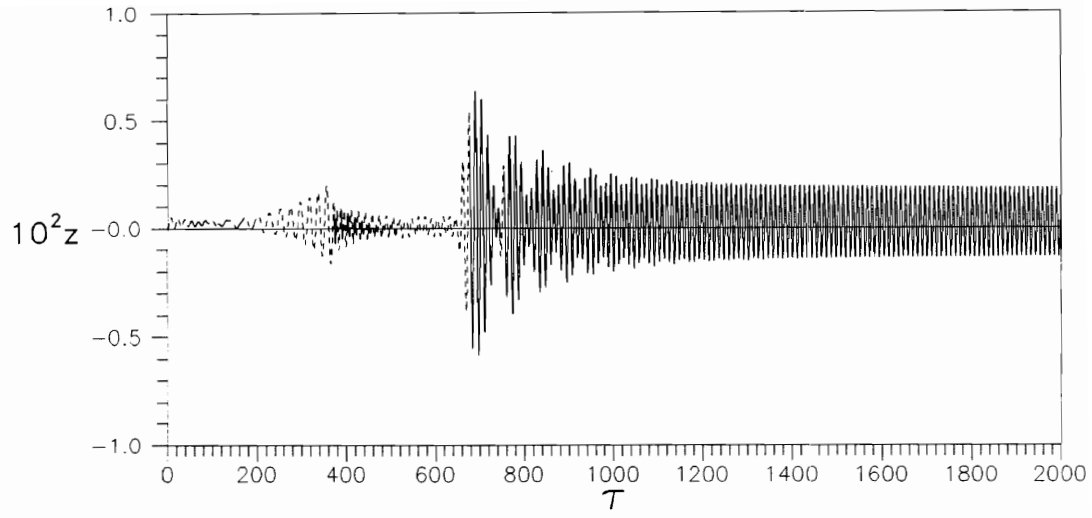

(a)

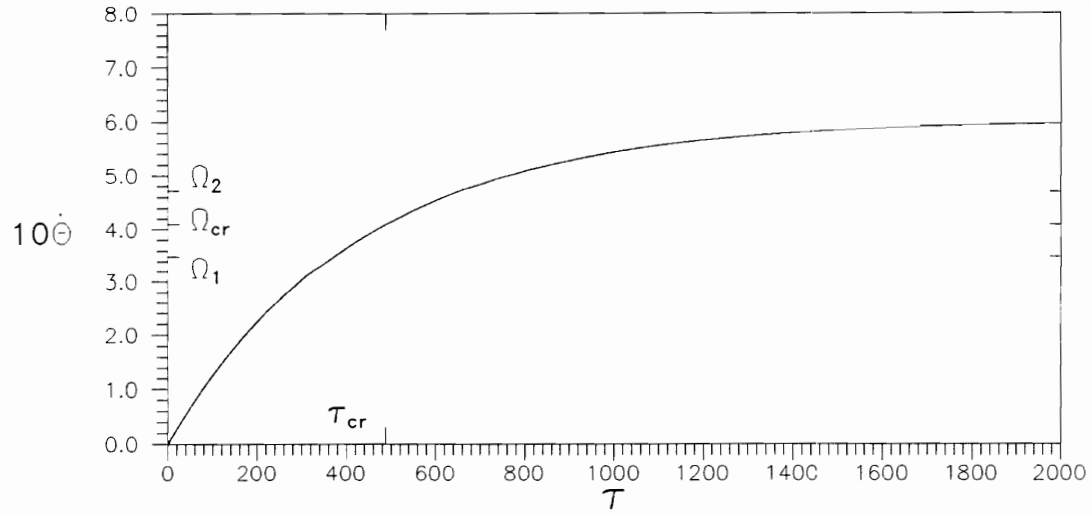

(b)

Fig. 4.43 Time Histories with Range Factor β=0.15

CHAPTER 5

CONCLUSIONS

5.1. Conclusions

In the first part of this study, the dynamic behavior of the cracked rotating shaft with a disk is analyzed, with an ideal and a nonideal motor, passing through its critical speed. The influence of the support stiffness and damping, the inclusion of the gyroscopic moments, and the effect of the overhangs with mass at one end are investigated. For a nonideal motor, the interaction between the shaft and the motor is included.

The general conclusions regarding the dynamic behavior of the cracked rotating shaft are as follows:

- Increasing the support stiffness and damping usually increases the maximum response in the present example, due to the involvement of more flexure and less a rigid body translation.
- The inclusion of the gyroscopic moments tends to increase the response, but the magnitude of the change is small.
- Changing the eccentricity (unbalance) angle may be an effective way to detect a crack.

- Increasing the internal damping may cause the system to become unstable. A relation between the external damping and the internal damping determines the stability of the system.
- An increase in the overhang length and the mass of the overhung disk causes a decrease in the maximum response.
- Certain motor characteristics for a nonideal motor can cause an almost-constant, large displacement due to the Sommerfeld effect. The angular velocity approaches, but does not pass, the critical speed in this case.

In the second part of this study, the vibration suppression of the cracked, simply supported, rotating shaft with a rigid disk is examined, with an ideal and a nonideal motor, passing through the critical speed. The vibration is suppressed by activating a flexible internal support at a certain location along the shaft to change the stiffness of the system. The influence of the types and times of the activation of the internal support, the stiffness and location of the internal support, the motor characteristic, and the external damping magnitude is investigated.

The general conclusions of the second part of this study are as follows:

- By activating the flexible internal support for a certain duration near the critical time, the angular velocity of the system is prevented from coinciding with the critical speed of the original system, and the vibration can be reduced significantly.

- A sudden switching gives more reduction than a gradual switching, in the examples studied.
- An increase of the stiffness of the internal support causes a slightly greater reduction of displacement.
- There is a tendency to get more displacement reduction when the internal support is located closer to the disk location.
- An increase of the external damping causes the displacement to decrease and the angular velocity to increase more slowly. Then, the Sommerfeld effect is seen more clearly.
- The internal support can be activated based on the time or on the angular velocity. In both cases, the internal support is activated before passing the critical speed and deactivated after passing the critical speed. The reduction of maximum displacement tends to be greater if the support is active for a longer time.
- A restoring torque gives a smaller displacement reduction, due to the discontinuity caused by the application or removal of this torque.
- In the examples studied, the use of internal support often reduces the maximum displacement of the disk by more than 50 percent.
- Application of the internal support may overcome the insufficient power of nonideal motor passing through the critical speed.

5.2. Recommendations for Further Research

In the case of the vibration suppression of the rotating shaft, more study is needed. Several topics for further research are suggested as follows:

- It would be interesting to analyze influence of flexible supports at the ends of the shaft on the reduction of the vibration.
- A non-circular cross section might have a significant effect on the behavior.
- An experimental study should be carried out to verify the results.

REFERENCES

Abdel-Mooty, M., and Roorda, J., 1991, "Free Vibrations of Continuous Beams with Singularities in Inertia and Stiffness Distribution," **Dynamics and Stability of Systems**, Vol. 6, No. 1, pp. 1-16.

Aiba, S., 1976., "On the Vibration of a Rotating Shaft Passing Through the Critical Speed," **Bulletin of the JSME**, Vol. 19, No. 128, pp. 95-102.

Andruet, R. H., 1991, **Behavior of a Cracked Shaft During Passage Through a Critical Speed**, M.S. Thesis, Virginia Polytechnic Institute and State University, Blacksburg, Virginia.

Bachschmid, N., Diana, G., and Pizzigoni, B., 1984, "The Influence of Unbalance on Cracked Rotors," in: **Vibrations in Rotating Machinery**, The Institution of Mechanical Engineers, London, pp. 193-198.

Baker, J. G., 1939, "Mathematical-Machine Determination of the Vibration of an Accelerated Unbalanced Rotor," **Transactions of the ASME**, Vol. 61, pp. A145-A150.

Bently, D. E., 1993, "Shaft Crack Detection in Rotating Machinery," in: **The Systems Engineering Approach to Mechanical Failure Prevention**, The Vibration Institute, Willowbrook, Illinois, pp. 27-36.

Bently, D. E., and Muszynska, A., 1986, "Detection of Rotor Cracks," **Texas A&M 15th Turbomachinery Symposium**, Corpus Christi, Texas, pp. 129-139.

Bodger, W. K., 1967, "Deceleration of an Unbalanced Rotor Through a Critical Speed," **Journal of Engineering for Industry**, Vol. 89, pp. 582-586.

Capello, A., 1967, "On the Acceleration of Rotors Through Their Critical Speed," **Meccanica**, Vol. 2, pp. 144-152.

Chang, C. O., and Cheng, J. W., 1993, "Non-linear Dynamics and Instability of a Rotating Shaft-Disk System," **Journal of Sound and Vibration**, Vol. 160, No. 3, pp. 433-454.

Chen, L.-W., and Ku, D.-M., 1992, "Dynamic Stability of a Cantilever Shaft-Disk System," **Journal of Vibration and Acoustics**, Vol. 114, No. 3, pp. 326-329.

Christ, H., 1969, "An- und Auslauf eines gedämpften, unwuchterregten Schwingers," **VDI-Berichte**, No. 135, pp. 109-114.

Collins, K. R., Plaut, R. H., and Wauer, J., 1991, "Detection of Cracks in Rotating Timoshenko Shafts Using Axial Impulses," **Journal of Vibration and Acoustics**, Vol. 113, No. 1, pp. 74-78.

Collins, K. R., Plaut, R. H., and Wauer, J., 1992, "Free and Forced Longitudinal Vibrations of a Cantilevered Bar with a Crack," **Journal of Vibration and Acoustics**, Vol. 114, No. 2, pp. 171-177.

Craggs, A., 1993, "Effect of Distributed Bearing Stiffness on the Critical Speeds of Shafts," **Journal of Sound and Vibration**, Vol. 160, No. 3, pp. 559-565.

De Choudhury, P., 1986, "Torsional System Design Relative to Synchronous Motor Start-Up with a Variable Frequency Power Supply System," in: **Proceedings of the International Conference on Rotordynamics (IFToMM)**, Tokyo, pp. 325-328.

Dimarogonas, A. D., 1993, "Bilinear Analysis for Closing Cracks in Rotating Shafts," in: **Rotating Machinery - 1992**, W.-J. Yang and J. H. Kim, eds., Begell House, New York, Vol. 2, pp. 1009-1014.

Dimarogonas, A.D., 1995, "Vibration Monitoring of Cracked Structures: A State of the Art Review," **Engineering Fracture Mechanics**, to appear.

Dimentberg, M., Chapdelaine, J., Harrison, R., and Norton, R. L., 1994, "Passage Through Critical Speed with Limited Power by Switching System Stiffness," in: **Nonlinear and Stochastic Dynamics**, A. K. Bajaj, N. S. Namachchivaya, and R. A. Ibrahim, eds., AMD-Vol. 192, DE-Vol. 78, ASME, New York, pp. 57-67.

Dirr, B. O., Popp K., and Rothkegel, W., 1994, "Detection and Simulation of Small Transverse Cracks in Rotating Shafts," **Archive of Applied Mechanics**, Vol. 64, pp. 206-222.

El-Dannanh, E. H., and Farghaly, S. H., 1994, "Natural Vibrations of Cracked Shafts Carrying Elastically Mounted End Masses," **Journal of Sound and Vibration**, Vol. 170, No. 5, pp. 607-620.

Evan-Iwanowski, R. M., 1976, **Resonance Oscillations in Mechanical Systems**, Elsevier, New York.

Fang, Z. C., and Luo Z. H., 1989, "Transient Vibration of an Asymmetric Rotor System Through Critical Speed," in: **Rotating Machinery Dynamics**, T. S. Sankar et al., eds, DE-Vol. 18-1, ASME, New York, pp. 191-197.

Gao, J.-M., and Zhu, X.-M., 1992, "The Resonance of a Vertical Rotor Containing a Transverse Crack," **Acta Mechanica Solida Sinica** (English Edition), Vol.5, No. 2, pp. 167-174.

Gasch, R., 1976, "Dynamic Behaviour of a Simple Rotor with a Cross-Sectional Crack," in: **Vibrations in Rotating Machinery**, The Institution of Mechanical Engineers, London, pp. 123-128.

Gasch, R., Markert, R., and Pfützner, H., 1979, "Acceleration of Unbalanced Flexible Rotors Through the Critical Speeds," **Journal of Sound and Vibration**, Vol. 63, pp. 393-409.

Genta, G., and Delprete, C., 1995, "Acceleration Through Critical Speed of an Anisotropic, Non-linear, Torsionally Stiff Rotor with Many Degrees of Freedom," **Journal of Sound and Vibration**, Vol. 180, No. 3, pp. 369-386.

Horrigan, D. P. W., Williams, J. F., and Parszewski, Z. A., 1993, "Modal Aspects of Cracks in Rotors," in: **Rotating Machinery - 1992**, W.-J. Yang and J. H. Kim, eds., Begell House, New York, Vol. 2, pp. 1035-1043.

Huang, S. C., Huang, Y. M., and Shieh, S. M., 1993, "Vibration and Stability of a Rotating Shaft Containing a Transverse Crack," **Journal of Sound and Vibration**, Vol. 162, No. 3, pp. 387-401.

Ishida, Y., Hirokawa, K., and Hirose, M., 1995, "Vibrations of a Cracked Rotor (3/2-Order Super-Subharmonic and 1/2-Order Subharmonic Resonances)," in: **Vibration of Nonlinear, Random, and Time-Varying Systems**, DE-Vol. 84-1, ASME, New York, pp. 605-612.

Ishida, Y., Ikeda, T., Yamamoto, T., and Murakami, S., 1989, "Nonstationary Vibration of a Rotating Shaft with Nonlinear Spring Characteristics During Acceleration Through a Critical Speed," **JSME International Journal**, Series III, Vol. 32, No. 4, pp. 575-584.

Ishida, Y., and Yamamoto, T., 1993, "Vibrations of a Rotating Shaft Containing a Transverse Crack (Vibrations at the Secondary Critical Speed)," in: **Rotating Machinery - 1992**, W.-J. Yang and J. H. Kim, eds., Begell House, New York, Vol. 2, pp. 1015-1024.

Ishida, Y., Yamamoto, T., and Hirokawa, K., 1994, "Vibrations of a Rotating Shaft Containing a Transverse Crack (Major Critical Speed of a Horizontal Shaft)," in: **Proceedings of the 4th International Conference on Rotor Dynamics**, R. L. Eshleman and N. F. Rieger, eds, The Vibration Institute, Willowbrook, Illinois, pp. 47-52.

Iwata, Y. and Nonami, K., 1984, "Vibration Control of Rotating Shaft with Self-optimizing Support System," **Bulletin of the JSME**, Vol. 27, No. 228, pp. 1306-1311.

Iwatsubo, T., 1976, "Vibration of Rotors Through Critical Speeds," **Shock and Vibration Digest**, Vol. 8, No. 2, pp. 89-98.

Iwatsubo, T., Arii, S., and Oks, A., 1992, "Detection of a Transverse Crack in a Rotor Shaft by Adding External Force," in: **Vibrations in Rotating Machinery**, The Institution of Mechanical Engineers, London, pp. 275-282.

Iwatsubo, T., Kanki, H., and Kawai, R., 1972, "Vibration of Asymmetric Rotor Through Critical Speed with Limited Power Supply," **Journal of Mechanical Engineering Science**, Vol 14, No. 3, pp. 184-194.

Iwatsubo, T., Yamamoto, Y., and Kawai, R., 1986, "Startup Torsional Vibration of Rotating Machine Driven by Synchronous Motor," in: **Dynamics of Multibody Systems**, G. Bianchi and W. Schiehlen, eds., Springer-Verlag , Berlin, pp. 91-102.

Jialiu, G., and Nanqei, W., 1986, "Vibrational Characteristics of the Cantilever Rotor with a Cracked Shaft," in: **Proceedings of the International Conference on Vibration Problems**, Xi'an, China, pp. 793-798.

Jiang, W.-K, and Luo, Z. H., 1992, "The Vibrational Behavior of Vertical Rotor with Cracked Shaft," in: **Proceedings of International Conference on Rotordynamics**, Venice, Italy, pp. 27-34.

Jiang, W.-K., Luo, Z., and Fang, Z., 1990, "A Transient Analysis of Vertical Cracked Rotor Through Critical Speed," in: **Proceedings of International Conference on Hydrodynamic Bearing-Rotor System Dynamics**, X'ian, People's Republic of China, pp. 278-282.

Jun, O. S., Eun, H. J., Earmme, Y. Y., and Lee, C. -W., 1992a, "Modelling and Vibration Analysis of a Simple Rotor with a Breathing Crack," **Journal of Sound and Vibration**, Vol. 155, pp. 273-290.

Jun, O. S., Lee, C.-W., Earmme, Y. Y., and Eun, H. J., 1992b, "Analysis of Crack Growth in a Simple Rotor with a Breathing Crack," **Machine Vibration**, Vol. 1, pp. 231-235.

Jun, O. S., Lee, C.-W., Earmme, Y. Y., and Eun, H. J., 1993, "New Approach for the Modeling and Simulation of Simple Cracked Rotor," in: **Rotating Machinery - 1992**, W.-J. Yang and J. H. Kim, eds., Begell House, New York, Vol. 2, pp. 1025-1034.

Kato, M., Ota, H., and Nakamura S., 1992, "Equations of Motion of a Shaft-Rotor System with Variable Rotating Speed," in: **Vibrations in Rotating Machinery**, The Institution of Mechanical Engineers, London, pp. 469-473.

Kavarana, F. H., and Kirk, R. G., 1995, "Cracked Shaft Detection Using the Unbalance Excitation Technique," in: **Acoustics, Vibrations, and Rotating Machines**, DE-Vol. 84-2, ASME, New York, pp. 1001-1007.

Kemke, M. A., Brandon, J. A., Holford, K., and Bieberstein, B., 1994, "Condition Monitoring of Cracked Rotating Shafts by Signal Analysis," **Machine Vibration**, Vol. 3, pp. 62-68.

Khader, N., 1995, "Stability of Rotating Shafts Loaded by Follower Axial Force and Torque Load," **Journal of Sound and Vibration**, Vol. 182, No. 5, pp. 759-773.

Kirk, R. G., and Gunter, E. J., 1972, "The Effect of Support Flexibility and Damping on the Synchronous Response of a Single-Mass Flexible Rotor," **Journal of Engineering for Industry**, Vol. 94, pp. 221 -228.

Kotera, T., 1974, "Vibration of Flexible Rotor Driven by Limited Torque Through its Critical Speed," **Bulletin of the JSME**, Vol. 17, No. 108, pp. 686-692.

Lee, A.-C., Kang, Y., Tsai, K.-L., and Hsiao, K.-M., 1992a, "Transient Analysis of an Asymmetric Rotor-Bearing System During Acceleration," **Journal of Engineering for Industry**, Vol. 114, pp. 465-475.

Lee, C.-W., Yun, J.-S., and Jun, O. S., 1992b, "Modeling of a Simple Rotor with a Switching Crack and its Experimental Verification," **Journal of Vibration and Acoustics**, Vol. 114, pp. 217-225.

Leipholz, H. H. E., 1987, **Stability Theory: An Introduction to the Stability of Dynamic Systems and Rigid Bodies**, Wiley, New York.

Lewis, F. M., 1932, "Vibration During Acceleration Through a Critical Speed," **Transactions of the ASME**, Vol. 54, pp. 253-261.

Liao, M., and Gasch, R., 1992, "Crack Detection in Rotating Shafts - An Experimental Study," in: **Vibrations in Rotating Machinery**, The Institution of Mechanical Engineers, London, pp. 289-295.

Li-Tang, Y., and Qi-Han, L., 1981, "Experiments on the Vibration Characteristics of a Rotor with Flexible, Damped Support," **Journal of Engineering for Power**, Vol. 103, pp. 174-179.

Macchia, D., 1963, "Acceleration of an Unbalanced Rotor Through the Critical Speed," **Transactions of the ASME**, Vol. 85, pp. 2-7.

Matsuura, K., 1977, "A Method for Estimating the Conditions that a Rotor can Pass Through Resonance," **Bulletin of the JSME**, Vol. 20, No. 145, pp. 801-810.

Meng, G., and Gasch, R., 1992, "The Nonlinear Influences of Whirl Speed on the Stability and Responses of a Cracked Rotor," **Machine Vibration**, Vol. 1, pp. 216-230.

Meng, G., and Gasch, R., 1993, "Stability and Stability Degree of a Cracked Flexible Rotor Supported on Journal Bearings," in: **Vibration of Rotating Systems**, K.W. Wang and D. Segalman, eds., DE-Vol. 60, ASME, New York, pp. 315-323.

Meng, G., and Hahn, E.J., 1993, "Dynamic Responses of a Rotor with a Small Crack and the Detection of Crack," School of Mechanical and Manufacturing Engineering, The University of New South Wales, Australia, pp. 1-24

Müller, P. C., Bajkowski, J., and Söffker, D., 1994, "Chaotic Motions and Fault Detection in a Cracked Rotor," **Nonlinear Dynamics**, Vol. 5, pp. 233-254.

Muszynska, A., 1982, "Shaft Crack Detection," in**: Proceedings, 7th Machinery Dynamics Seminar**, Edmonton, Canada.

Muszynska, A., Goldman, P., and Bently, D. E., 1992, "Torsional/Lateral Vibration Cross-Coupled Responses due to Shaft Anisotropy: A New Tool in Shaft Crack Detection," in: **Vibrations in Rotating Machinery**, The Institution of Mechanical Engineers, London, pp. 257-262.

Nagaya, K., Takeda, S., Tsukui, Y., and Kumaido, T., 1987, "Active Control Method for Passing Through Critical Speeds of Rotating Shafts by Changing Stiffnesses of the Supports with Use of Memory Metals," **Journal of Sound and Vibration**, Vol. 113, No. 2, pp. 307-315.

Naveh, B. M., and Brach, R. M., 1977, "On the Transition of a Shaft Through Critical Speeds," **Journal of Dynamic Systems, Measurement, and Control**, Vol. 99, pp. 48-50.

Nelson, H. D., and Nataraj, C., 1986, "The Dynamics of a Rotor System with a Cracked Shaft," **Journal of Vibration, Acoustics, Stress, and Reliability in Design**, Vol. 108, pp. 189-196.

Nonami, K., 1983a, "Response in Passing Through Critical Speed of Arbitrarily Distributed Flexible Rotor System (Part 1, Case Without Gyroscopic Effect)," **Bulletin of the JSME**, Vol. 26, No. 217, pp. 1198-1204.

Nonami, K., 1983b, "Response in Passing Through Critical Speed of Arbitrarily Distributed Flexible Rotor System (Part 2, Case With Gyroscopic Effect)," **Bulletin of the JSME**, Vol. 26, No. 217, pp. 1205-1212.

Nonami, K., and Miyashita, M., 1978, "Problem of Rotor Passing Through Critical Speed with Gyroscopic Effect (Analysis by Asymptotic Method and Experiments)," **Bulletin of the JSME**, Vol. 21, No. 151, pp. 56-63.

Nonami, K., and Miyashita, M., 1980, "Problem of Rotor Passing Through Critical Speed with Gyroscopic Effect (3th Report, Case of Rotating Shaft on Flexible Supports)," **Bulletin of the JSME**, Vol. 23, No. 186, pp. 2104-2110.

Ostachowicz, W. M., and Krawczuk, M., 1992, "Coupled Torsional and Bending Vibrations of a Rotor with an Open Crack," **Archive of Applied Mechanics**, Vol. 62, pp. 191-201.

Papadopoulos, C. A., and Dimarogonas, A. D., 1987a, "Coupled Longitudinal and Bending Vibrations of a Rotating Shaft with an Open Crack," **Journal of Sound and Vibration**, Vol. 117, No. 1, pp. 81-93.

Papadopoulos, C. A., and Dimarogonas, A. D., 1987b, "Coupling of Bending and Torsional Vibration of a Cracked Timoshenko Shaft," **Ingenieur-Archiv**, Vol. 57, pp. 257-266.

Papadopoulos, C. A., and Dimarogonas, A. D., 1988a, "Coupled Longitudinal and Bending Vibrations of a Cracked Shaft," **Journal of Vibration, Acoustics, Stress, and Reliability in Design**, Vol. 110, pp. 1-8.

Papadopoulos, C. A., and Dimarogonas, A. D., 1988b, "Stability of Cracked Rotors in the Coupled Vibration Mode," **Journal of Vibration, Acoustics, Stress, and Reliability in Design**, Vol. 110, pp. 356-359.

Papadopoulos, C. A., and Dimarogonas, A. D., 1992, "Coupled Vibration of Cracked Shafts," **Journal of Vibration and Acoustics**, Vol. 114, pp. 461-467.

Peeken, H., Troeder, C., and Diekhans, G., 1980, "Torsional Vibrations during the Starting Process in Driving Systems with Three Phase Motors," in: **Vibrations in Rotating Machinery**, The Institution of Mechanical Engineers, London, pp. 427-435.

Plaut, R. H., Andruet, R. H., and Suherman, S., 1994, "Behavior of a Cracked Rotating Shaft During Passage Through a Critical Speed," **Journal of Sound and Vibration**, Vol. 173, No. 5, pp. 577-589.

Plaut, R. H., and Wauer, J., 1995, "Parametric, External, and Combination Resonances in Coupled Flexural and Torsional Oscillations of an Unbalanced Rotating Shaft," **Journal of Sound and Vibration**, Vol. 183, No. 5, pp. 889-897.

Prabhu, B. S., Bhat, R. B., and Sankar, T. S., 1987, "Analysis of Deceleration Phenomenon of High Speed Rotor Systems," **Mechanical Systems and Signal Processing**, Vol . 1, No. 3, pp. 293-299.

Qiu, J., 1992, "The Vibrations of Mechanical and Electromagnetic Coupling of an A.C. Motor in the Starting Process," in: **Vibrations in Rotating Machinery**, The Institution of Mechanical Engineers, London, pp. 523-527.

Rajac, T. J., and Evan-Iwanowski, R. M., 1976, "Interaction of a Motor with Limited Power with Dissipative (Hysteretic) Foundation," in**: Developments in Theoretical and Applied Mechanics**, R. P. McNitt, ed., Proceedings, 8th SECTAM, pp. 349-361.

Rajalingham, C., Bhat, R. B., and Xistris, G. D., 1992, "Influence of Support Flexibility and Damping Characteristics on the Stability of Rotors with Stiffness Anisotropy About Shaft Principal Axes," **International Journal of Mechanical Sciences**, Vol. 34, No. 9, pp. 717-726.

Ratan, S., Baruh, H., and Rodriguez, J., 1993, "On-Line Identification and Location of Rotor Cracks," in: **Nonlinear Vibrations**, R. A. Ibrahim, A. K. Bajaj, and L. A. Bergman, eds., DE-Vol.54, ASME, New York, pp. 161-170.

Ratan, S., Baruh, H., and Rodriguez, J., 1996, "On-Line Identification and Location of Rotor Cracks," **Journal of Sound and Vibration**, to appear.

Schmied, J., and Krämer, E., 1984, "Vibrational Behaviour of a Rotor with a Cross-Sectional Crack," in: **Vibrations in Rotating Machinery**, The Institution of Mechanical Engineers, London, pp. 183-192.

Seibold, S., Fritzen, C.-P., and Wagner, D., 1995, "Employing Identification Procedures for the Detection of Cracks in Rotors," in: **13th International Modal Analysis Conference**, Vol. II, Society of Engineering Mechanics, Bethel, Connecticut, pp. 1378-1384.

Segalman, D. J., Parker, G. G., and Inman, D. J., 1993, "Vibration Suppression by Modulation of Elastic Modulus Using Shape Memory Alloy," in: **Intelligent Structures, Materials and Vibrations**, M. Shahinpoor and H. S. Tzou, eds., DE-Vol.58, ASME, New York, pp. 1-5.

Sekhar, A. S., and Prabhu, B. S., 1994a, "Vibration and Stress Fluctuation in Cracked Shafts," **Journal of Sound and Vibration**, Vol. 169, No. 5, pp. 655-667.

Sekhar, A. S., and Prabhu, B. S., 1994b, "Transient Analysis of a Cracked Rotor Passing Through Critical Speed," **Journal of Sound and Vibration**, Vol. 173, No. 3, pp. 415-421.

Shneerson, Y. B., 1993, "Dynamic Stability and Forced Vibrations of a Horizontal Rotor with a Cracked Shaft," in: **Asymptotic Methods in Mechanics**, R. Vaillancourt and A. L. Smirnov, eds., American Mathematical Society, Providence, Rhode Island, pp. 245-253.

Söffker, D., Bajkowski, J., and Müller, P. C., 1993, "Crack Detection in Turbo Rotors-Vibrational Analysis and Fault Detection," in: **Vibration of Rotating Systems**, DE-Vol. 60, ASME, New York, pp. 277-287.

Suherman, S., 1992, **Response of a Cracked Rotating Shaft with a Disk During Passage Through a Critical Speed**, M.S. Thesis, Virginia Polytechnic Institute and State University, Blacksburg, Virginia.

Suherman, S., and Plaut, R. H., 1993, "Flexural-Torsional Response of a Cracked Rotating Shaft with a Disk During Passage Through a Critical Speed," in: **Dynamics and Vibration of Time-Varying Structures and Systems**, S. C. Sinha and R. M. Evan-Iwanowski, eds., DE-Vol. 56, ASME, New York, pp. 287-293.

Suherman, S., and Plaut, R. H., 1995, "Effects of Flexible Supports and Gyroscopic Moments on Passage of a Cracked Shaft Through a Critical Speed," in: **Vibration of Nonlinear, Random, and Time-Varying Systems**, DE-Vol. 84-1, ASME, New York, pp. 251-257.

Tsuchiya, K., 1982, "Passage of a Rotor Through a Critical Speed," **Journal of Mechanical Design**, Vol. 104, pp. 370-374.

Turkstra, T. P., and Semercigil, S. E., 1993a, "An Add-On Suspension for Controlling the Vibrations of Shafts Accelerating to Supercritical Speeds," **Journal of Sound and Vibration**, Vol. 163, No. 2, pp. 327-341.

Turkstra, T. P., and Semercigil, S. E., 1993b, "Elimination of Resonance with a Switching Tensile Support," **Journal of Sound and Vibration**, Vol. 163, No. 2, pp. 359-362.

Viderman, Z., and Porat, I., 1987, "An Optimal Control Method for Passage of a Flexible Rotor Through Resonances," **Journal of Dynamic Systems, Measurement and Control**, Vol. 109, pp. 216-223.

Wang, Y. B., Duan, Z. S., Huang, X. L., and Wen, B. C., 1987, "The Response of the Simple Rotor with Surface Transverse Crack," in: **Rotating Machinery Dynamics**, 11th Biennial Conference on Mechanical Vibration and Noise, Boston, DE-Vol. 2, ASME, New York, pp. 595-600.

Wauer, J., 1986, "Secondary Effects in Transient Vibrations of Rotating Shafts Through Critical Speeds," in: **Proceedings, 1st International Conference on Vibration Problems in Engineering**, X'ian, People's Republic of China, pp. 763-768.

Wauer, J., 1990a, "Modelling and Formulation of Equations of Motion for Cracked Rotating Shafts," **International Journal of Solids and Structures**, Vol. 26, No. 8, pp. 901-914.

Wauer, J., 1990b, "On the Dynamics of Cracked Rotors: A Literature Survey," **Applied Mechanics Reviews**, Vol. 43, pp. 13-17.

Wauer, J., and Suherman, S., 1996, "Vibration Suppression of Rotating Shafts Passing Through Resonances by Switching Shaft Stiffness," **Journal of Vibration and Acoustics**, to appear.

Wauer, J., and Wei, H., 1991, "On the Dynamics of a Horizontal, Rotating, Curved Shaft," **International Series of Numerical Mathematics**, Vol. 97, pp. 361-365.

Yamakawa, H., 1988, "Optimum Designs of Rotating Shaft Systems for Nonlinear Dynamic Responses," in: **Structural Optimization**, G. I. N. Rozvany and B. L. Karihaloo, eds., Kluwer Academic Publishers, Dordrecht, The Netherlands, pp. 363-370.

Yamakawa, H., and Murakami, S., 1989, "Optimum Designs of Operating Curves for Rotating Shaft Systems with Limited Power Supplies," in: **Current Topics in Stuctural Mechanics - 1989**, H. Chung, ed., PVP-Vol. 179, ASME, New York, pp. 181-185.

Yanabe, S., 1980, "Vibration of a Shaft Passing Through a Critical Speed (4th Report, Effect of Gyroscopic Moment)," **Bulletin of the JSME**, Vol. 23, No. 180, pp. 945-952.

Yanabe, S., and Tamura, A., 1980, "Vibration of a Rotating Shaft Passing Through Two Critical Speeds," in: **Vibrations in Rotating Machinery**, The Institution of Mechanical Engineers, London, pp. 29-35.

Ying, S.-J., 1987, "Transient Whirling of a Rotating Shaft with an Unbalanced Disk," in: **Rotating Machinery Dynamics,** A. Muszynska and J. C. Simonis, eds., DE-Vol. 2, ASME, New York, Vol. 2, pp. 537-543.

Young, T. H., and Liou, G. T., 1993, "Dynamic Response of Rotor-Bearing Systems with Time-Dependent Spin Rates," **Journal of Engineering for Gas Turbines and Power**, Vol. 115, pp. 239-245.

Yun, J.-S., and Lee, C.-W., 1993, "Dynamic Analysis of Flexible Rotors Subjected to Torque and Force," in: **Vibration of Rotating Systems**, K.W. Wang and D. Segalman, eds., DE-Vol. 60, ASME, New York, pp. 331-338.

Zobnin, A. P., Kelzon, A. S., and Neigebauer, I. I., 1987, "Influence of Gyroscopic Effect on Resonance Avoidance During Acceleration of Unbalanced Flexible Rotors," **Vibration Engineering**, Vol. 1, pp. 269-281.

APPENDIX A

DERIVATION OF EQUATIONS OF MOTION

FOR IDEAL MOTOR

Hamilton's Principle:

$$\delta \int_{t_0}^{t_1} (T - V)\, dt + \int_{t_0}^{t_1} \delta W\, dt = 0 \tag{A.1}$$

Kinetic Energy (T):

$$T = \int_{-l_1}^{L+l_2} \frac{1}{2} \mu \left(v_t^2 - 2\dot{\theta} w v_t + \dot{\theta}^2 w^2 + w_t^2 + 2\dot{\theta} v w_t + \dot{\theta}^2 v^2 \right) dx$$

$$+ \int_{-l_1}^{L+l_2} \frac{1}{2} m\delta(x-c) \Big[v_t^2 - 2\dot{\theta} v_t (w + e_d \sin\delta_d) + \dot{\theta}^2 (w + e_d \sin\delta_d)^2$$

$$+ w_t^2 + 2\dot{\theta} w_t (v + e_d \cos\delta_d) + \dot{\theta}^2 (v + e_d \cos\delta_d)^2 \Big] dx$$

$$+ \int_{-l_1}^{L+l_2} \frac{1}{2} I_d\, \delta(x-c) \left(v_{tx}^2 - 2\dot{\theta} v_{tx} w_x + \dot{\theta}^2 w_x^2 \right) dx$$

$$+ \int_{-l_1}^{L+l_2} \frac{1}{2} I_d\, \delta(x-c) \left(w_{tx}^2 + 2\dot{\theta} w_{tx} v_x + \dot{\theta}^2 v_x^2 \right) dx$$

$$+\int_{-l_1}^{L+l_2}\frac{1}{2}I_p\,\delta(x-c)\left[\dot\theta^2\left(1-w_x{}^2-v_x{}^2\right)+2\dot\theta\,v_{tx}\,w_x\right]dx$$

$$+\frac{1}{2}\left(m_b|_{x=0,L}+m_c|_{x=L+l_2}\right)\left(v_t{}^2-2\dot\theta\,w\,v_t+\dot\theta^2w^2+w_t{}^2-2\dot\theta\,v\,w_t+\dot\theta^2v^2\right)$$

$$+\frac{1}{2}I_{dc}\left(v_{tx}{}^2-2\dot\theta\,v_{tx}w_x+\dot\theta^2w_x{}^2\right)+\frac{1}{2}I_{dc}\left(w_{tx}{}^2+2\dot\theta\,w_{tx}v_x+\dot\theta^2v_x{}^2\right)$$

$$+\frac{1}{2}I_{pc}\left[\dot\theta^2\left(1-w_x{}^2-v_x{}^2\right)+2\dot\theta\,v_{tx}w_x\right] \qquad \text{(A.2)}$$

Potential Energy (V):

$$V=\int_{-l_1}^{b_-}\frac{1}{2}EI\left(v_{xx}{}^2+w_{xx}{}^2\right)dx+\int_{b_+}^{L+l_2}\frac{1}{2}EI\left(v_{xx}{}^2+w_{xx}{}^2\right)dx$$

$$-\int_{-l_1}^{L+l_2}m\delta(x-c)\left[g\sin\theta\left(v+e_d\cos\delta_d\right)+g\cos\theta\left(w+e_d\sin\delta_d\right)\right]dx$$

$$-\int_{-l_1}^{L+l_1}\left(\mu\,g\,v\sin\theta+\mu\,g\,w\cos\theta\right)dx+m_b\,g\left(v\sin\theta+w\cos\theta\right)\Big|_{x=0,L}$$

$$+m_c\,g\left(v\sin\theta+w\cos\theta\right)\Big|_{x=L+l_2}+\frac{1}{2}s\left(v^2+w^2\right)\Big|_{x=0,L} \qquad \text{(A.3)}$$

Virtual work (δW):

$$\delta W=-\int_{-l_1}^{L+l_2}d_e\,\mu\left[\left(v_t-\dot\theta\,w\right)\delta v+\left(w_t+\dot\theta\,v\right)\delta w\right]dx$$

$$
-\int_{-l_1}^{b_-} d_i\, EI\left(v_{txx}\,\delta v_{xx} + w_{txx}\,\delta w_{xx}\right) dx - \int_{b_+}^{L+l_2} d_i\, EI\left(v_{txx}\,\delta v_{xx} + w_{txx}\,\delta w_{xx}\right) dx
$$

$$
+\int_{-l_1}^{L+l_2} \left(M_\zeta + m_\zeta\right)\left[\delta(x-b_+) - \delta(x-b_-)\right]\delta v_x\, dx
$$

$$
-\int_{-l_1}^{L+l_2} \left(M_\eta + m_\eta\right)\left[\delta(x-b_+) - \delta(x-b_-)\right]\delta w_x\, dx
$$

$$
-p\left[\left(v_t - \dot\theta\, w\right)\delta v + \left(w_t + \dot\theta\, v\right)\delta w\right]_{x=0,L} \qquad \text{(A.4)}
$$

$$
\delta \int_{t_0}^{t_1} (T - V)\, dt + \int_{t_0}^{t_1} \delta W\, dt =
$$

$$
\int_{t_0}^{t_1}\int_{-l_1}^{L+l_2} \left[\mu + m\delta(x-c)\right]\left(-v_{tt} + 2\dot\theta\, w_t + \dot\theta^2\, v + \ddot\theta\, w\right)\delta v\, dx\, dt
$$

$$
+\int_{t_0}^{t_1}\int_{-l_1}^{L+l_2} \left[\mu + m\delta(x-c)\right]\left(-w_{tt} - 2\dot\theta\, v_t + \dot\theta^2\, w - \ddot\theta\, v\right)\delta w\, dx\, dt
$$

$$
+\int_{t_0}^{t_1}\int_{-l_1}^{L+l_2} m e_d \delta(x-c)\left[\left(\ddot\theta \sin\delta_d + \dot\theta^2 \cos\delta_d\right)\delta v + \left(-\ddot\theta \cos\delta_d + \dot\theta^2 \sin\delta_d\right)\right]\delta w\, dx\, dt
$$

$$
+\int_{t_0}^{t_1}\int_{-l_1}^{L+l_2} I_d\left[\delta(x-c)\left(v_{ttxx} - 2\dot\theta\, w_{txx} - \dot\theta^2 v_{xx} - \ddot\theta\, w_{xx}\right)\right]\delta v\, dx\, dt
$$

$$
+\int_{t_0}^{t_1}\int_{-l_1}^{L+l_2} I_d\left[\delta'(x-c)\left(v_{ttx} - 2\dot\theta\, w_{tx} - \dot\theta^2 v_x - \ddot\theta\, w_x\right)\right]\delta v\, dx\, dt
$$

$$+\int_{t_0}^{t_1}\int_{-l_1}^{L+l_2} I_d\left[\delta(x-c)\left(w_{ttxx}+2\dot\theta\, v_{txx}-\dot\theta^2 w_{xx}+\ddot\theta\, v_{xx}\right)\right]\delta w\, dx\, dt$$

$$+\int_{t_0}^{t_1}\int_{-l_1}^{L+l_2} I_d\left[\delta'(x-c)\left(w_{ttx}+2\dot\theta\, v_{tx}-\dot\theta^2 w_{x}+\ddot\theta\, v_{x}\right)\right]\delta w\, dx\, dt$$

$$+\int_{t_0}^{t_1}\int_{-l_1}^{L+l_2} I_p\left[\delta(x-c)\left(\dot\theta\, w_{txx}+\dot\theta^2 v_{xx}+\ddot\theta\, w_{xx}\right)\right]\delta v\, dx\, dt$$

$$+\int_{t_0}^{t_1}\int_{-l_1}^{L+l_2} I_p\left[\delta'(x-c)\left(\dot\theta\, w_{tx}+\dot\theta^2 v_{x}+\ddot\theta\, w_{x}\right)\right]\delta v\, dx\, dt$$

$$+\int_{t_0}^{t_1}\int_{-l_1}^{L+l_2} I_p\left[\delta(x-c)\left(-\dot\theta\, v_{txx}+\dot\theta^2 w_{xx}\right)+\delta'(x-c)\left(-\dot\theta\, v_{tx}+\dot\theta^2 w_{x}\right)\right]\delta w\, dx\, dt$$

$$-\int_{t_0}^{t_1}\int_{-l_1}^{L+l_2}\left\{EI\, v_{xxxx}-\left[\mu+m\delta(x-c)\right]g\sin\theta\right\}\delta v\, dx\, dt$$

$$-\int_{t_0}^{t_1}\int_{-l_1}^{L+l_2}\left\{EI\, w_{xxxx}-\left[\mu+m\delta(x-c)\right]g\cos\theta\right\}\delta w\, dx\, dt$$

$$-\int_{t_0}^{t_1}\left[EI\, v_{xx}\,\delta v_x-EI\, v_{xxx}\,\delta v+EI\, w_{xx}\,\delta w_x-EI\, w_{xxx}\,\delta w\right]_{-l_1,\ 0_+,\ L_+}^{0_-,\ L_-,\ L+l_2} dt$$

$$-\int_{t_0}^{t_1}\int_{-l_1}^{L+l_2}\left[d_e\,\mu\left(v_t-\dot\theta\, w\right)+d_i EI\, v_{txxxx}\right]\delta v\, dx\, dt$$

$$-\int_{t_0}^{t_1}\int_{-l_1}^{L+l_2}\left[d_e\,\mu\left(w_t+\dot\theta\, v\right)+d_i EI\, w_{txxxx}\right]\delta w\, dx\, dt$$

$$-\int_{t_0}^{t_1} d_i \left[EI\, v_{txx}\, \delta v_x - EI\, v_{txxx}\, \delta v + EI\, w_{txx}\, \delta w_x - EI\, w_{txxx}\, \delta w \right]_{-l_1,\ 0_+,\ L_+}^{0_-,\ L_-,\ L+l_2} dt$$

$$-\int_{t_0}^{t_1} \int_{-l_1}^{L+l_2} \Lambda \left[\delta'(x-b_+) - \delta'(x-b_-) \right] \left[\left(M_\zeta + m_\zeta \right) \delta v - \left(M_\eta + m_\eta \right) \delta w \right] dx\, dt$$

$$+\int_{t_0}^{t_1} m_b \left[\left(-v_{tt} + 2\dot{\theta} w_t + \dot{\theta}^2 v + \ddot{\theta} w \right) \delta v + \left(-w_{tt} - 2\dot{\theta} v_t + \dot{\theta}^2 w - \ddot{\theta} v \right) \delta w \right]_0^L dt$$

$$+\int_{t_0}^{t_1} m_c \left[\left(-v_{tt} + 2\dot{\theta} w_t + \dot{\theta}^2 v + \ddot{\theta} w \right) \delta v + \left(-w_{tt} - 2\dot{\theta} v_t + \dot{\theta}^2 w - \ddot{\theta} v \right) \delta w \right]_{x=L+l_2} dt$$

$$-\int_{t_0}^{t_1} \left[I_{dc} \left(v_{ttxx} - 2\dot{\theta} w_{tx} - \dot{\theta}^2 v_x - \ddot{\theta} w_x \right) + I_{pc} \left(\dot{\theta} w_{tx} + \dot{\theta}^2 v_x + \ddot{\theta} w_x \right) \right] \delta v_x \Big|_{x=L+l_2} dt$$

$$+\int_{t_0}^{t_1} \left[I_{dc} \left(-w_{ttxx} - 2\dot{\theta} v_{tx} + \dot{\theta}^2 w_x - \ddot{\theta} v_x \right) + I_{pc} \left(\dot{\theta} v_{tx} - \dot{\theta}^2 w_x \right) \right] \delta w \Big|_{x=L+l_2} dt$$

$$-\int_{t_0}^{t_1} \left[m_b\, g \sin\theta\, \delta v + m_b\, g \cos\theta\, \delta w \right]_0^L dt$$

$$-\int_{t_0}^{t_1} \left[m_c\, g \sin\theta\, \delta v + m_c\, g \cos\theta\, \delta w \right]_{x=L+l_2} dt \; - \int_{t_0}^{t_1} \left(s_v \delta v + s_w \delta w \right) \Big|_{x=0,L} dt$$

$$-\int_{t_0}^{t_1} p \left[\left(v_t - \dot{\theta} w \right) \delta v + \left(w_t + \dot{\theta} v \right) \delta w \right]_{x=0,L} dt \;=\; 0 \qquad \text{(A.5)}$$

APPENDIX B

INTEGRATION FORMULAS

$$\int_a^b f(x)\,\delta(x-\xi)\,dx = f(\xi), \quad a < \xi < b$$

$$\int_0^L \sin\frac{n\pi x}{L}\,dx = \frac{L}{n\pi}\left[1-(-1)^n\right]$$

$$\int_{-l_1}^0 \sin\frac{n\pi x}{L}\,dx = -\frac{L}{n\pi}\left[1-\cos\frac{n\pi l_1}{L}\right]$$

$$\int_L^{L+l_2} \sin\frac{n\pi x}{L}\,dx = -\frac{L}{n\pi}\left[\cos\frac{n\pi(L+l_2)}{L}-(-1)^n\right]$$

$$\int_0^L \sin\frac{k\pi x}{L}\sin\frac{n\pi x}{L}\,dx = \begin{cases}\dfrac{L}{2} & \text{if } k = n\\ 0 & \text{if } k \neq n\end{cases}$$

$$\int_{-l_1}^0 \sin\frac{k\pi x}{L}\sin\frac{n\pi x}{L}\,dx = \begin{cases}-\dfrac{L}{4k\pi}\sin\dfrac{2k\pi l_1}{L}+\dfrac{l_1}{2} & \text{if } k = n\\ -\dfrac{1}{2}\left[\dfrac{L}{(k+n)\pi}\sin(k+n)\pi\dfrac{l_1}{L}\right] & \\ \quad +\dfrac{1}{2}\left[\dfrac{L}{(k-n)\pi}\sin(k-n)\pi\dfrac{l_1}{L}\right] & \text{if } k \neq n\end{cases}$$

$$\int_{L}^{L+l_2} \sin\frac{k\pi x}{L}\sin\frac{n\pi x}{L}\,dx = \begin{cases} -\dfrac{L}{4k\pi}\sin\dfrac{2k\pi(L+l_2)}{L} + \dfrac{l_2}{2} & \text{if } k = n \\ -\dfrac{1}{2}\left[\dfrac{L}{(k+n)\pi}\sin(k+n)\pi\dfrac{(L+l_2)}{L}\right] & \\ \quad +\dfrac{1}{2}\left[\dfrac{L}{(k-n)\pi}\sin(k-n)\pi\dfrac{(L+l_2)}{L}\right] & \text{if } k \neq n \end{cases}$$

$$\int_0^L x\sin\frac{n\pi x}{L}\,dx = -\frac{L^2}{n\pi}\cos n\pi$$

$$\int_{-l_1}^{0} x\sin\frac{n\pi x}{L}\,dx = \frac{L^2}{(n\pi)^2}\sin\frac{n\pi l_1}{L} - \frac{Ll_1}{n\pi}\cos\frac{n\pi l_1}{L}$$

$$\int_L^{L+l_2} x\sin\frac{n\pi x}{L}dx = \frac{L^2}{(n\pi)^2}\sin\frac{n\pi(L+l_2)}{L} - \frac{L(L+l_2)}{n\pi}\cos\frac{n\pi(L+l_2)}{L} + \frac{L^2}{n\pi}\cos n\pi$$

$$\int_0^L x\cos\frac{n\pi x}{L}\,dx = \frac{L^2}{(n\pi)^2}\left(\cos n\pi - 1\right)$$

$$\int_0^L \delta'(x-b_+)\sin\frac{n\pi x}{L}\,dx - \int_0^L \delta'(x-b_-)\sin\frac{n\pi x}{L}\,dx =$$

$$= \left[\delta(x-b_+)\sin\frac{n\pi x}{L}\right]_0^L - \int_0^L \delta(x-b_+)\frac{n\pi}{L}\cos\frac{n\pi x}{L}\,dx$$

$$-\left[\delta(x-b_-)\sin\frac{n\pi x}{L}\right]_0^L - \int_0^L \delta(x-b_-)\frac{n\pi}{L}\cos\frac{n\pi x}{L}\,dx$$

$$= -\frac{n\pi}{L}\left(\cos\frac{n\pi b_+}{L} - \cos\frac{n\pi b_-}{L}\right) = -\frac{n\pi}{L}\left(-2\sin\frac{n\pi b}{L}\sin\frac{n\pi\varepsilon}{2L}\right)$$

$$= -\frac{n\pi}{L}\left(-2\sin\frac{n\pi b}{L}\cdot\frac{n\pi\varepsilon}{2L}\right) = \left(\frac{n\pi}{L}\right)^2 \varepsilon\sin\frac{n\pi b}{L}$$

$$\int_0^L \delta'(x-b_+)\,x\,dx - \int_0^L \delta'(x-b_-)\,x\,dx = 0$$

$$\int_0^L \delta'(x-b_+)\,dx - \int_0^L \delta'(x-b_-)\,dx = 0$$

$$\int_0^L \delta'(x-c)\,x\,dx = -1$$

$$\int_0^L \delta'(x-c)\sin\frac{n\pi x}{L}\,dx = -\frac{n\pi}{L}\cos\frac{n\pi c}{L}$$

$$\int_0^L \delta'(x-c)\cos\frac{n\pi x}{L}\,dx = \frac{n\pi}{L}\sin\frac{n\pi c}{L}$$

$$\int_0^L \delta'(x-c)\cos\frac{n\pi x}{L}\,x\,dx = -\cos\frac{n\pi c}{L} + \frac{n\pi c}{L}\sin\frac{n\pi c}{L}$$

$$\int_0^L \delta'(x-c)\sin\frac{n\pi x}{L}\cos\frac{k\pi x}{L}\,dx = \frac{k\pi}{L}\sin\frac{k\pi c}{L}\sin\frac{n\pi c}{L} - \frac{n\pi}{L}\cos\frac{k\pi c}{L}\cos\frac{n\pi c}{L}$$

APPENDIX C

DERIVATION

OF $\dot{\theta}$ - EQUATION OF MOTION

Additional $\dot{\theta}$ - equation of motion derivation by Hamilton's Principle:

$$\delta \int_{t_0}^{t_1} (T - V)\, dt + \int_{t_0}^{t_1} \delta W\, dt =$$

$$\int_{t_0}^{t_1} \int_{-l_1}^{L+l_2} \mu \left[v_{tt} w - v w_{tt} - 2\dot{\theta}\left(v v_t + w w_t\right) - \ddot{\theta}\left(w^2 + v^2\right) \right] \delta\theta \, dx \, dt$$

$$+ \int_{t_0}^{t_1} \int_{-l_1}^{L+l_2} m\delta(x - c) \left[v_{tt}\left(w + e_d \sin\delta_d\right) - w_{tt}\left(v + e_d \cos\delta_d\right) - 2\dot{\theta} w_t \left(w + e_d \sin\delta_d\right) \right.$$

$$\left. -2\dot{\theta} v_t \left(v + e_d \cos\delta_d\right) - \ddot{\theta}\left(w + e_d \sin\delta_d\right)^2 - \ddot{\theta}\left(v + e_d \cos\delta_d\right)^2 \right] \delta\theta \, dx \, dt$$

$$+ \int_{t_0}^{t_1} \int_{-l_1}^{L+l_2} I_d \delta(x - c) \left[-v_{ttx} w_x - w_{ttx} v_x - 2 v_{tx} w_{tx} + 2\dot{\theta}\left(w_x w_{tx} + v_x v_{tx}\right) \right.$$

$$\left. + \ddot{\theta}\left({w_x}^2 + {v_x}^2\right) - 2\ddot{\theta} \right] \delta\theta \, dx \, dt$$

$$+ \int_{t_0}^{t_1} \int_{-l_1}^{L+l_2} m\delta(x - c) \left[g\cos\theta\left(v + e_d \cos\delta_d\right) - g\sin\theta\left(w + e_d \sin\delta_d\right) \right] \delta\theta \, dx \, dt$$

$$+\int_{t_0}^{t_1}\int_{-l_1}^{L+l_2}\left[\mu g v\cos\theta - \mu g w\sin\theta - d_e\,\mu\dot{\theta}\left(r_1^{\,2}+r_2^{\,2}\right)\right]\delta\theta\,dx\,dt$$

$$+\int_{t_0}^{t_1} m_b\left[wv_{tt} - vw_{tt} - 2\dot{\theta}\left(w w_t + v v_t\right) - \ddot{\theta}\left(w^2+v^2\right)\right]_{x=0,L}\delta\theta\,dt$$

$$+\int_{t_0}^{t_1} m_c\left[wv_{tt} - vw_{tt} - 2\dot{\theta}\left(w w_t + v v_t\right) - \ddot{\theta}\left(w^2+v^2\right)\right]_{x=L+l_2}\delta\theta\,dt$$

$$+\int_{t_0}^{t_1} I_{dc}\left[-v_{ttx}w_x - w_{ttx}v_x - 2v_{tx}w_{tx} + 2\dot{\theta}\left(w_x w_{tx} + v_x v_{tx}\right)\right.$$

$$\left.+\ddot{\theta}\left(w_x^{\,2}+v_x^{\,2}\right) - 2\ddot{\theta}\right]_{x=L+l_2}\delta\theta\,dt$$

$$-\int_{t_0}^{t_1}\left[m_b g\left(v\cos\theta - w\sin\theta\right)\right]_{x=0,L}\delta\theta\,dt$$

$$-\int_{t_0}^{t_1}\left[m_c g\left(v\cos\theta - w\sin\theta\right)\right]_{x=L+l_2}\delta\theta\,dt \;+\int_{t_0}^{t_1}\bar{\kappa}\;\delta\theta\,dt$$

VITA

Surjani Suherman was born on November 19, 1964 in Bandung, Indonesia. She graduated from Parahyangan Catholic University in March 1988 with a Bachelor of Civil Engineering degree. After graduation, she worked as a teaching assistant at her university until mid-1990. Besides that, she also worked as a structural design engineer for INACON Civil Engineering Consultant in Indonesia until early 1991.

In August 1991 she began pursuing a Master of Science degree in Civil Engineering at Virginia Polytechnic Institute and State University. She completed this degree in December 1992. Starting in January 1993, she continued her study for a doctoral degree in Civil Engineering. She worked as a research assistant in the Civil Engineering Department. After completion of her Ph.D. research, she worked on research in the area of inflatable frameworks.